TWO-DIMENSIONAL MATERIALS SATURABLE ABSORBER FOR GENERATION OF ULTRASHORT PULSE FIBER LASERS

ANAS BIN ABDUL LATIFF

INSTITUTE OF GRADUATE STUDIES
UNIVERSITY OF MALAYA
KUALA LUMPUR

2018

TWO-DIMENSIONAL MATERIALS SATURABLE ABSORBER FOR GENERATION OF ULTRASHORT PULSE FIBER LASERS

ANAS BIN ABDUL LATIFF

THESIS SUBMITTED IN FULFILMENT OF THE REQUIREMENTS FOR THE DEGREE OF DOCTOR OF PHILOSOPHY

INSTITUTE OF GRADUTE STUDIES
UNIVERSITY OF MALAYA
KUALA LUMPUR

2018

UNIVERSITY OF MALAYA

ORIGINAL LITERARY WORK DECLARATION

Name of Candidate: **ANAS BIN ABDUL LATIFF** [redacted]

Registration/Matric No: **HHE 140002**

Name of Degree: **DOCTOR OF PHILOSOPHY (PHOTONICS)**

Title of Thesis ("this Work"):

TWO-DIMENSIONAL MATERIALS SATURABLE ABSORBER FOR GENERATION OF ULTRASHORT PULSE FIBER LASERS

Field of Study:

PHYSIC (PHOTONICS ENGINEERING)

I do solemnly and sincerely declare that:

(1) I am the sole author/writer of this Work;
(2) This Work is original;
(3) Any use of any work in which copyright exists was done by way of fair dealing and for permitted purposes and any excerpt or extract from, or reference to or reproduction of any copyright work has been disclosed expressly and sufficiently and the title of the Work and its authorship have been acknowledged in this Work;
(4) I do not have any actual knowledge nor do I ought reasonably to know that the making of this work constitutes an infringement of any copyright work;
(5) I hereby assign all and every rights in the copyright to this Work to the University of Malaya ("UM"), who henceforth shall be owner of the copyright in this Work and that any reproduction or use in any form or by any means whatsoever is prohibited without the written consent of UM having been first had and obtained;
(6) I am fully aware that if in the course of making this Work I have infringed any copyright whether intentionally or otherwise, I may be subject to legal action or any other action as may be determined by UM.

Candidate's Signature Date:

Subscribed and solemnly declared before,

Witness's Signature Date:

Name:

Designation:

TWO-DIMENSIONAL MATERIALS SATURABLE ABSORBER FOR GENERATION OF ULTRASHORT PULSE FIBER LASERS

ABSTRACT

Two-dimensional (2D) material likes graphene, topology insulators (TIs), transition metal dichalcogenides (TMDs), Black Phosphorus (BP) and transition metal oxides (TMOs) have recently emerged as a promising solution for generating ultrashort pulse fiber lasers. These lasers have a high market potential for laser sensing and spectroscopy, material processing, and also medical applications since it has more compact in geometry and simpler in setup. Sharing some advantages from fiber technology, the developed laser is more robust, zero-alignment, and less operational cost. This study aims to develop ultrashort pulse fiber lasers operating at 1-, 1.55-, and 2-micron regions using new 2D materials as a saturable absorber (SA). Three new materials; MoS2, BP, and TiO2 are explored in this thesis. These SAs are fabricated and characterized in term of nonlinear absorption parameters. Furthermore, field emission scanning electron microscope (FESEM), electron dispersion spectroscopy (EDS), and Raman spectroscopy are being performed to confirm the presence of 2D materials in the fabricated SA. To validate the fabricated SA's performance, the SA is integrated into the laser cavity by sandwiching a piece of SA in between two fiber ferrules. The ultrashort pulsed fiber lasers are based on all-fiber ring cavity configuration utilizing Ytterbium doped fiber (YDF), Erbium doped fiber (EDF), Thulium doped fiber (TDF), and Thulium-Holmium co-doped fiber (THDF) as a gain medium as well as to provide a sufficient nonlinearity in the cavity. To avoid a self-pulsing instability, the free-polarization isolator is used to suppress a Brillouin backscattering. This can guarantee the pulse generation from the fiber laser owes from the SA. In some condition, additional nonlinear fiber is required to induce sufficient nonlinear effects in the cavity. Dispersion is one of another important cavity parameters where a large anomalous dispersion is normally preferable in the cavity to produce short

pulse width and higher peak power. Ultrashort pulse fiber lasers operating at 1-, 1.55-, and 2-micron regions with various performances are successfully achieved in this work. For instance, MoS_2 based mode-locked EDF laser produces a stable pulse train at 4 MHz repetition rate with 1.71 ps pulse width and the maximum pulse energy of 1.66 nJ is obtained at 250 mW pump power. These findings show that 2D nanomaterials have a great potential for photonic applications.

Keywords: Fiber lasers; Q-switching; mode-locking; ultrashort pulse generation; semiconductor materials.

PENYERAP TEPU BAHAN DUA-DIMENSI UNTUK PENGHASILAN LASER GENTIAN DENYUT ULTRA-PENDEK

ABSTRAK

Bahan dua-dimensi (2D) seperti graphene, penebat topologi (TI), peralihan logam *dichalcogenide* (TMD), fosforus hitam (BP), dan peralihan logam oksida (TMO) baru-baru ini muncul sebagai penyelesaian dalam menghasilkan laser gentian denyut ultra-pendek. Laser ini mempunyai potensi pasaran yang besar dalam pengesanan laser dan kespektroskopan, pemprosesan bahan, dan aplikasi perubatan, kerana geometri yang lebih padat dan mudah disediakan. Berdasarkan kelebihan sedia ada oleh teknologi gentian, laser yang dibangunkan bersifat lasak, penjajaran sifar, dan kos operasi yang rendah. Kajian ini bertujuan untuk membangunkan laser gentian denyut ultra-pendek yang beroperasi di kawasan 1-, 1.55- dan 2-mikron menggunakan bahan 2D yang baru sebagai penyerap boleh tepu (SA). Tiga bahan baharu; MoS_2, BP, dan TiO_2 diterokai dalam tesis ini. SA ini difabrikasi dan dicirikan dengan tujuan mempunyai parameter penyerapan tidak-linear. Tambahan pula, mikroskop pengimbasan pancaran medan elektron (FESAM), kespektroskopan serakan elektron (EDS), dan kespektroskopan Raman akan digunakan untuk mengesah kehadiran bahan 2D dalam SA yang difabrikasi. Untuk mengesahkan prestasi SA yang diperolehi ini, SA disepadukan ke dalam rongga laser dengan cara meletakkannya di antara dua gentian *ferrule*. Laser gentian denyut ultra-pendek berdasarkan konfigurasi rongga gelang jenis semua gentian menggunakan gentian terdop Ytterbium (YDF), gentian terdop Erbium (EDF), gentian terdop Thulium (TDF), and gentian terdop Thulium-Holmium (THDF) sebagai medium gandaan serta membekalkan kesan tidak-linear yang memadai ke dalam konfigurasi rongga. Untuk mengelakkan ketidakstabilan denyut-diri, penebat pengutuban bebas digunakan untuk menindas penyerakan balik Brillouin. Ini dapat menjamin penjanaan denyut oleh laser gentian adalah dari SA. Dalam keadaan tertentu, gentian tidak-linear tambahan

diperlukan untuk mendorong kesan tidak-linear yang mencukupi dalam rongga. Penyebaran merupakan salah satu parameter penting untuk rongga laser dimana kekuatan penyebaran negatif biasanya lebih baik untuk menghasilkan lebar denyut yang pendek dan kuasa puncak yang lebih tinggi. Laser gentian denyut ultra-pendek yang beroperasi pada kawasan 1-, 1.55- dan 2-mikron dengan pelbagai prestasi berjaya dicapai dalam kerja ini. Sebagai contoh, laser EDF mod-kunci berasaskan MoS_2 menghasilkan deretan denyut yang stabil pada kadar ulangan 4 MHz dengan lebar 1.71 ps lebar denyut dan tenaga denyut maksimum 1.66 nJ diperolehi dengan kuasa pam 250 mW. Penemuan ini menunjukkan bahawa bahan 2D mempunyai potensi besar untuk aplikasi fotonik.

Kata kunci: Laser gentian; Q-suis; mod-kunci; penghasilan denyut ultra-pendek; bahan separuh pengalir

ACKNOWLEDGEMENTS

In the name of Allah, the Most Gracious, the Most Merciful.

"The only way to do great work is to love what you do"

-Steve Jobs-

It is with immense gratitude that I would like to acknowledge the support and help of my supervisor, Professor Ir. Dr. Sulaiman Wadi Harun and Distinguished Professor Dr. Harith Ahmad. He has been a source of inspiration and has convincingly conveyed a spirit of adventure in regard to research. The initial ideas he suggested and his vast knowledge on fiber lasers were invaluable in helping me get set on the right track. The successful completion of my task would not have been possible without his constant encouragement and guidance throughout the whole period of my research work.

I would like to thank Universiti Teknikal Malaysia Melaka (UTeM) and Ministry of Higher Education Malaysia (MOHE) for sponsoring my PhD program under SLAB/ SLAI scholarship.

I am also extremely grateful for the companionship and support of my lab team (Farid, Haziq, Badrol, Ir. Hanafiah, Ezza, Ameelia, Ummi, Fauzi). For because of their companionship and help, the lab is a home and the experiments are pleasures.

My deepest appreciations from bottom of my heart go to my family for all support and love.

Thank you to my wife Anissuhailin for her love and encouragement.

TABLE OF CONTENTS

LIST OF FIGURES

LIST OF TABLES

LIST OF SYMBOLS AND ABBREVIATIONS

BP	:	black phosphorus
EDF	:	erbium doped fiber
EDFA	:	erbium doped fiber amplifier
EDFL	:	erbium doped fiber laser
Er^{3+}	:	erbium
FWHM	:	full-wave half-maximum
GVD	:	group velocity dispersion
Ho^{3+}	:	holmium
MMF	:	multimode fiber
MoS_2	:	molybdenum disulfide
OSA	:	optical spectrum analyzer
PVA	:	polyvinyl alcohol
QD	:	quantum dot
RF	:	radio frequency
SA	:	saturable absorber
ScDF	:	scandium doped fiber
SDS	:	sodium dodecyl sulfate
SMF	:	single mode fiber
SNR	:	signal-to-noise ratio
SPM	:	self-phase modulation
TBP	:	time bandwidth product
TDF	:	thulium doped fiber
TDFL	:	thulium doped fiber laser
THDF	:	thulium holmium co-doped fiber

THDFL	:	thulium doped fiber laser
TI	:	topological insulator
TiO_2	:	titanium dioxide
TIs	:	topological insulators
Tm^{3+}	:	thulium
TMD	:	transition metal dichalcogenide
TMDs	:	transition metal dichalcogenides
TMO	:	transition metal oxide
TMOs	:	transition metal oxides
WDM	:	wavelength division multiplexing
Yb^{3+}	:	ytterbium
YDF	:	ytterbium doped fiber
YDFL	:	ytterbium doped fiber laser
$\Delta\lambda_{3dB}$	:	3-dB spectral bandwidth
α	:	absorption coefficient
L	:	cavity length
v_m	:	degree of light slow down in material
D	:	dispersion
v	:	frequency
β_2	:	GVD
D_M	:	material dispersion
α_{ns}	:	non-saturable absorption
λ_o	:	operating wavelength
P_o	:	output power
P_p	:	peak power
E	:	photon energy

Q	:	pulse energy
T_r	:	pulse period
t	:	pulse width
n	:	refractive index
f_r	:	repetition rate
α_n	:	saturable absorption
I_{sat}	:	saturation intensity
c	:	speed of light in material
c_o	:	speed of light in vacuum
D_W	:	waveguide dispersion
λ	:	wavelength

CHAPTER 1: INTRODUCTION

1.1 Background

Ultrashort pulse lasers are an extremely useful type of laser and they are generated through a mode-locking technique. The mode-locking generates a phase coherent train of pulses with a repetition rate in a range of MHz and a pulse width in a range of nanoseconds to femtoseconds. The term mode-locking refers to the requirement of phase-locking many different frequency modes of a laser cavity in order to realize this type of laser. This locking mechanism induces a laser to produce a continuous train of extremely short pulses rather than a continuous-wave (CW) of light. The usefulness of such a system is its ability to generate an immense peak power. Application of these lasers range from micro-machining metals (Liu et al., 1997) all the way to facilitating the most precise frequency measurements ever made (Onae et al., 2000). Based on the many proposals for new technologies that utilize mode-locked lasers (Fermann & Hartl, 2013; Sun et al., 2010), it is clear that these lasers will be an invaluable tool for future technologies.

Typically, laser can be categorized based on a gain medium form either in solid-state, dye, or gas. This thesis deals with developments of new mode-locked fiber lasers operating in a range from 1- to 2-micron region. These lasers have received much attention due to their low cost, low power consumption, long term robustness, and ease of long distance transmission (through a standard silica single-mode fiber). This thesis only focused on ytterbium, erbium, thulium, and holmium rare earth elements as an active medium. All commercial available rare-earth doped silica glass fibers are summarized in Figure 1.1. As shown in the figure, standard rare-earth elements used in this thesis can generate laser emission at 1-, 1.55- and 2-micron region spectra. The red line shows the laser attenuation inside a silica glass fiber within a wavelength range from 350 to 2000 nm. It is shown that the fiber attenuation in silica glass fiber is nearly zero at wavelength region ranging from 1000 nm to 1700 nm. In this work, a newly developed saturable

absorber (SA) device is incorporated in a laser cavity to generate mode-locking pulses trains as described in Figure 1.2. The SA functions to convert CW laser into an ultrashort pulse laser with high peak power.

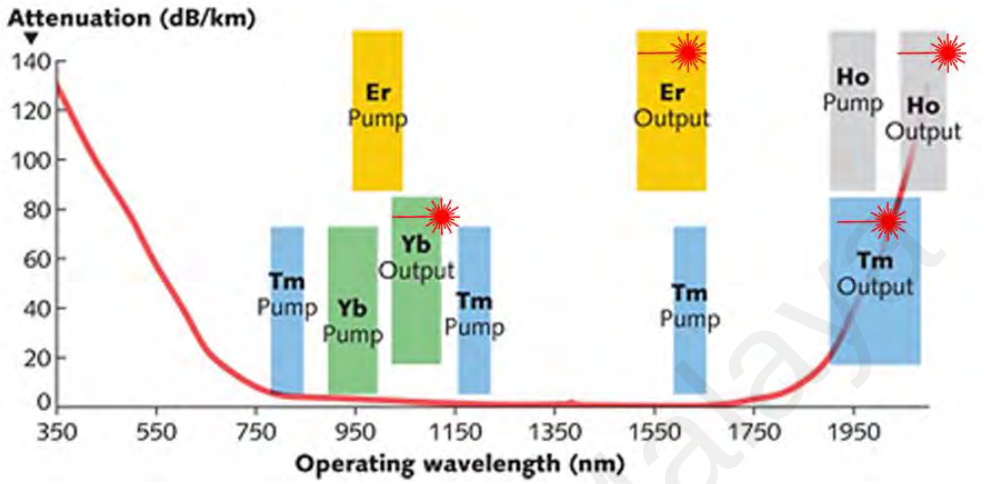

Figure 1.1: Fiber laser pump and laser emission region between 1- to 2-micron region spectra. The red line indicates silica attenuation. (Hecht, 2014)

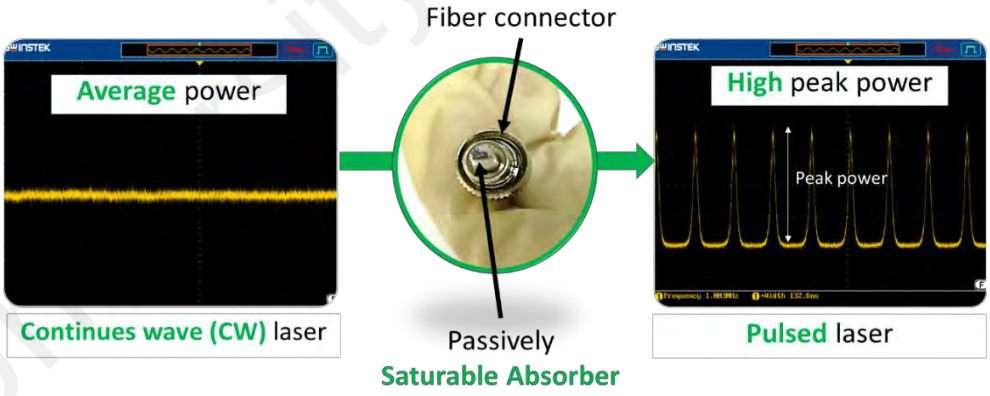

Figure 1.2: Conversion of CW laser to pulsed laser using a passive SA device.

1.2 History of Laser

The first conceptual building block of the laser was established in 1916 when Einstein proposed that photons could stimulate emission of identical photons from excited atoms (Straumann & Zürich, 2017). In 1951, Townes took the next conceptual step, suggesting that stimulated emission at microwave frequencies could oscillate in a resonant cavity, producing coherent output. In 1954, Townes and Gordon demonstrated the first microwave maser, directing excited ammonia molecules into a resonant cavity where they oscillated at 24 GHz (Gordon et al., 1954). In 1957, Gould sketched out a plan for the now-familiar Fabry-Perot resonator and had notarized about resonators mirrors in a notebook. The first word "LASER" was triggered from his notebook (Hecht, 2010). In the following year, Townes and Schawlow published a details proposal about the optical maser (Schawlow & Townes, 1958). The first laser was demonstrated by Maiman in 1960 at Hughes Research Labs. The ruby laser was constructed by slipping a small ruby rod inside the coil of a photographic flash-lamp and enclosing the assembly in a reflective cylinder. Then, he focused intense pump light into the ruby rod (Maiman, 1960a). Since that, lasers have become rich and complex history over the half-century. The first CW laser was demonstrated at Bell Telephone Labs by using the first gas laser which constructed from a helium-neon gas (Javan et al., 1961).

In 1961, Snitzer demonstrated the first neodymium-glass laser in a millimeter-scale rod with the neodymium glass in a high index core, making it essentially the first fiber laser (Snitzer, 1961). Three years after that, he demonstrated the first fiber amplifier by using a spring-shaped coil of fiber he slipped around a linear flash-lamp (Koester & Snitzer, 1964). More than two decades later, the fiber laser technology finally came into its own. Paynes et al. demonstrated a single-mode fiber laser incorporating a neodymium-doped silica glass as a gain medium in 1985 (Mears et al., 1985). He constructed an all-fiber neodymium-doped fiber ring cavity laser by pumping a neodymium-doped fiber

with 595 nm dye-laser. The schematic diagram is shown in Figure 1.3. The laser operated at 1078 nm with a 3-dB spectral bandwidth of 2 nm. Maximum output power of 2 mW was achieved at the maximum dye-laser power of 280 mW. The progressive research and development for fiber laser are not stopped here. The research work keeps continues by Payne's group (Mears et al., 1987; Reekie et al., 1986) and Desurvire (Desurvire et al., 1987) using an erbium-doped fiber for fiber laser and fiber amplifier applications at 1.55-micron region.

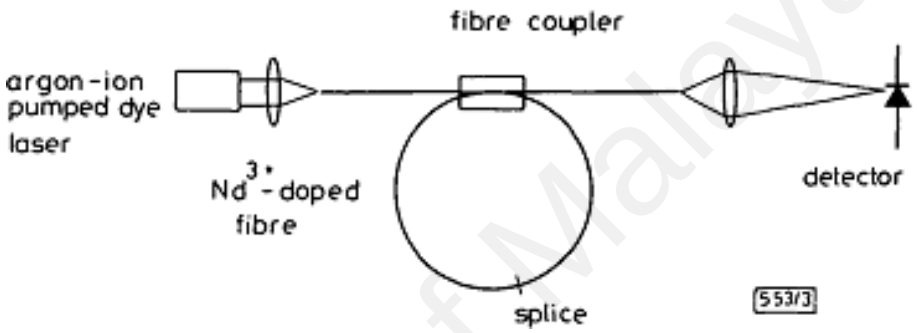

Figure 1.3: Schematic diagram of dye-laser-pumped fiber ring cavity laser by Paynes. (Mears et al., 1985)

Meanwhile, ytterbium also is an attractive ion for use in fiber lasers (Etzel et al., 1962). Hanna from the University of Southampton has successfully generated a laser using ytterbium-doped fiber to operate at 1-micron region (Pask et al., 1995). Objective to achieve high-power applications in fiber lasers was realized in 2009. IPG Photonics used a single-mode ytterbium-fiber oscillator amplifier to produce CW output power of 10 kW. While, for multimode fiber lasers, they manage to generate up to 50 kW (Gapontsev et al., 2009). In 2013, IPG Photonics demonstrated the most powerful continues-wave fiber laser which produces 100 kW at 1070 nm (Shcherbakov et al., 2013). In 1965, Johnson demonstrated a thulium and holmium ion as a gain medium to generate continues-wave lasers at 2-micron region wavelength (Johnson et al., 1965). The broad spectral bandwidth

of dye lasers opened the door to ultrashort pulse laser generation. In 1964, Willis Lamb showed that mode-locking a laser could generate pulses limited in duration by the Fourier transform of the bandwidth (Lamb, 1964). The research work on pulsed laser development still progressive until today.

1.3 Motivation of the Study

Ultrashort pulse fiber lasers are fundamental building blocks of many photonic systems used in industrial and medical applications as well as for scientific research (Fermann et al., 2013). More interesting, an essential subset of the lasers used today in the industry can be seen for example in machining glass for smartphone screens for the former, and laser eye surgery (Blackmon et al., 2015; Grudinin, 2013). Types of ultrashort pulse scientific lasers include oscillators and amplifiers, either of which can be constructed by using bulk or fiber-based components. The use of fibers (especially single-mode fibers) can lead to smaller geometry size, more rugged pulsed scientific lasers, nearly zero maintenance, high peak powers, and also high intensities.

The evolution of ultrashort pulse lasers development over the years can be seen in Figure 1.4. The first ultrashort pulse lasers, based on a dye gain medium, were expensive and unreliable while laser types based on solid-state gain medium have high reliability and costs appropriate for commercial lasers (Wallace, 2015). The technology was shifted to the solid-state gain medium such as Nd-YAG and then fiber laser. Over the past two decades, fiber laser technology has remarkably progressed and ultrafast lasers operating in the near-IR spectral region based on ytterbium, erbium, thulium, and holmium doped active fibers have replaced solid state lasers in many applications. Many of the components used in fiber lasers have been previously developed for mass production for telecommunications, thereby significantly decreasing the price for fiber lasers. Due to the

nature of optical fiber, fiber lasers do not require beam alignment and high maintenance. Since the light propagates entirely inside the optical fiber, which can be coiled to have very small volume, fiber laser systems are significantly more compact compared to solid-state lasers.

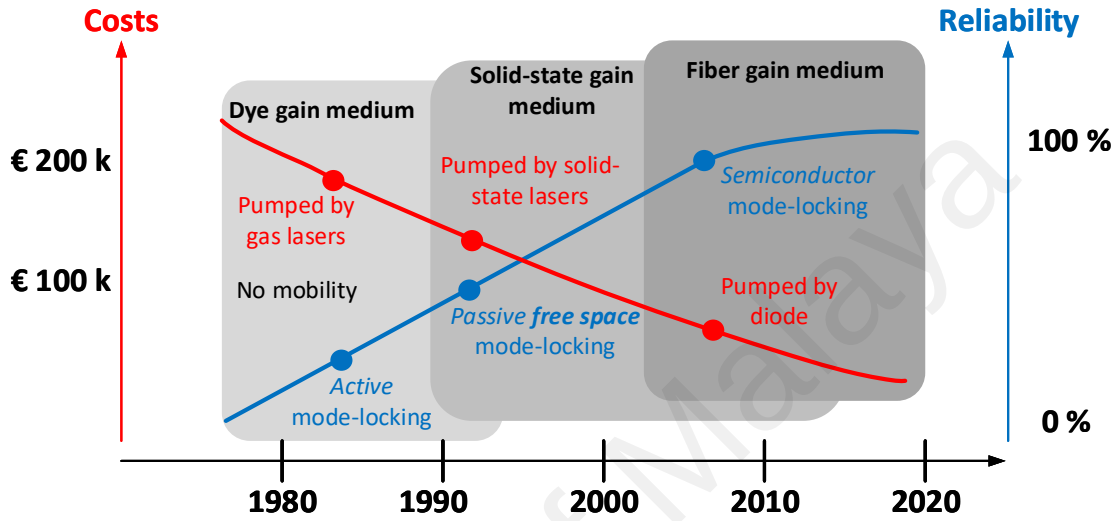

Figure 1.4: Pulsed lasers evolution from 1980. (Wallace, 2015)

SA is often preferred for generating pulsed laser emission, as they enable a wide space of pulse parameters to be accessed without employing costly and complex electrically-driven modulators that ultimately impose a lower limit on the pulse durations achievable directly from the laser source (Fermann et al., 2013; Sun et al., 2009). These devices can be broadly divided into two categories: real and artificial SA. Real SAs are based on materials that exhibit an intrinsic nonlinear decrease in absorption with increasing light intensity while artificial SA devices exploit nonlinear effects to mimic the action of a real SA by inducing an intensity-dependent transmission. Here, the work is restricted to real SAs, considering the role of emergent two-dimensional (2D) materials for this function and highlighting the benefits that they offer in terms of wideband operation, switching speed, and engineerable properties. Advances in SA technologies are almost synonymous

with the evolution of the laser itself: the first demonstrations of SA-based pulse generation in 1964 using both a "reversibly bleachable" dye (Soffer, 1964) and a colored glass filter (Bret & Gires, 1964) to Q-switch a ruby laser were reported just four years after Maiman's successful demonstration of laser operation (Maiman, 1960b).

Figure 1.5 shows the historical evolution of the salient SA technologies. After the initial demonstration of lasers in the 1960s, reversibly bleachable (or saturably absorbing) dyes were widely applied in mode-locked lasers, where the gain medium was also a dye, leading to the first demonstration of CW mode-locking (Ippen et al., 1972). With continued development in low-loss optical fiber, mode-locked lasers based on actively-doped fiber amplifiers emerged, including an early 1983 report of unstable mode-locking of a Nd:fiber laser using a dye SA (Dzhibladze et al., 1983). However, the passive generation of stable mode-locked pulses using an SA in fiber systems remained challenging until the semiconductor saturable absorber mirror (SESAM) was proposed in the early 1990s (U Keller et al., 1992; Zirngibl et al., 1991).

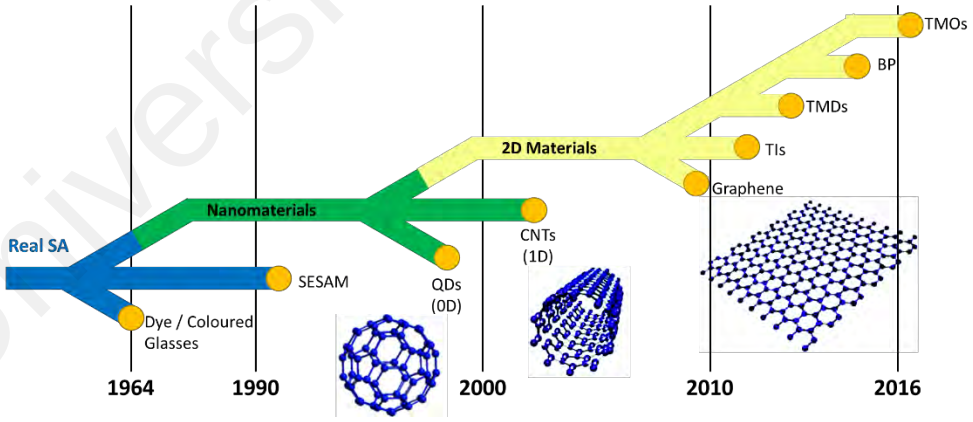

Figure 1.5: SA evolution from 1964. (Woodward & Kelleher, 2015)

SESAMs quickly became, and remain to be, a highly successful technology for generating ultrafast mode-locked pulses and high-energy Q-switched emission from fiber lasers. However, they offer only a narrow operating bandwidth, require costly fabrication and packing, and the relaxation speed is limited to picosecond time scales (unless expensive post-processing techniques are employed) (Keller, 2003). These limitations are driving research into novel materials for SA applications; of particular interest are nanomaterials, where reduced dimensionality leads to strong quantum confinement, new physical phenomena and remarkable optoelectronic properties (Novoselov et al., 2005; Wang et al., 2012). While it could be argued that early reports of saturable absorption using colored glass filters exploited nanomaterials, since the glasses were doped with semiconductor nanocrystals (zero-dimensional (0D) quantum dots (QDs)), such as cadmium selenide (Bret et al., 1964), to modify their color, it was not until 1997 that QDs were explicitly engineered for the purpose of pulse generation (Guerreiro et al., 1997). After this demonstration, the field of nanomaterial SAs gained traction as 1D carbon nanotubes (CNTs) (Set et al., 2004b) and 2D graphene (Bao et al., 2009; Hasan et al., 2009) emerged as promising materials exhibiting intensity-dependent absorption and sub-picosecond relaxation times (Martinez & Sun, 2013).

Graphene, a single atomic layer of carbon atoms that can be exfoliated from graphite, attracted particular interest, as its 2D structure and zero band gap enable wideband optical operation [10]. However, graphene is only one of a family of 2D materials that can be extracted as monolayer and few-layer crystals from a variety of bulk materials, including topological insulators (TIs), transition metal dichalcogenides (TMDs) and black phosphorous (BP). Transition metal oxides (TMOs) is also considered as another 2D material which has a potential to be utilized as SA. All of these materials offer distinct, yet complementary properties (Latiff et al., 2016; Li et al., 2015; Sobon, 2015; R. Woodward et al., 2015) and hence, new opportunities for optical applications in fiber-

based systems. The possibility of combining layers of 2D materials to form van der Waals heterostructures also offers an exciting prospect for a wide range of new engineerable photonic devices (Geim & Grigorieva, 2013), as does the potential to vary nanomaterial properties through their growth conditions, doping and electronic control (Lee et al., 2015; Lin et al., 2015). Table 1.1 describes a recent 2D materials group. It shows a molybdenum disulfide (MoS_2) and titanium dioxide (TiO_2) used in this work is categorized under 2D materials.

Table 1.1: Current 2D materials. (Geim et al., 2013)

<table>
<tr><td>Graphene family</td><td>Graphene</td><td colspan="2">hBN
'white graphene'</td><td>BCN</td><td>Fluorographene</td><td>Graphene oxide</td></tr>
<tr><td rowspan="2">2D chalcogenides</td><td colspan="2" rowspan="2">MoS_2, WS_2, $MoSe_2$, WSe_2</td><td colspan="2" rowspan="2">Semiconducting dichalcogenides:
$MoTe_2$, WTe_2,
ZrS_2, $ZrSe_2$ and so on</td><td colspan="2">Metallic dichalcogenides:
$NbSe_2$, NbS_2, TaS_2, TiS_2, $NiSe_2$ and so on</td></tr>
<tr><td colspan="2">Layered semiconductors:
GaSe, GaTe, InSe, Bi_2Se_3 and so on</td></tr>
<tr><td rowspan="2">2D oxides</td><td>Micas, BSCCO</td><td>MoO_3, WO_3</td><td colspan="2" rowspan="2">Perovskite-type:
$LaNb_2O_7$, $(Ca,Sr)_2Nb_3O_{10}$,
$Bi_4Ti_3O_{12}$, $Ca_2Ta_2TiO_{10}$ and so on</td><td colspan="2">Hydroxides:
$Ni(OH)_2$, $Eu(OH)_2$ and so on</td></tr>
<tr><td>Layered Cu oxides</td><td>TiO_2, MnO_2, V_2O_5,
TaO_3, RuO_2 and so on</td><td colspan="2">Others</td></tr>
</table>

1.4 Research Objectives

The aim of this research is to develop ultrashort pulse fiber lasers operating at 1-, 1.55-, and 2-micron regions using new 2D materials as an SA. We explore three new materials; MoS_2, BP, and TiO_2 in this work. Through the current challenges faces, a few objectives have been identified to guide this research work to meet the goal. The research objectives are outlined as

1. To fabricate the MoS_2, BP, and TiO_2 as a passive SA.
2. To characterize the SA characteristics of the MoS_2, BP, and TiO_2.

3. To validate the fabricated SAs performance through the generation of ultrashort pulse fiber laser operating at 1-micron, 1.55-micron, and 2-micron region.

Four work packages are implemented to ensure meets all research objectives. The list of the work packages is described in Table 1.2.

Table 1.2: Work package for this research work.

Work Packages	Task
WP 1	SAs fabrication and preparation
WP 2	SAs characterization
WP 3	Experiment on ultrashort pulse fiber lasers
WP 4	Optimization of ultrashort pulse fiber parameters

Note: WP – work packages

1.5 Thesis Outline

This thesis consists of six chapters including this chapter which serves as an introduction. This current chapter describes the background and history of a laser. The motivation and objectives of this research work are also described in this chapter. **Chapter 2** provides literature reviews on various topics on fiber lasers such as energy diagrams, mode-locking principle, SA, 2D materials and important laser parameters. **Chapter 3** demonstrates the use of MoS_2 based SA as mode-locker for ultrashort pulse generation. This chapter discusses on the MoS_2 SA preparation and characterization and fiber laser configuration, and then presents analysis data for the spectral and temporal laser performances of mode-locking operation at 1-, 1.55-, and 2-micron region.

Chapter 4 demonstrates the fabrication of TiO_2 thin film and the application of the TiO_2 film as a new type of effective SA for ultrafast photonics. The generation of mode-locking pulses in 1.55-, and 2-micron regions and Q-switching pulses in 1-micron region are demonstrated using a TiO_2 film. The film is fabricated by mixing the dispersed TiO_2 into a polyvinyl alcohol solution before going through a drying process and sandwiched between two fiber ferrules. **Chapter 5** explores another intriguing 2D material, BP for SA applications. The BP bulk crystal is mechanically exfoliated to obtain a layer of BP. The material is attached to the end-facet of a fiber ferrule, making it an SA device. By placing the SA into various laser cavities, mode locking pulses train operating at 1-, 1.55-, and 2-micron spectral regions are achieved. The findings in this thesis are summarized and concluded in **Chapter 6**. Future work suggestions are also provided as an extension of the work presented in this thesis.

CHAPTER 2: LITERATURE REVIEW

2.1 Introduction

The perception of ultrashort pulse lasers (mode-locked lasers) as being complex or unreliable has changed. Serious end users now consider fiber lasers, which are simpler than the complex conventional bulk laser systems to be a tool for their various applications. Most of the ultrashort pulse fiber lasers are constructed based on passively mode-locked fiber oscillators, which are then amplified in several stages to reach the desired output pulse energies. This chapter provides literature reviews on various topics on fiber lasers such as working principal of Ytterbium doped fiber laser (YDFL), Erbium doped fiber laser (EDFL), Thulium doped fiber laser (TDFL), and Thulium Holmium co-doped fiber laser (THDF) are explained since its work an important role to generate a stable ultrashort pulse laser. Then, the principal of saturable absorber (SA) is highlighted as the main contribution to provide a passive loss modulation in the laser cavity for ultrashort pulses formation. It causes the light propagated inside the cavity to induce a self-amplitude modulation. A two-level electronic model is used to describe the basic working principal of SA in the particle form. The obtained pulse then propagates through the optical fiber and it pulse dynamics can be influenced by a group velocity dispersion (GVD) and self-phase modulation (SPM). The balanced interaction between GVD and SPM have contributed in generating a solid and robust laser pulse shape. The material-based SA used in this thesis is a 2D material including MoS2, TiO2, and BP. Those materials have a bandgap energy which capable to be engineered until matching to absorption spectrum of 1-, 1.55-, and 2-micron region. Subsequently, the ultrashort pulse laser performance dependency would be different between these three materials. In the last session, the standard pulsed laser measurements are explained, especially a temporal and spectral characteristic.

2.2 Fiber Laser

Fiber technology is becoming more mature, and the recent major change is that fiber lasers (especially continues-wave and Q-switched lasers) are generally becoming well-developed tools for industrial applications. Soon after first demonstration of the practical laser by Maiman in 1960 (Duan et al., 2013), fiber lasers were proposed and studied as a promising laser configuration. The ability of optical fibers to confine light and propagate it around bends and loops has fascinated many researchers. Various types of rare-earth ions doped optical fibers, such as ytterbium (Etzel et al., 1962), erbium, thulium, or holmium have been widely used as a gain medium in fiber lasers. These rare-earth doped fiber lasers offer very narrow infrared beam laser output with high beam quality and high optical-to-optical efficiency. These rare-earth elements are optically active, and thus they can absorb light at one wavelength and emit light at another (Méndez & Morse, 2011). The invention of rare-earth doped fiber has opened the door for the developments of many new active devices such as generating ultra-short pulses, which have many potentials for many applications. Typically, rare-earth ions are doped in the silica glass host (Tünnermann et al., 2010). Figure 2.1 shows the absorption and refractive index of silica glass within 900 nm to 2100 nm (Kitamura et al., 2007). As can be seen in Figure 2.1(a), the lowest absorption in the silica glass fiber is around 0.2 dB/km within 1.55-micron region. At 2-micron region, the silica glass absorption rises from 3.5 dB/km to 8 dB/km, and close to 1 dB/km absorption at 1-micron region. Figure 2.1(b) shows the refractive index level for the silica glass is average at 1.5 with a variation of ± 0.1 within 900 nm to 2100 nm wavelength. The most commonly developed fiber lasers are based on Ytterbium-doped fiber (YDF), Erbium-doped fiber (EDF) and Thulium-doped fiber (TDF), which operate at 1-, 1.55- and 2-micron region, respectively. The principle operation of these fiber lasers are described in this thesis. The operation of Thulium Holmium co-doped

fiber (THDF) is also described in this thesis, which allow the laser generation at 2-micron region.

(a)

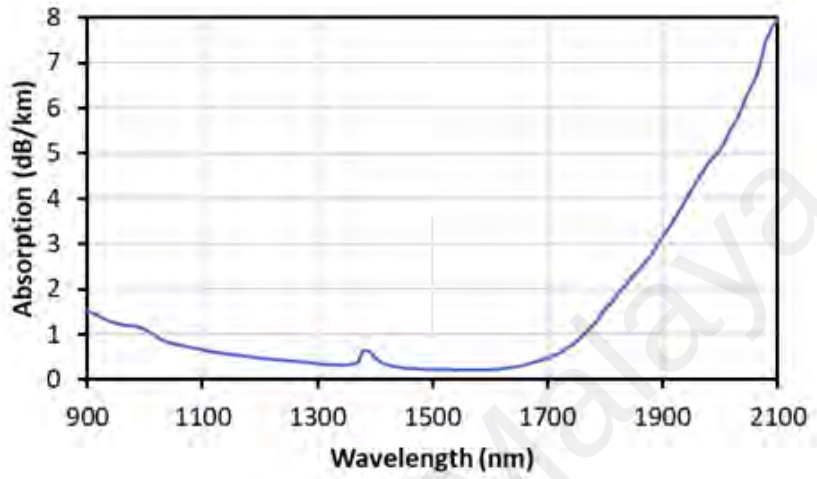

(b)

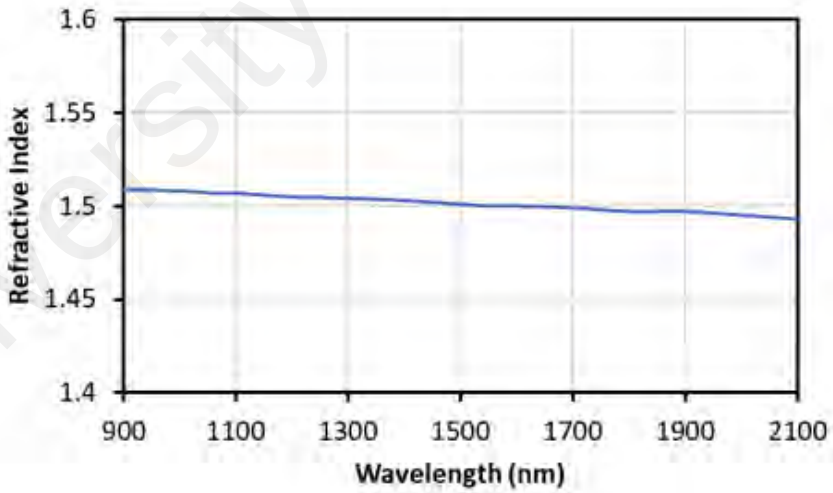

Figure 2.1: Optical characteristics of silica glass at near room temperature (a) absorption spectrum (b) refractive index profile. (Kitamura et al., 2007)

2.2.1 Ytterbium-doped Fiber Laser (YDFL)

In this thesis, YDF is used as a gain medium for producing a laser beam at 1-micron region based on 980 nm pumping. Figure 2.2 shows the absorption and emission cross-sections of a YDF, which indicates the high peak absorption at 980 nm region. Therefore, this wavelength is chosen as the pumping wavelength for the YDFL to emit laser operating in a wavelength region from 1020 nm to 1080 nm. Figure 2.3 shows the energy level diagram of the Ytterbium (Yb^{3+}) ions. It possesses a very simple electronic level structure with one excited state manifold ($^2F_{5/2}$) and one ground-state manifold ($^2F_{7/2}$). The small difference between absorption and emission spectrum leads to a small quantum defect that contributing to high optical-to-optical efficiency (>90%). Therefore, YDF is widely used to generate high power laser mainly for industrial application.

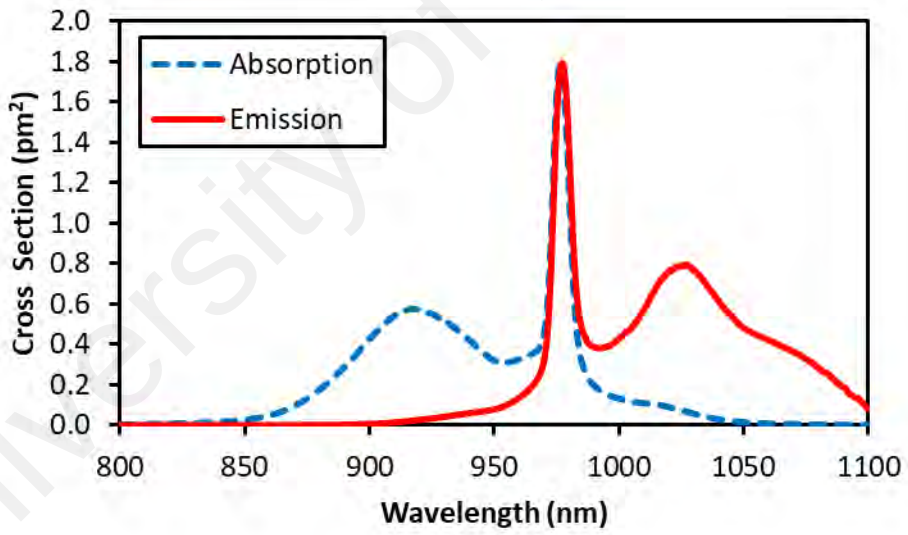

Figure 2.2: Absorption and emission cross-sections of Yb^{3+} ions.

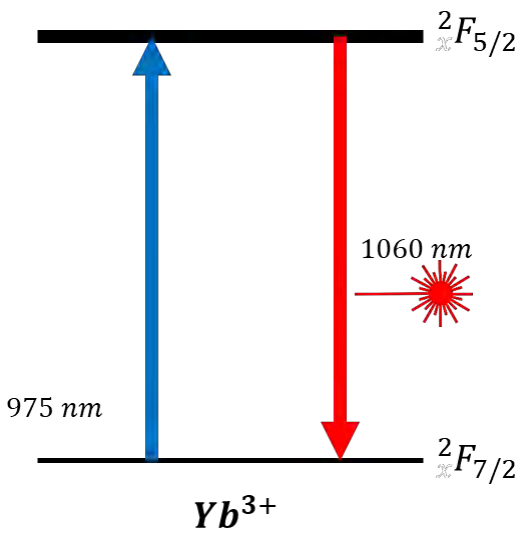

Figure 2.3: Simplified energy level diagram of the Yb^{3+} ions.

YDFL operates within 1-micron region and indicates that the transmission of laser beam inside the cavity is in normal dispersion region. Compared to EDF and TDF that having the transmission in anomalous dispersion, the YDF gain advantages since most of the laser operate in the normal dispersion. Therefore, there is no need for an external element to compensate the normal dispersion and to shift back the cavity into an anomalous dispersion in the case of using EDF and TDF. However, to generate a stable pulse, the YDFL design should take into account the nonlinearity effect such as group velocity dispersion (GVD) and self-phase modulation (SPM) that lead to pulse broadening and instability, respectively. The effect of these two opposing phenomena needs to balance out so that the cavity could produce soliton laser that can generate a stable and ultrashort pulse.

2.2.2 Erbium-doped Fiber Laser (EDFL)

Erbium (Er^{3+}) ion is usually used as an active element since it can operate at low loss region of 1.55-micron which suitable for optical communication application. Figure 2.4 shows the absorption and emission cross-section of Erbium doped fiber (EDF). The EDF can be used in both amplifier (erbium doped fiber amplifier, EDFA) and laser (Erbium doped fiber laser, EDFL) devices and both devices are operated based on the similar mechanism. EDFA can be transformed to EDFL device by incorporating a feedback system in the configuration. The EDF is usually used as a gain medium for ultra-short pulses generation due to its fiber gain spectrum, which is wide ranging and the fiber dispersion at 1.55-micron region is anomalous (Haris et al., 2014). This anomalous dispersion works with the nonlinearity in the fiber promising a good self-stable pulses generation that can be used in different type of practical application, especially in telecommunications window for wavelength division multiplexing (WDM) network (Tanabe, 2002).

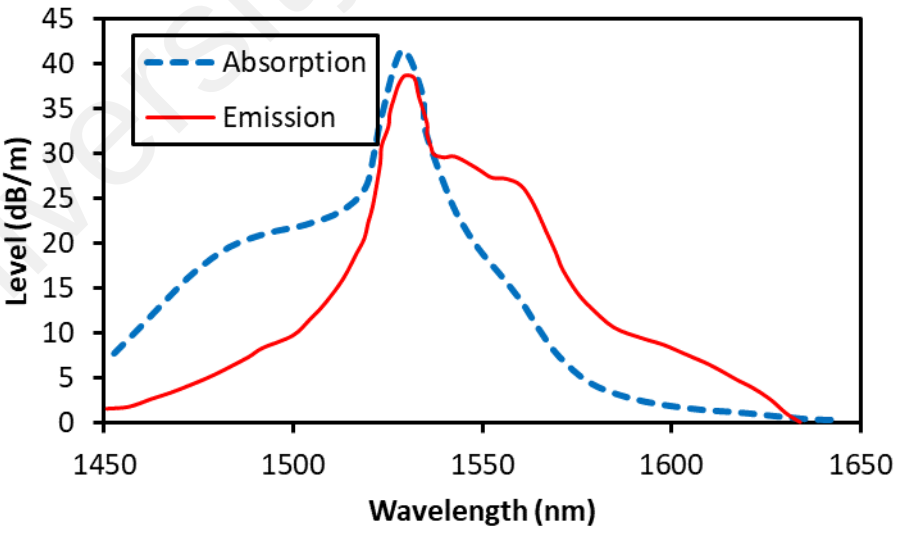

Figure 2.4: Absorption and emission cross-section of Er^{3+} ions.

EDF has emerged as a strong candidate for employment as the gain medium in a fiber ring laser, with particular desirable properties such as the broad gain bandwidth of typically tens of nanometers due to lack of sharpness in its energy level (Zhang et al., 2009). Figure 2.5 illustrates the energy level of Er^{3+} in silica fibers. The energy level $^4I_{15/12}$ corresponds to a ground state for laser transition. When the pump photon is absorbed, Er^{3+} ion is excited to a level of $^4I_{11/12}$ or $^4I_{13/12}$, depending on the pump wavelength used. In this research, erbium is excited by photons at 980 nm, and it has a nonradiative decay to a state $^4I_{13/12}$ where it can stay excited for relatively extended periods of time (lifetime ~ 10 ms) since the pump is provided from 980 nm laser diode pump. This property is extremely important, because the quantum efficiency of the device is dependent on how long it can stay in that excited state. If it relaxes too quickly, more photons are needed to keep it excited, meaning more input pump power is needed to make the amplifier work (Giles & Desurvire, 1991). Erbium can also be excited by photons at 1480 nm (energy level $^4I_{13/12}$). When excited that way, both the energy pumping process and the stimulated emission of the signal occur in the same wavelength and energy band.

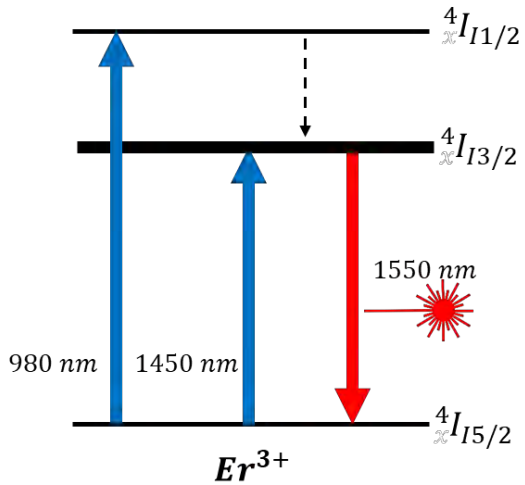

Figure 2.5: Simplified energy diagram of erbium ions in silica fibers.

2.2.3 Thulium-doped Fiber Laser (TDFL)

Thulium (Tm^{3+}) ion is a rare element with atomic number 69, which the main absorptions are located at 793 nm, 1210 nm, and 1560 nm wavelength regions. Typically, silica-based thulium-doped fibers (TDFs) have a vast emission spectrum, which ranging from 1800 nm to 2100 nm. The span is about 300 nm and thus it provides a wide flexibility in operating wavelength of the TDFL. This is due to the Tm^{3+} interaction with the local crystal field, its energy levels Stark split into broad energy bands, which is an inhomogeneous broadening effect (Agger & Povlsen, 2006). The increased phonon energies due to temperature changes also contribute to this broadening (Svelto & Hanna, 1976). TDFL operating at around 2-micron region can be realized by laser diode pumping at the wavelength near 790 nm ($^3H_4$) and 1560 nm ($^3F_4$). The 2-micron laser can be obtained in a single doped TDF due to the energy transition between the $^3F_4 \rightarrow {}^3H_6$ states.

The typical energy level diagram of the Tm^{3+} with possible laser transition and cross-relaxation process is shown in Figure 2.6. The $^3H_6 \rightarrow {}^3F_4$ absorption band of silica TDF possesses an extremely broad line-width, close to 130 nm, it is one of the broadest in any of the trivalent rare earth (Digonnet, 2001). The pump band mostly used for $^3H_6 \rightarrow {}^3H_4$ transition is at about 790 nm, which exhibits no significant excited-state absorption (ESA). The $^3H_6 \rightarrow {}^3H_4$ transition is very broad, and it allows pumping at the strong peak near 790 nm with either AlGaAs laser diode or sapphire laser. One important feature of this transition is the cross-relaxation between Tm^{3+} pairs, which takes place when the Tm^{3+} concentration is sufficiently high (Tropper et al., 1991). As shown in Figure 2.6, the cross-relaxation process leads to energy transfer from a Tm^{3+} ion in the $^3H_4$ level (donor) to a neighboring Tm^{3+} ion in the ground state (the acceptor). The latter is thus excited to the upper laser level ($^3F_4$ level), whereas the donor drops to the $^3F_4$ level, yielding two excited ions for one pump photon, or a quantum efficiency of 200 % as shown in Figure 2.6 (Moulton et al., 2009). In practice, Solodyankin et al. have demonstrated a quantum

efficiency of 180 % (Solodyankin et al., 2008). The phenomenon of cross-relaxation can be used to produce an efficient 2-micron laser using an 800 nm pumping in conjunction with TDF, which has high Tm^{3+} concentration. Another pump band for Tm^{3+} is at 1560 nm, where lasing near 2-micron in the pure TDF also occurs between the $^3F_4$ and $^3H_6$ states.

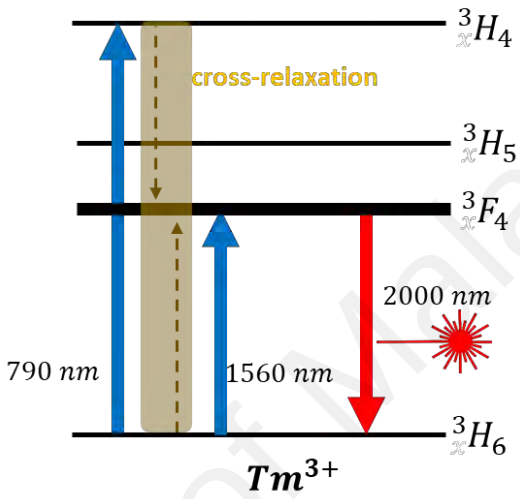

Figure 2.6: Simplified energy level diagram showing cross-relaxation of excited Tm^{3+} ion into the metastable level.

2.2.4 Thulium Holmium co-doped Fiber Laser (THDFL)

THDFL operation is based on energy transfer between Thulium (Tm^{3+}) and Holmium (Ho^{3+}) ions in THDF gain medium. To further understand the mechanism of energy transfer between Tm^{3+} and Ho^{3+} when pumped by 790 nm laser diode, the energy level diagram for silica THDF is shown in Figure 2.7. By pumping the fiber with 790 nm pump, Tm^{3+} ions can be excited to $^3H_4$ state from the $^3H_6$ ground state. When the quantities of Tm^{3+} ions are accumulated to a certain degree, most of the ions decay from the $^3H_4$ state to the $^3F_4$ state producing 1470 nm emissions. Meanwhile, other ions are excited from the $^3H_6$ ground state to the $^3F_4$ state, which is the cross relaxation between Tm^{3+}: state $^3H_4$ and Tm^{3+}: $^3H_6$ state ($^3H_4 + {}^3H_6 \rightarrow {}^3F_4 + {}^3F_4$). Once Tm^{3+} ions are saturated in $^3F_4$ level, on

one aspect, they decay to $^3H_6$ ground state with strong 1800 nm emission via $^3F_4 \rightarrow {}^3H_6$ transition; furthermore, Tm^{3+} ions in $^3F_4$ state transfer their energy to Ho^{3+}: $^5I_7$ state via energy transfer. When the ions are populated in $^5I_7$ state, the Ho^{3+} ions decay to $^5I_8$ ground state producing strong 2-micron emissions. Besides, ESA in Tm^{3+} and Ho^{3+} also produce fluorescence in weak visible at 480 nm and 550 nm from the Tm^{3+}: $^1G_4 \rightarrow {}^3H_6$ and Ho^{3+}: $^5S_2$, $^5F_4 \rightarrow {}^5I_8$ transitions, respectively.

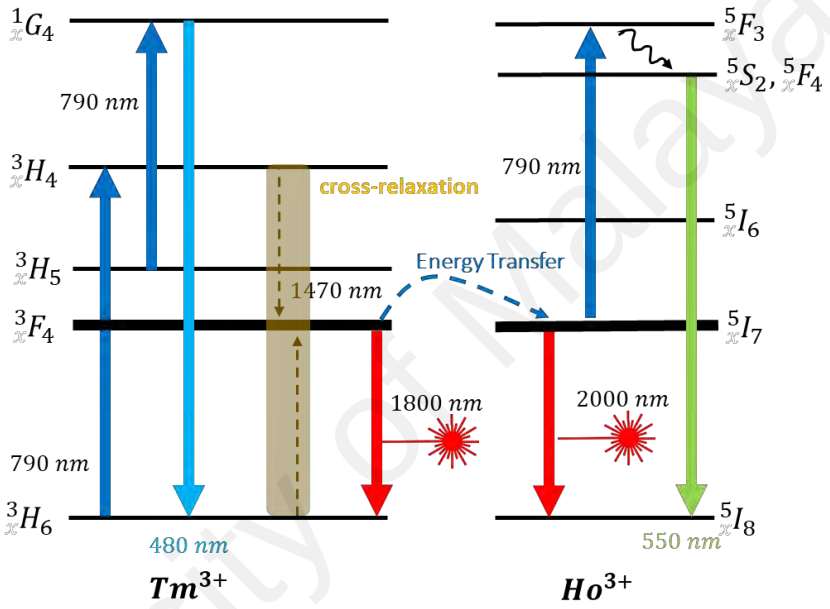

Figure 2.7: Simplified energy level diagram of Tm3+ and Ho3+ ions in silica glass fiber.

Figure 2.8 shows the energy-level diagram of silica THDF pumped by 1212- or 1560-nm laser. For 1560-nm pumping, there are four processes for generating 2-micron laser. First, the energy transfers from the $^3H_6$ to $^3F_4$ level of Tm^{3+} under the 1560-nm laser excitation. Then, the resonant energy exchange from the $^3F_4$ level of Tm^{3+} to the $^5I_7$ level of Ho^{3+} happens. In this step, a mass of Ho^{3+} accumulated in the $^5I_7$ level. After that, these Ho^{3+} ions return to the ground state ($^5I_8$ level) of Ho^{3+} through the spontaneous radiation. At last, by properly selecting an oscillation wavelength from the spontaneous radiation,

2-micron region laser by the stimulated radiation of Ho^{3+} ions can be achieved. For 1212-nm pumping, the energy-transfer process is different from the one of 1565-nm pumping above. First, the energy transfers from the $^3H_6$ to $^3H_5$ level of Tm^{3+} under the 1212-nm laser excitation. Then, two kinds of spontaneous emission could happen as follows: (1) originating from the $^3F_4$ to $^3H_6$ level of the Tm^{3+} ions centered around 1.8 ~ 1.9 μm and (2) originating from the $^5I_7$ to $^5I_8$ level of the Ho^{3+} ions centered around 2 μm. Thus, besides the conventional 1565-nm pumping, THDF with 1212-nm pumping also enables 2-micron laser emission.

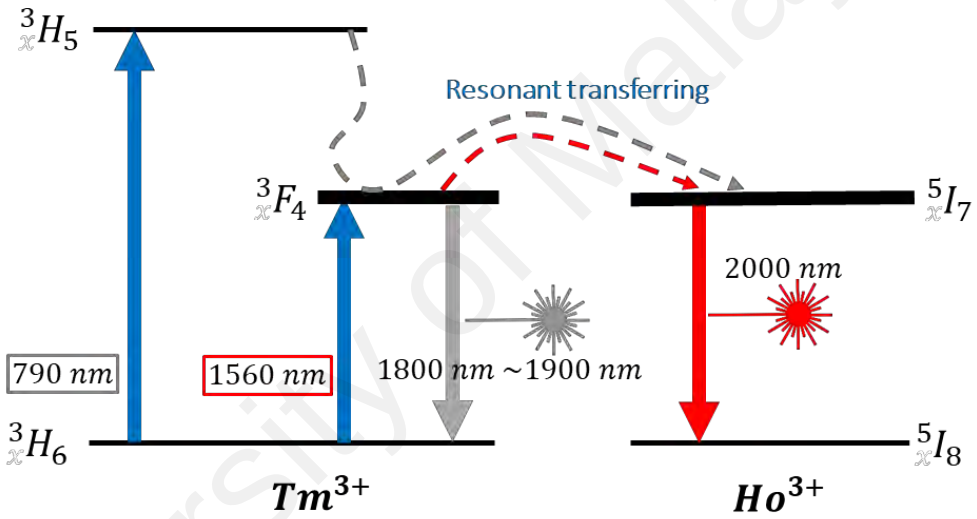

Figure 2.8: Simplified energy-level diagram of silica THDF pumped by 1212- or 1565-nm laser.

2.3 Ultrashort Pulse Fiber Laser with passive saturable absorber

A saturable absorber (SA) is a material in which the absorption of light decreases nonlinearly with increasing incident light intensity. It is incorporated into a fiber laser cavity for ultrashort pulse generation. Most of the SA is fabricated using a semiconductor material where the resonant nonlinearities that involve carrier transitions from the valance to conduction band produces the saturable absorption effect. To explain this phenomenon, ones often employ simple qualitative arguments based on a two-level electronic model, for which saturable absorption is symmetrical to gain saturation. Figure 2.9 illustrates the complete process of the saturable absorber based on two-level model in the particle form. As shown in the figure, the electrons in the ground state of the lower energy level or valance band (E_1) can absorb photons when their photon energy is the same as the difference between the two levels, and be excited to higher energy level or conduction band (E_2) if there is no electron at the upper state.

At wavelengths near the bandgap energy in direct gap materials the change in absorption and refractive index with intensity is particularly large. The primary source of the saturable absorption is due to band-filling. As the intensity increases, strong photoexcitation causes the states near the edge of the conduction and valence bands to fill, blocking further absorption. Band filling occurs because no two electrons can fill the same state. Significantly the absorption decreased due to the fact that less electrons at the ground state and less un-occupied states at the upper state. At high enough intensity, the material becomes transparent to light at photon energies just above the band edge. This process is also known as a Pauli blocking or phase space filling and was first predicted in 1969 (Zitter, 1969). As a result, the absorption is saturated and the light can be transmitted through the material without being absorbed. The electrons at upper state decay to ground state after reaching specific electron lifetime and the process continuously repeated.

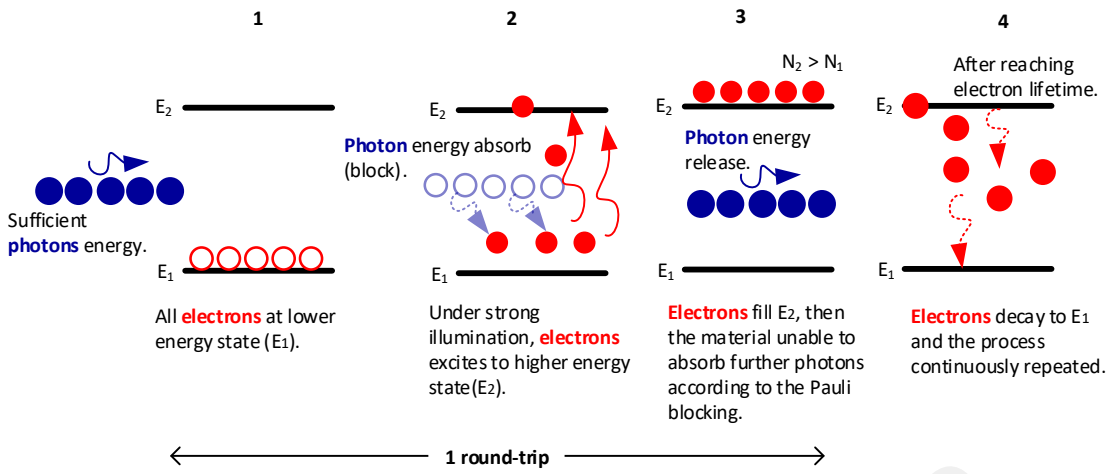

Figure 2.9: Illustration of saturable absorber working mechanism based on a two-level model in particle form.

Based on this simple framework, the optical nonlinearities are directly related to incident light intensity based on the following simple two-level SA model (Bao et al., 2009; Garmire, 2000; Zheng et al., 2012);

$$\alpha(I) = \frac{\alpha_s}{(1 + I/I_{sat})} + \alpha_{ns} \tag{2.1}$$

where $\alpha(I)$ is the absorption coefficient, α_s is the low-intensity (or sometimes called as linear) absorption coefficient, I is the incident light intensity, and I_{sat} is the saturation intensity, a phenomenological parameter, at which α decreases to a half of its value at low incident light intensity ($\alpha(I_{sat}) = \alpha_s/2$). The saturation intensity is an important parameter in determining the performance of a saturable absorber. This nonlinear relationship between the absorption coefficient and the incident light intensity is shown in Figure 2.10. The SA device can be used in passive mode-locking for ultrashort pulse laser generation because of this nonlinear relationship.

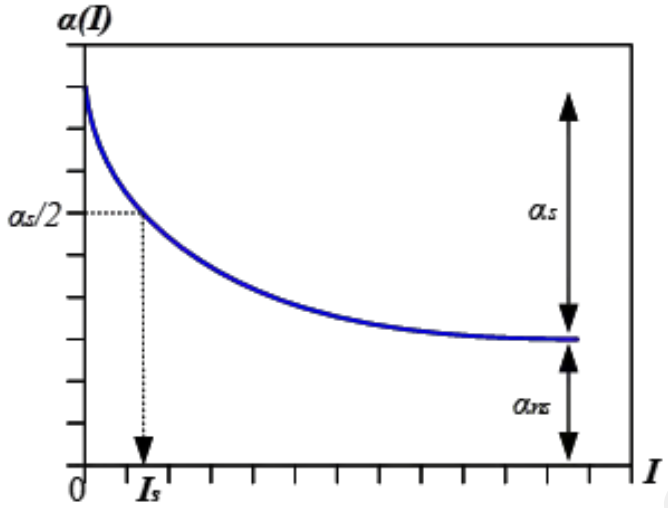

Figure 2.10: Nonlinear optical profile of the absorption coefficient of a two-level system as a function of the incident light intensity.

Mode-locking is a technique to generate ultrashort pulses from a laser cavity. Typically, the repetition rate of the mode-locking pulses is determined by the cavity per round-trip time $T_r = nL/c_o$, where n is the refractive index at laser operating wavelength, L is the laser total cavity length, and c_o is the speed of light in vacuum. In mode-locking operation, various longitudinal modes induce from the laser oscillation may force to be locked in phase to one another. Figure 2.11 shows the sum of oscilloscope train after phase locked by three longitudinal modes of E_A, E_B, and E_C in the laser cavity. Locking the phases of multiple longitudinal modes in the laser cavity initiates a periodic constructive interference which presence as a form of pulse with a pulse separation equivalent to the repetition rate. This process will generate pulses with an extremely short pulse width (picoseconds to femtoseconds).

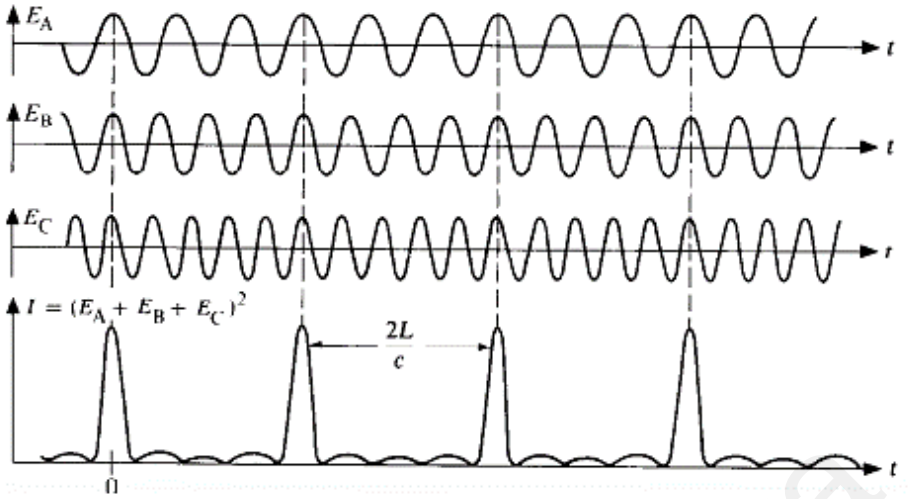

Figure 2.11: Phase locking process.

Active mode-locking uses the acousto-optic or electro-optic modulator as an external signal. However, it is not an ideal solution for generating pulses with a pulse width less than few picoseconds. This issue is due to limiting factor come from the speed of the modulation electronics. Passive mode-locking technique can be obtained by integrating the SA device inside the laser cavity as described in Figure 2.12. The SA is a nonlinear element which provides attenuation for the wing of the pulse with a low light intensity and minimum losses for dominant part of the pulse with a high intensity. Thus, it used to obtain a self-amplitude modulation of the light inside the laser cavity. This absorber induces some loss to the intra-cavity laser radiation.

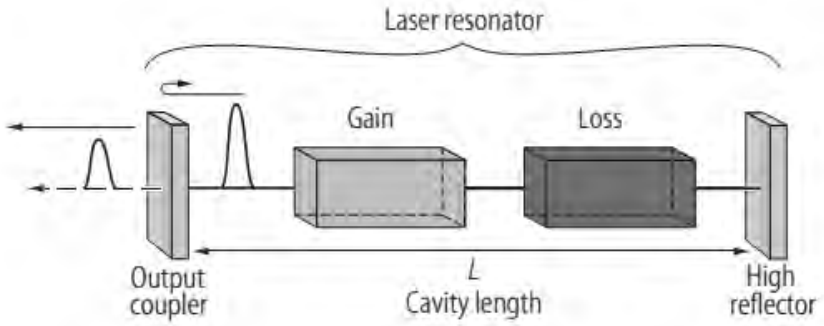

Figure 2.12: Schematic configuration of mode-locked lasers using a saturable absorber. (Keller, 2003)

Figure 2.13 illustrates the short pulse evolution in a SA based mode-locked fiber laser. In the laser, fluctuating normal noise generated from the incoherent interference of random modes (longitudinal modes) in the laser becomes a key start for passive mode-locking (Figure 2.13(a)). A single strong noise spike experiences less loss compared to the weak noises when passing through the SA. This strong noise spike suppresses all other background noises through small amount of saturable absorption to build up in highly energetic intensity. This is attributed to the spike that saturating the gain to a level (below I_s) of the other background noises can only experience net losses in each round-trip (Figure 2.13(b)). In the following round trips, the dominant noise spike is strongly amplified and significantly reduce its loss in the SA, so that the stronger noise spike continues to further reduce its loss and continues its growth until reaching steady state where a stable pulse train can be formed (Figure 2.13(c)).

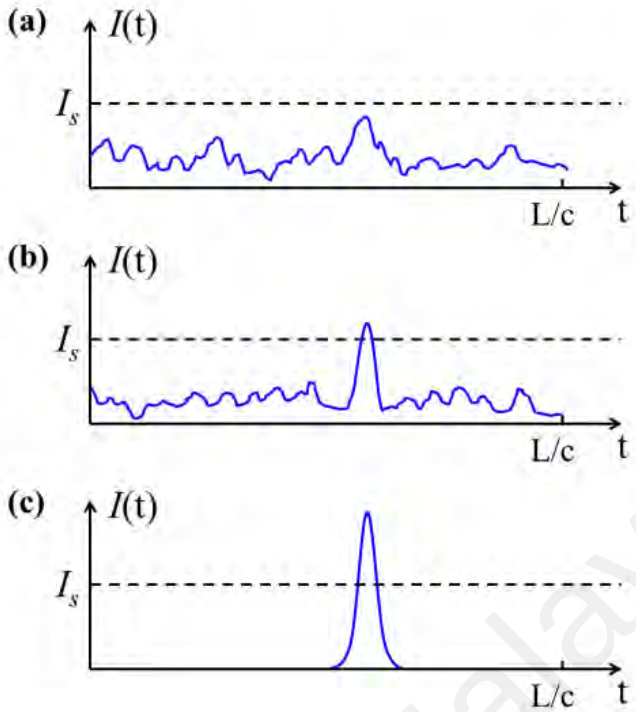

Figure 2.13: Short pulse evolution process of passive mode-locking technique by a saturable absorber. (a) Low intensity regime ($\boldsymbol{I_i < I_s}$), with random fluctuations. (b) $\boldsymbol{I_i = I_s}$, the onset of the discrimination of the weak peaks. (c) Final energy distribution.

Figure 2.14 shows the temporal evolution of gain and loss inside the laser cavity. It is shown that the loss is relatively large for low intensity of laser radiation and significantly smaller for a short pulse with high intensity (stronger noise spike). Then, a short pulse produces a loss modulation because the high intensity at the peak of the pulse saturates the absorber more strongly than its low intensity wings. This results in a loss modulation with a fast-initial loss saturation (reduction of loss) determine by the pulse width and typically slow recovery which depends on the detailed mechanism of the absorption process in the SA. In effect, the circulating pulse saturates the laser gain to a level which is just sufficient to compensate the losses for the pulse itself, while any other circulating low-intensity light experience more loss than gain, and thus dies out during the following round trips.

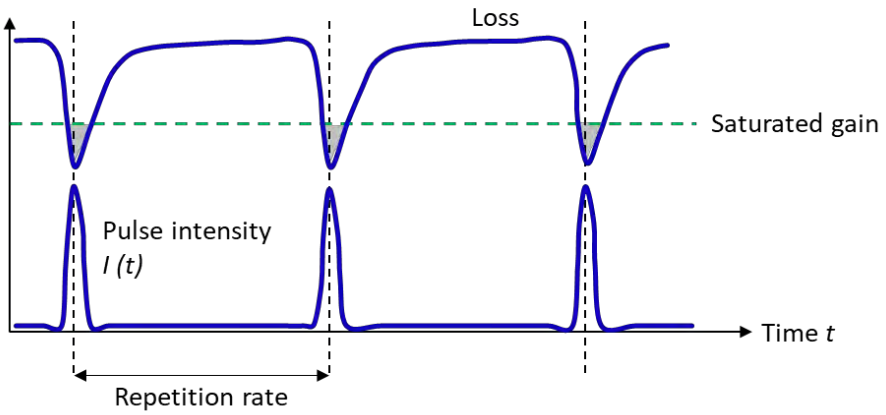

Figure 2.14: Temporal evolution of gain and loss inside the laser cavity. (Keller, 2003)

The relation between the number of longitudinal modes locked in phase and oscilloscope train generated by a mode-locking technique is shown in Figure 2.15. The typical continues wave lasers have unstable pulse train due to multiple modes propagate in incoherent phase (Figure 2.15(a)). The full pulse train generates coherent phases during four oscillated modes (Figure 2.15(b)) and the extremely short pulse generates coherent phases during 90 oscillated modes (Figure 2.15(c)). Therefore, it is clear that the mode-locked pulse becomes shorter when more phases are in-line coherently.

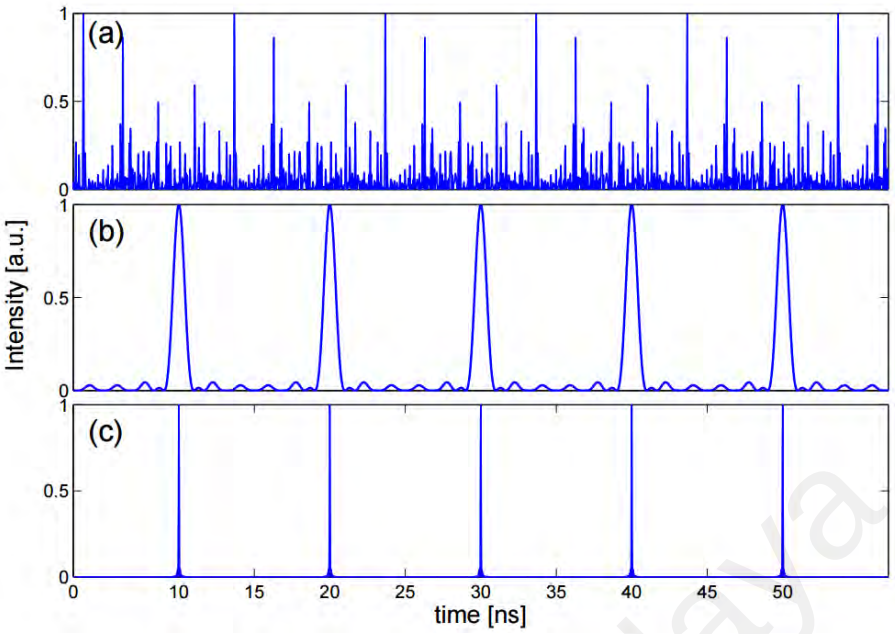

Figure 2.15: Pulse train of the mode-locked laser. (a) continues laser with no phase coherence, (b) 4 phase coherent modes, and (c) 90 phase coherent modes.

Another technique to generate pulses from a laser is a Q-switching. By using this technique, the obtained laser pulses are short pulse width (nanoseconds to picoseconds) and high pulse energy. The Q-switched lasers are always having a repetition rate much lower than the time per cavity round-trip. The principle of the technique is based on a shutter inside the laser cavity. If the shutter is closed, laser cannot generate and excess of population inversion reached over the threshold population of non-present shutter condition. If the shutter is now open suddenly, greater gain obtained from laser is exceeded the losses, and the stored energy will be released in the form of a short and intense light pulse. Since this technique involves switching the cavity Q-factor from low to high value, it is known as Q-switching. SA is replacing the shutter in passive Q-switching technique.

2.4 Propagation of Optical Pulses in a Fiber

Because of the difference between the refractive indices of the core and the cladding, it is possible to transmit of light inside the fiber. The refractive index of the core must be always higher than the refractive index of the cladding. The modal theory can explain the existence of an angle of incidence that enables the phenomenon of total internal reflection (Okamoto, 2010). Light, while propagating in the fiber, can be seen as an electromagnetic phenomenon, and the whole propagating mechanism, which can be described by the electromagnetic optical fields associated to it, is governed by Maxwell equations (Agrawal, 2013). Any pulse, while propagating in an optical fiber, especially in the linear regime, suffers the effect of time dispersion, which causes its broadening and may create interference between symbols, which can greatly limit the bandwidth of the signal to be transmitted.

Pulse propagation in nonlinear regime is affected by the optical Kerr effect. The propagation of impulses in Nonlinear Dispersive Regime (NLDR) is governed by the SPM and the group velocity dispersion (GVD) simultaneously (Agrawal, 2013). In the anomalous dispersion region, SPM effect is contrary to the GVD, thereby allowing the propagation of pulses very interesting because it does not change its shape over propagation in the fiber. These pulses are called soliton. In this section, the dispersion phenomena, SPM and soliton generation are briefly discussed.

2.4.1 Dispersion

The light-wave travels at a constant speed c when propagating through a free space. However, when light travel through a material it speed is slowed down due to interaction between the light's electromagnetic field and the material's electron cloud. The degree to

which the light is slowed down is represented as a material refractive index n, which relates to the speed of the light in the material by

$$v_m = \frac{c}{n} \tag{2.2}$$

Since the interaction of the electromagnetic field with the material depends on the frequency of the light (wavelength), the refractive index also depends on the frequency of light. This property is referred to as chromatic dispersion. Chromatic dispersion is also called material dispersion and is given by

$$D_M(\lambda) = \frac{\lambda}{n}\frac{d^2n}{d\lambda^2} \tag{2.3}$$

in which the refractive index n is a function of wavelength λ. Chromatic dispersion plays a critical role in the propagation of laser pulses. If the laser pulses contained only one frequency component, it would travel through the material without any distortion. In practical, pulse is consisted of a range of different frequencies. The shorter the pulse (time domain) the wider the range of frequency it covers (frequency domain). Unfortunately, different frequency components will travel at different speeds; some travel faster, some lag behind. This making pulse width become broadening.

Besides chromatic dispersion, the light also experiences an additional dispersion caused by the structure of the optical fiber. It is known as waveguide dispersion and can be described as

$$D_w(\lambda) = -\frac{n_2(\lambda)\Delta}{c\lambda}V\frac{d^2(Vb)}{dV^2} \tag{2.4}$$

where $n_2(\lambda)$ is the refractive index of the fiber core, Δ is the refractive index different, b is the normalize propagation constant and V is the normalized frequency. The total dispersion of the fiber is the combination of chromatic dispersion and waveguide dispersion:

$$D(\lambda) = D_M(\lambda) + D_W(\lambda) \tag{2.5}$$

The propagation of a laser pulse in a fiber is characterized by a mode propagation constant β. The mode propagation constant β can be expanded in a Taylor series about the center frequency ω_0

$$\beta(\omega) = \frac{n(\omega)\omega}{c} = \beta_0 + \beta_1(\omega - \omega_0) + \frac{1}{2}\beta_2(\omega - \omega_0)^2 + \cdots \tag{2.6}$$

where

$$\beta_m = \left.\frac{d^m\beta}{d\omega^m}\right|_{\omega=\omega 0} (m = 0,1,2, \dots) \tag{2.7}$$

The pulse envelope moves at the group velocity ($v_g = 1/\beta_1$) while the parameter β_2 is responsible for pulse broadening. β_2 is generally referred to as the GVD parameter and relates to the chromatic dispersion parameter D by

$$\beta_2 = -\frac{\lambda^2 D}{2\pi c} \tag{2.8}$$

The fiber is said to exhibit normal dispersion for $\beta_2 > 0$, and to exhibit anomalous dispersion for $\beta_2 < 0$. In the normal dispersion regime, high frequency (blue-shifted) components of an optical pulse travel slower than the low frequency (red-shifted) components. The opposite occurs in the anomalous dispersion regime.

Pulse broadening induced from dispersion degrades initial pulse's intensity, which can cause two adjacent pulses to overlap. This leads to errors at receiver in fiber optic communication systems. However at a good side, combination dispersion and SPM effect can lead to the formation of an optical soliton, where the wave is stable and unchanged during its propagation through the fiber.

2.4.2 Nonlinear Effect

Nonlinear effect phenomena occur in any dielectric medium as a consequence of the modification of the optical properties of a material system by the presence of sufficient intense laser light. These phenomena are "nonlinear" in the sense that they occur when the response of a material system to an applied optical field depends in a nonlinear manner on the strength of the optical field. Therefore, the dielectric medium behaves like a nonlinear medium. A year after Maiman demonstrates on first working laser in 1960 (Maiman, 1960a), Franken et al. discover a second-harmonic generation and thus become a stepping stone to field of nonlinear optics (Franken et al., 1961).

An optical nonlinearity can be considered as how the polarization $\tilde{P}(t)$ of a material system depends on the strength $\tilde{E}(t)$ of an applied optical field (Agrawal, 2013). At first, the induced polarization depends linearly on the field strength which can be describe as

$$\tilde{P}(t) = \epsilon_0 \chi^{(1)} \tilde{E}(t) \tag{2.9}$$

where the constant of proportionality $\chi^{(1)}$ is known as the linear susceptibility and ϵ_0 is the permittivity of free space. From the Equation 2.9, nonlinear effect can be express in the polarization $\tilde{P}(t)$ as a power series in the field strength $\tilde{P}(t)$ as

$$\tilde{P}(t) = \epsilon_0 [\chi^{(1)} \tilde{E}^1(t) + \chi^{(2)} \tilde{E}^2(t) + \chi^{(3)} \tilde{E}^3(t) + \cdots] \tag{2.10}$$

The quantities $\chi^{(2)}$ and $\chi^{(3)}$ are known as the second- and third-order nonlinear optical susceptibilities, respectively. Second-order nonlinear optical interactions can occur only in noncentrosymmetric crystals (crystals that do not display inversion symmetry). Since liquids, gases, amorphous solids (such as glass), and even many crystals display inversion symmetry, $\chi^{(2)}$ vanishes identically for such media, and consequently such materials cannot produce second-order nonlinear optical interactions. On the other hand, third-order

nonlinear optical interactions describe by $\chi^{(3)}$ susceptibility can occur for both centrosymmetric and noncentrosymmetric media.

In optical fiber, the nonlinear effects occur either due to intensity dependence of refractive index of the silica glass medium or due to inelastic-scattering phenomenon. The power dependence of the refractive index is responsible for the Kerr-effect. This Kerr-nonlinearity manifests itself in three difference effects such as self-phase modulation (SPM), cross-phase modulation (CPM), and four-wave mixing (FWM). For inelastic-scattering phenomenon, silica glass medium can induce stimulated Brillouin-scattering (SBS) and stimulated Raman-scattering (SRS) at only high-power level. In this thesis, only the relevant nonlinear effects including SPM is discussed.

2.4.2.1 Self-phase modulation (SPM)

Inside the optical fiber, the fiber refractive index is not only varied with wavelength but also varied with the intensity of the propagated light. The interaction between light and the material electron cloud increases nonlinearly with the light intensity, so the high-intensity light travels slower than the low-intensity one. As a result, the fiber refractive index increases with the intensity of light and can be described as

$$n_{eff} = n_l + n_{nl} I \tag{2.11}$$

where n_{eff} is the effective refractive index, n_l is the linear refractive index, n_{nl} is the nonlinear refractive index, and I is the light intensity inside the fiber.

SPM is one of the most concern effects of the fiber nonlinearity on the pulse propagation theory. Under the SPM effect, the optical pulse experiences a phase shift induced by the intensity-dependent refractive index while the pulse shape remains

unchanged. The nonlinear phase constant ϕ_{nl} introduced by a field $\tilde{E}$ over a fiber length L is

$$\phi_{nl} = \frac{2\pi}{\lambda} n_{eff} L \tag{2.12}$$

where λ is the operating wavelength of pulse laser propagating in fiber of effective refractive index n_{eff} along the optical path length of L.

Inside the fiber, the propagated light intensity is time varying and has caused to produce a time varying refractive index. So, the leading edge of a pulse will experience a positive refractive index gradient $(+dn/dt)$ which leads to red shift, and for trailing edge of a pulse, a negative refractive index gradient leads $(-dn/dt)$ to blue shift. This temporally varying index change results in a temporally varying phase change, as shown in Figure 2.16. The optical phase changes with time in exactly the same way as the optical signal.

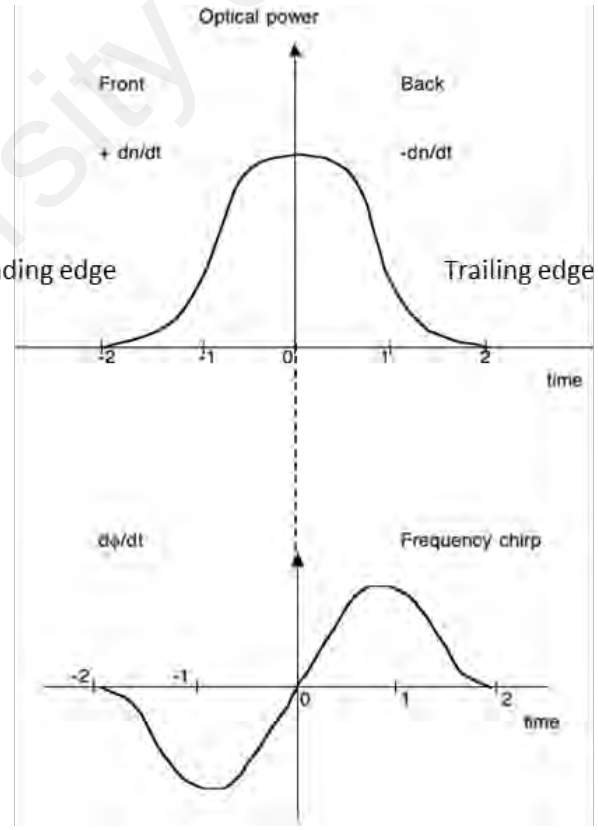

Figure 2.16: Phenomenological description of spectral broadening of pulse due to SPM. (Singh & Singh, 2007)

If intensity is time dependent, the wave is temporally modulated and phase ϕ will also depend on time. This variation in phase ϕ_{nl} with time is responsible for change in frequency spectrum ω, which is given by

$$\delta\omega = \frac{d\phi_{nl}}{dt} \tag{2.13}$$

The time dependence of $\delta\omega$ is referred as a frequency chirping. This chirping phenomenon is generated along the temporal pulse profile where ϕ_{nl} increases with the interaction fiber length. This denotes to the new instantaneous frequency generation at $\omega_0 + \delta\omega(t)$ as the pulse propagates inside a fiber and therefore leads to the spectral broadening of the pulse. Important application of SPM concept is in solitons.

2.4.3 Soliton

Consider the case that pulse laser operates under anomalous dispersion regime ($\beta_2 < 0$). SPM lead to lower frequency (longer wavelength) components at the leading edge of the pulse and higher frequency (shorter wavelength) components at the trailing edge. In the anomalous dispersion regime, lower frequency (longer wavelength) components travel slower than higher frequency (shorter wavelength) components. Therefore, the anomalous dispersion causes the leading edge of the pulse to slow down while the trailing edge travels faster. Effectively, SPM compensate the broadening of the pulse and undo the dispersion induce by laser. If the pulse has the shape so that the effects of SPM and GVD cancel out with each other, then the pulse maintains its initial width along the entire length of the fiber. In such situation, the pulse would propagate undistorted by mutual compensation of dispersion and SPM. This solitary wave pulse is called a soliton. Since

soliton pulse does not broaden during its propagation, it has tremendous potential for applications in super high bandwidth optical communication systems.

Typical soliton pulse laser consists of narrow sidebands visible at both left and right of the center wavelength of the soliton spectrum (Figure 2.17). These sidebands can be addressed as a Kelly sideband. Kelly sidebands are lower intensity and have sharp and narrow peaks. The wavelength separation between the orders Kelly sidebands from the center of the soliton spectrum can be described by

$$\Delta\lambda = \frac{1.763\lambda^2}{2\pi c_o \tau}\sqrt{\frac{m4\tau^2}{L|\beta_2|} - 1} \tag{2.14}$$

where λ is the center soliton wavelength, τ is the pulse width, c is the speed of light, m is the order of sidebands, and β_2 is the GVD with a cavity length of L (Dennis & Duling, 1994; Nelson et al., 1997; Smith et al., 1992).

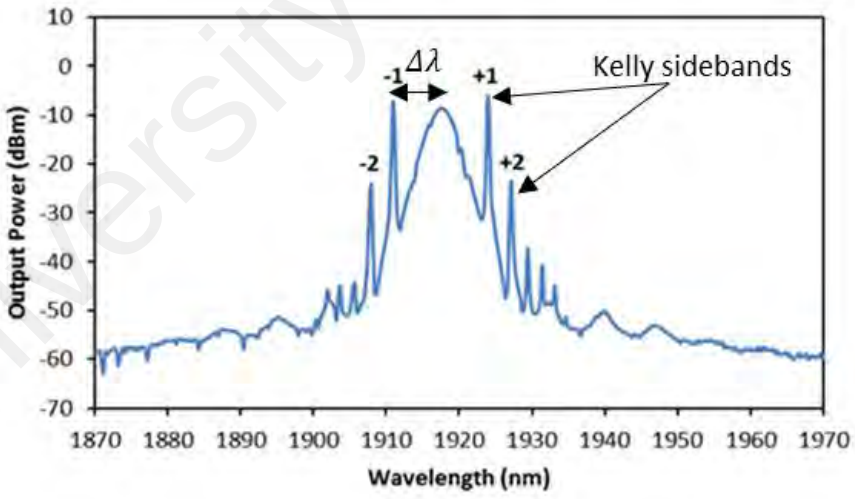

Figure 2.17: Output spectrum of soliton pulse laser.

Soliton pulses require a delicate energy-mediated balance between the nonlinearity and the dispersion, which limits the pulse energy Q for a fundamental soliton to

$$Q = \frac{1.763 \times 2|\beta_2|}{\gamma\tau} \tag{2.15}$$

where γ is the nonlinear coefficient of the optical fiber mode, τ is the pulse width, and β_2 is the GVD. One way to better understand the balanced interaction between nonlinearity and dispersion is through characteristic length. The characteristics nonlinear length L_{nl} in the optical fiber can be described as

$$L_{nl} = 1/\gamma P_p \tag{2.16}$$

where P_p is the peak power pf the pulse, and the characteristic length for dispersion L_d as

$$L_d = (t/1.763)^2/\beta_2 \tag{2.17}$$

In fiber cavity condition of $L_{nl} > L_d$, nonlinearity dominates and causes pulse distortion. When $L_d > L_{nl}$, dispersion dominates and results in temporal broadening of the pulse. To form a fundamental soliton, L_{nl} and L_d must equal (Agrawal, 2013).

2.5 Two-dimensional Materials

The saturable material used in this thesis has two-dimensional (2D) atomic structure. Since the invention of 2D graphene material by Geim and Novoselov (Geim & Novoselov, 2007), the research areas of the 2D materials have been expanded to various fields including electronics and optoelectronics (Li et al., 2017). Figure 2.18 illustrates the flat atomic structure of 2D materials where the plane area bounded by x- and y-axis. Typically, the 2D materials layered structure has a strong inplane coupling and a weak Van der Waals coupling between layers. Therefore, monolayer or few-layer 2D perfect samples could be easily fabricated by mechanical exfoliation or chemical exfoliation (Luo

et al., 2015; Mas-Balleste et al., 2011; Sobon, 2015). Many potential functional applications in terms of 2D materials in some aspects will be realized in the near future, including optical modulators, photodetectors, logic transistors, high-frequency transistors, energy storage, and sensor devices (Butler et al., 2013).

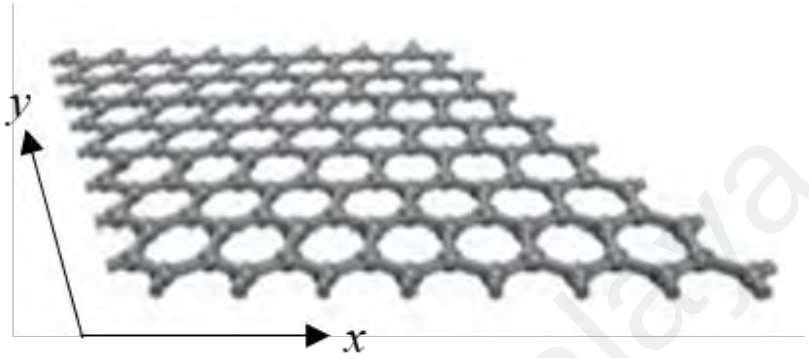

Figure 2.18: Atomic structure of 2D materials.

With abundance of fantastic physics, various other novel 2D materials are discovered and brought into the people's horizon, such as transition metal dichalcogenides (TMDs), topological insulators (TIs), black phosphorus (BP), and transition metal oxides (TMOs). The scope of 2D materials in this thesis are limited to MoS_2 (TMD group), BP, and TiO_2 (TMO group). These 2D materials are classified under semiconductor materials. Most 2D semiconductor materials show a simple two energy band structure of the conduction band and the valence band. Light of higher energy than the bandgap energy can excite carriers from valance band to the conduction band. If the excitation has stronger intensity (noise spike), all possible initial states are depleted and the final states are partially occupied in accordance with the Pauli blocking effect such that the absorption will be saturated (Saraceno et al., 2012). In the context of saturable absorber applications, the energy bandgap is one of the most important properties. The photons with greater energy than that of the bandgap energy of the materials can be readily absorbed. Therefore, the

bandgap energy of the saturable absorber should at least match to the photon energy generated from the laser cavity. For indirect bandgap semiconductor materials, photon absorption process much less efficient since additional phonon must be absorbed to supply the difference in momentum. For direct bandgap, the photon absorption process is quite easily, because electron excitation from valence band to conductance band does not require very much momentum since these two bands sharing the same value of momentum. The photon energy of eV unit can be translated from operating wavelength of the cavity by following equation,

$$E = h\frac{c_o}{\lambda} \tag{2.18}$$

where λ is the operating wavelength, h is the Planck' constant, and c_o is speed of light in vacuum. According to the equation, longer wavelength requires a small amount of bandgap energy. In opposite situation, shorter wavelength requires a high amount of bandgap energy. The bandgap energy that matches to 1 μm, 1.55 μm, and 2 μm are 1.24 eV, 0.8 eV, and 0.62 eV, respectively. Figure 2.19 shows the allocation of bandgap energy for MoS_2, BP, TiO_2, and also graphene. The bandgap of a semiconductor determines the responding wavelength and every semiconductor has its specialized bandgap. Based on the photoelectric effect, the semiconductors materials with a narrow bandgap have broad responding wavelength bands. Therefore, besides the narrow bandgap, for 2D materials such as graphene and BP, the modulation of the bandgap should be important, especially for the materials with large bandgaps such as MoS_2 (Woodward et al., 2015) and TiO_2 (Tang et al., 1994).

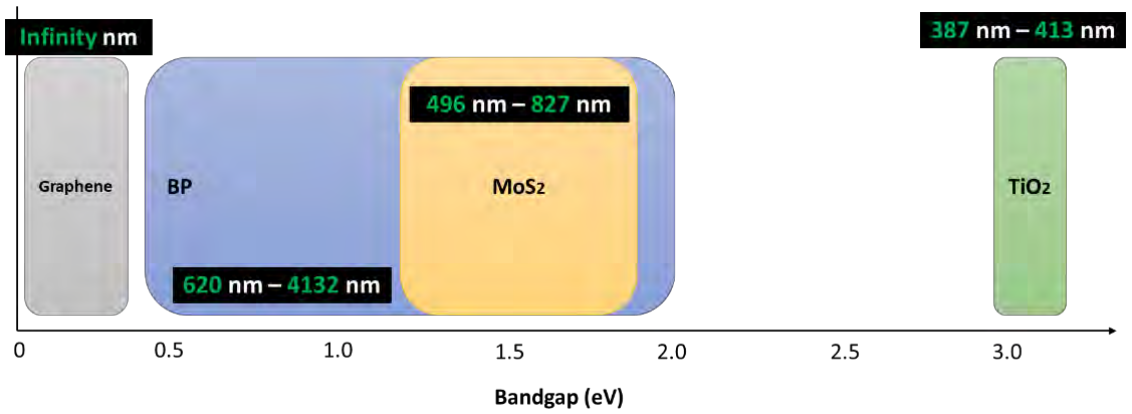

Figure 2.19: Bandgap energy of the 2D materials.

Another important characteristic of saturable absorber is a relaxation time. The faster relaxation time, the shorter the pulse width. The fast relaxation time also can be indicated by electron mobility of the materials. As the relaxation time is slow, the formation of pulse width will be in nanoseconds to picoseconds. To achieve the effective pulse shaping, the saturable absorber should recover to its initial state in a short time (a few picoseconds to femtoseconds) (Keller, 2003; Woodward et al., 2015).

2.5.1 Molybdenum Disulfide (MoS_2)

MoS_2 compounds is formulated in form of MX_2, where M is a transition metal typically from groups 4-7 and X is a chalcogen such as S, Se, or Te. Figure 2.20 illustrates the atomic structure of MoS_2 consists three atomics layers in which the transition metal is sandwiched by two chalcogens. Each of sandwiches is combined by van der Waals interactions and form a strong intralayer bonding in S-Mo-S trilayers. Monolayer MoS_2 has a direct bandgap of 1.8 eV (0.7 μm) and an indirect bandgap in range of 0.86 eV (1.4 μm) – 1.29 (1.0 μm) eV as in bulk form (Wang et al., 2014). This indicates ideally MoS_2 is far from the application as a saturable absorption device in lasers, especially for the

wavelength region cover by fiber lasers in this thesis. Thus, the bandgap of MoS_2 should be reduced to match to the 1-, 1.55-, and 2-micron region laser operation. Introducing some defect in Mo or S with suitable range can reduced the bandgap (Martín-Palma et al., 2006; Wang et al., 2014). The smaller bandgap means the broadband saturable absorption of defective MoS_2 becomes possible. MoS_2 has an electron mobility of 200 cm^2/Vs with a relaxation time of 2.1 ps Wang et al., 2013).

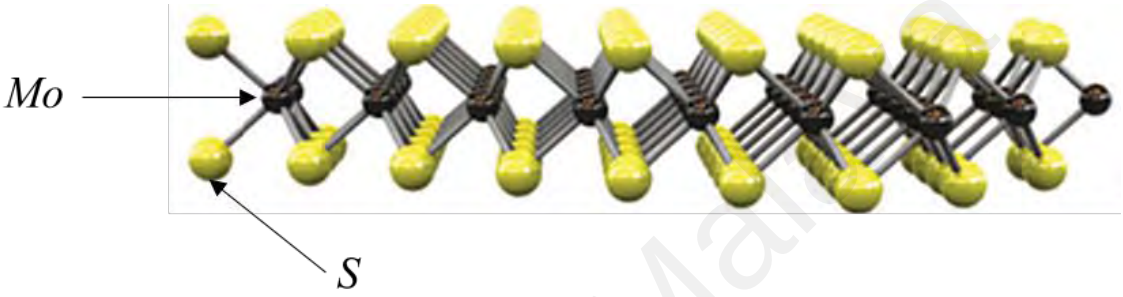

Figure 2.20: Atomic structure of MoS_2.

2.5.2 Titanium Dioxide (TiO_2)

TiO_2 is a group of 2D oxide crystals (Geim et al., 2013). As oxides, TiO_2 is less susceptible to air but they tend to lose oxygen and may react with minority chemicals such as water and hydrogen. The photo-activity of TiO_2 has been shown to be dependent on several key properties, one of them is defects in the lattice. This is similar to MoS_2, where introduction of some defect in TiO_2 can tune other properties such as mid-band-gap electronics states which can produce a red shit in the absorption spectrum (Satoh et al., 2008). Thus, bandgap of TiO_2 from 3.2 eV (387 nm) can reduce to a smaller bandgap which match to the wavelength region cover in this thesis. Elim et al. reported the TiO_2 with anatase phase has a relaxation time of 1.5 ps at the room temperature. This indicates anatase TiO_2 has a capability to be an ultrafast saturable absorber. Anatase TiO_2 is more favorable because of its high performance in various applications. Figure 2.21 illustrates

the anatase TiO_2 atomic structure by each of octahedron is in contact with eight neighbors (four sharing an edge and four sharing a corner.

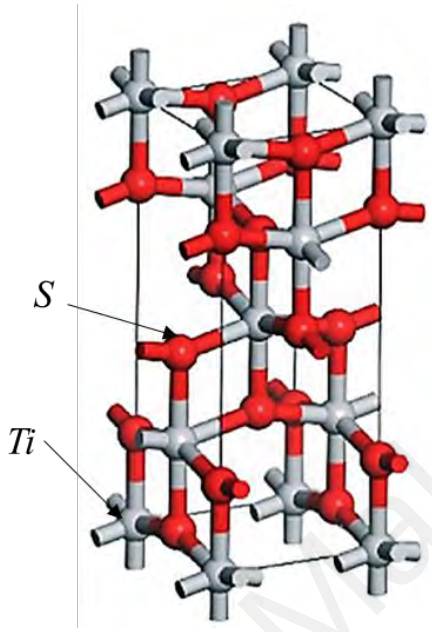

Figure 2.21: Atomic structure of TiO_2. (Yang et al., 2015)

2.5.3 Black Phosphorus (BP)

BP is anisotropic material for optoelectronic and electronics applications (Xia et al., 2014). Bulk BP crystal is the most stable allotrope of phosphorus because of its unique orthorhombic crystal structure as shown in Figure 2.22. Each phosphorus atom is connected to three adjacent phosphorus atoms in BP to form a stable, linked ring structure, with each ring consisting of six phosphorus atoms. Narrow bandgap of BP (0.3 eV) can fill the space between zero bandgap graphene and large bandgap TMDs, making it an ideal material for near and mid-infrared optoelectronics (Xia et al., 2014). Monolayer bandgap of BP is as large as 2 eV. The bandgap of BP is strongly dependent on the layer number because of the layer-layer coupling (Xia et al., 2014). That means the bandgap can be tuned by controlling the number of BP layer. The electron mobility above 1000

cm^2/Vs indicates BP has a fast relaxation time of 24 fs (Wang et al., 2015). As a result, BP as a saturable absorber is promising to generate a shorter pulse.

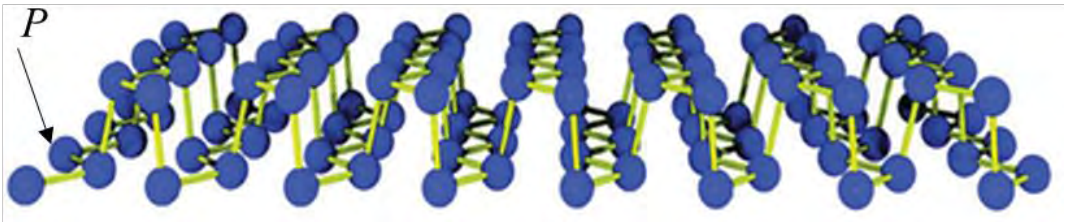

Figure 2.22: Atomic structure of BP.

2.6 Measurement of Pulsed Laser Performances

Temporal and spectral characteristics including repetition rate, pulse width, pulse energy and peak power are some basic quantities often needed when working with laser pulses(Standardization, 2006). Optical spectrum analyzer is used to observe the optical spectrum of the pulse laser, and optical power meter via thermal detector is used to measure it average output power. Through photodetector, laser pulses in optical signal is converted into electrical signal than be observed in time-domain and frequency-domain by oscilloscope and RF spectrum analyzer, respectively. Figure 2.23 shows a regularly repeating train of optical pulses with a repetition rate $f = 1/T$.

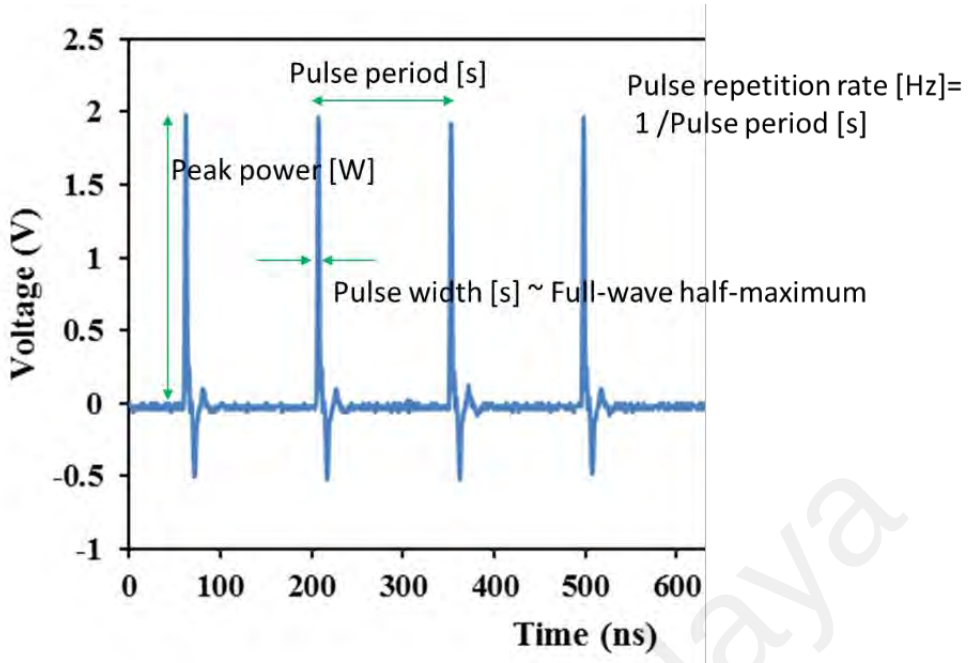

Figure 2.23: Pulse train of pulsed lasers.

2.6.1 Repetition Rate and its Stability

Repetition Rate f is a number of emitted pulses per second or the inverse temporal pulse shaping as shown in Figure 2.23. For the mode-locking, repetition rate is fixed on the length of the laser cavity. For Q-switching, changes of the pump power only influence the repetition rate. This repetition rate trend is inversely proportional to the pulse width.

Stability of the laser pulse can be confirmed through a frequency domain observation. Figure 2.24 shows the RF spectrum of the pulse train records using optical spectrum analyzer via fast photodetector. As shown in the figure, the green color area at the first fundamental frequency represents the repetition rate of the pulse train and the subsequent frequency is a harmonic. The different intensity within a peak and signal floor of the spectrum is known as signal-to-noise ratio (SNR). SNR indicates the stability of the attainable pulse, where more than 30 dB SNR is considered as stable.

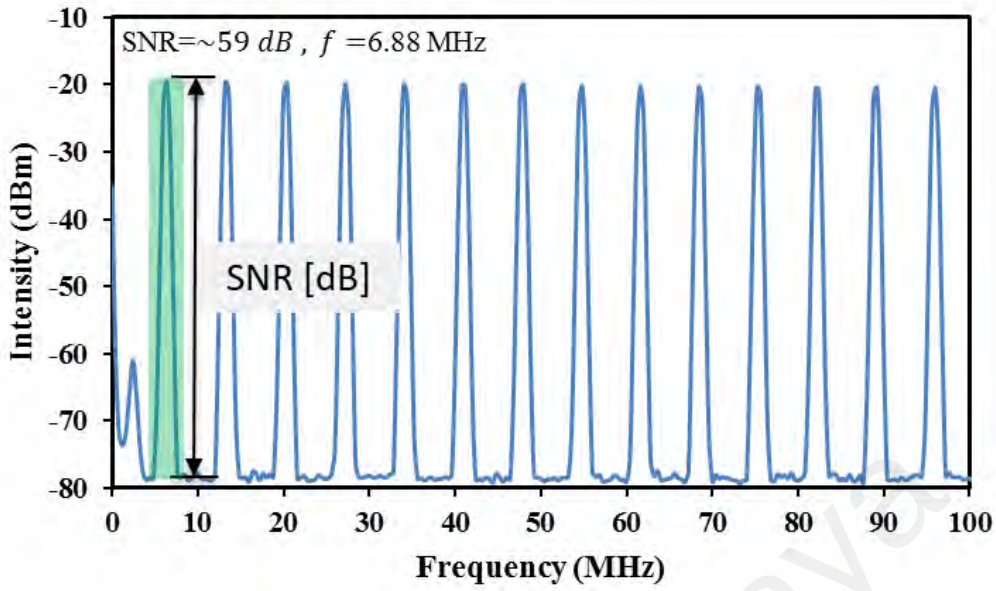

Figure 2.24: RF spectrum of pulsed lasers.

2.6.2 Pulse width or Pulse Duration

Pulse width τ is defined as the width of the pulse within which the power is at the half peak power. In the other word, full width at half maximum (FWHM). Intuitively, the pulse shape can be represented by a bell-shaped function, such as a Gaussian and Hyperbolic secant ($sech^2$) function. According to Haus' master equation, anomalous dispersion regime used $sech^2$ pulse shape such as soliton regime lasers, while Gaussian pulse shape is used for normal dispersion regime. The details of pulse shape function parameters are included in Table 2.1. These functions fitting are used in the autocorrelation of the pulse to describe the pulse shape, where the FWHM intensity autocorrelation pulse is represented as τ_{AC}. For the Q-switching technique, the pulse width is in between nanoseconds to picoseconds regime, while for mode-locked the pulsed are in few picoseconds to femtoseconds regime.

Table 2.1: Pulse characterization.

Pulse shape	$\tau.\Delta\lambda_{3dB}$	τ/τ_{AC}
Gaussian	0.441	0.7071
Sech^2	0.315	0.6482

Since actual half-maximum quantities are experimentally easier to measure by using auto-correlator, the relationship between the pulse width and 3-dB spectral bandwidth of laser pulse can be written as

$$\tau.\Delta\lambda_{3dB} \geq TBP \tag{2.19}$$

where τ is the FWHM from single pulse envelope, $\Delta\lambda_{3dB}$ is the 3-dB spectral bandwidth measure from optical output spectrum in Hz, and TBP is the time-bandwidth product which refer to Fourier-transform limit. If the equality is achieved in Equation 2.19, the measured pulse width reaches a transform limit and the attainable pulse width meets the minimum possible pulse width that could produce from this condition of laser. Thus, to achieve an ultrashort laser pulse in time domain, the developed laser in this thesis should generate a broad spectral bandwidth laser.

In other way round, the minimum possible pulse width of a pulse can be calculated by giving a spectrum with $\Delta\lambda_{3dB}$ (nm) at FWHM, central peak wavelength λ_o (nm), and the speed of light (m/s) c:

$$\tau \geq TBP\frac{{\lambda_o}^2}{\Delta\lambda_{3dB}.c} \tag{2.20}$$

From Equation 2.20, the pulse width of mode-locked lasers for 1- and 2-micron region are mathematically obtained due to no available autocorrelator in the laboratory.

2.6.3 Pulse Energy and Peak Power

Figure 2.25 shows the autocorrelation pulse envelope which contains the energy of pulse lasers. Pulse Energy Q is a total optical energy content in every of single pulse envelope or integral of its optical power over time.

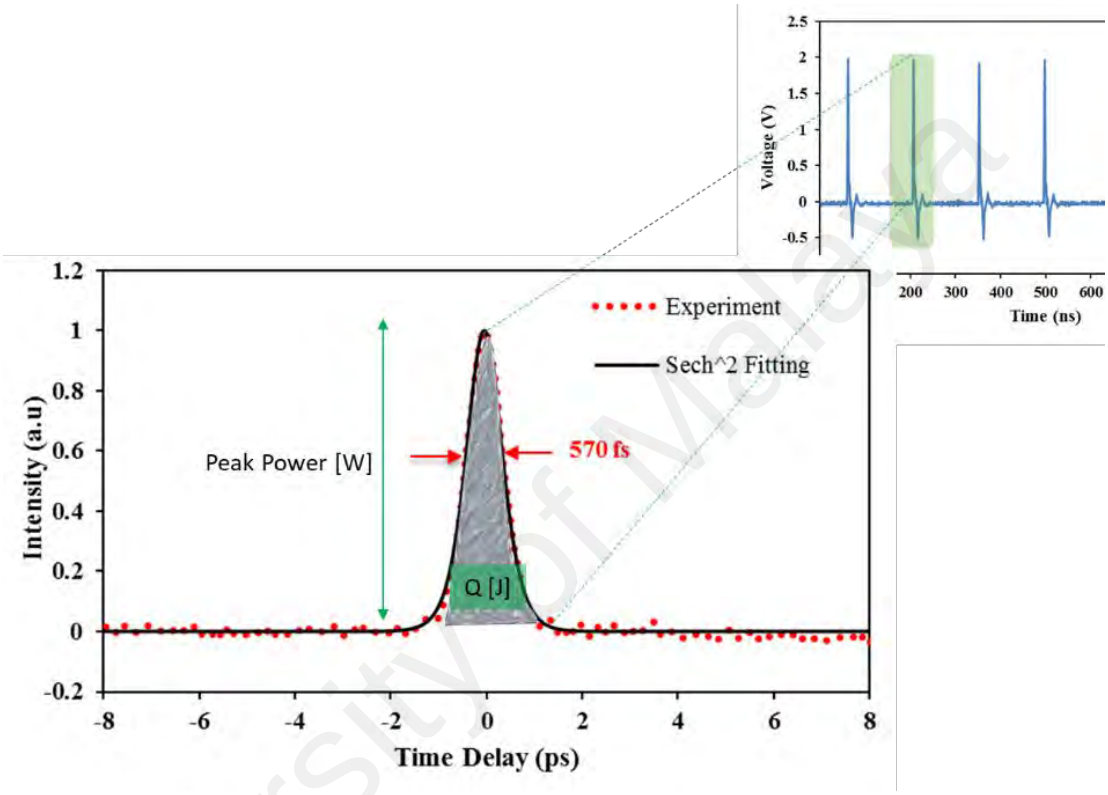

Figure 2.25: Autocorrelation pulse envelope of mode-locked lasers. Inset image is oscilloscope train.

For Q-switching the typical pulse energy is within the range from microjoules to millijoules, and for the mode-locking the pulse energy much lower in the range picojoules and nanojoules. Typically, the pulse energy is calculated by dividing the average output power by the repetition rate as

$$Q\ [J] = \frac{P_o}{f_r} \tag{2.21}$$

where P_o is the average output power and f_r is the repetition rate.

Peak power P_p is the highest instantaneous optical power level in the pulses. In other word, it is a rate of energy flow in every pulse envelope as described in Figure 2.25. Short pulse width can generate higher peak power even for the moderately energetic pulses. By dividing the pulse energy by the pulse width, the peak power can be written as

$$P_p[W] = 0.88\frac{Q}{\tau} \tag{2.22}$$

where Q is the pulse energy and τ is the pulse width. The conversion of the peak power depends on the temporal shape of the pulse. As per discussed earlier, the transform limit of the single envelope is only represented in Gaussian function or $Sech^2$ function.

2.6.4 Time-Frequency Relationship

Temporal characteristic of the pulsed lasers can be observed in time and frequency domain. Strong relationship between these domains can be explained via Fourier transform of a pulse as

$$E(\omega) = \int_{-\infty}^{+\infty} E(\omega)e^{i\omega t}dt \tag{2.23}$$

where $E(\omega)$ represent the frequency of the electric field of the pulse with $\omega = 2\pi\upsilon$, and υ is the frequency from output laser. Figure 2.26 illustrates the laser pulse in time and frequency domain.

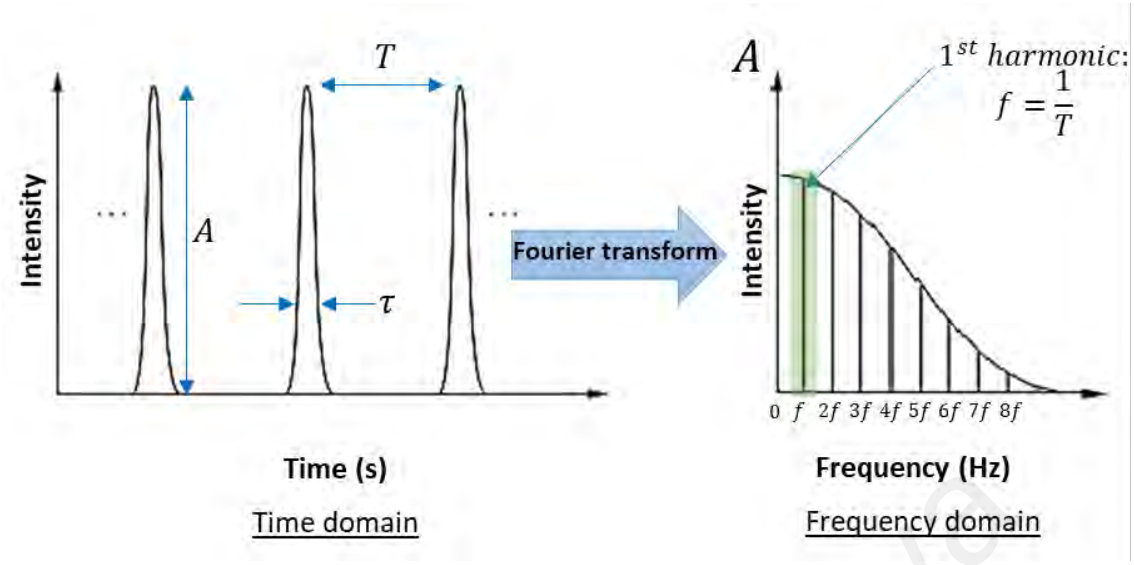

Figure 2.26: Temporal characteristic of laser pulse in time and frequency domain.

In time domain, the duty cycle of the pulse train should be determined first. Duty cycle d is the fractional amount of time the laser is "on" during any given period. The calculation of duty cycle is

$$d = \frac{\tau}{T} \tag{2.24}$$

where τ is the pulse width, and T is the pulse period. From Fourier series equation, DC component a_0 is calculated by giving an amplitude A at zero frequency, and duty cycle d as

$$a_0 = Ad \tag{2.25}$$

Amplitude of the cosines wave a_n and sine wave b_n are written as

$$a_n = \frac{2A}{n\pi}\sin\left(\frac{n\pi}{2}\right) \tag{2.26}$$

$$b_n = 0 \tag{2.27}$$

Combination of these equations have formed a shape of the laser pulses in frequency domain as illustrated in Figure 2.26. Shorter pulse width formation in time domain can

be identified by formation of constant amplitude in frequency domain over the range of infinite frequency, similar to impulse waveform. Figure 2.27 shows a simulation of RF spectrum based on Fourier transform equation, which time domain is obtained from experimental. It is shown that the pulse width obtained from the simulated RF spectrum is almost similar to the pulse width measured from experimental pulse train in time domain.

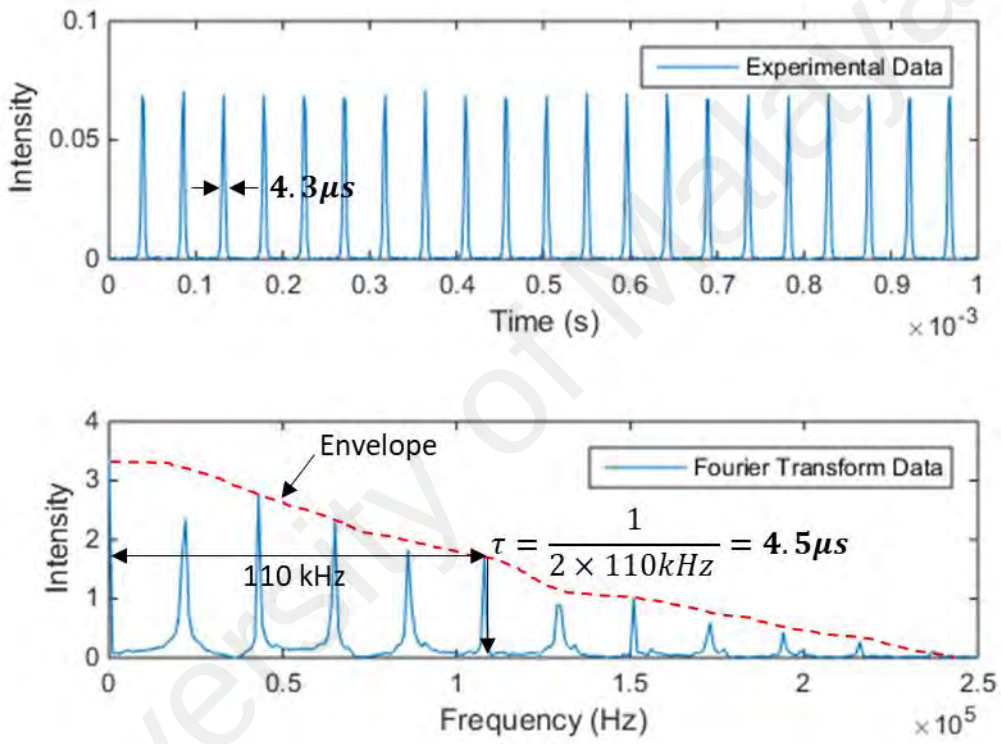

Figure 2.27: Simulation of RF spectrum.

CHAPTER 3: MOLYBDENUM DISULFIDE SATURABLE ABSORBER

3.1 Introduction

The growth of ultrashort pulse laser technology has been driven by a high demand from the medical and optoelectronics fields that capitalize on their promising advantages (Grudinin, 2013). Evolution of ultrashort pulse laser starts by using a dye gain medium in the 80s, and a decade later by the solid-state gain medium. This type of laser can be achieved through a mode-locking technique. The mode-locked fiber lasers provide output pulse train with high peak power, high repetition rate, and ultra-short pulse duration.

There are two techniques of making mode-locked pulse which are active and passive. The active mode-locking technique typically uses an externally controlled device such as acoustic-optic modulator to actively modulate the intra-cavity light (Kim et al., 2017). On the other side, the passive mode-locking technique did not use external signal. Instead, it is achieved by placing an SA or another passive element into laser cavity which causes a change in the intra-cavity light to generate pulsed laser (Daud et al., 2006). Passive mode-locking can occur when an SA modulates the loss once per cavity round-trip dominant to the generation of a train of the ultrashort (ps-fs duration) pulse at defined repetition rate corresponding to the free spectral range of cavity (MHz for few meter fiber laser) (Woodward et al., 2015). The passive mode-locking technique is compact, simple to construct and flexible in comparing to active mode-locking (Mao et al., 2013).

The use of saturable absorber (SA) to generate pulsed fiber laser has been the method of choice for increasingly many researchers nowadays (Fermann et al., 2013; Nishizawa, 2014; Scholle et al., 2010). Numerous SA mechanism have been developed so far using an artificial technique such as nonlinear polarization rotation (NPR) and the real SA such as semiconductor saturable absorber mirror (SESAM)(Zhang et al., 2014), carbon nanotube (CNT)(Martinez et al., 2013), ion-doped crystal(Latiff et al., 2017), and carbon

materials (graphene nano-sheets, nano-scale graphite, charcoal powder) (Bonaccorso et al., 2010; Latiff et al., 2015; Novoselov et al., 2012). The NPR and SESAM are two commonly used SA because of their high flexibility, stability, and fast amplitude modulation. However, SESAM is more expensive that requires complicated fabrications and packaging processes, and has a limited bandwidth of optical response (Keller et al., 1996). Therefore, high performance, low-cost and broadband operated SA from other materials has gained the attention of experts in the field.

The most popular SA previously was graphene as they have shown saturable absorption at very low optical intensities due to the 3rd order nonlinearities that exhibit wavelength-independent absorption (Lu et al., 2013; Yan et al., 2015). The success of graphene has led to the discovery of new 2D materials such as topological insulators (TIs) and transition-metal dichalcogenides (TMDs), which are capable of shaping the future direction of fiber laser (Mas-Balleste et al., 2011). Furthermore, graphene suffers from the absence of band-gap and low absorption co-efficiency. Recently, TIs materials such as bismuth telluride (Bi_2Te_3) (Lin et al., 2015; Lin et al., 2014) and TMDs materials such as tungsten disulfide (WS_2) (Kadir et al., 2017; Yan et al., 2015) and molybdenum disulfide (MoS_2)(Woodward et al., 2015) have captivated plenty of interest due to their unique absorption property in ultrafast laser application (Wang et al., 2012).

TMDs has thickness dependent band-gap, while TIs has indirect band-gap in the insulating bulk state. However, those materials compound consist of two different elements which lead to the complicated preparation process. TMD has attracted a considerable amount of attention due to their potential in many fields such as microelectronics, lithium batteries, medical and optoelectronics (Bonaccorso et al., 2010; Wang et al., 2012). TMD is a group of 40+ layered materials with the chemical structure of MX_2 with a single plane of hexagonally-arranged transition metal (M) atoms

covalently bonded together with two hexagonal planes of chalcogen (X) atoms (Woodward et al., 2015). TMD materials became popular mostly in optical communication field because of their thickness dependent band-gap(Liu et al., 2014), their broadband saturable absorption (Zhang et al., 2014), high 3rd order nonlinearity susceptibility (Wang et al., 2013), and ultrafast carrier dynamics (Shi et al., 2013). TMD mode-locked laser was reported first by Zhang et al., where the MoS_2 thin film was deposited on a fiber ferrule and integrated into a ytterbium fiber ring cavity (Zhang et al., 2014). This MoS_2 film is highly crystalline as their size can up to several millimeters which can be used in electronics as a transistor and optics as emitter and detectors (Zhang et al., 2014). MoS_2 devices have been fabricated and characterized at 1-μm (Woodward et al., 2014), 1.55-μm (Xia et al., 2014) and 2-μm (Tian et al., 2015) which are corresponding to the gain bands. Strong SA has also been observed in other MoS_2-based devices such as MoS_2-coated fiber tips where modulation depths up to 32 % and saturation intensities of 0.35 MW/cm^2 have been reported, although this was accompanied by very high non-saturable losses of ~35 (Woodward et al., 2015; Xia et al., 2014).

In this chapter, the use of MoS_2 based SA as mode-locker for ultrashort pulse generation is investigated and demonstrated. This chapter discusses on the MoS_2 SA preparation and characterization and fiber laser configuration, and then presents analysis data for the spectral and temporal laser performances of mode-locking operation at 1-, 1.55-, and 2-micron region.

3.2 Preparation of Molybdenum Disulfide based SA

In this work, the MoS_2 tape prepared by mechanical exfoliation method was used as an SA. The mechanical exfoliation method has been widely used in preparing graphene-based SA for ultra-fast fiber laser application (Chang et al., 2010; Martinez et al., 2011). This method is advantageous due to its simplicity and reliability, whereby the entire fabrication process is free from complicated chemical procedures and expensive instruments. Figure 3.1 shows the step by step preparation process of the MoS_2 tape based SA. As shown in the figure, at first relatively thin flakes is peeled off from a big block of commercially available MoS_2 crystal (with purity of 99%) using a transparent scotch tape. Then the flakes are repeatedly pressed so that MoS_2 flakes become thin enough to transmit light with high efficiency. The last step for preparation of MoS_2 is to cut a small piece of the MoS_2 tape, then attached to a standard FC/PC fiber ferrule end surface with the assistance of index matching gel.

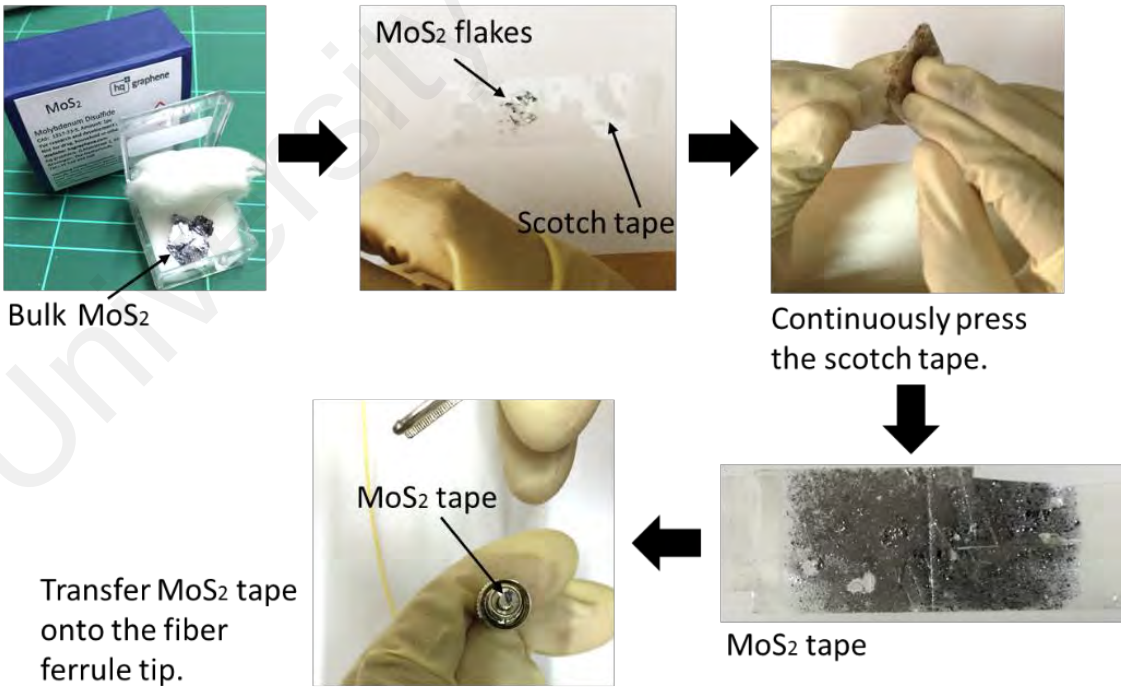

Figure 3.1: Mechanical exfoliation process.

3.3 Characterization of the SA

The presence of MoS_2 in the prepared SA sample is verified through various measurements using field emission scanning electron microscopy (FESEM), energy dispersive spectroscopy (EDS) and Raman spectroscopy. Figure 3.2(a) shows the FESEM image of MoS_2 tape, which indicates the existence of the uniform layers. This image also confirms the absence of >100 nm aggregates or voids on the tape, which otherwise results in non-saturable scattering losses. The material composition of the MoS_2 tape was confirmed by the energy dispersive spectroscopy (EDS) analysis on the FESEM image, as shown in Figure 3.2(b). At an energy of 2 keV, the molybdenum (Mo) and sulfur (S) elements are dominated and verified to be in our SA tape. Raman spectroscopy was used to confirm the presence of MoS_2 and as well as estimates the number of layers (Lee et al., 2010; Li et al., 2012). Figure 3.2(c) shows Raman spectrum, which was recorded by a spectrometer when a 514-nm beam of an Argon laser with 10 mW exposure power was radiated onto the MoS_2 tape within 10 seconds. As shown in the figure, the sample exhibits two characteristic peaks, in parallel with two phonon modes; out of plane vibration of Sulfide atoms at 408 cm^{-1}, and in-plane vibration of Molybdenum and Sulfide atoms at 383 cm^{-1}, with a frequency difference of 25 cm^{-1}. It is observed that the E_{2g}^1mode is present due to the in-plane motion red shifts after complete exfoliation, indicating that the few layer MoS_2 with thicknesses of 5-6 layers had been successfully fabricated (Lee et al., 2010; Li et al., 2012). The full-width-half-maximum (FWHM) of E_{2g}^1 and A_{1g} bands are calculated to be 5.0 and 5.5 cm^{-1}, respectively, which agree with other reported results (Wu et al., 2015).

(a)

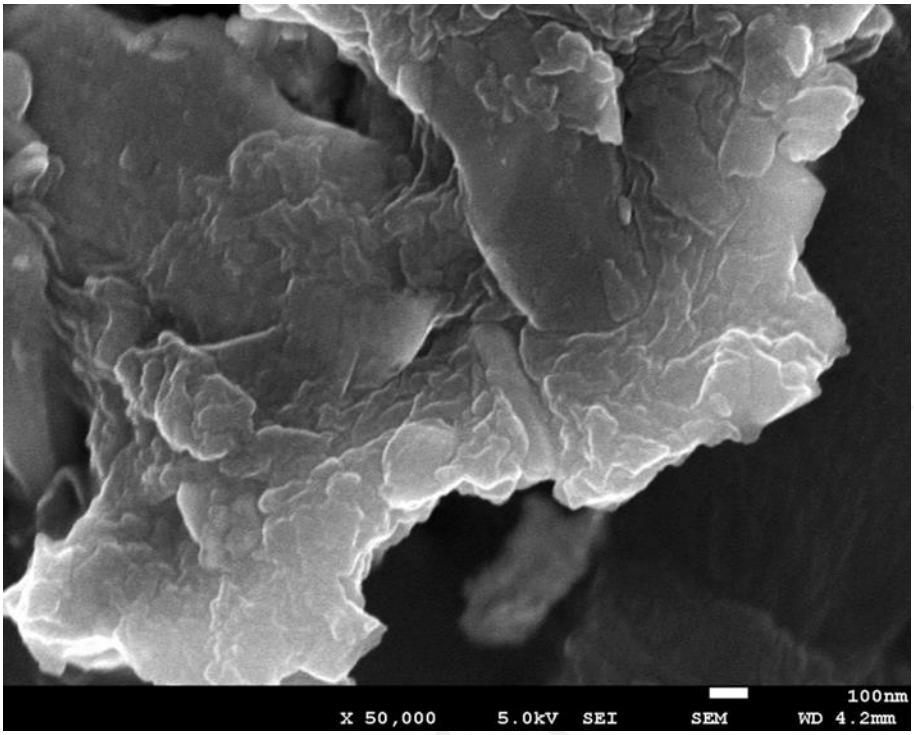

(b)

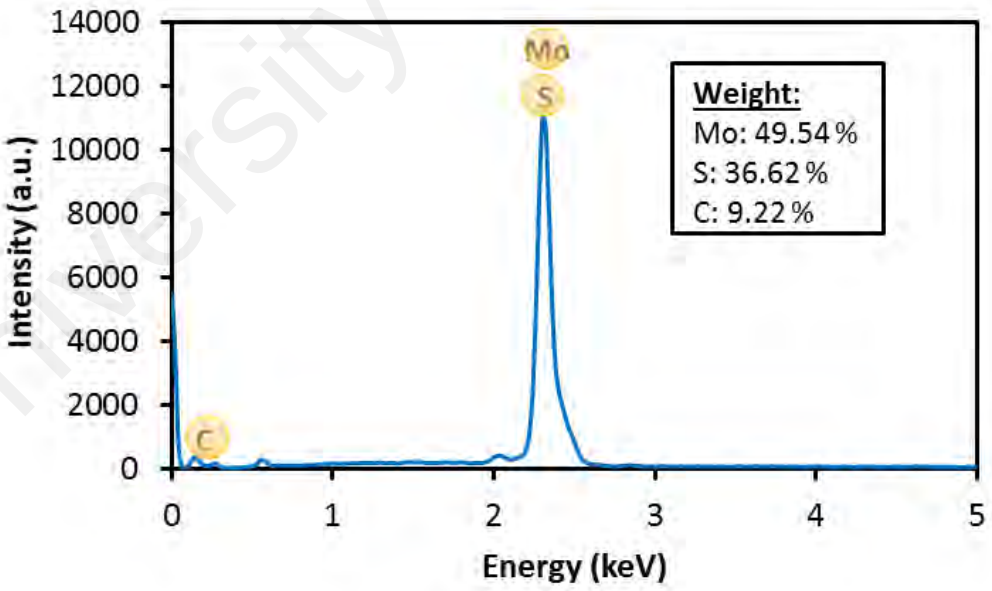

(c)

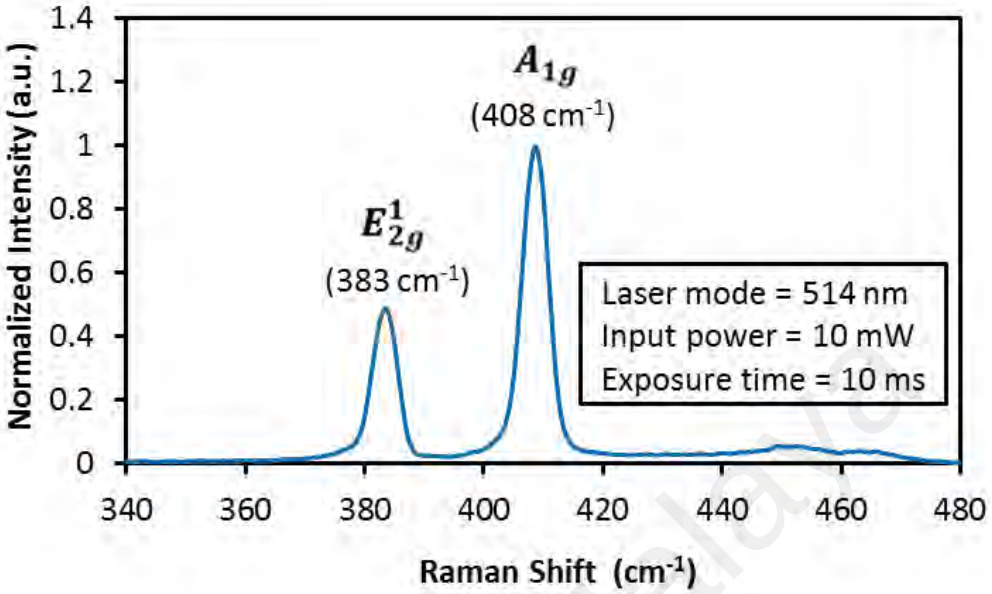

Figure 3.2: The characterization result of the MoS_2 tape: (a) FESEM image, (b) EDS data, and (c) Raman spectrum.

Another important parameter for SA is a nonlinear optical response. The amplified mode-locked pulsed fiber laser is launched onto our MoS_2 tape to measure a nonlinear optical response. The nonlinear optical response property for the MoS_2 tape was investigated to confirm its saturable absorption ability. Through balanced twin-detector measurement, the transmitted power is recorded as a function of incident intensity on the device by varying the input laser power. The experimental data for absorption are fitted according to a simple two-level SA model (Bao et al., 2009), which is given by

$$\alpha(I) = \frac{\alpha_s}{1+\left(\frac{I}{I_{sat}}\right)} + \alpha_{ns} \tag{3.1}$$

where $\alpha(I)$ is the absorption coefficient, α_s is the saturable absorption or modulation depth, α_{ns} is the non-saturable absorption, I is the input intensity, and I_{sat} is the saturation intensity. The I_{sat} is defined as the optical intensity required in a steady state to reduce

the absorption to half of its unbleached value. The nonlinear transmission analysis of the MoS_2 tape is shown in Figure 3.3. As shown in the figure, the saturable absorption, non-saturable absorption, and saturation intensity are obtained to be 10 %, 12 %, and 100 MW/cm^2, respectively. This large saturable absorption of 10 % is expected to be able to suppress a wave breaking effect in the mode-locked fiber laser, and thus improves the attainable pulse energy.

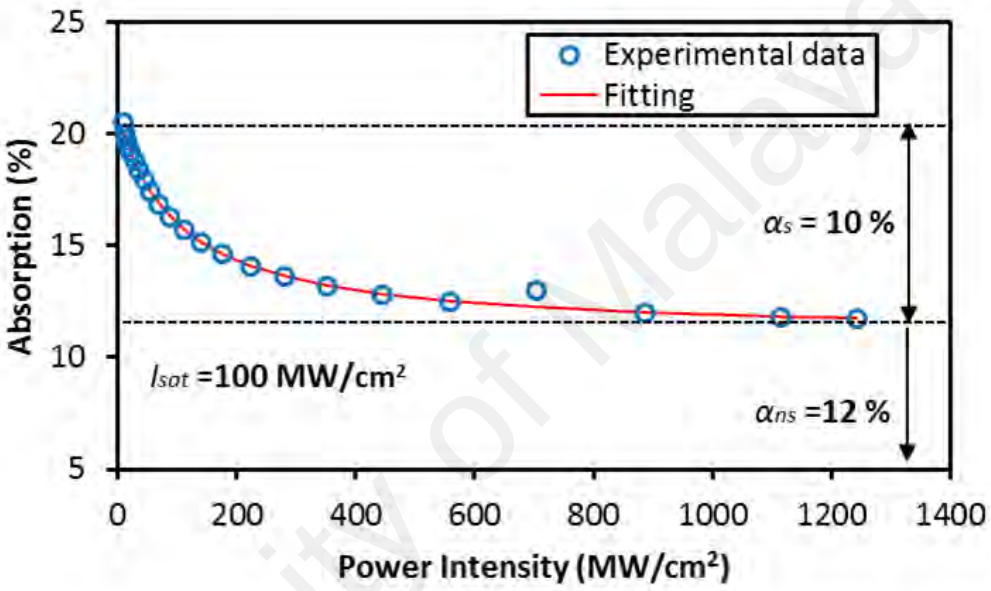

Figure 3.3: Nonlinear saturable absorption profile of the MoS_2 tape.

3.4 Mode-locked fiber laser at 1.55-micron region

A mode-locked Erbium-doped fiber laser (EDFL) operating in 1.55 μm region is demonstrated using the fabricated MoS_2 tape as a passive SA. This MoS_2 tape has a low insertion loss of ~ 1.05 dB. Figure 3.4(a) shows the proposed configuration of the ring laser which employs an Erbium-doped fiber (EDF: Fibercore, I-25) as a gain medium. The EDF has a core diameter of 4 μm, the numerical aperture (NA) of 0.16 and erbium ion absorption of 23 dB m^{-1} at 980 nm. The cavity consists of 2.4 m long EDF, 40 m Scandium-doped fiber (ScDF) and 6.6 m long standard single mode fiber (SMF, SMF-

28), with group velocity dispersion (GVD, β_2) of 27.6, -34.9 and -21.7 ps^2/km, respectively. The ScDF is used to gain sufficient nonlinearity effects for a mode-locked generation as well as to tailor the cavity to operate in anomalous dispersion region. ScDF has a core composition of SiO_2-GeO_2-Sc_2O_3 with core diameter and NA of 7.5 μm and 0.12, respectively. The total cavity length is around 49 m, and the total net group delay dispersion (GDD) in the cavity operates in anomalous dispersion condition of -0.217 ps^2. The generated lasing propagates in unidirectional and maintain its direction after pass through the isolator. The similar MoS_2 SA device is incorporated into the cavity as a mode-locker. The mode-locked laser output is collected from 10 % of output coupler while the remaining of 90 % is allowed to oscillate in the cavity continuously. The optical spectrum analyzer (OSA: Yokogawa, AQ6370B & AQ6375) with a spectral resolution of 0.02 nm is used to analyze the spectrum of the mode-locked laser, a 500 MHz oscilloscope (GW Instek, GDS-3352) via a 1.2 GHz fast photodetector (Thorlabs, DET101CFC) is used to analyze the output pulse train of the mode-locking operation, and rise/fall time than 1 ns with a peak response of 0.95 A/W at 1.55-micron region. The temporal characteristic of the laser is also investigated with 7.8 GHz RF spectrum analyzer (RFSA: Anritsu, MS2683A) via the photodetector.

Figure 3.4(a) shows the amplified spontaneous emission (ASE) of the EDF as a 980 nm pump forward pumps it. The ASE operates in the region between 1520 nm to 1565 nm, and thus the laser is expected to be generated in the same region. The dispersion and nonlinearity characteristics of the EDFL cavity were schematically designed to evaluate MoS_2 SA ability to produce mode-locking pulse at a wavelength of 1.55 μm.

(a)

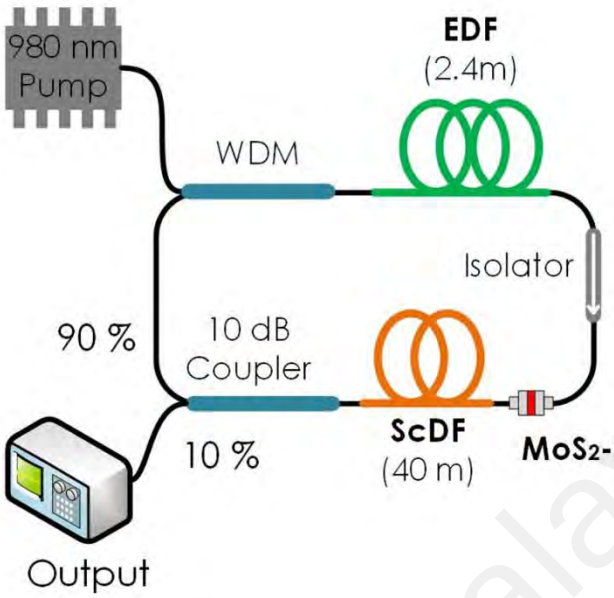

(b)

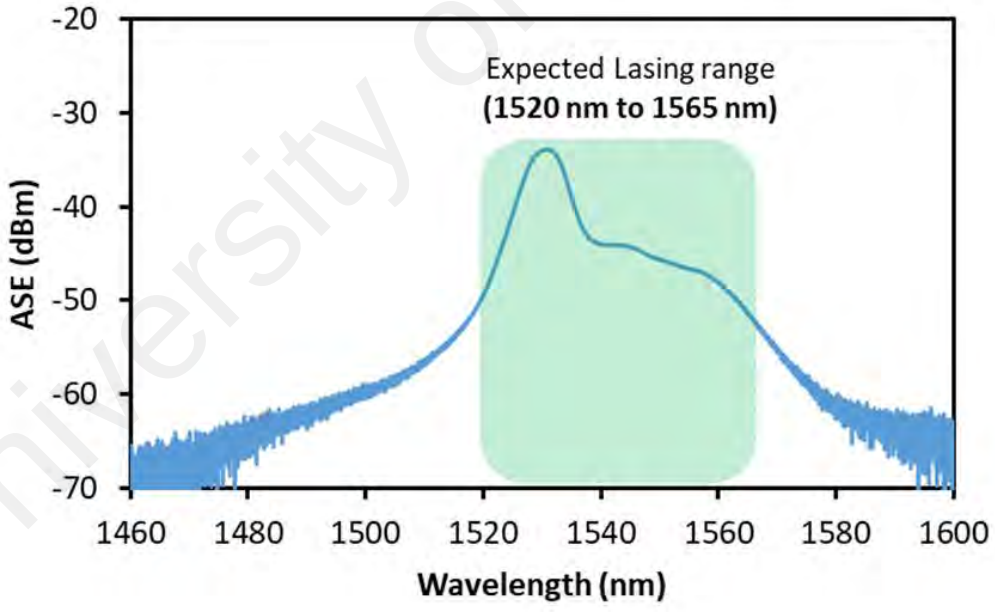

Figure 3.4: (a) Schematic diagram of the mode-locked EDFL with MoS_2 SA. (b) ASE spectrum obtained from the 2.4 m long EDF.

Under a pump power of 166 mW, which corresponds to the mode-locking threshold of the current laser cavity, the operation of the stable mode-locked pulse can be readily obtained without any use of the intra-cavity polarization controllers. The relatively high mode-locking threshold was caused by the high insertion loss of the SA and the ScDF. Figure 3.5 shows the optical spectrum measured under a pump power of 166 mW, which centered at 1562.7 nm with the 3dB spectral bandwidth of 1.8 nm (221.17 GHz). The net cavity GVD is anomalous, and thus it facilitates soliton pulse shaping through the interplay of GVD and self-phase modulation (SPM). This is confirmed by the observation of narrow peaks superimposed on the soliton pulse spectrum or Kelly sidebands in the output spectrum. The sidebands arise from resonances between the soliton and dispersive wave components emitted after soliton perturbations.

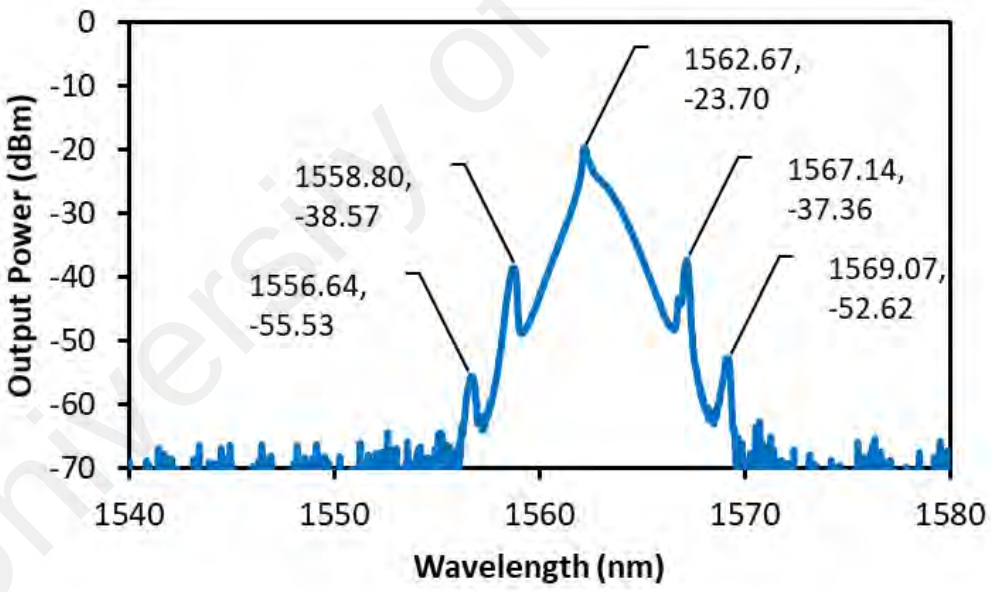

Figure 3.5: Output Spectrum of the soliton mode-locked EDFL at a threshold pump power of 166 mW.

The typical pulse trains measured under a pump power of 166 mW, 210 mW and 250.0 mW, respectively were shown in Figure 3.6. The mode-locked pulse trains are stable, and they are observed at the fundamental repetition frequency of 4 MHz, which matches with the cavity length of 49 m. It can be seen from the figure that the pulse train is quite uniform with a pulse period of 250 ns. Figure 3.7 shows the autocorrelation trace of the soliton pulse, which takes on a $sech^2$ pulse profile with a pulse duration of 1.71 ps as measured at the FWHM. This pulse duration, combined with the above-mentioned spectral width, gives a time-bandwidth product (TBP) of ~0.378. The small deviation from the transform-limited TBP for the $sech^2$ pulse of 0.315, indicates a low chirp. This chirp may partially be due to third-order dispersion. Another factor may be spectral filtering by the non-uniform erbium gain medium (Fermann, 1994). This small chirp suggests that a reduction in pulse duration would be possible by managing the dispersion of the cavity.

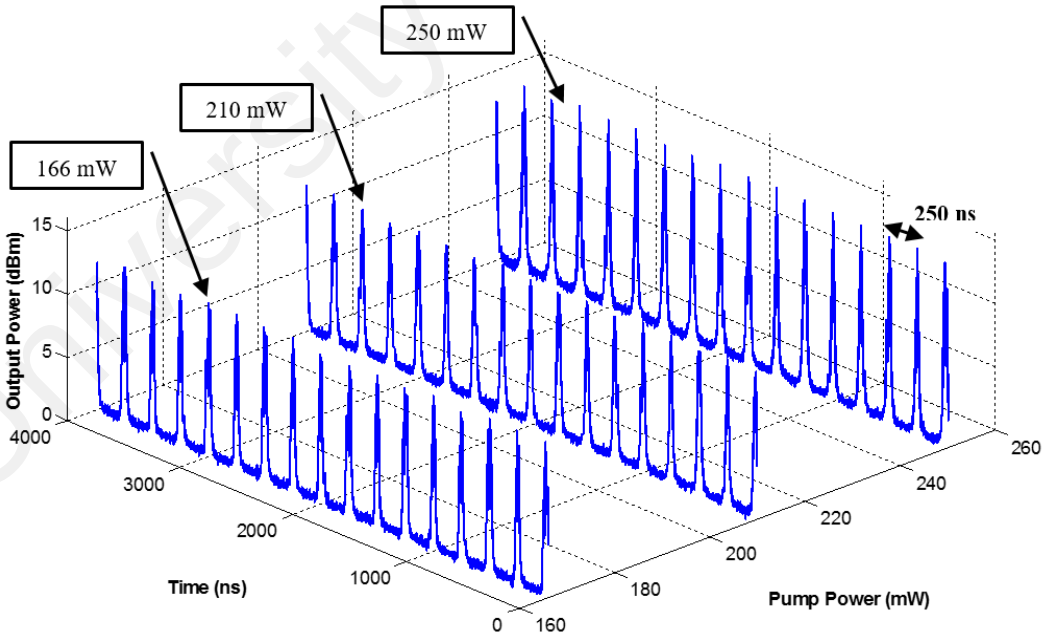

Figure 3.6: Typical pulse trains of the soliton mode-locked EDFL at three different pump powers.

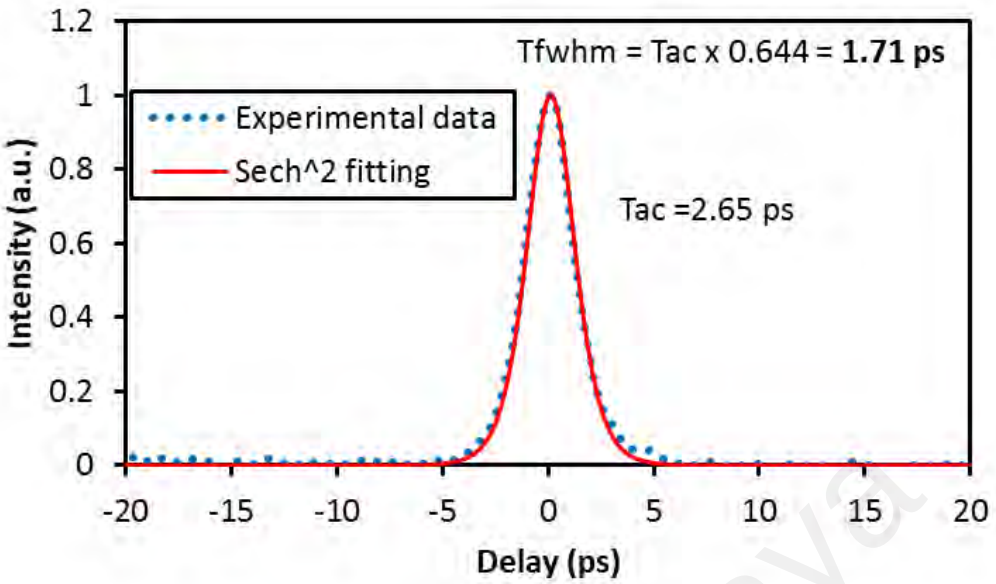

Figure 3.7: Autocorrelation trace of soliton mode-locked EDFL with the sech^2 fitting curve.

The RF spectrum of the proposed laser is also investigated to evaluate laser stability. The RF spectrum recorded in a span of 36 MHz is shown in Figure 3.8. It indicates that the proposed laser cavity operates at the stable regime, given that the fundamental frequency of 4 MHz has a high signal to background extinction ratio of ~57 dB. The relations of input pump power with average output power and the calculated pulse energy for the mode-locked pulse are presented in Figure 3.9. It is clear to note that the output power increases from 1.2 mW to 6.7 mW with the corresponding pump power increasing from 166 mW to 250 mW. The optical-to-optical efficiency is relatively low (6.3%) because of the high insertion loss from the SA and ScDF. It is observed that the pulse energy increases linearly with the pump power and the maximum pulse energy of 1.66 nJ is obtained at the maximum pump power of 250 mW. The output power could be scaled by chirped pulse amplification, resulting in higher pulse energies. Since there is no degradation in the mode-locked pulse performance at the maximum pump power, it is expected that damage threshold for the MoS_2 SA is higher than 250 mW. Beyond MoS_2,

a number of MoS_2-like layered nanomaterials can also be developed as promising optoelectronic devices with high power tolerance. This may offer inroads for more practical applications, such as large energy laser mode-locking, nonlinear optical modulation and signal processing, etc.

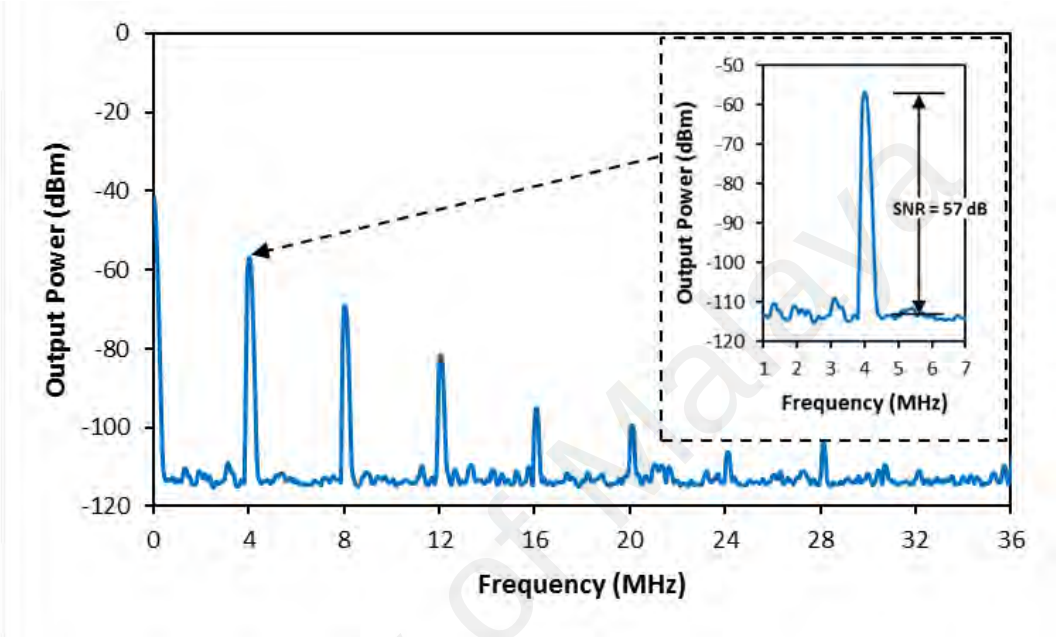

Figure 3.8: RF spectrum of the soliton mode-locked EDFL with 36 MHz spans. Inset shows the enlarged image of the fundamental repetition rate.

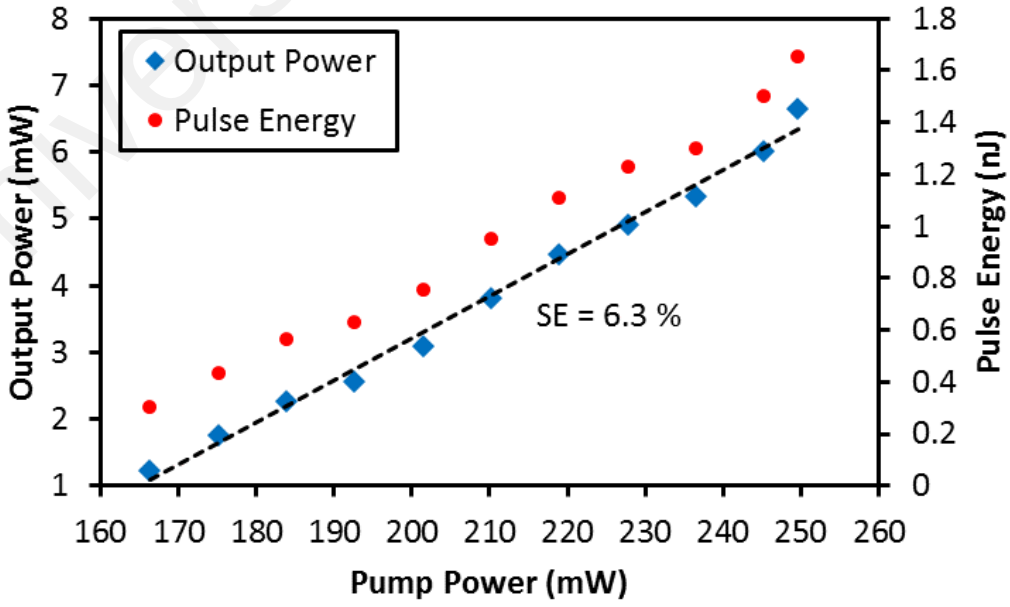

Figure 3.9: Output power and calculated pulse energy within 166 to 250 mW pump power.

3.5 Molybdenum disulfide based mode-locked fiber laser operating in 1-micron region

In this section, the application of the MoS_2 SA for a fiber laser operating in 1-micron region using a double-clad ytterbium-doped fiber (YDF) is demonstrated. The stable mode-locked double-clad fiber laser is configured by sandwiching the MoS_2 tape between two fiber ferrules via a fiber connector in the cavity. The double-clad fiber laser system is used to determine the robustness of the SA material to stand the incoming high-power laser. The laser exhibits stable mode-locking pulse train and with the highest power obtained so far which made MoS_2 a suitable candidate as an effective SA for high power laser. Moreover, high power mode-locked fiber laser offers many useful applications in various fields such as nuclear fusion, nonlinear optics, femtosecond laser nano-machining, medical, surgery, military and photonic sampling by utilizing high accuracy laser beam (Keller, 2003; Xia et al., 2014).

The schematic diagram of the proposed mode-locked double-clad YDF laser (YDFL) is illustrated in Figure 3.10(a). The laser cavity consists of a 980-nm multimode pump, a multimode combiner (MMC), a 10 m long double-clad Ytterbium-doped fiber (Nufern, LMA-YDF-10/130-VII), a 10-dB coupler OC, and a polarization controller (PC) in a ring configuration. The YDF has a cladding absorption coefficient of 3.95 dB/m at 975 nm and the GVD of -18 ps^2/km. Other fibers in the ring cavity is a standard SMF with a GVD of 44.2 ps^2/km. Thus, the total net cavity dispersion is estimated to be ~ 0.032 ps^2, which indicates the laser operates in normal dispersion condition. The total cavity length is 14.8 m.

The lasing is obtained after a multimode laser diode (LD) pump with emission centered at 980 nm was pumped into YDF via MMC. The YDF was employed as a gain medium, while MMC was used to combine pump and feedback signal together in a single optical

fiber. Through 10 dB coupler, 10% of lasing was coupled out as an output, and 90 % of the oscillating light was retained in the cavity. The polarization of oscillating light in the cavity was adjusted by using PC so that it matches with the optimum SA transmission axis. A small piece (1 x 1 mm) of the MoS_2 tape was sandwiched between two fiber connector ferrules via an adapter with the help of index matching gel inside the ring cavity. Stable pulse train was obtained with some adjustment made manually at the SA device.

It is worthy to note that the MoS_2 tape based SA can still work effectively as SA even though the EDF was pumped with a pump power of more than 1006 mW. This proves that the fabricated SA has a high damage threshold characteristic. The spectral characteristic of the mode-locked laser was investigated by using an OSA while the temporal characteristics were observed by an oscilloscope and an RF spectrum analyzer. Figure 3.10(b) shows the ASE spectrum of the double-clad YDF, which expecting an effective lasing can be realized in the wavelength region between 1050 nm to 1110 nm.

(a)

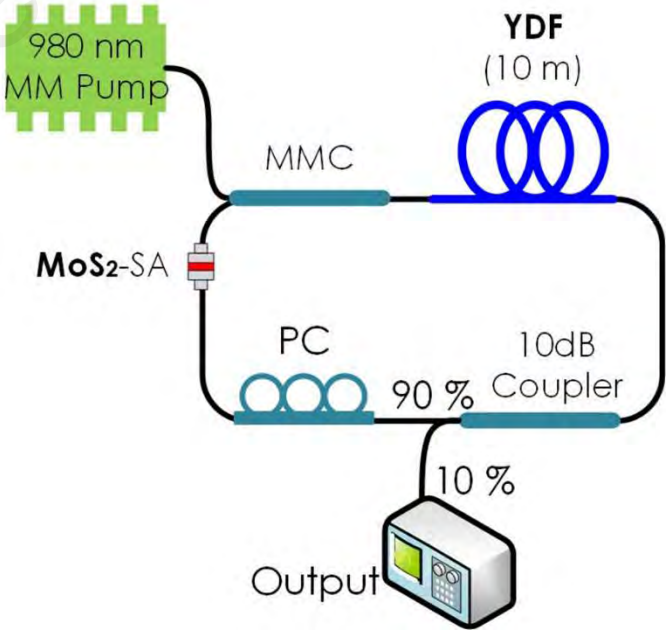

(b)

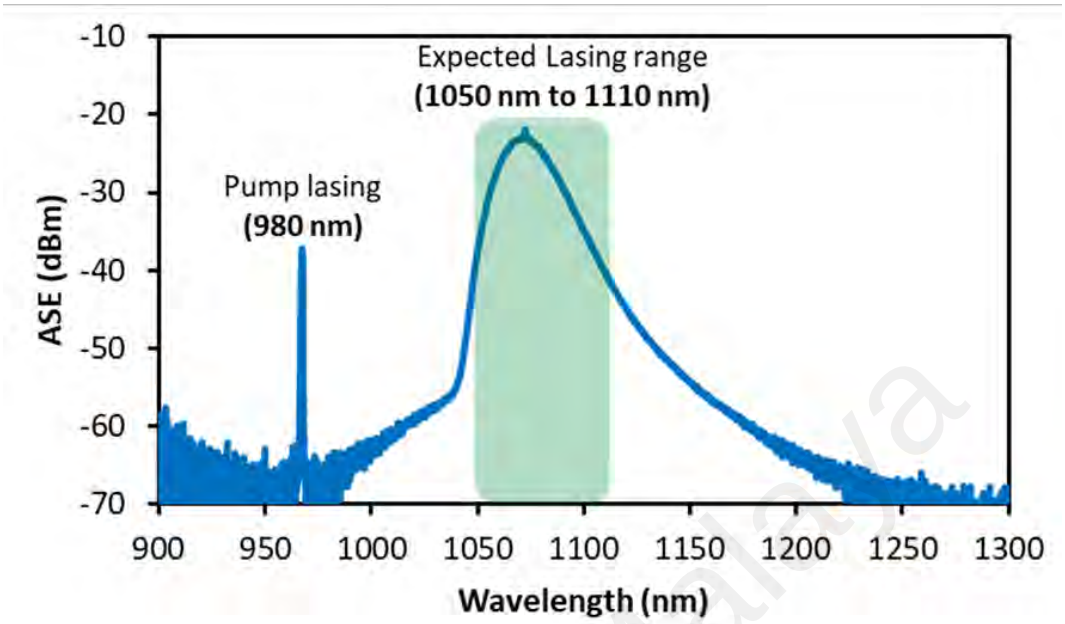

Figure 3.10: (a) Schematic diagram of mode-locked double-clad YDFL. (b) ASE spectrum from the 10 m long YDF with 980 nm multimode pumping.

At first, a continuous-wave (CW) laser was generated by the YDFL as the multimode pump power is increased to 431 mW. As the pump power is further increased to 689 mW, the laser starts to generate the mode-locking pulse train. The mode-locking operation remains stable as the pump power is increased until 1006 mW, but it becomes unstable and disappears as the pump power is continued to increase. Stable mode-locking operation with a fundamental repetition rate of 13.2 MHz is generated in between 689 mW to 1006 mW pump power. Figure 3.11(a) shows the output spectrum of mode-locked YDFL which is obtained at the threshold pump power. It shows that the laser operates at 1090 nm wavelength with 3-dB spectral bandwidth of 0.08 nm (20.19 GHz). Figure 3.11(b) shows the output power and pulse energy of the mode-locked YDFL with a slope efficiency of 1.72 %. At a maximum pump power of 1006 mW, the measured output power is 20 mW and the maximum pulse energy is calculated to be about 1.48 nJ.

(a)

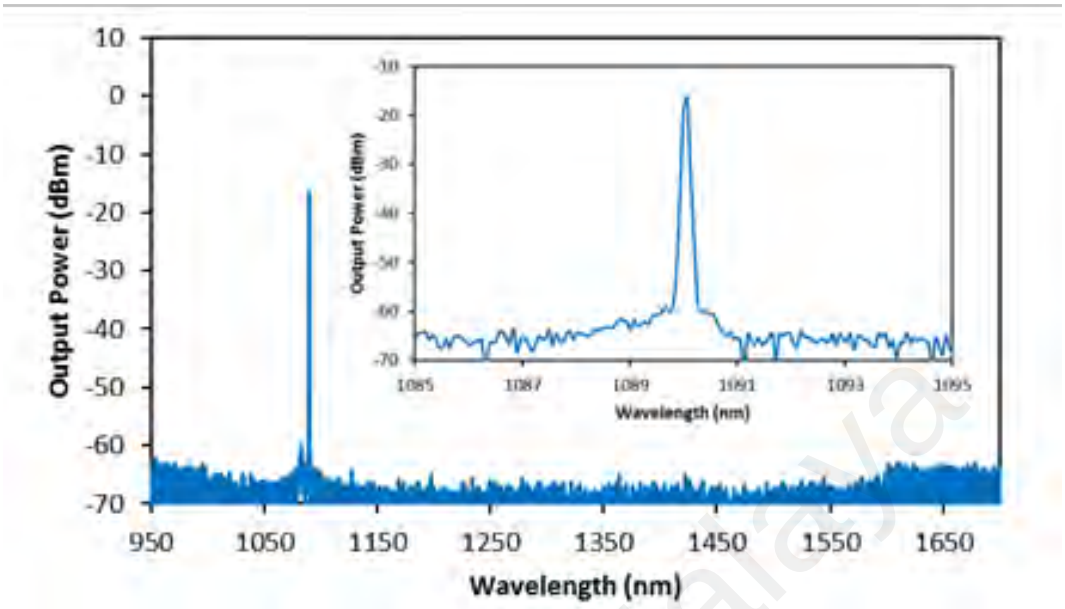

(b)

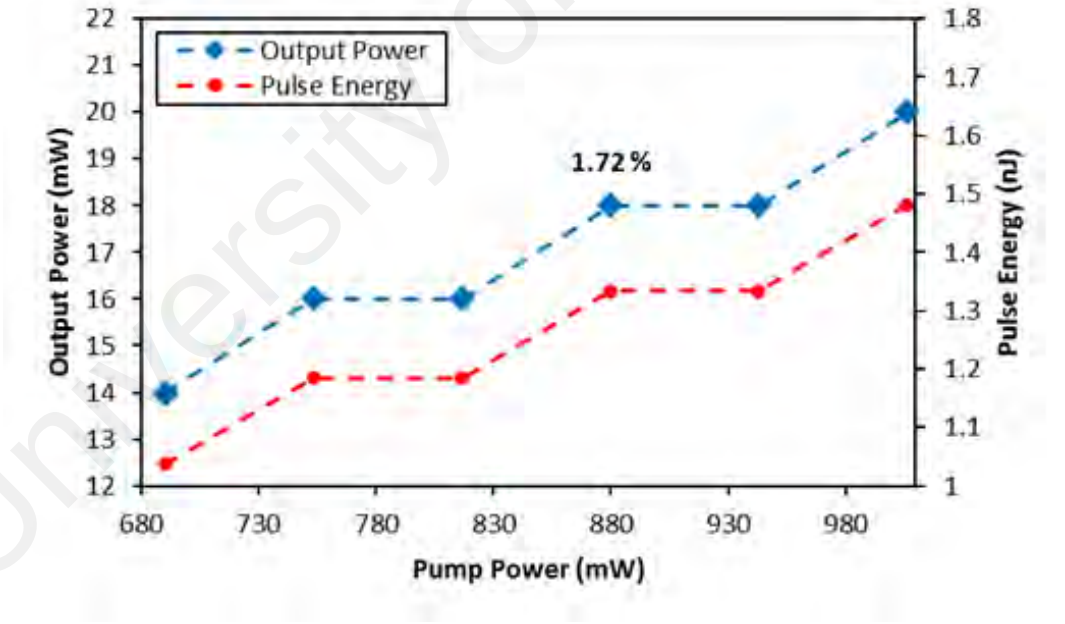

Figure 3.11: (a) Output spectrum at a pump power of 689 mW. (b) Output power and pulse energy.

Figure 3.12(a) shows the mode-locked YDFL pulse train with a pulse period of 76 ns. The obtained fundamental repetition rate of 13.2 MHz matches the cavity length of 14.8 m. Direct from the oscilloscope, the obtained pulse width of 32.5 ns is much broader than the actual pulse width. This happens due to resolution limitation of the oscilloscope. As an alternative, the pulse width can be measured using an auto-correlator or calculation using a formula based on the TBP. The minimum possible pulse width is estimated around 21.84 ps with TBP of 0.441 for Gaussian pulse profile and 3-dB spectral bandwidth of 20.19 GHz. Figure 3.12(b) shows the RF spectrum with 100 MHz spans. The repetition rate existence limits to seven harmonics, and preliminary indicates the pulse width is not too short. The RF spectrum confirms the mode-locked YDFL has a fundamental repetition rate of 13.2 MHz with a signal-to-noise ratio (SNR) is about 29 dB. This SNR corresponds to the 10 % amplitude fluctuation presence in pulse train within one hour mode-locking operation. This small fluctuation is expected due to the inhomogeneous of MoS_2 flakes adhere on the scotch tape. The peak power is obtained about 0.154 kW. The long-term stability is also good since the pulse is stable for at least 48 hours. The small changes in room temperature and environment do not affect the mode-locking performance of the laser.

(a)

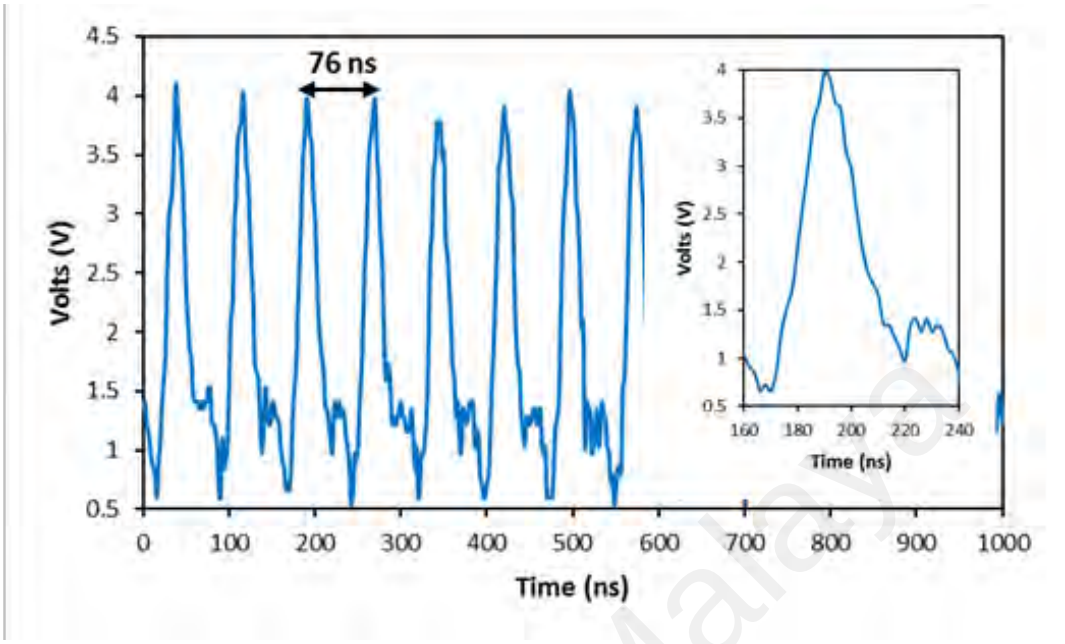

(b)

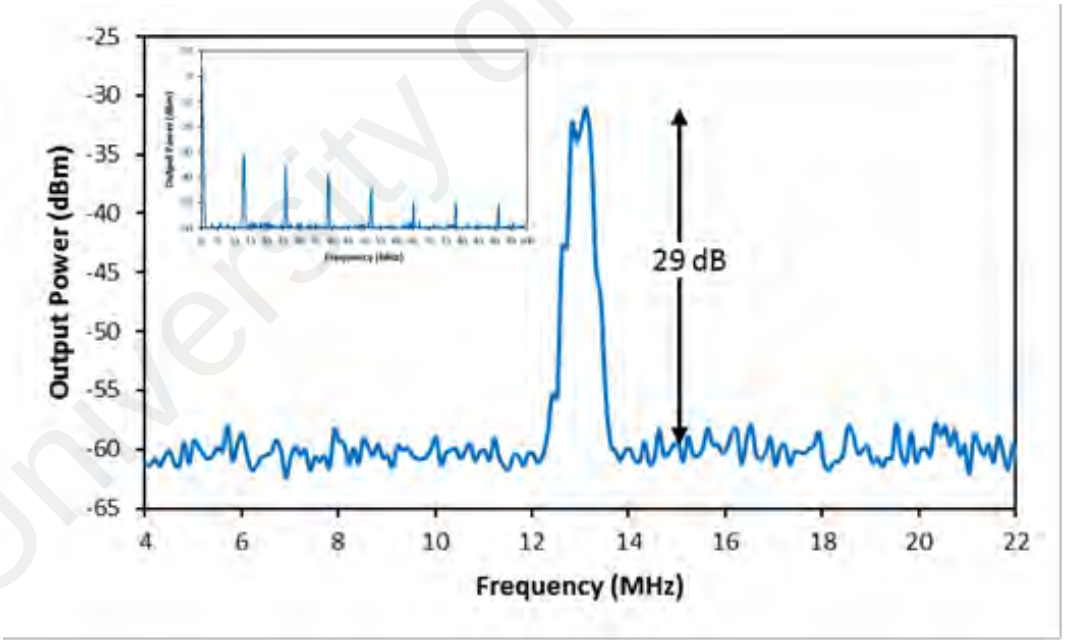

Figure 3.12: Temporal performances of mode-locked YDFL. (a) Pulse train at 1006 mW. Insert image of enlarging pulse train. (b) RF spectrum at a maximum pump power of 1006 mW. Insert is the RF spectrum with 100 MHz spans.

3.6 Mode-locked fiber lasers with molybdenum disulfide SA operating at 2-micron region

The mode-locked laser systems operating in the "eye safe" spectral range around 2-micron become a subject of growing interest and rapid development because of their increasing application requirements in free-space optical communication, LiDAR, military, medical surgery, material processing, etc (Fermann & Hartl, 2013; Fried et al., 2008). In 2-micron region, mode-locked fiber lasers are also highly transmissive in the air and favorable absorb in organic tissues and water. The 2-micron pulsed fiber lasers can be realized using either thulium (Tm) or Holmium (Ho) doped fiber as a gain medium. However, there are still many issues to be addressed such as low quantum efficiency of generated laser in high phonon energy glass host matrix such as silica-based glass fibers. Therefore, Thulium-doped fibers (TDFs) are adopted since they normally employ low phonon energy glass hosts, e.g. - fluoride glass, in which the up-conversion intensity is reported to be quite high in the ultraviolet region (Jackson et al., 2007). Nevertheless, since the fluoride host is a rather soft type of glass, it is very hard to draw optical fiber from the preform due to its lower melting temperature. Recently, the interest has shifted back to silica based host TDFs as the phonon energy of silica glass can be reduced by incorporating silica network modifiers like Aluminum (Al) and Germanium (Ge). Thus TDFs with modified silica host have emerged as a promising gain medium for achieving an efficient Thulium-doped fiber (TDFL) (Rustad & Stenersen, 1996).

Progressive development of Holmium-doped fiber attracts much interest since it offers a unique opportunity for operation at the long-wavelength edge of transparency of silica-based glass at ~2.1 μm (Chamorovskiy et al., 2012). Due to the limited pump sources for the direct Holmium ion pumping, co-doping is the best approach for developing Holmium-based fiber laser systems. Thulium-Holmium co-doped fiber lasers (THDFLs) can be realized by laser diode pumping at a wavelength near 1.56 μm. TDFL is obtained

through the ion transition between the $^3F_4$ - $^3H_6$ states when pumped at around 1.56 μm. The co-doping with Holmium ion allows for energy transfer from the Thulium ion $^3F_4$ to the Holmium ion $^5I_7$ state. The Holmium ion transition of $^5I_7$ - $^5I_8$ generates lasing at wavelengths near 2.1 μm (Oh et al., 1994). Until recently, there is still a lack of research work on generating ultrafast all-fiber laser based on TDF and THDF. THDFLs provide an efficient method of generating high average power in the 1.8 – 2.2 μm spectral region. TDFLs typically operate efficiently between 1.85 – 2.09 μm (Clarkson et al., 2002). In this section, a mode-locked TDFL and THDFL operating at 2-micron region are demonstrated by integrating the prepared MoS_2 tape into the cavity.

3.6.1 Thulium doped fiber laser (TDFL)

The mode-locked TDFL is generated by using all-fiber ring cavity configuration as shown in Figure 3.13(a). As shown in the figure, all optical components are connected in a ring with a 5 m long single-clad TDF (Nufern, SM-TSF-9/125) was used as a gain medium. The GVD parameter for TDF is about -84.6 ps^2/km. According to the ASE spectrum, as depicted in Figure 3.13(b), this TDF is expected to generate effective lasing between 1840 nm to 1980 nm by 1552 nm wavelength pumping. Other fibers in the cavity is a 10 m long ScDF with -127 ps^2/km and a standard SMF with - 80 ps^2/km, which constituted the rest of the ring. The total cavity length is around 27.9 m, and the total net GDD in the cavity is operates in anomalous dispersion condition of -2.725 ps^2.

The 1552 nm homemade Erbium-Ytterbium co-doped fiber laser (EYDFL) with 38 % efficiency was used to pump a 5m long TDF up to 1.5 W optical power via 1550/2000 nm fused wavelength division multiplexing (WDM). This TDF has a core diameter of 9 μm with core NA and absorption of 0.15 and 27 dB/m at 793 nm, respectively. The oscillating ASE light oscillated in the ring cavity to generate laser. The laser propagates

in unidirectional and maintains its direction after pass through the isolator. The 10 m long ScDF was added in the cavity to gain sufficient nonlinearity effects for mode-locked generation. ScDF has a core composition of SiO_2-GeO_2-Sc_2O_3 with core diameter and NA of 7.5 µm and 0.12, respectively. The mode-locked laser performances were collected from 10 % of output coupler, the remaining of 90 % continuously oscillated in the cavity. With FC fiber adapter, the 1 mm x 1 mm MoS_2 tape was sandwiched in between two fiber ferrules. Index matching gel was used as an adhesive and also as an element to fill the air-gap.

(a)

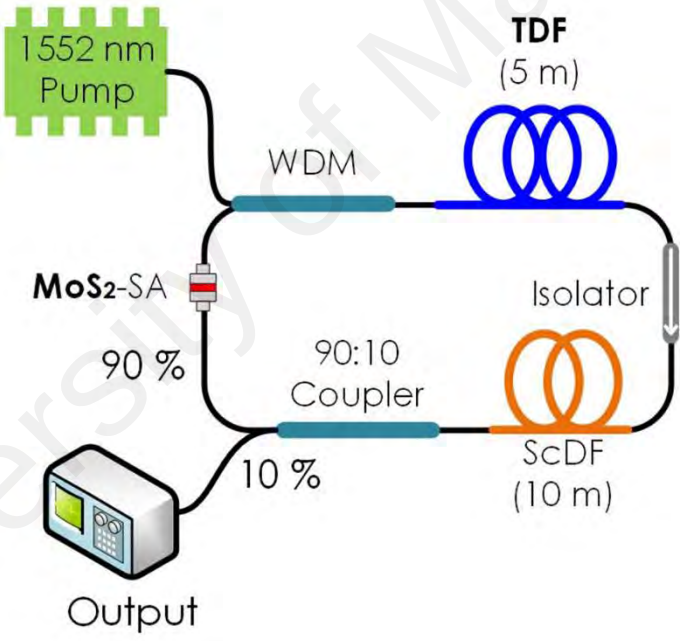

(b)

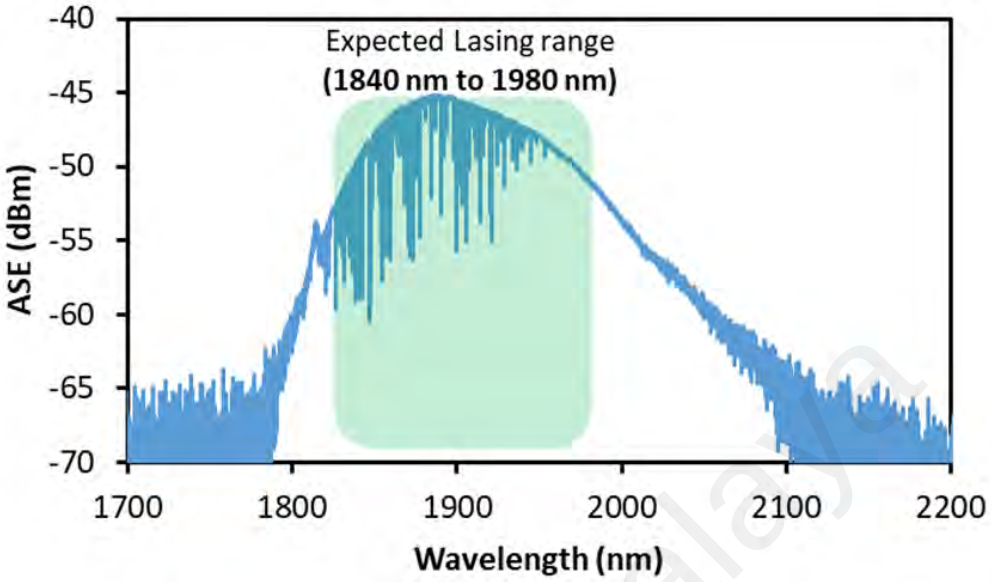

Figure 3.13: (a) Schematic configuration for mode-locked TDFL. (b) ASE spectrum of the 5 m long TDF.

The output spectrum was observed by using an optical spectrum analyzer (OSA, Yokogawa: AQ6375) with a resolution of 0.05 nm. An optical power meter (OPM, OPHIR: AN-2) was connected via thermal sensor (OPHIR: D30A-SA_V1) to measure laser output power. Through 7 GHz InGaAs photodetector (EOT: ET-5010F) with rise and fall time less than 50 ps, temporal characteristics were observed by using 500 MHz oscilloscope (LeCroy: WAVEJET 352A) and confirm by 7.8 GHz radio frequency spectrum analyzer (RFSA, Anritsu: MS2683A). The laser output is also observed by removing the SA to eliminate the mode-locking mode. This can confirm that the presence of mode-locking pulse was owned to this SA.

The CW laser was converted to mode-locking mode at 491 mW pump power, and the mode-locking operation continues dominant until it reaches 711 mW pump level. Figure 3.14 depict the spectral and output power performances of the mode-locked TDFL generated by incorporating the MoS_2 tape. Figure 3.14(a) shows the output spectrum of mode-locked TDFL with peak lasing obtainable at 1928 nm. The 3-dB spectral bandwidth is measured about 3.4 nm (274 GHz), which pre-indicates the existence of more phase-locked of longitudinal modes. Overall, mode-locked TDFL has a slope efficiency (SE) of 7.7 % within 481 mW to 711 mW pump power as shown in Figure 3.14(b). The self-started mode-locking operation at 481 mW pump level has a minimum output power of 16 mW, and maximum output power of 32 mW at 711 mW pump level. The pulse energy is relatively calculated from the measured average output power over the measured repetition rate. The maximum pulse energy of 4.5 μJ is obtained at maximum pump level.

(a)

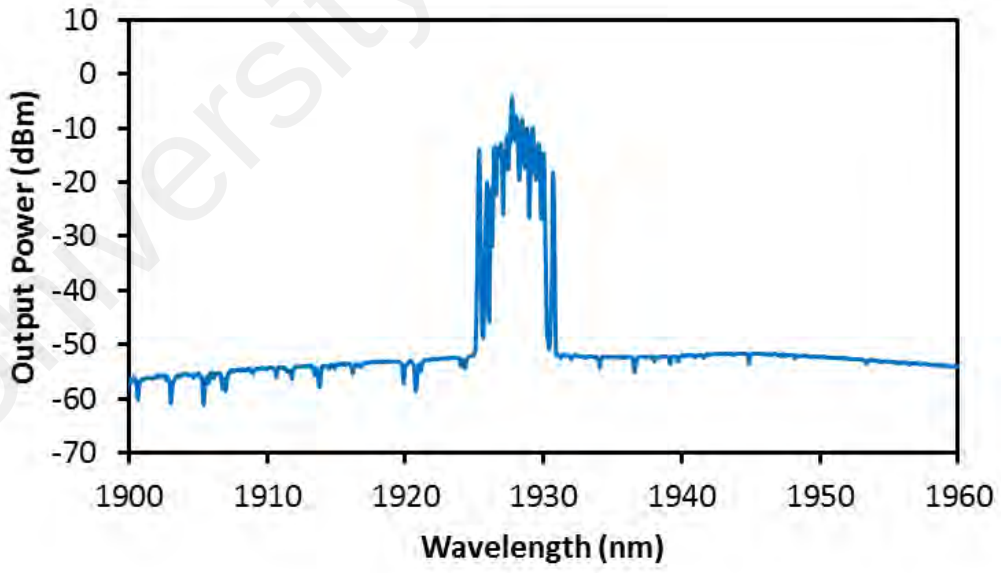

(b)

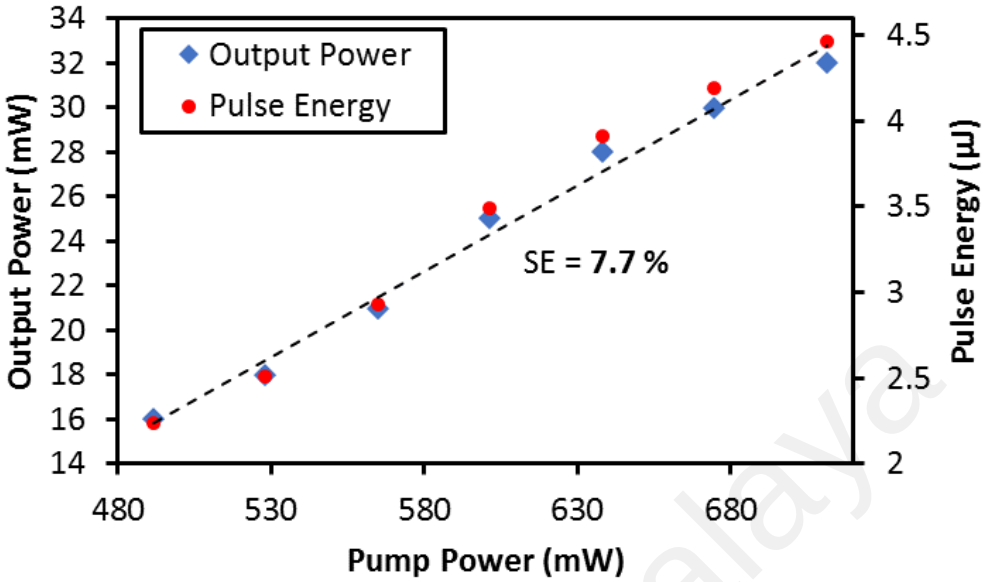

Figure 3.14: Performances of mode-locked TDFL. (a) Output spectrum. (b) Output power and pulse energy characteristics against the pump power.

Temporal characteristic of the mode-locking pulses train is observed by using the oscilloscope in time-domain. As shown in Figure 3.15(a), the pulse period between two adjacent peaks is measured about 139.88 ns, corresponds to the repetition rate of 7.16 MHz with a pulse width of 52.26 ns. Consequently, the reading for the pulse width is not accurate due to the limited resolution of the oscilloscope. As an alternative, the pulse width size can be determined from the formula of TBP. In anomalous regime cavity, the $sech^2$ pulse profile of 0.315 is used to calculate the pulse width size based on actual measurement of 3-dB spectral bandwidth taken from the OSA. The minimum possible pulse width is calculated to be 1.15 ps. Smooth oscilloscope train presence at the obtained pulse. The existence of the pulse can be confirmed through the RF spectrum analyzer. Figure 3.15(b) represent the RF spectrum of mode-locked TDFL with the occurrence of four harmonics within 40 MHz spans. A stable repetition rate presences at the fundamental frequency of 7.16 MHz with SNR of 48 dB.

(a)

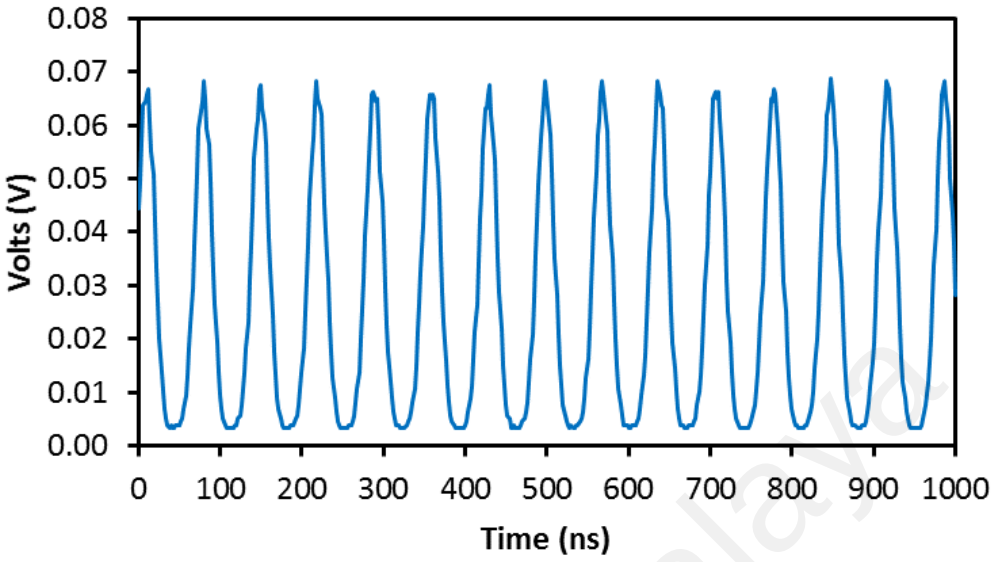

(b)

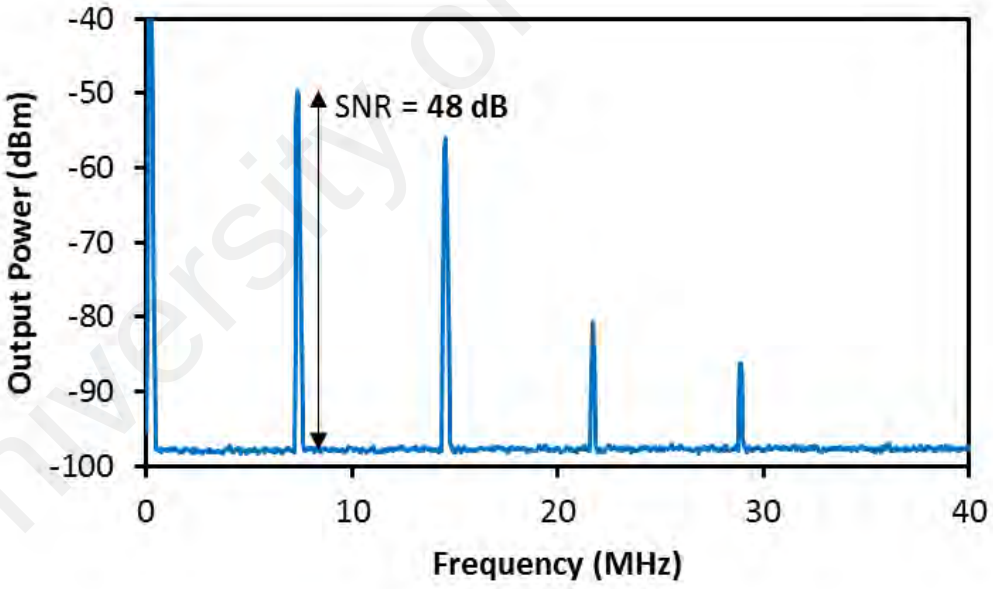

Figure 3.15: Temporal characteristics of mode-locked TDFL. (a) Pulse train. (b) RF spectrum with 40 MHz spans.

3.6.2 Mode-locked Thulium Holmium co-doped fiber laser

Next, the MoS_2 tape is integrated into the THDFL cavity. Figure 3.16(a) illustrates the schematic diagram for THDFL cavity which consists of similar configuration like in the previous section of the TDFL cavity. The 5 m long single-clad THDF (CorActive: TH550) with 11.5 µm core diameter was used as a gain medium. According to the ASE spectrum as depicted in Figure 3.16(b), this THDF is expected to generate effective lasing between 1960 nm to 2160 nm by 1552 nm wavelength pumping. The GVD parameter for THDF is about -72.8 ps^2/km. This THDF has a core NA and absorption of 0.14 and 100 dB/m at 790 nm, respectively. For this configuration, the rest of the cavity is connected by 6.4 m long SMF. Thus, contributing to the total cavity length of 21.4 m which also includes the ScDF. The total net GDD in the cavity is operated in anomalous dispersion condition of -2.146 ps^2.

(a)

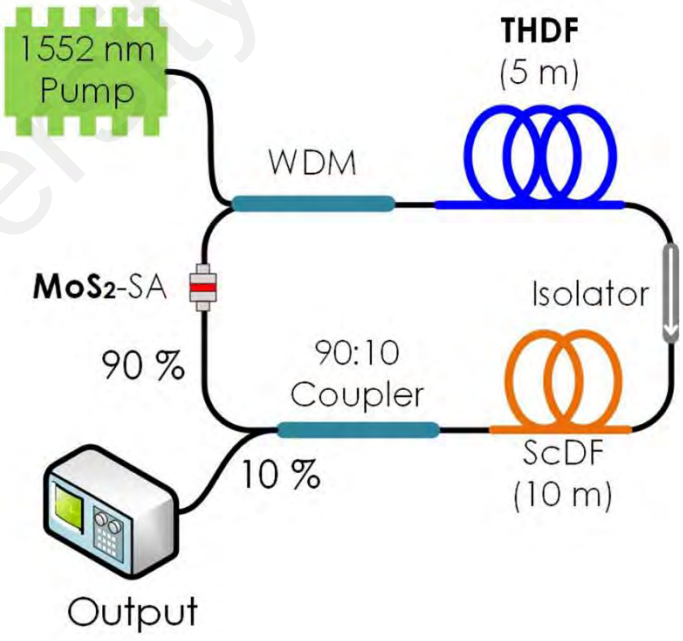

(b)

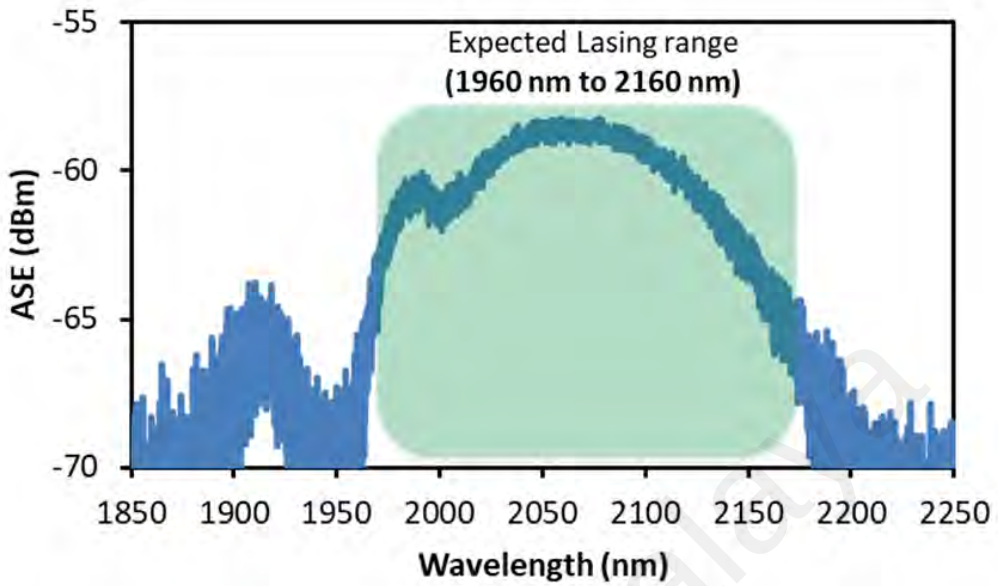

Figure 3.16: (a)Schematic diagram of mode-locked THDL ring cavity. (b) ASE spectrum of 5 m long THDF.

As the MoS_2 tape is integrated into the THDFL cavity, the mode-locking operation can be achieved as the pump power is varied from 775 mW to 852 mW. Figure 3.17(a) shows the mode-locked THDFL output spectrum which was obtained from the output port (10%) of the coupler. The peak lasing is observed to operate at a wavelength of 1979 nm with a 3-dB spectral bandwidth of 2.1 nm (160 GHz). The relation between the output power and pump power is shown in Figure 3.17(b). Under the mode-locking regime, the obtained output power increases from 13 mW to 20 mW as the pump power is increased from775 mW to 852 mW. This gives the SE of 8.9 %. The relation between the pulse energy and pump power is also investigated. It is observed that the pulse energy increases linearly with the pump, with the maximum pulse energy of 2.2 nJ.

(a)

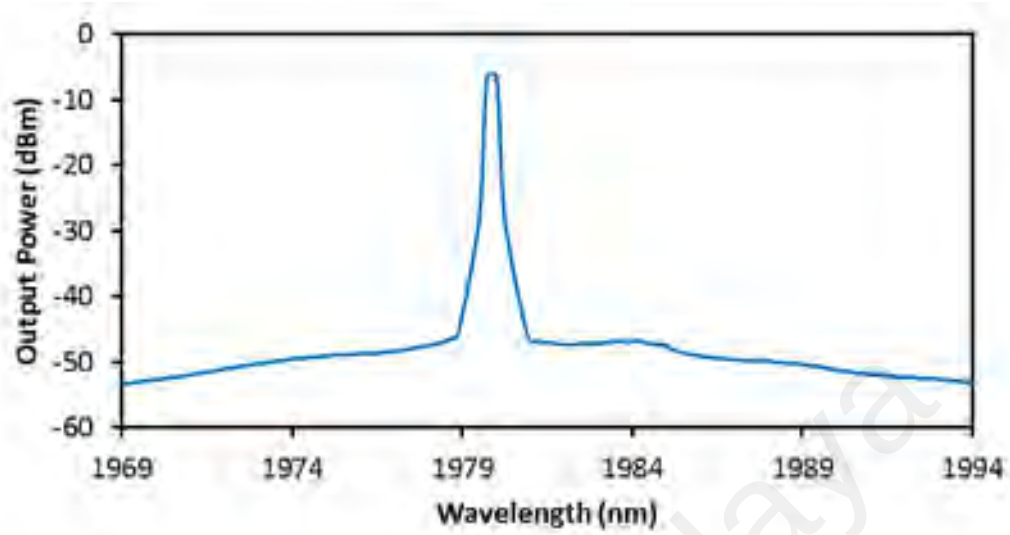

(b)

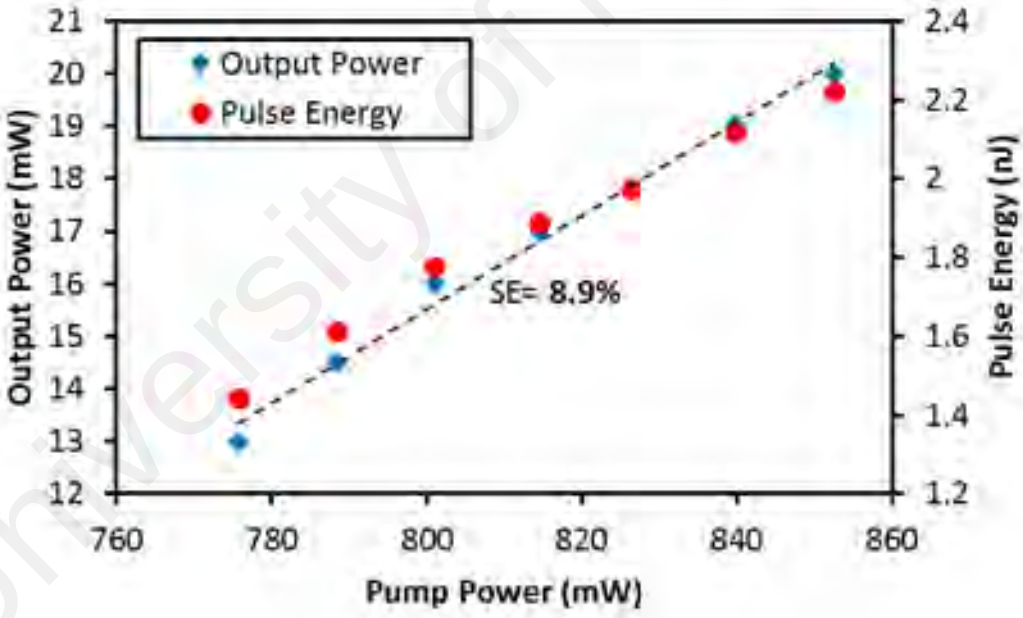

Figure 3.17: Performances of mode-locked THDFL. (a) Output spectrum. (b) Output power and pulse energy.

Figure 3.18 shows the temporal characteristics of the THDFL A stable mode-locking pulse train with a pulse period of 109.74 ns is obtained as illustrated in Figure 3.18(a). This pulse period can be translated to a repetition rate of 9.12 MHz, which corresponds to the total cavity length. The FWHM of 56.08 ns in the pulse train does not represent the actual pulse width size. Through TBP of $sech^2$ pulse profile, the minimum possible pulse width size is relatively determined about 1.97 ps. A pulse stability can be confirmed through the investigation on RF spectrum. Figure 3.18(b) shows the RF spectrum of the mode-locked THDFL with two harmonics at 9.12 MHz and 18.6 MHz. The fundamental frequency of repetition rate has an SNR of 45 dB, validates this generation of mode-locked THDL is stable. In the next chapter, another 2D nanomaterial, titanium dioxide is explored for potential applications in ultra-short pulse generation

(a)

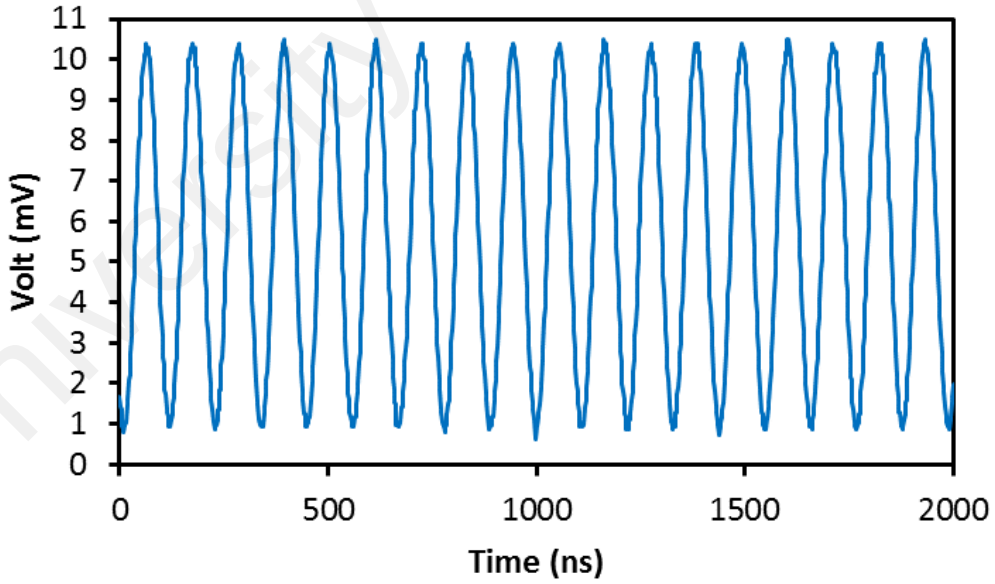

(b)

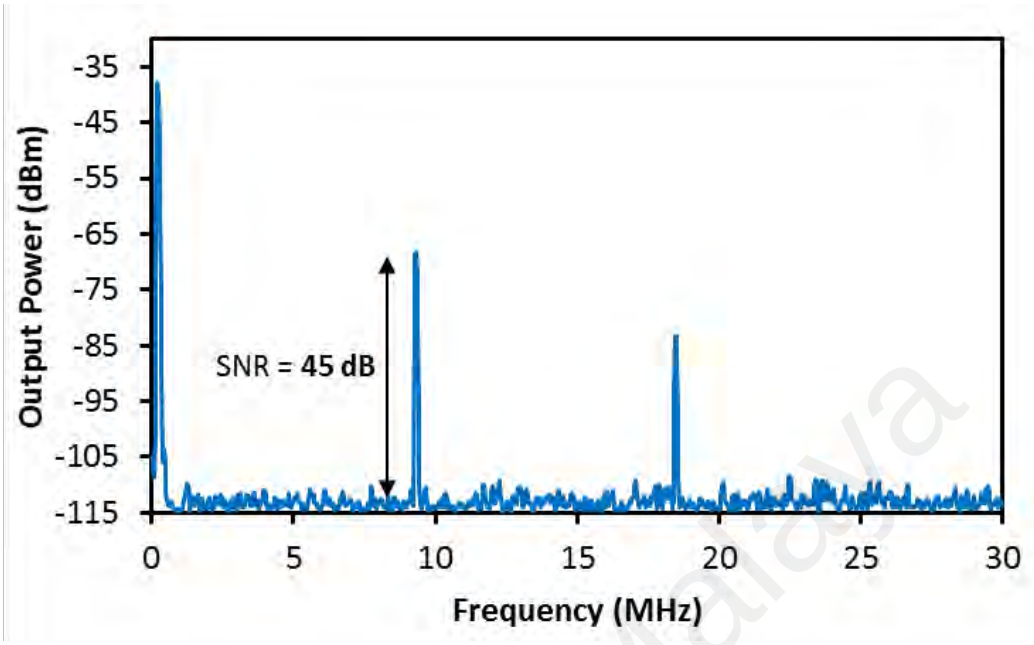

Figure 3.18: Temporal characteristics of mode-locked THDFL. (a) Pulse train. (b) RF spectrum with 30 MHz span.

3.7 Summary

The generations of mode-locking pulses train in 1-, 1.55-, and 2-micron regions have been successfully demonstrated using a MoS_2 tape as SA. This MoS_2 tape has a saturable absorption, non-saturable absorption, and saturation intensity of 10 %, 12 %, and 100 MW/cm^2, respectively. The SA was prepared from a commercial crystal of MoS_2 without any chemical procedures. A few layers MoS_2 was mechanically exfoliated by using a clear scotch tape. Then, a piece of 1 × 1 mm tape containing MoS_2 thin flakes is inserted between two fiber ferrules and is integrated into various ring laser cavities. At first, the SA device is incorporated into the EDFL cavity with a total length of around 49 m and operates in anomalous dispersion condition of -0.217 ps^2. Self-starting, stable picosecond pulses operating at 1562.7 nm were generated as the pump power is increased from the threshold of 166.3 mW, up to 250 mW with a consistent pulse repetition rate of 4.0 MHz. Maximum pulse energy calculated is 1.66 nJ at a pump power of 250 mW, where a pulse

width of 1.71 ps is achieved based on $sech^2$ pulse profile. The stable mode-locking operation is also attained at 1090 nm in double-clad YDFL cavity with a repetition rate of 13.2 MHz. The mode-locked YDFL has a maximum output power of 20 mW with 1.48 nJ pulse energy. The mode locking of a TDFL operating at 1928 nm was also demonstrated using the MoS_2 based SA. At 1552 nm pump power of 481 mW, the mode-locked TDFL self-starts to generate an optical pulse train with a repetition rate of 7.16 MHz. Based on TBP, the minimum possible pulse width is calculated to be 1.15 ps. The maximum pulse energy of 4.5 μJ is obtained at a maximum pump level of 711 mW. As the MoS_2 tape is integrated into the THDFL cavity, the mode-locking operation can be achieved at 1979 nm with a repetition rate of 9.12 MHz. These results validate that the MoS_2 has a broad operating wavelength which covers the operation region from 1 to 2 micron. This may contribute to a growing body of work focused on studying the nonlinear optical properties of MoS_2, suggesting new opportunities for ultrafast photonics applications.

CHAPTER 4: TITANIUM DIOXIDE SATURABLE ABSORBER

4.1 Introduction

Fiber lasers have been extensively developed so far due to their many advantages compared to other types of lasers such as dye, gas, chemical, solid state and semiconductor. They have many potential applications in telecommunication, bio-sensing, medicine, imaging, range finding and material processing (Fermann et al., 2013; Godard, 2007; Jackson, 2012). Recently, many works have also been devoted to mode-locked fiber lasers especially on passively mode-locked fiber lasers, which can be realized without the involvement of electro-mechanical component. These lasers also operate at much higher frequency regime compared to that of Q-switched lasers. Up to date, there are various types of mode-locking pulses have been experimentally demonstrated such as soliton, stretched pulse, noise-like pulse, and square pulse. Among them, soliton pulse approaches a platform to investigate different nonlinear phenomena such as the configuration of the conventional soliton, dissipative soliton, bound-state soliton, vector soliton, and dissipative soliton resonance (Haris et al., 2015).

As previously discussed, the passively mode-locked fiber lasers can be realized by using various types of the saturable absorber (SA) such as semiconductor saturable absorber mirrors (SESAMs), two-dimensional (2D) materials (graphene, topological insulators, transition-metal dichalcogenides) and doped-fiber SA (Woodward et al., 2015). However, the applications of most of these SAs are restricted due to their drawbacks such as complex optical alignments, environmental sensitivity, complicated fabrication and limited operating bandwidth. Therefore, there are many new attempts in recent years to develop new SAs with better performance for mode-locking laser operation (Latiff et al., 2017). In the previous chapter, various mode-locked fiber lasers have been demonstrated using MoS_2 as an SA in various laser cavities. An ideal SA

should have a broadband absorption, ultrafast recovery time (~ps), low saturation intensity, suitable modulation depth, high damage threshold as well as cost- and time-efficient to construct.

Most recently, many research works have been focused on titanium dioxide (TiO_2) nanomaterial. TiO_2 is 2D transition metal oxide material which has a low electrical resistivity (Banakh et al., 2002) and exhibits high efficiency as a diffusion barrier against the inter-diffusion of aluminum and silica. It is also reported that conductive TiO_2 could be used as a thin film material for applications in microelectronic layered structures (Martev, 2000). Recovery time is an important parameter to determine the pulsing ability of saturable absorber. Elim et al. reported the TiO_2 polymer film has a recovery time of ~ 1.5 ps (Elim et al., 2003). This saturable absorption ability is due to the Pauli-blocking principle. Of late, many investigations on TiO_2 optical properties such as the light absorption have been conducted (Zhang & Wu, 2014). For instance, the light absorption properties of blue titanium suboxide nanoparticles were investigated (Wang et al., 2005). Although the bandgap of TiO_2 is ~3.2 eV or 5.13 x 10^{-19} Joules (387 nm), spectral absorption by TiO_2 can extend until the near-infrared (NIR) region. This can be explained by the quantum size effect of TiO_2, where the absorption depends on the crystal form and particle size (Set et al., 2004a). On the other hand, Polyvinyl alcohol (PVA) has been intensively used in many applications because of its capability to form a film and favorable physical properties such as good chemical resistance, biocompatibility, and hydrophilicity (Chen, 2002). As a 2D material, TiO_2 sheets can be easily exfoliated mechanically or chemically due to its strong in-plane bonding and weak van der Waals coupling between layers.

This chapter demonstrates the fabrication of TiO_2 thin film and the application of the TiO_2 film as a new type of effective SA for ultrafast photonics. By placing such optical SA devices inside the EDFL and THDFL cavity, the stable passive mode-locking operation of the fiber laser could be obtained, hence suggests that TiO_2 could be developed as an effective SA for ultrafast photonics. Using YDFL and TDFL cavity, the only Q-switching operation was generated.

4.1 Preparation of titanium dioxide SA film

SA film fabrication process involves a preparation of base material and polymer solutions. Through drop-casting method, the base material and polymer solution are mixed to form an SA film. The base material used in this work is a commercial anatase TiO_2 powder with 99% purity, from Sigma-Aldrich. This powder has a diameter of less than 45 μm and a weight of 79.87 g/mol. All the main peaks which determine the phase composition of TiO_2 material were observed by X-ray diffraction (XRD) analysis as shown in Figure 4.1.

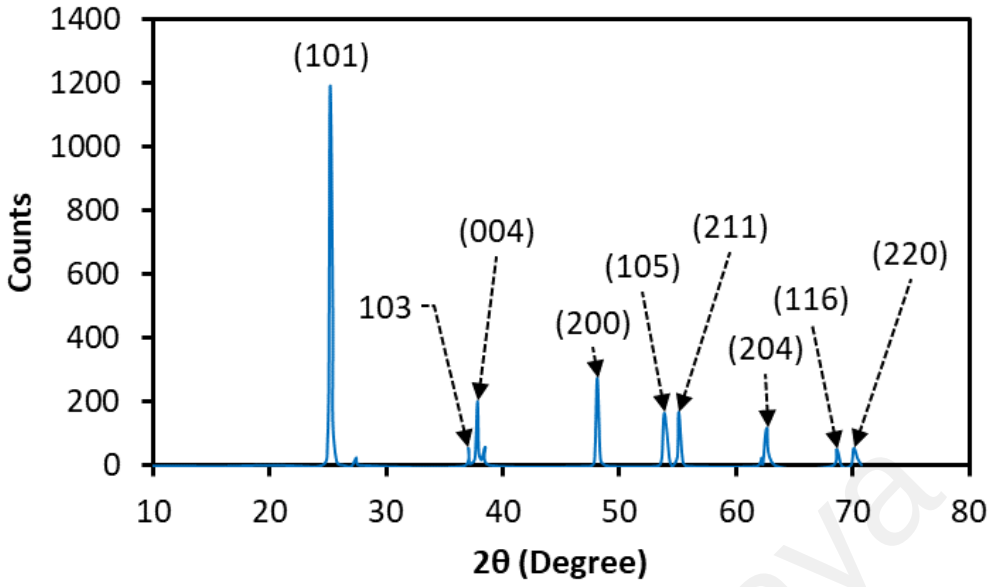

Figure 4.1: XRD pattern of TiO_2 powder.

Figure 4.2 illustrates the step by step process of TiO_2 film fabrication. The process can be divided into three stages; the process of making a base material solution (1st stage); the process of making a polymer solution (2nd stage); the process of mixing a base material and polymer solution (3rd stage). At first (1st stage), the TiO_2 solution was prepared by solving a TiO_2 powder in 40 ml distilled water with an assistance of 1% sodium dodecyl sulfate (SDS) solvent. The mixture was stirred for 5 minutes so that the Van der Waals forces between powders break and completely disperse. Then, the TiO_2 solution was centrifuged at 3000 rpm for 15 minutes, and the supernatant containing TiO_2 suspension in solution was collected for use.

In the next process (2nd stage), the polymer solution was obtained by mixing 1 g of polyvinyl alcohol (PVA) powder with 120 ml deionized water (DI). The mixture was stirred at 90 ^{o}C until the polymer dissolved homogeneously. The polymer solution was then cooled down to room temperature. The PVA is more favorable compared to another type of biocompatible polymer such as polyethylene oxide (PEO). Compared to PVA,

melting point for PEO is low. For last process (3rd stage), add the dispersed TiO_2 solution into a PVA solution. The TiO_2 and PVA mixture is thoroughly mixed through the two hours ultrasonication process in forming a composite precursor solution. Finally, the precursor solution was poured into a glass petri dish and dried at a room temperature for nearly two days to form a free-standing film. This film has obtained a thickness of ~ 30 µm.

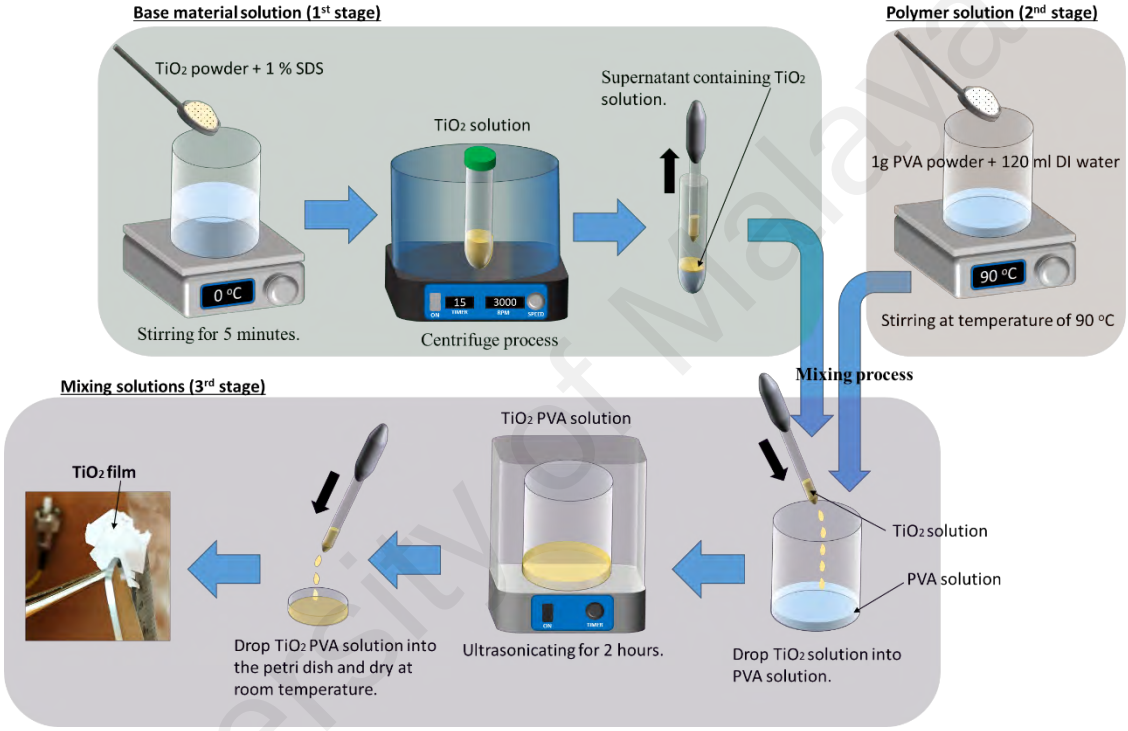

Figure 4.2: Fabrication process of the TiO2 film.

4.2 Characterization of titanium dioxide SA film

Like in Chapter 3, the obtained TiO_2 film was then going for the characterization work (FESEM, EDS and Raman spectroscopy). The surface morphology of the fabricated film was tested by ultra-high resolution FESEM imaging, as shown in Figure 4.3(a). From the FESEM image, the TiO_2 particles presence continuous across the imaging region with a non-uniform diameter from 100 nm to 500 nm. The film was smooth-surfaced and quite

clean, showing a good quality. Figure 4.3(b) shows the constitutive elements in the TiO_2 film by EDS analysis on the FESEM image. It is evident, the obtained film has dominated the amount of titanium (Ti) element with the weight of 30.38 %, at 0.5 keV and 4.5 keV. The oxygen (O) element of 37.57 % is contributed from TiO_2 and PVA film. About 26.54 % of carbon (C) results from PVA film. A few extraneous elements are presented without affecting the performance of TiO_2 film SA. The extraneous elements are suspected obtained from FESEM machine during the preparation of tested sample.

(a)

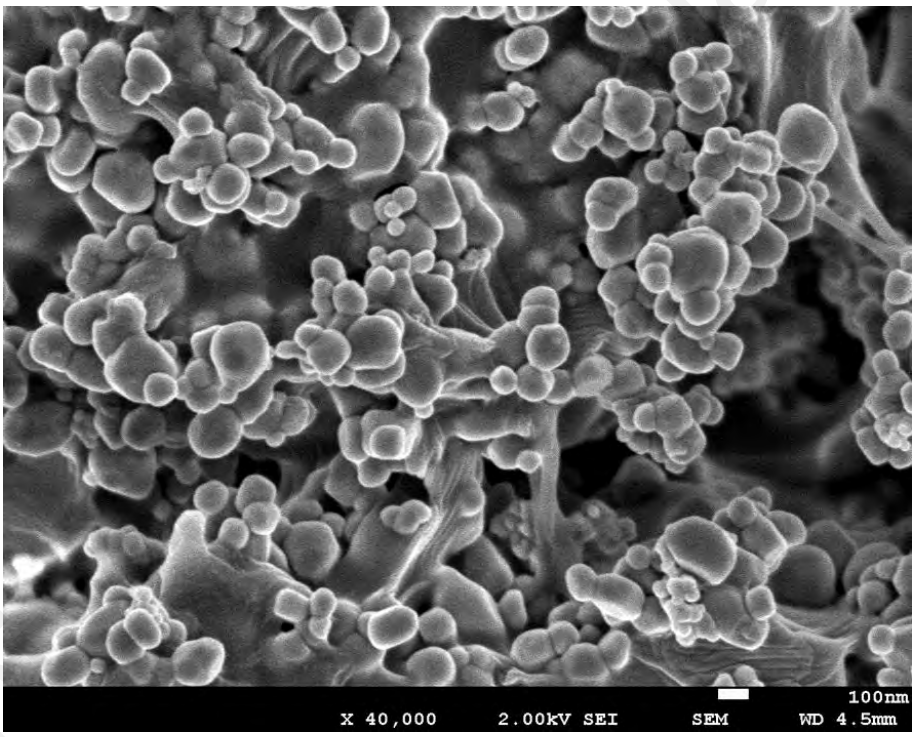

(b)

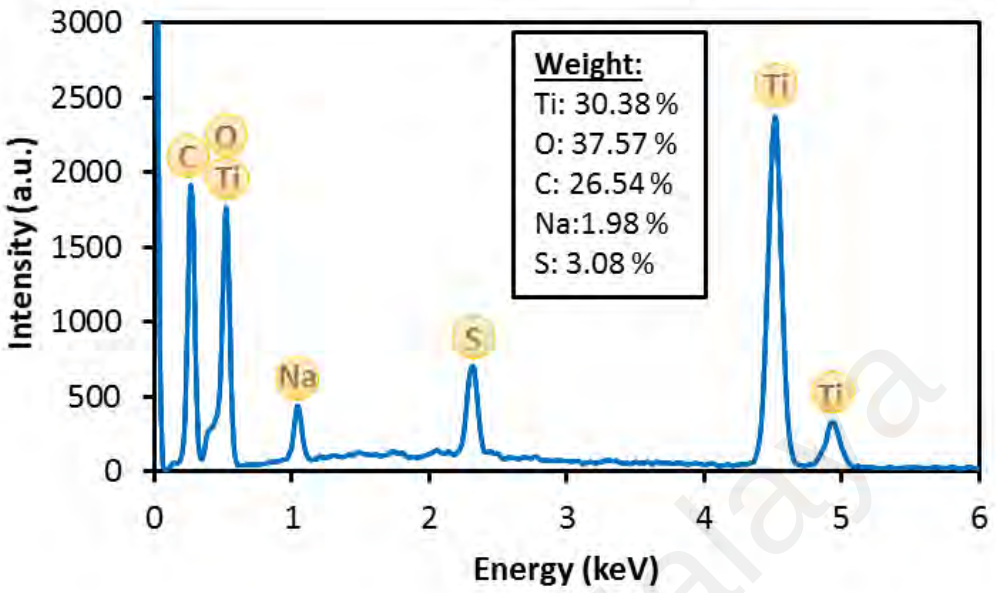

Figure 4.3: (a) FESEM image of the TiO_2 film. (b) EDS data.

The presence of TiO_2 material on the film was verified by conducting Raman spectroscopy measurement on the fabricated TiO_2 film sample. Additionally, broadening and shifts of Raman bands of TiO_2 also can be used to investigate the decreasing particle size (Bradley et al., 2012; Choi et al., 2005). Figure 4.4 shows the Raman spectrum, which is recorded by a spectrometer when a 514-nm beam of an Argon laser is radiated on the film for 10 ms with an exposure power of 50 mW. As reported by Oshaka (Ohsaka et al., 1978), the sample exhibits five distinct Raman peaks at approximately 145 cm^{-1}, 198 cm^{-1}, 399 cm^{-1}, 516 cm^{-1}, and 640 cm^{-1}, which corresponds to the first-E_g, second-E_g, B_{1g}, A_{1g}, and third-E_g band, respectively. High peak intensity at 145 cm^{-1} confirms this TiO_2 is only observed in the Raman spectrum of anatase crystalline structure.

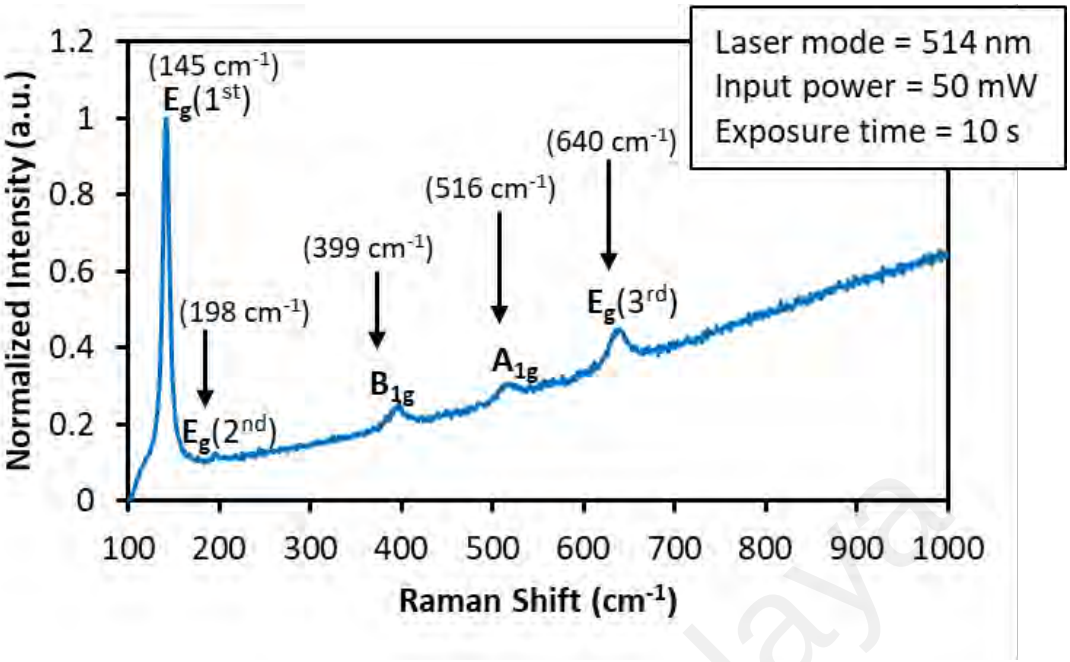

Figure 4.4: Raman spectrum of TiO_2 film.

For optical characteristics, nonlinear absorption measurements for SA was performed by launching a mode-locked laser (wavelength of 1550 nm, the pulse width of 1.5 ps, repetition rate of 17.4 MHz). By performing a balance twin-detector measurement, the modulation depth of the film is measured to be around 34 % as shown in Figure 4.5. The measurement data was fitted by the formula of $\alpha(I)=\alpha_{sat}/(1+I/I_{sat})+\alpha_{ns}$, where $\alpha(I)$ is the absorption coefficient, α_{sat} is the modulation depth, I is the input intensity, I_{sat} is the saturation intensity, and α_{ns} is the non-saturable absorption. The mode-locked source here is a self-constructed passively mode-locked fiber laser.

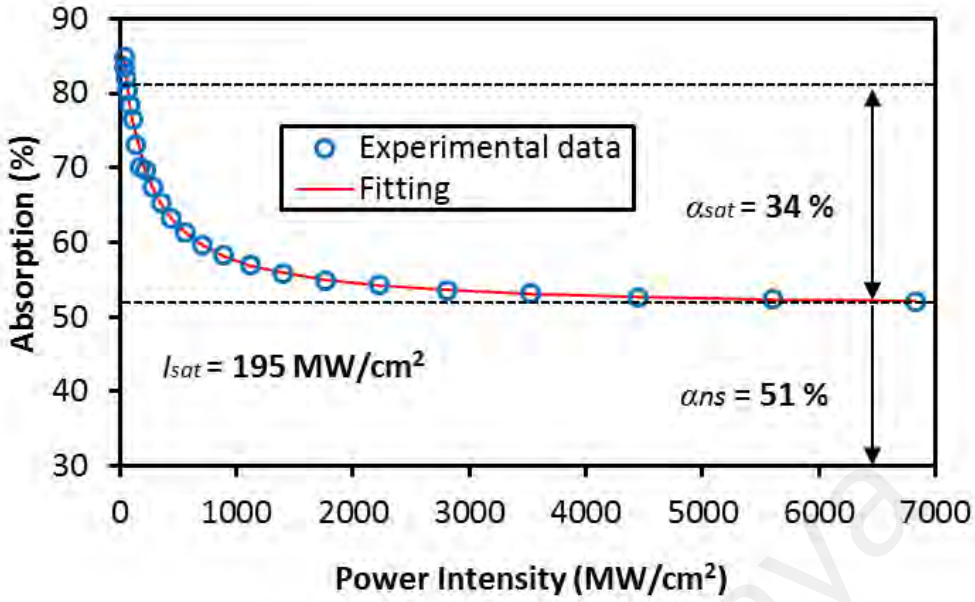

Figure 4.5: Characteristics of the TiO_2 film. (a) Raman spectrum. (b) Linear absorption measurement. (c) Nonlinear transmission measurement.

4.3 Mode-locking Pulses Generation in EDFL cavity

The fabricated TiO_2 film is then integrated into an EDFL cavity for pulse generation. The fiber ring laser was constructed with 202.4 m long cavity length as shown in Figure 4.6. A 2.4 m long EDF with 2000 ppm concentration was pumped by a 980-nm laser diode via a 980/1550 nm WDM. This EDF is working as a gain medium. It has a numerical aperture of 0.24 and a core absorption of 24 dB/m at 1550 nm. Inset of Figure 4.6 shows a small piece of TiO_2 film, which was sandwiched between two fiber ferrule connectors by using index matching gel as adhesive. The pulsed laser light oscillates in single direction after passing through polarization independent isolator. About 10 % of the laser was tapped out for observing laser output performance via 90:10 coupler, while another 90 % was looped back in the cavity. Then, 3-dB coupler was employed at 10 % coupler port which output performance can be simultaneously monitored using the same measuring devices as discussed in Chapter 3. Additional 195 m long SMF was placed inside the same cavity, between SA connector and coupler to provide a non-linearity

effect in the cavity. A mode-locked fiber laser tends to have a longer length of cavity setup compared to Q-switched fiber laser. Further reduce the additional SMF length may decrease the cavity dispersion and compressing the pulse width (Lin & Lin, 2013; Yang et al., 2015).

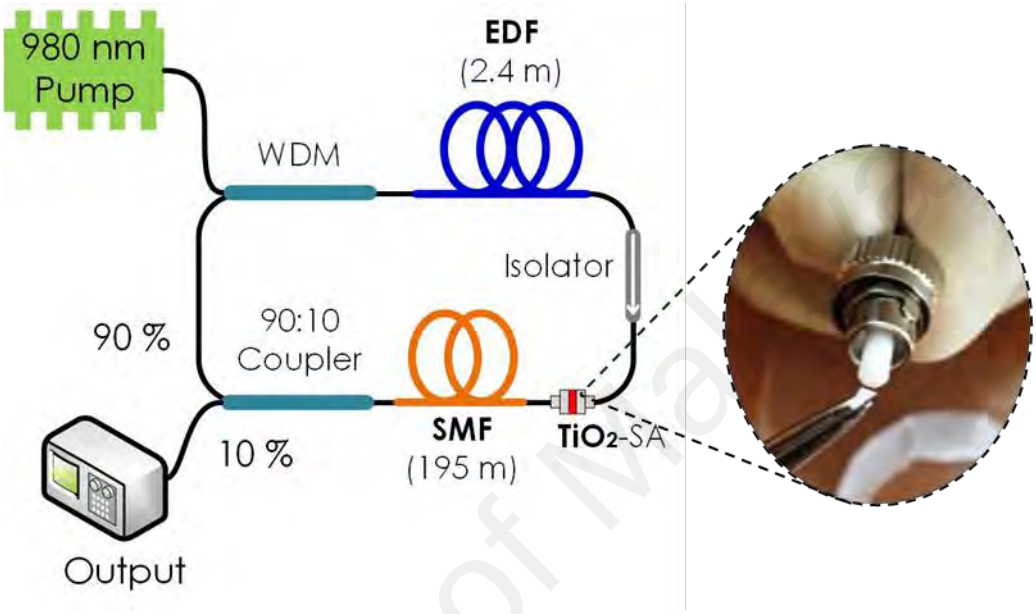

Figure 4.6: Schematic diagram of EDFL incorporating the TiO_2 film SA.

As the TiO_2 film is placed inside the cavity, the soliton pulse structure observes at 1562.20 nm with a peak power of –12.01 dBm and a spectral bandwidth of 0.74 nm (90.93 GHz) as shown in Figure 4.7. The first- and second-order Kelly sidebands are visible at the left and right within the center of soliton spectrum. Sidebands on the shorter wavelength from the center wavelength are indicated by '-1' and '-2', whereas '+1' and '+2' represents the sidebands on the longer wavelength. The first-order Kelly sidebands are located at 1560.22 nm and 1564.30 nm with peak power of – 40.2 dBm and – 40.1 dBm, respectively. The second-order Kelly sidebands are notable at 1559.27 nm and 1565.29 nm with peak power of -52.43 dBm and -52.48 dBm, respectively. The presence of first-order Kelly sidebands confirms that this mode-locked is operating in anomalous

dispersion regime. Also, through a calculation, this ring cavity operates in the anomalous dispersion of - 4.27 ps^2, where the GVD for EDF and SMF is about 27.6 ps^2/km and - 21.7 ps^2/km, respectively. Pump power is approximately 109 mW when a stable mode-locking occurred and produced soliton pulse shaping with the presence of Kelly sideband. The spectrum is maintained until pump power reached 250 mW. The generation of soliton mode-locked pulsed laser is due to the SPM caused by SMF that balance with a total cavity dispersion. As shown in the figure, the intensity of the soliton become higher as corresponds to the pump power.

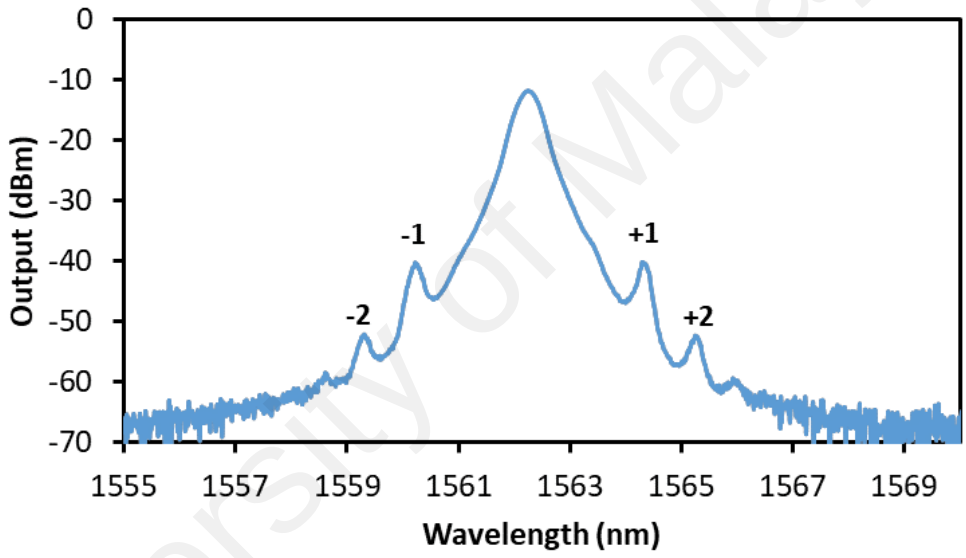

Figure 4.7: Schematic diagram of EDFL incorporating the TiO_2 film SA.

Output power and pulse energy increase linearly with the pump power as presented in Figure 4.8. At a pump power of 250 mW, the average output power of the soliton mode-locked is 9.74 mW. Thus the pulse energy is estimated at 248.6 nJ. The maximum slope efficiency has been obtained 3.70 % corresponding to the pump power and output power. Overall, pulse operation of EDFL only stably obtained from 109 mW until 250 mnW.

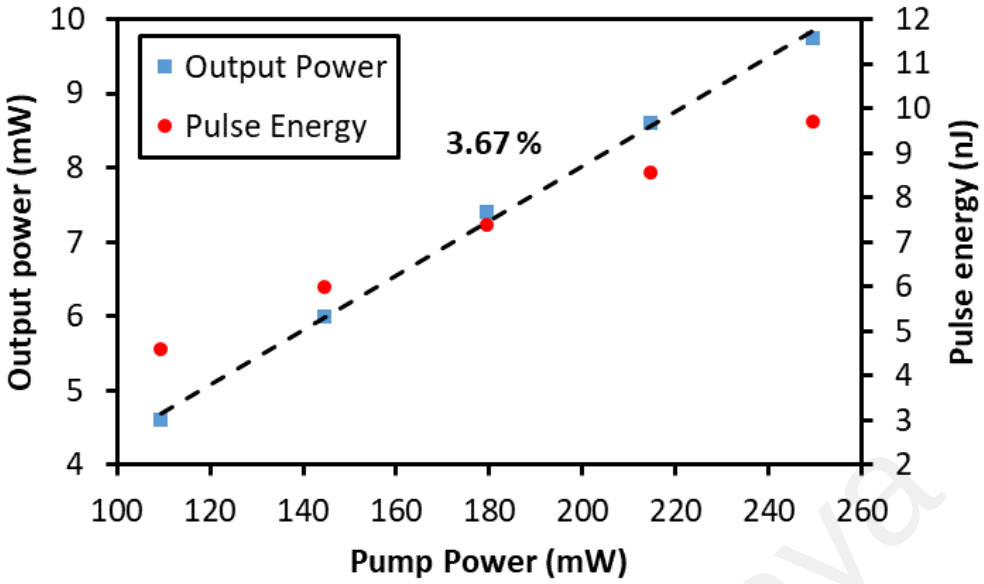

Figure 4.8: Output power and pulse energy performance.

The typical mode-locked pulse train with a pulse period of 3.51 ps which correspond to the repetition rate of 1 MHz is recorded using a fast photodetector (PD) with a bandwidth of 1.2 GHz as shown in Figure 4.9(a). The repetition rate is increased rapidly from 75.30 kHz to 1 MHz once SMF was placed inside the cavity. The ring cavity is increased in length which will affect the pulse period since the pulse period increased with the cavity length. At a fundamental, repetition rate of 1 MHz will maintain pulsing until available pump power. This obtained repetition rate value is well agreed to the total cavity length of 202.4 m. Since the pulse width of mode-locked cannot be recorded using oscilloscope due to the resolution constraint, auto-correlator was used to trace the value of pulse width. It can be observed that our experimental data of soliton mode-locked is perfectly fitted with the $sech^2$ fitting curve as shown in Figure 4.9(b). The direct FWHM width from autocorrelation trace is about 5.45 ps, yielding the actual pulse width of 3.51 ps. The TBP is calculated to be 0.319, indicating the pulse is slightly chirp.

(a)

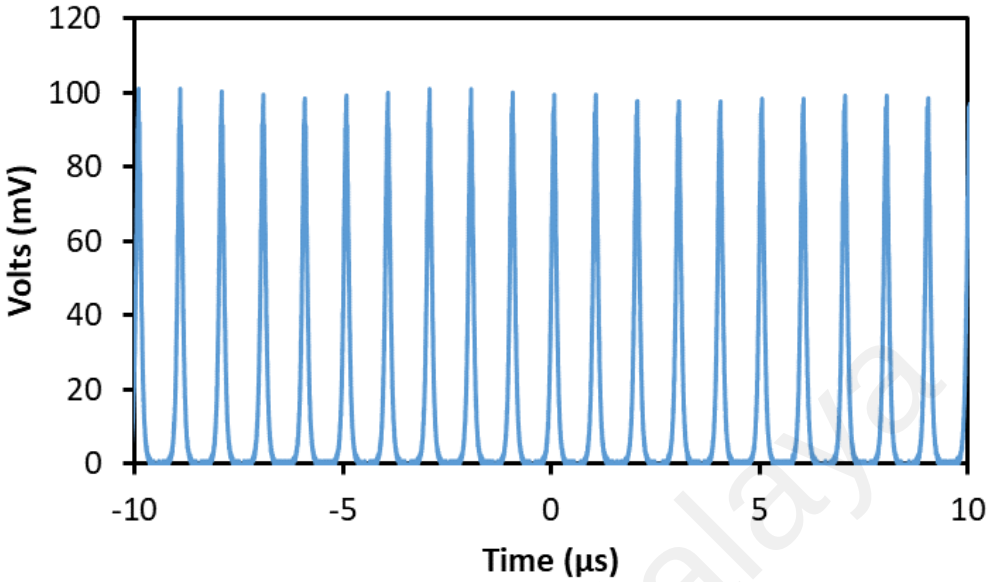

(b)

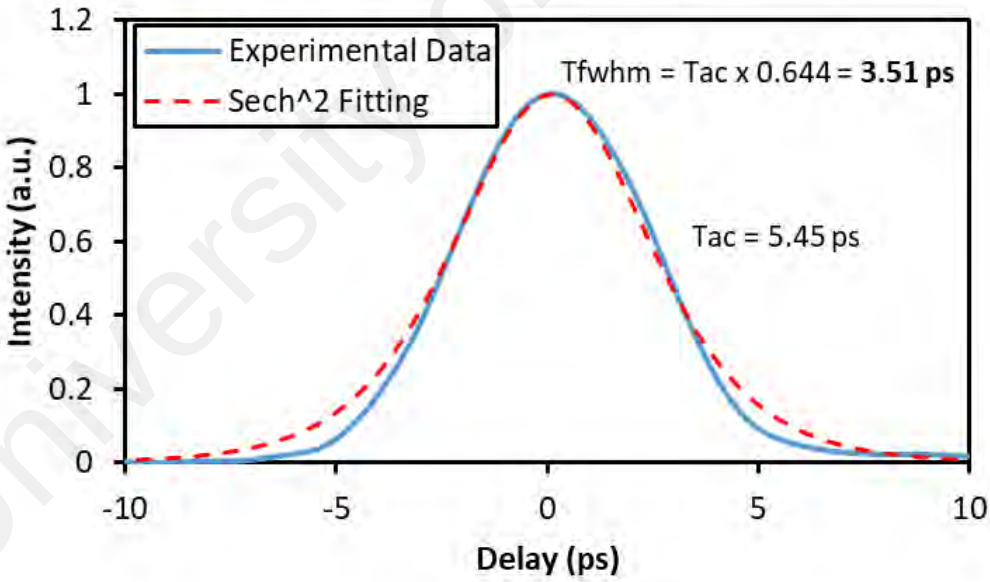

Figure 4.9: (a) Oscilloscope pulse train. (b) Autocorrelator measurement for single pulse profile.

Figure 4.10 shows the RF optical spectrum where SNR can be obtained at 63 dB, which the stability of the pulsed laser is confirmed. The 1st until 3rd harmonic have owned an SNR more than 30 dB, which usually reported as a minimum SNR. Finally, the TiO_2 film is purposely removed from the surface of fiber ferrule and pumped until maximum available power to verify the absence of mode-locked operation caused by the absorption from the SA. No mode-locking pulse is observed even under the maximum available pump power. Hence, this result indicates that soliton pulse is generated by TiO_2 SA.

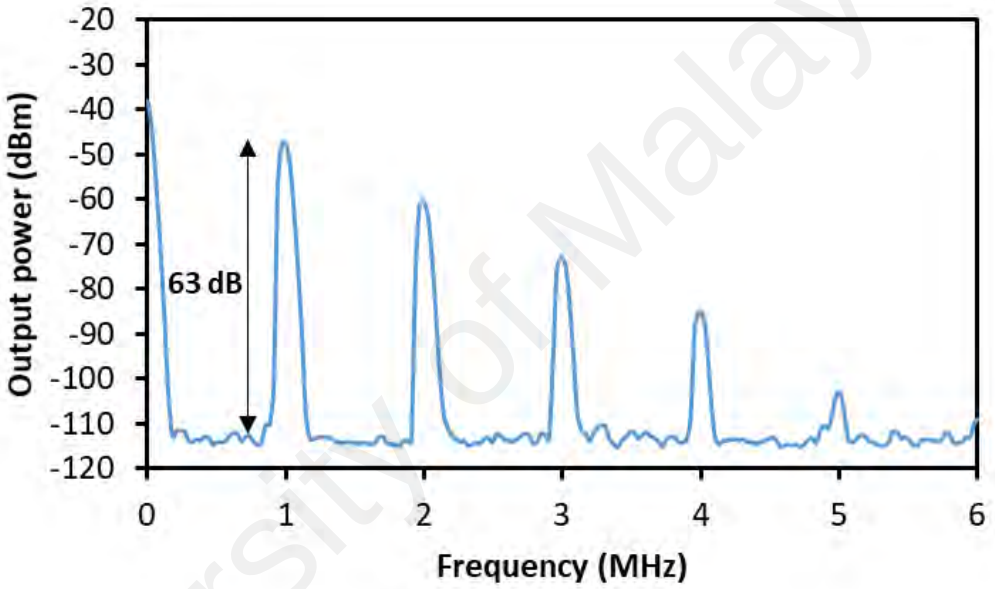

Figure 4.10: RF spectrum of Mode-locked EDFL with 6 MHz spans.

4.4 Q-switching Pulse Generation in YDFL cavity

The fabricated TiO_2 film was integrated into a YDFL cavity with a double-clad Ytterbium-doped fiber (YDF) as a gain medium cavity for pulse generation. It is worth to note that, the mode-locking pulses train was not successfully realized with the laser cavity. Nevertheless, Q-switching pulses were managed to be obtained with careful alignment of the setup. In this section, the Q-switching operation is reported.

Q-switched fiber lasers have gained a significant attention due to their several uses for cutting application such as material processing and medical surgery (Grudinin, 2013). It is acquired via two different techniques, active and passive. Since active Q-switching requires additional switching electronics (Giles et al., 1991), passive Q-switching fiber lasers are useful and cost-effective to produce pulsed laser because of the attractive superiority regarding cost, compactness and design simplicity (Harun et al., 2012). Q-switched fiber based laser offers a small footprint, better beam quality and can simply dissipate heat as compared with laser based on bulk gain media due to the widely used in optical fiber technology (Svelto & Hanna, 1998). Compare to the mode-locking operation, Q-switching operation owns high pulse energy due to low repetition rate characteristics, but it has a broader pulse width size. Like a passive mode-locking operation, several ways have been discovered to achieve stable passive Q-switching operation including induction of artificial or real SA. Here, the Q-switched YDFL is demonstrated and reported using the fabricated TiO_2 film SA as a Q-switcher.

Figure 4.11 shows the experimental setup of the Q-switched double-clad YDFL. It uses a 980-nm multimode LD to pump a 10 m long double-clad YDF via an MMC. The YDF has an NA of 0.46, core radius of 5.5 μm, cladding radius of 65 μm and cladding absorption of 3.9 dB/m at 975 nm. A 1 mm x 1 mm TiO_2 film was sandwiched between 2 ceramic ferrules of fiber connectors adhered with index matching gel, which forms a passive Q-switcher medium. The cavity output was split by 90/10 optical coupler which divides the output of 10 % for measurement of the spectrum, pulse, and power while the rest 90 % being feedback to the ring cavity and oscillated along the line. The rest of ring resonator comprises a 4 m long SMF fiber, and thus the total cavity length is approximately 14 m.

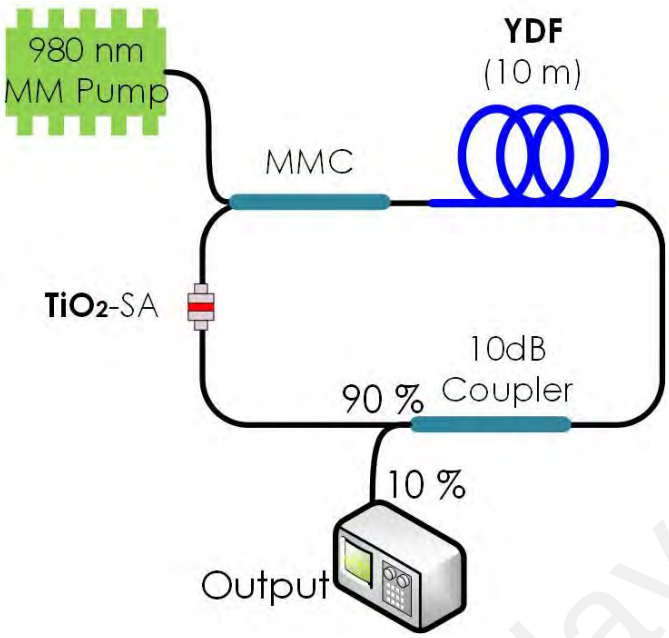

Figure 4.11: Schematic illustration of YDFL in ring cavity configuration.

In the experiment, stable Q-switched EDFL self-started at 1006 mW pump power and was maintained up to the maximum pump power of 1196 mW. Figure 4.12(a) displays the output spectrum of the suggested Q-switched YDFL constructed utilizing the TiO_2 film SA. The output spectrum has a span setting of 100 nm and a resolution setting of 0.02 nm acquired from a Yokogawa AQ6370B OSA at the end of 10% port of the YDFL setup. Under these conditions, an absolute lasing wavelength at 1094 nm with a peak power of 2 dBm and a 3-dB spectral bandwidth of 1.3 nm (325.63 GHz) is examined. The spectral broadening is observed mainly due to the self-phase modulation (SPM) effect in the laser cavity. Figure 4.12(b) shows the corresponding RF spectrum at a pump power of 1006 mW, which was obtained within 200 kHz span. As illustrated in the figure, the fundamental repetition rate of the laser is 16.57 kHz which agrees with the pulse period of 48.57 µs measured in the oscilloscope. The SNR of the RF spectrum is observed at 35 dB, and the presence of harmonic peaks gradually decrease up to 10^{th} harmonic,

then disappear. This indicates the Q-switching operation has a broad pulse width (microseconds) and the frequency domain transformation corresponds to its time-domain.

(a)

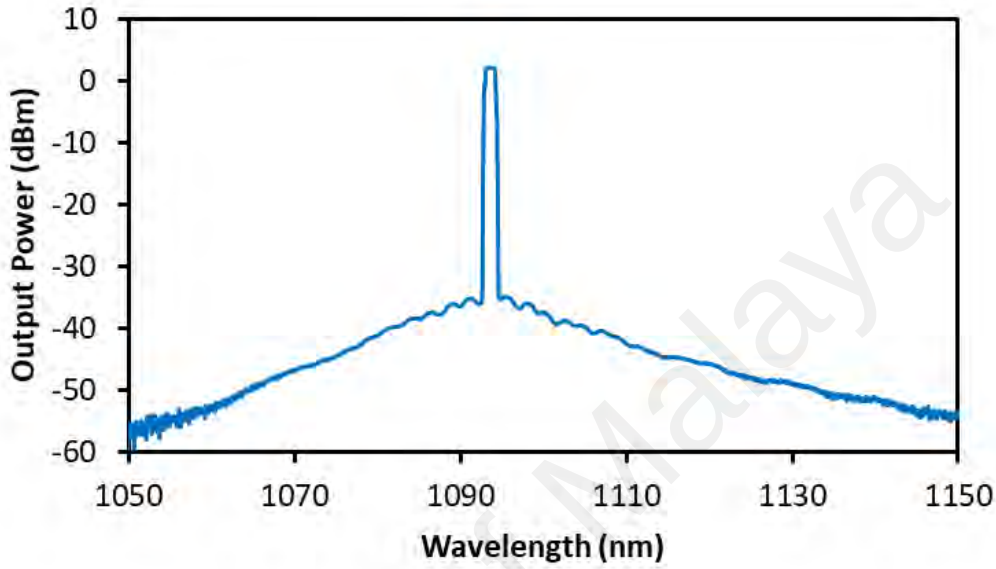

(b)

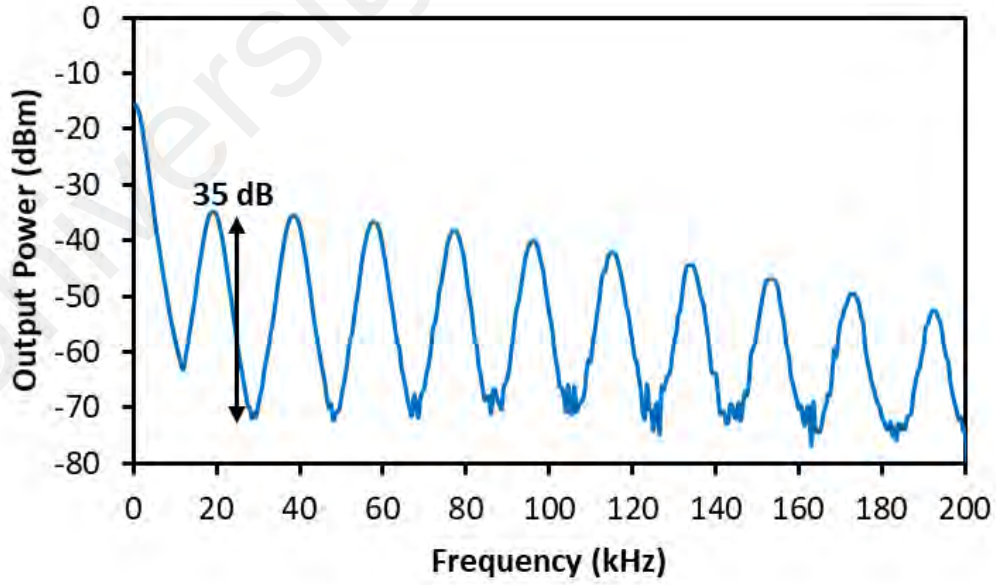

Figure 4.12: Q-switched YDFL performance at 1006 mW pump power. (a) Output spectrum. (b) RF spectrum with 200 kHz span.

The output pulse trains under different pump power were detected using a 350 MHz digital oscilloscope and are shown in Figure 4.13. At 1006 mW pump power, the repetition rate is 16.57 kHz, and it increases to 19.37 kHz at 1101 mW pump power. At the maximum pump power of 1196 mW, the repetition rate is 20.59 kHz. The increment in repetition rate in tandem with pump power is a characteristic of Q-switched laser (Yan et al., 2015). Noting that the output pulses trains were still stable with relatively uniform intensity distribution during the entire process of tuning the pump power, we can reasonably presume that the fiber laser works in the highly stable Q-switching regime. As the pump power is increased above 1196 mW, the Q-switching operation would disappear. This indicates the damage threshold of the SA is 1196 mW. To verify that the TiO_2 film was responsible for the Q-switching pulse generation. Then, the film was removed from the experimental setup. In this case, no Q-switching pulse was observed on the oscilloscope at any pump powers, which confirms the Q-switching operation was attributed to the TiO_2 film SA.

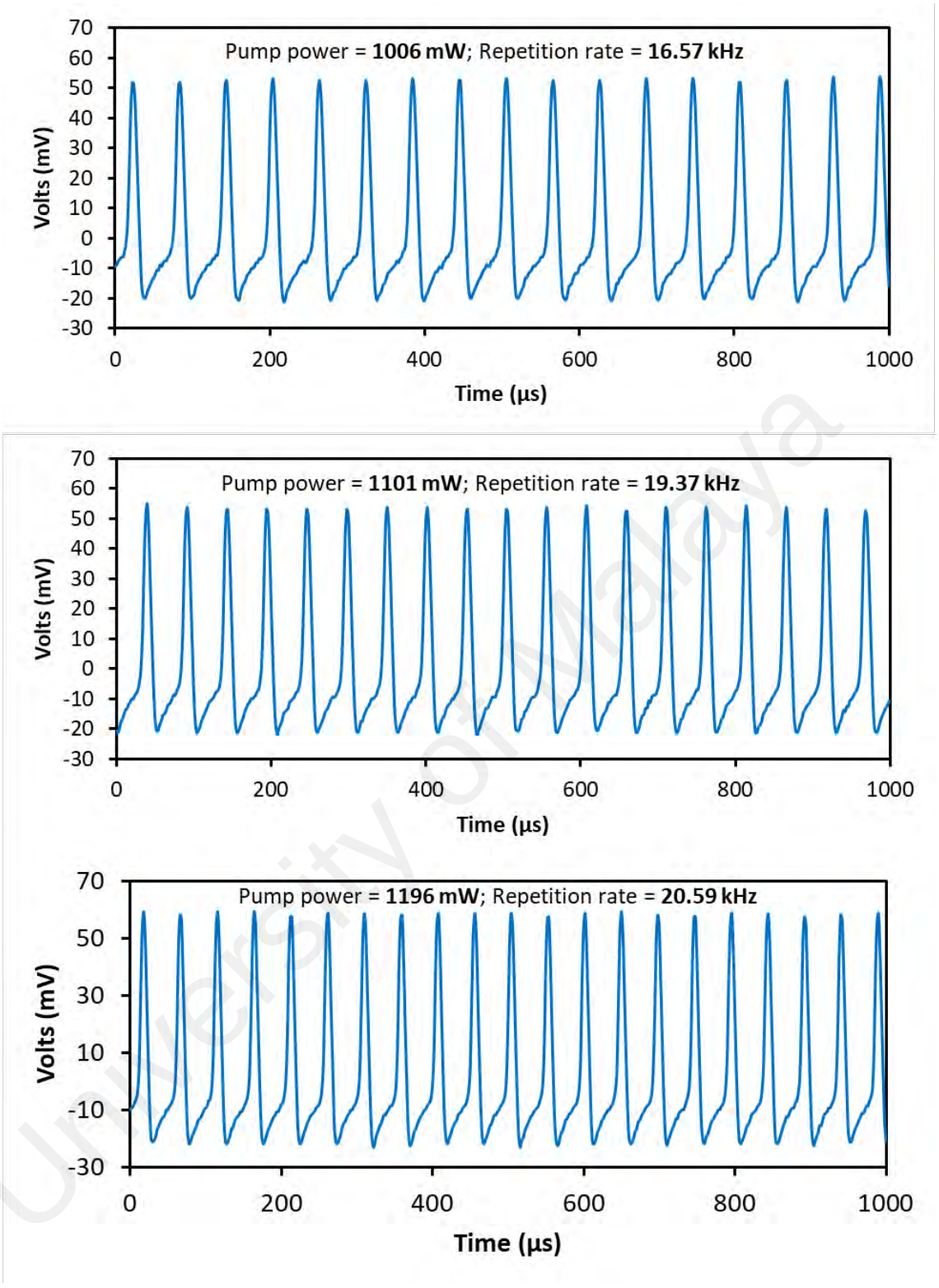

Figure 4.13: Pulse train under different pump power.

In addition, the average output power and the corresponding single-pulse energy of the laser are also investigated at various pump powers. Figure 4.14 indicates the output power and pulse energy as a function of the pump power for the YDFL with TiO_2 film. As shown in the figure, the pulse energy is increasing as the pump power raising. The optical-to-optical efficiency obtained is 2.03 %. The maximum pulse energy and peak power are obtained at 0.56 µJ and 55.34 mW, respectively. These results show that the TiO_2 material is a great potential for pulsed laser applications at 1-micron wavelength region.

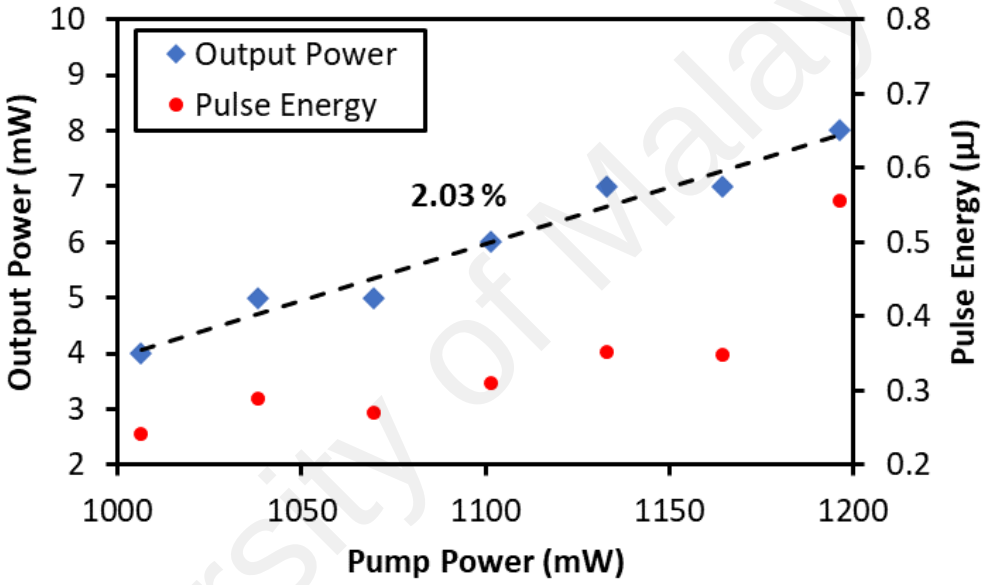

Figure 4.14: Output power and pulse energy.

The pulse repetition rate and pulse duration of the Q-switched fiber laser as functions of the occurrence pump power were indicated in Figure 4.15. As expected, the repetition rate increased, and the pulse width decreased as the input pump was raised from 1006 mW to 1196 mW. The repetition rate expanded from 16.57 kHz to 20.59 kHz while the pulse width narrowed starting from 12.18 µs to 10.12 µs and at the same time the incident pump power shifted starting with 1006 mW to 1196 mW. Toward each pump energy and pulse repetition rate, no amplitude modulations in these pulse trains were observed, and

the Q-switched pulse output was stable. This demonstrates that there might have been no self-mode locking (SML) impact throughout the Q-switching operation. To generate mode-locking operation, additional special fiber for 1-micron region is required to interplay between the normal cavity dispersion and nonlinear fiber effect. However, the insertion loss of the cavity becomes high and more power is required to pump this cavity. At the moment, the mode-locking operation cannot be generated by using this cavity.

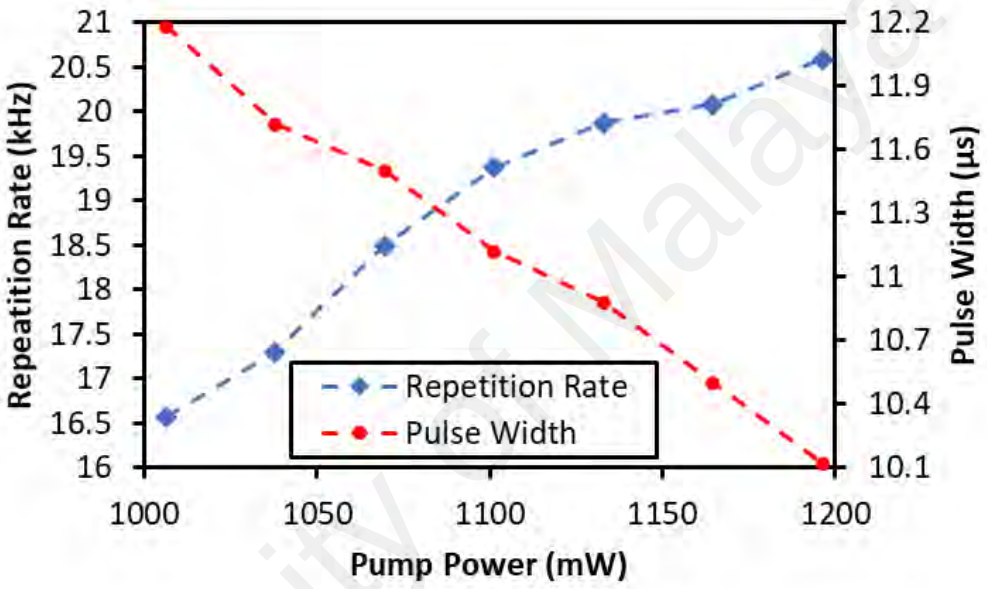

Figure 4.15: Repetition rate and pulse energy against pump power.

4.5 Mode-locking Pulse Generation in THDFL cavity

The mode-locked THDFL is generated by using all-fiber ring cavity configuration. Figure 4.17 illustrates all optical components are connected in a ring. The 5 m long single-clad THDF was used as a gain medium. The GVD parameter for THDF is about -72.8 ps^2/km. Other fibers in the cavity is a 10 m ScDF with -127 ps^2/km and a standard SMF with - 80 ps^2/km, which constituted the rest of the ring. The total cavity length is around 17.3 m and the total net GDD in the cavity is operates in anomalous dispersion condition of -1.818 ps^2. We used 1552 nm EYDFL with 38 % efficiency to pump 11.5 µm core

diameter of THDF up to 1.5 W via 1550/2000 nm fuse WDM. This THDF has a core NA and absorption of 0.14 and 100 dB/m at 790 nm, respectively. The generated lasing propagates in unidirectional and maintain its direction after pass through the isolator. The 10 m long ScDF was added in the cavity to gain sufficient nonlinearity effects for a mode-locked generation. ScDF has a core composition of SiO_2-GeO_2-Sc_2O_3 with core diameter and NA of 7.5 μm and 0.12, respectively. The mode-locked laser performances were collected from 10 % of output coupler, the remaining of 90 % continuously oscillated in the cavity. With FC fiber adapter, the 1 mm x 1 mm TiO_2 film was sandwiched by two fiber ferrules. Index matching gel was used as an adhesive and also as an element to fill the air-gap. Then, we removed the film to eliminate the mode-locked mode which can confirm the presence of mode-locked was owned to this film. According to the obtain cavity dispersion, the soliton mode-locking operation with Kelly sideband spectrum is possible to be generated. In this cavity, a polarization controller (PC) can be added to fine-tune the birefringence which important for soliton generation. Adding PC this cavity will increase the cavity loss and eliminate a self-started mode-locking generation. The spectral and temporal performances were observed by using same measuring devices as in subchapter 3.6. By changing the gain medium to 5 m long TDF, just a Q-switching operation was achieved.

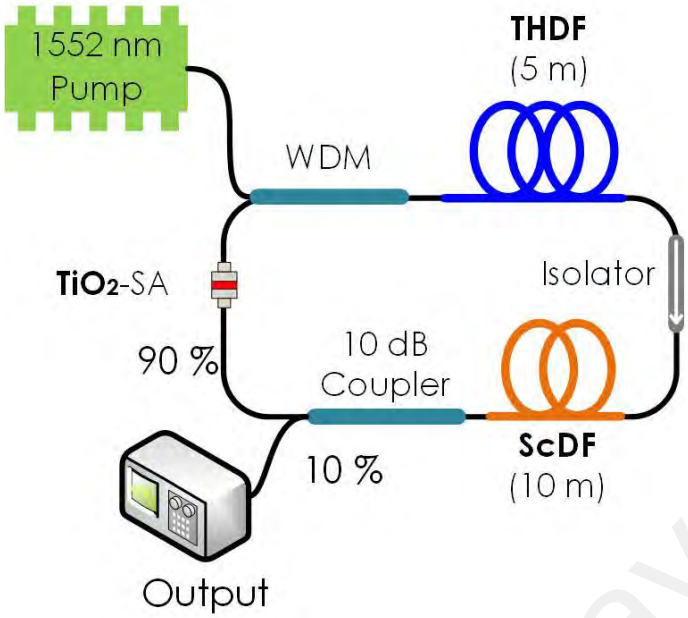

Figure 4.16: Mode-locked THDFL configuration.

At first, a piece of 1 mm x 1 mm TiO_2 film was inserted in between two fiber ferrules and lock by fiber adapter to construct an SA device. As the SA is incorporated into the THDFL cavity, the mode-locked mode starts at 902 mW pump power and continue stable until 1062 mW before disappears. The high modulation depth of the SA generates a self-started conventional mode-locking in the cavity, not a sign or value of total cavity dispersion (Gumenyuk et al., 2011). In other word, conventional mode-locking operation generation is fully depended on the optical properties of SA and also the appropriate cavity length. The dispersion and nonlinearity must be balance in generating mode-locked in soliton regime. Figure 4.17(a) show the output spectrum at 902 mW pump power and pulsed output spectrum at 1979 nm with a narrow 3-dB spectral bandwidth of 0.4 nm (30.61 GHz). The output power performance is recorded as illustrated in Figure 4.17(b). Overall performance, the mode-locked THDFL has a slope efficiency of 2.67 %. At pump power of 1062 mW, the output power and calculated pulse energy are 15 mW and 1.66 nJ, respectively.

(a)

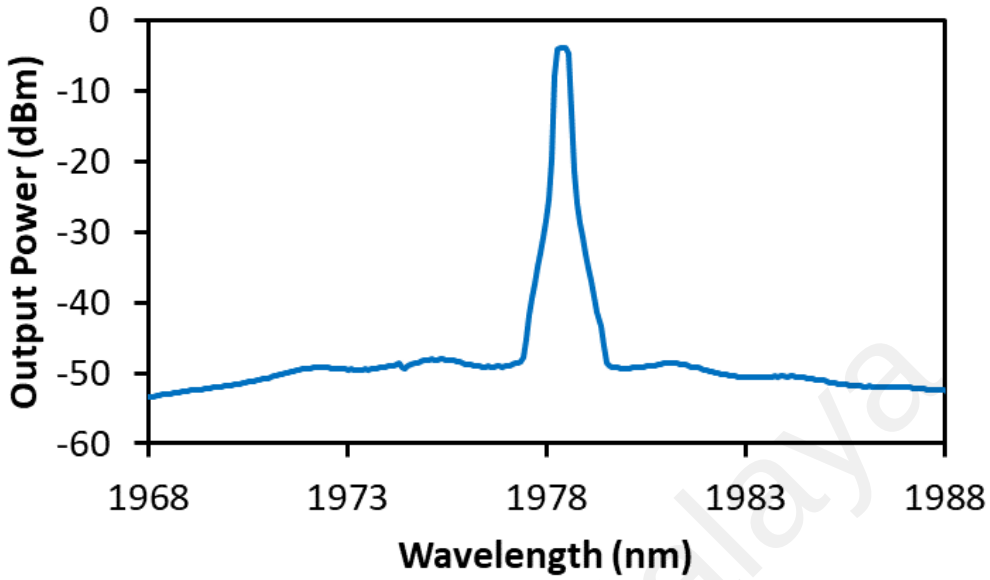

(b)

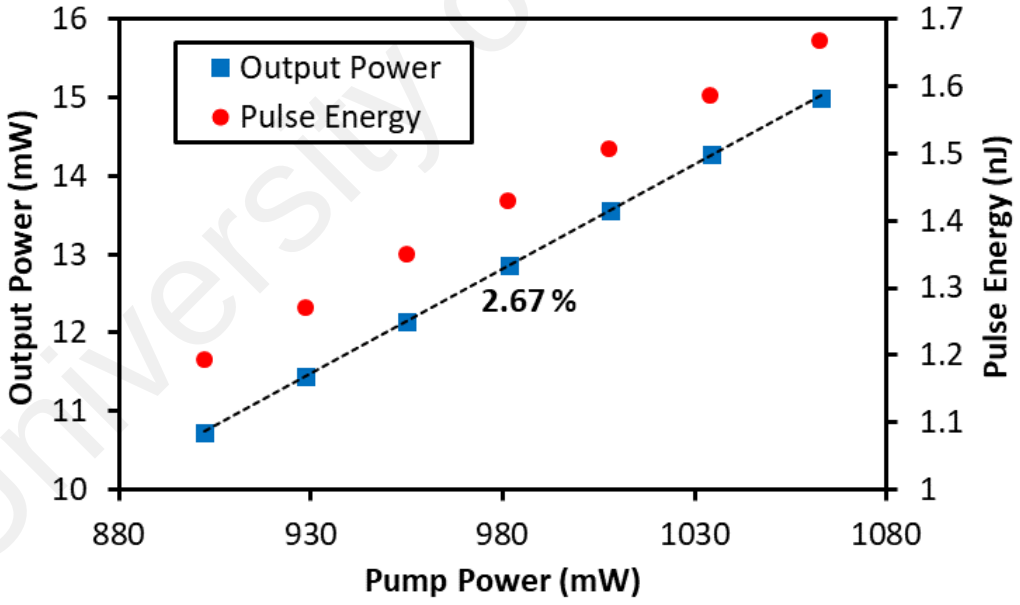

Figure 4.17: a) Output spectrum with SA at 902 mW pump power. (b) Output power and pulse energy under pump power from 902 mW to 1062 mW.

Temporal characteristics are measured by using oscilloscope and RFSA via PD. Figure 4.18 shows pulse train and frequency at the threshold and maximum pump power. As

shown in the figure, the pulse period of 112 ns is corresponded to the repetition rate of 9 MHz and remain stable until 1062 mW pump power. The repetition rate matched well with the fundamental cavity round trip frequency. However, the obtained pulse width of 28 ns is not well measured due to resolution limitation of the oscilloscope. Due to 2-micron region autocorrelation is not available at our side, the pulse width can only be obtained through TBP which the pulse shape fit the $Sech^2$ profile (0.315). The minimum possible pulse width is calculated to be 10.29 ps. Much broader the mode-locked pulse width indicates the narrower spectral width of the mode-locked spectrum (Kobtsev, Kukarin et al., 2011; Tian et al., 2015). Sotor et al. have done similar works in anomalous dispersion (-0.387 ps^2) with a spectral bandwidth of 5.8 nm and pulse width of 739 fs (measured by Femtochrome FR-103XL auto-correlator) (Sotor, Sobon et al., 2015). In their work, the obtained TBP is about 0.352 indicates very slightly chirped at output pulse. So, this strongly proves the measured pulse width will normally near above the minimum possible bandwidth.

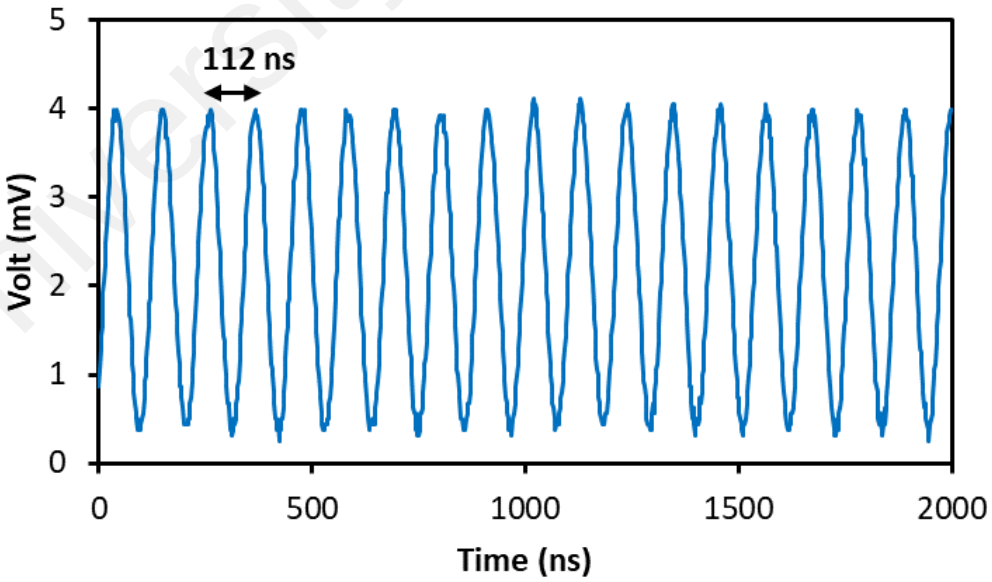

Figure 4.18: Pulse train of mode-locked THDFL.

Figure 4.19 shows the RF spectrum confirms the repetition rate of 9 MHz presence in the mode-locked THDFL. The SNR is measured about 58 dB. With a single repetition rate appear in RFSA (frequency domain), this indicates the waveform in the oscilloscope (time domain) is a cosine wave pattern which corresponds to the broad pulse width. The mode-locked operation will disappear as we remove a TiO_2 film in the cavity. Without ScDF, the cavity can only generates the Q-switched laser.

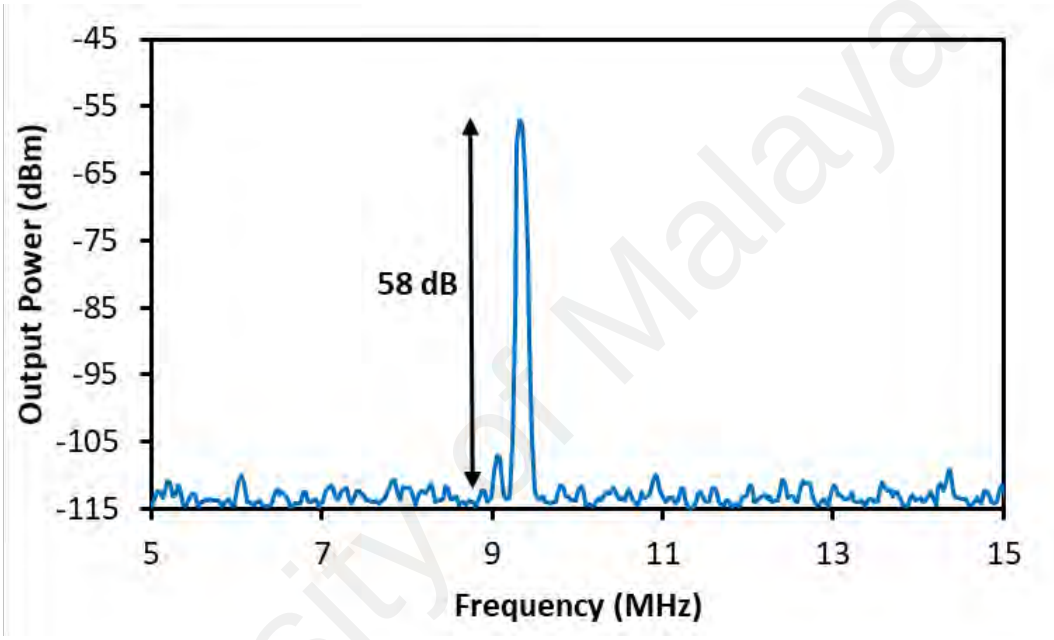

Figure 4.19: RF spectrum of Mode-locked THDFL fundamental repetition rate.

4.6 Summary

The generation of mode-locking pulses in 1.55-, and 2-micron regions and Q-switching pulses in 1-micron region have been successfully demonstrated using a new type of SA based on the TiO_2 film. The film was fabricated by mixing the dispersed TiO_2 into a polyvinyl alcohol solution before going through a drying process and sandwiched between two fiber ferrules. The passively mode-locking pulses train was generated by incorporating the TiO_2 film into the EDFL cavity with a total length of 202.4 m. The ring cavity operates in the anomalous dispersion of -4.27 ps^2. The mode-locked EDFL operates

at 1562.2 nm and is capable of delivering 248.6 nJ pulse energy at 1 MHz repetition rate. The laser has a pulse width of 3.51 ps and TBP of 0.319.

By incorporating TiO_2 film into the double-clad YDFL cavity, the passively Q-switched pulsed laser was generated which is capable of delivering a pulse train with tunable pulse width and repetition rate. The repetition rate can be varied from 16.57 kHz to 20.59 kHz while the pulse width diminished starting from 12.18 μs to 10.12 μs as the pump power is varied from 1006 mW to 1196 mW. However, the mode-locking pulses could not be realized in the double-clad YDFL cavity.

The generation of mode-locked THDFL was also successfully demonstrated at 1979 nm with 1552 nm pumping. The stable 9 MHz repetition rate of mode-locking pulse train with 58 dB SNR was generated at pump power region from 902 to 1062 mW. At maximum pump power, the mode-locked THDFL has output power and pulse energy of 15 mW and 1.66 nJ, respectively. These results demonstrate the TiO_2 can be used promisingly in ultrafast photonics applications.

CHAPTER 5: ULTRASHORT PULSE GENERATION WITH BLACK PHOSPHORUS SATURABLE ABSORBER

5.1 Introduction

In the previous chapter, MoS_2 and TiO_2 have been demonstrated as an SA for short pulse generations operating at 1-, 1.55- and 2-micron regions. In this chapter, another intriguing 2D material, black phosphorus (BP) will be explored for SA applications. BP possesses a controllable bandgap size that can be fine-tuned by adjusting the number of layers in the material (Churchill & Jarillo-Herrero, 2014). It is also the most thermodynamically stable allotrope (Churchill & Jarillo-Herrero, 2014). Many interesting findings on its unique electronic properties have been discovered and reported (Koenig et al., 2014; Li et al., 2014). However, its optical properties are much less explored, except for its polarization dependent optical response as dictated by the anisotropic feature of BPs (Hong et al., 2014; Xia et al., 2014). The broadband nonlinear optical response in BP is promising for infrared and mid-infrared optoelectronics (Lu et al., 2015).

Stimulated by the similarity between graphene and BP regarding single elemental component and direct band-gap, it is natural to find out whether BP could be used as an SA for Q-switching and mode-locking applications. Similar to graphene, Van der Waals forces attract the individual atomic layers of BP making it the most stable phosphorus allotrope in the group (Chen et al., 2015; Koenig et al., 2014; Li et al., 2014). Lu et al. fabricated multi-layers BP film embedded polymethyl-methacrylate (PMMA) which has modulation depth and saturable intensity of 12.4% and 334.6 GW/cm^2, respectively (Lu et al., 2015). In the meantime, Luo et al. deposited the few-layers BP solution onto microfiber (Luo et al., 2015). This BP SA has 1-3 layers with 9% modulation depth and 25 MW/cm^2 saturable intensity. Both Lu et al. and Luo et al. prepared their BP solution through liquid phase exfoliation (LPE) method, where involves complex chemical procedures. Thin (15-layers) and thick (25-layers) BP flakes as SA were mechanically

exfoliated from commercial BP bulk (Chen et al., 2015). The modulation depth and saturable intensity of thin BP were 8.1% and 6.55 MW/cm^2, respectively. Its optical properties trend relatively close to fabricated BP SA as in this chapter. However, the number of layers is high.

This chapter presents a new and simple approach to generate mode-locked fiber laser by employing a BP based SA as a mode-locker. The BP bulk crystal is mechanically exfoliated to obtain a layer of BP. The material could be attached to the end-facet of a fiber ferrule, making it an SA device. By placing the SA into various laser cavities, mode locking pulses train operating at 1-, 1.55-, and 2-micron spectral regions are achieved.

5.2 Preparation of black phosphorus based SA device

The fabrication of the multi-layer BP samples through mechanical exfoliation approach is summarized in Figure 5.1. A similar approach has been widely used in the preparation of graphene-based saturable absorbers for ultra-short pulse laser applications (Martinez et al., 2011; Novoselov, 2011). This technique is advantageous mainly because of its simplicity and reliability, where the entire fabrication process is free from complicated chemical procedures and expensive instruments. As illustrated in Figure 5.1, relatively thin flakes were peeled off from a big block of commercially available BP crystal (purity of 99.995 %) using a clear scotch tape. Then, we repeatedly pressed the flakes on the transparent plastic surface so that the BP flakes become thin enough to transmit light with a high efficiency. Lastly, we cut a small piece of the BP thin flakes and attached it onto a standard FC/PC fiber ferrule end surface with index matching gel. After connecting it with another FC/PC fiber ferrule with a standard flange adapter, the all-fiber BP based SA was finally ready. The BP materials are very hydrophilic, and thus the SA is easily damaged by the exposure to oxygen and water molecules. Therefore, the

whole preparation process was done very fast in less than 2 minutes. Inset of **Figure 5.1** shows the BP thin flakes position on the top of fiber ferrule surface which entirely covers the fiber core.

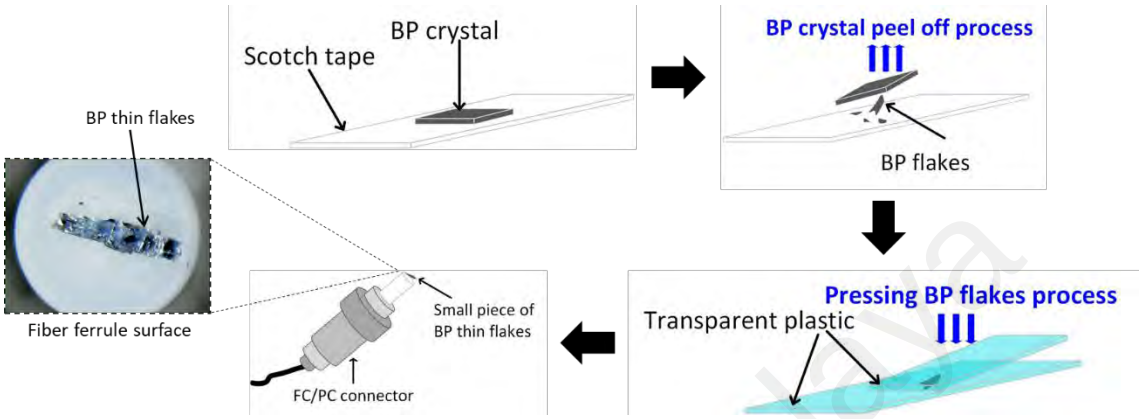

Figure 5.1: Illustration of mechanical exfoliation process for BP.

5.3 SA Characterization

The characterization of the BP thin flake, which was fabricated via mechanical exfoliation approach is discussed in this section. Figure 5.2(a) shows the FESEM image of the BP thin flakes at 100 nm scale. The image indicates the existence of the uniform layers and confirms the absence of > 1μm aggregates or voids in the composite SA, which otherwise result in non-saturable scattering losses. The composition of the transferred layers is confirmed by the EDS on the FESEM image as shown in Figure 5.2(b). The presence of BP material on the sample flakes is verified by the presence of the peak of phosphorus in the spectroscopy data as shown in Figure 5.2(b).

(a)

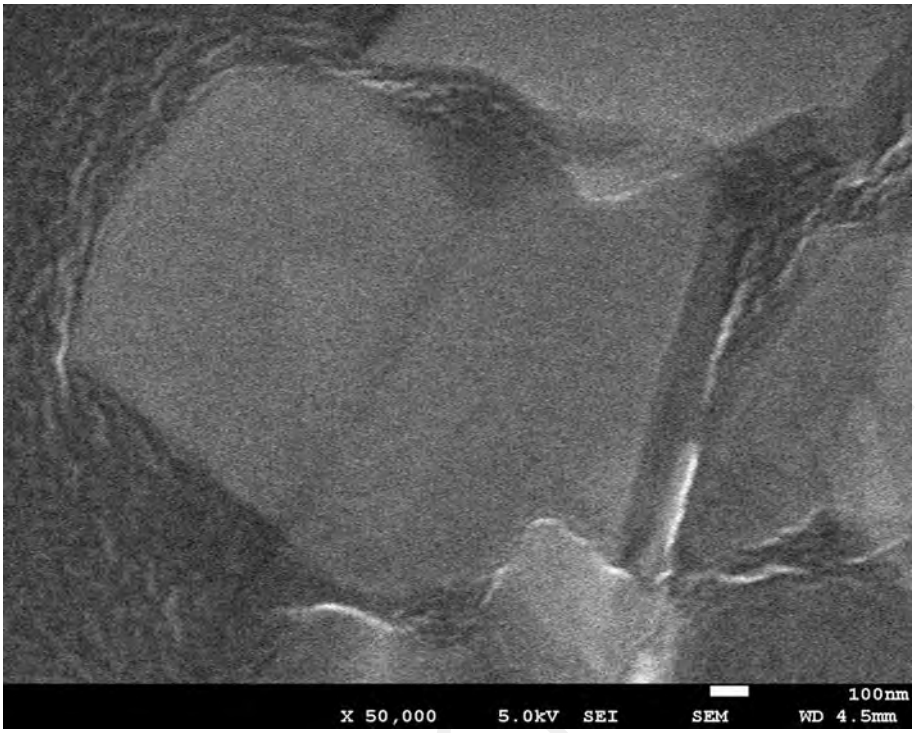

(b)

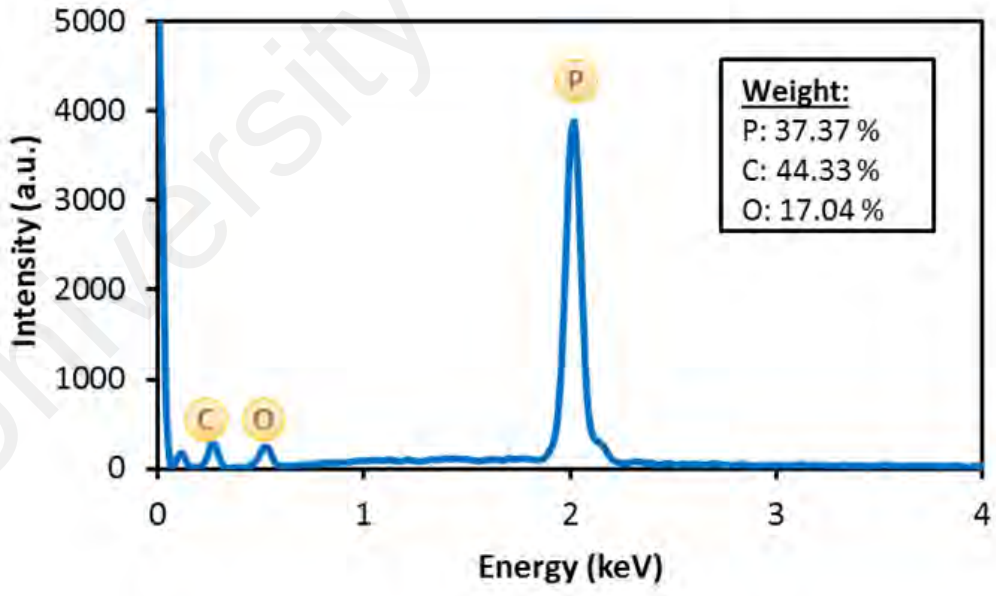

Figure 5.2: (a) FESEM image. (b) EDS profile.

Figure 5.3 shows the BP optical properties examined by Raman Spectrum and non-linear absorption. This Raman spectrum is recorded by a spectrometer when a 514 nm Argon laser radiated on the flakes for 10 s with an exposure power of 50 mW. Three unique Raman peaks are evident at 360 cm^{-1}, 438 cm^{-1}, and 465 cm^{-1}, related to the $\boldsymbol{A_g^1}$, $\boldsymbol{B_{2g}}$ and $\boldsymbol{A_g^2}$ vibration modes of layered BP. Both $\boldsymbol{A_g^2}$ and $\boldsymbol{B_{2g}}$ vibration modes correspond to the in-plane oscillation of phosphorus atoms in the BP layer while the $\boldsymbol{A_g^1}$ mode is related to the out-of-plane vibration. The ratio of the $\boldsymbol{A_g^1}$ and silicon (**Si**) peaks provides an estimate of the thickness of the BP layer which is around 4 to 5 nm (Castellanos-Gomez et al., 2014). Since the thickness of single-layer BP is approximately 0. 6 - 0. 8 nm (Luo et al., 2015; Xia et al., 2014), we expect the SA to have 5 - 8 layers of BP. Guo et al. reported the peak $\boldsymbol{A_g^2}$ at 462 cm^{-1} indicates this BP SA has more than 4 layers (Guo et al., 2015). BP has a direct bandgap from 0.3 eV (bulk) to 1.51 eV (monolayer), while 0.8 eV and 0.59 eV for 3-layers and 5-layers, respectively (Guo et al., 2015; Luo et al., 2015). In this chapter, the saturable absorption condition occurs after photon (1561 nm) possesses bandgap energy (0.8 eV) above the respective SA bandgap (0.59 eV). This generates electron-hole pairs with excess photon energy. Then, excess photon energy will induces kinetic energy to the electron and may dissipated in form of heat (phonon).

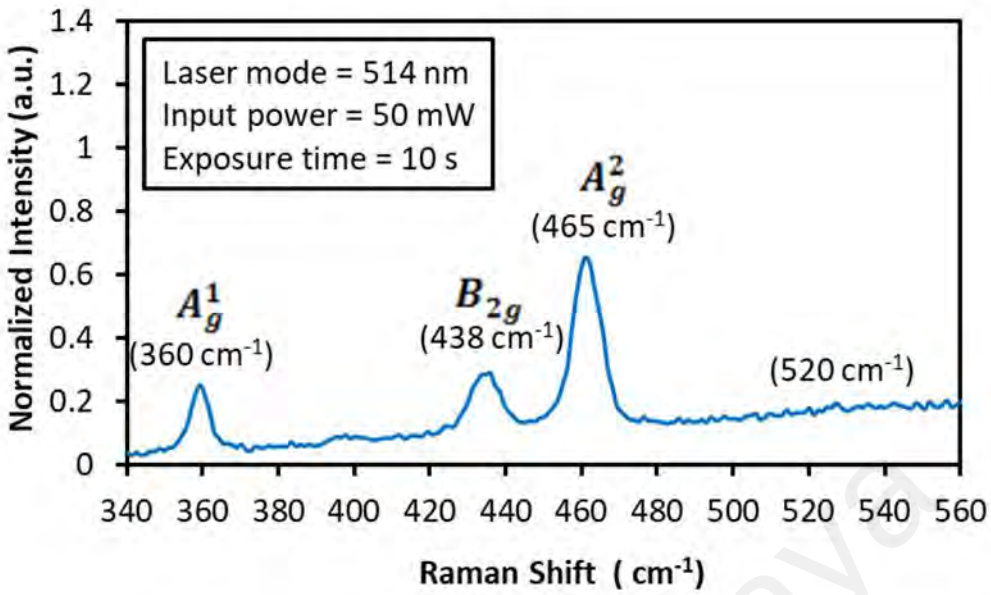

Figure 5.3: Raman spectrum of BP thin flakes.

The nonlinear optical characteristic for the multilayer BP thin flakes was then investigated to confirm its saturable absorption by applying the balance twin-detector measurement technique. In the experiment, the polarization state was controlled by a polarization controller (PC). A self-constructed mode-locked fiber laser (1562 nm wavelength, 1.05 ps pulse width, 16.3 MHz repetition rate) was used as the input pulse source. The transmitted power and also a reference power for normalization were recorded as a function of incident intensity on the BP thin flakes by varying the input laser power. With increasing peak intensity, the material absorption decreases as shown in Figure 5.4, confirming saturable absorption. The experimental data for absorption are fitted according to a simple two-level SA model which similar to MoS_2 and TiO_2 in the previous chapter. As shown in the figure, the modulation depth, non-saturable intensity, and saturation intensity are obtained to be 7 %, 58 %, and 100 MW/cm^2, respectively. Taking into account that the nonlinear optical response leading to absorption saturation was obtained at relatively low fluence, the mechanically exfoliated BP meets basic criteria

of a passive SA for fiber lasers. This BP thin flakes has an insertion loss of ~ 1.5 dB. From a material perspective, BP is an anisotropic crystal; its linear absorption is sensitive to the light polarization state. Further investigation was done by varying the polarization state to various angles using a PC. It is found that the output intensity of the laser indicates only two states; one with output power trend similar to Figure 5.4 or low output power (almost near to zero reading). This proves that the BP based SA is polarization-dependent due to anisotropic layered material characteristic (Xia et al., 2014). Thus, a PC is employed in the proposed laser cavity to adjust the polarization of oscillating light so that it matches the SA transmission axis.

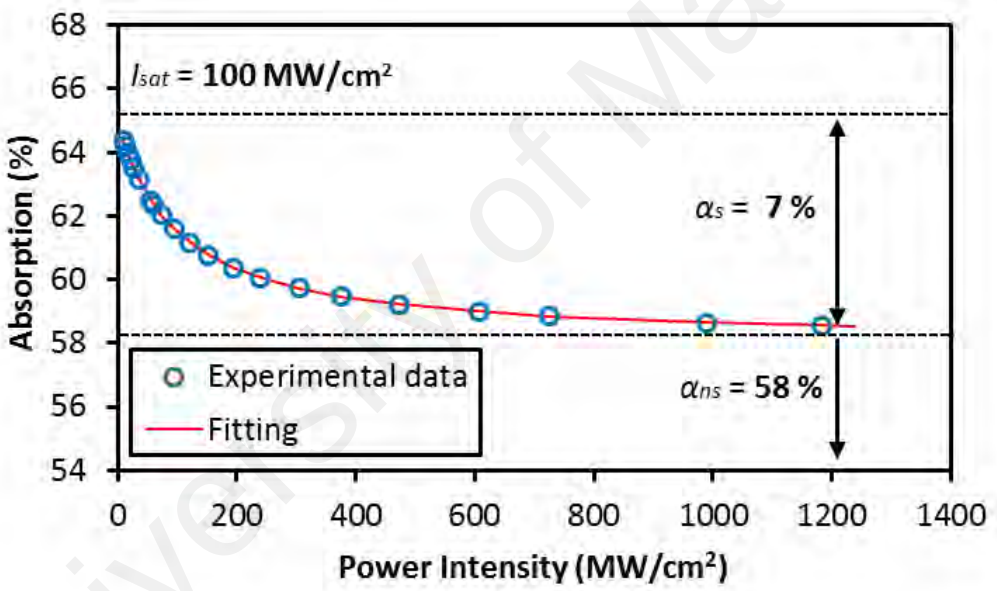

Figure 5.4: Nonlinear absorption properties of BP thin flakes.

5.4 Mode-locked Erbium-doped fiber laser (EDFL) with BP SA

The schematic configuration of the suggested mode-locked laser is shown in Figure 5.5. To realize mode-locking operation, the obtained BP thin flake is sandwiched between two fiber connectors with index matching gel as adhesive. The mode-locked EDFL has a total cavity length of 204 m which enables it to operate in anomalous dispersion region of -4.44 ps^2. The cavity length consists of 2.4 m long EDF and 6.6 m long SMF, with GVD of 27.6, and -21.7 ps^2/km, respectively. Additional 195 m long standard SMF was added into the cavity to increase the non-linearity effect which induced spectral broadening and allows the generation of a stable mode-locking pulse. The fiber laser was pumped by a 980-nm LD via a 980/1550 nm WDM. The gain medium used in the ring cavity is an EDF with an erbium concentration of 2000 ppm. The EDF has a numerical aperture of 0.24 and absorption of 24 dB/m at 1550 nm. A polarization free isolator is employed to guarantee unidirectional light propagation in the cavity and hence encourage self-starting laser (Tamura et al., 1993). The laser yield is obtained through a 90/10 output coupler, which allows 10% of the laser to be channeled out and analyzed.

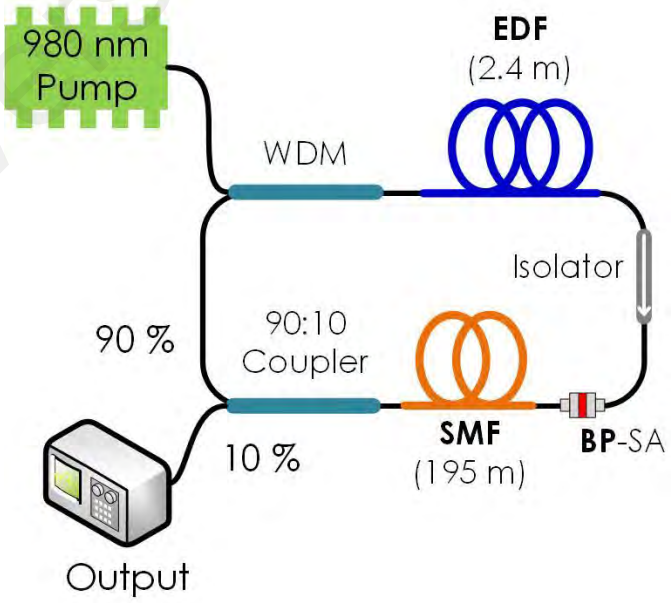

Figure 5.5: Schematic configuration of Mode-locked EDFL incorporating BP SA.

In the experiment, the self-starting mode locking pulse was obtained at 52 mW pump power. Figure 5.6(a) shows the optical spectrum of mode-locked pulses. The spectrum centered at around 1561 nm with the 3-dB spectral bandwidth of 0.985 nm (121.19 GHz). A weak Kelly side-band is also observed in the spectrum, which indicates that the generated pulse is at the edge of entering a soliton regime (Y. H. Lin et al., 2013). This corresponds to the strong anomalous dispersion (-4.44 ps^2) in the cavity. Further reduce the additional SMF length may decrease the cavity dispersion and compressing the pulse width (Yang et al., 2015). However, stable soliton mode-locking regime can be generated only with this appropriate cavity length (additional 195 m long SMF). Additional SMF length including 10 m, 30 m, 50 m, and 100 m have been added to generate pulsing operation. Unfortunately, it is unsuccesful and not suitable with this EDFL cavity. Figure 5.6(b) shows the average output power and single pulse energy of the mode-locked laser against the input pump power. As shown in the figure, the output power increases from 1.224 mW to 7.38 mW as the pump power is raised from the threshold value of 52 mW to 250 mW. The slope efficiency is calculated to be around 3.14%, which is relatively high due to the low insertion reduction from the SA. The pulse energy is also linearly increased with the pump power where the maximum pulse energy of 7.35 nJ was obtained at a pump power of 250 mW.

(a)

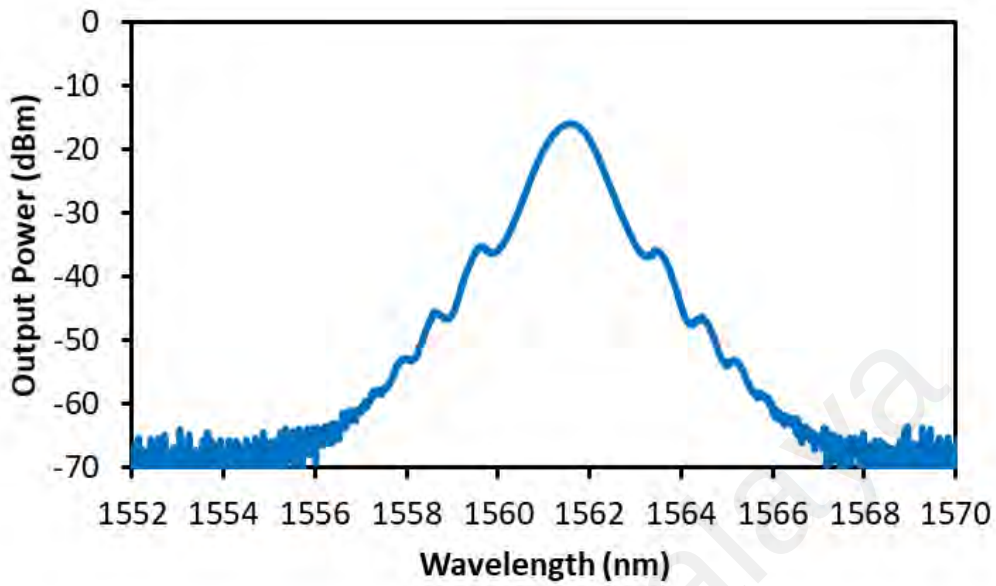

(b)

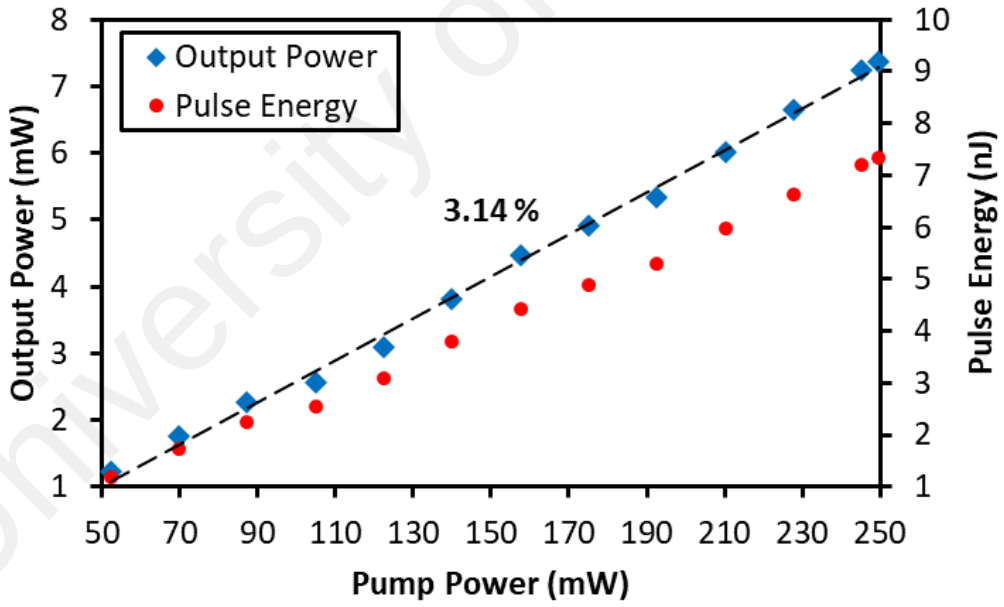

Figure 5.6: (a) Output spectrum of soliton mode-locked EDFL. (b) Output power and pulse energy as a function of pump power.

The temporal characteristics of the mode-locked EDFL after the 10 dB coupler are also investigated by using an autocorrelator and oscilloscope. Figure 5.7(a) shows a stable mode-locked pulse train with a peak to peak spacing of 1 ns (repetition rate of 1 MHz), which matches with a cavity length of 204 m. The peak power of pulse train taken was 53 mV. The oscilloscope trace shows a pulse width of 88 ps, but the actual pulse width is so much smaller due to the resolution limitation of the oscilloscope. The pulse width can be measured utilizing an auto-correlator or mathematically calculated based on time-bandwidth product (TBP). However, for EDFL the autocorrelator (Alnair Labs, HAC-200) is used to ascertain the pulse width. Its pulse width can be measured between 0.3 ps to 15 ps by applying a two-photon absorption method. Then, the measured optical pulses are instantaneously displayed in real-time with a temporal resolution of 25 fs. The function of assumed pulse shape can be converted from the FWHM auto-correlator trace width to the FWHM pulse width. Figure 5.7(b) indicates the measured auto-correlator pulse trace with FWHM of 4.13 ps and $sech^2$ pulse profile. The actual FWHM of the pulse is about 2.66 ps for the assumed $sech^2$ pulse shape. So, the TBP is calculated to be 0.322 which indicates the pulse slightly chirp. The broad pulse width can be further compressed through cavity dispersion management and also by improving the modulation depth of the SA.

(a)

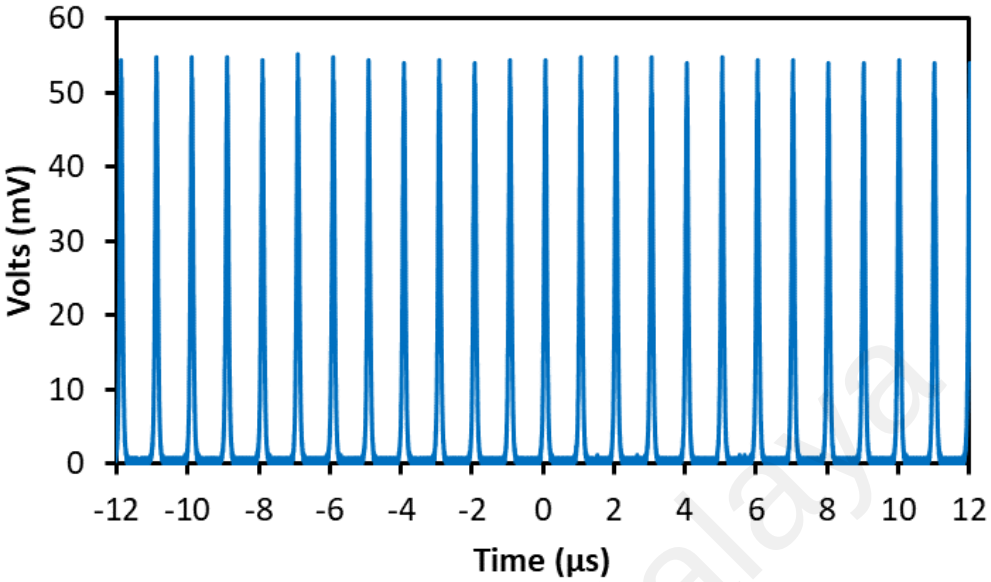

(b)

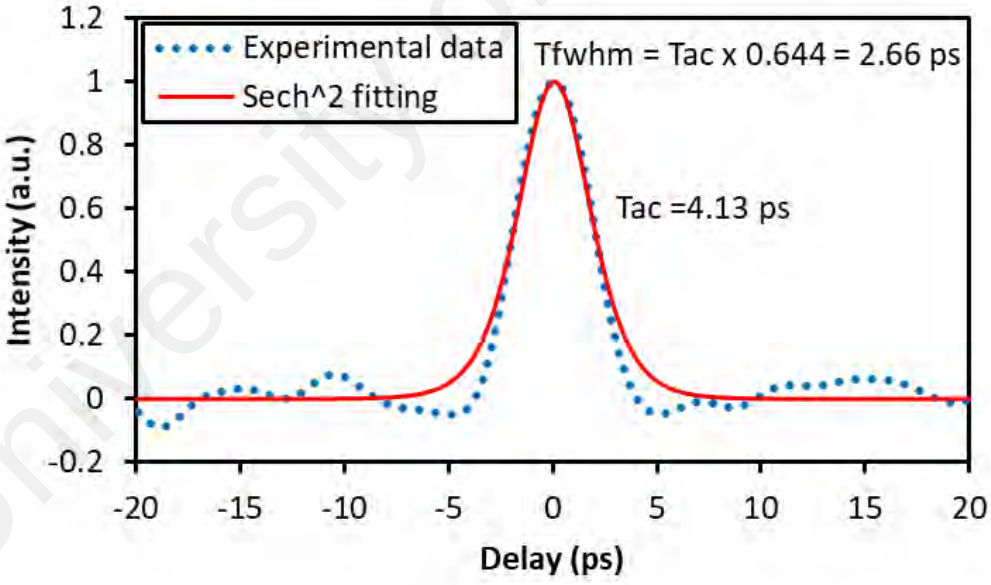

Figure 5.7: Temporal performance of soliton mode-locked EDFL. (a) Oscilloscope train (b) Autocorrelation trace for single pulse envelope.

The output picosecond pulses were observed at the room temperature, and the output is very stable which corresponding to the RF spectrum as indicated in Figure 5.8(a). Our laser cavity demonstrates a clear continuous mode-locked operation at the stable regime toward the maximum power at 250 mW which provided the fundamental frequency of 1 MHz and no other radio frequency component be observed which has a very high SNR up to 70 dB. In this experiment, the pulse breakup effect cannot be measured since the maximum pump power operation is limited to 250 mW. Overall, the long-term stability is good since the pulse has a good repeatibility. The obtained 70 dB SNR is confirming the stability of the fabricated device. During the mode-locking operation (52 mW to 250 mW pump power), this stable pulse only obtained at 1 MHz. Figure 5.8(b) shows the repetition rate against the pump power. As shown in the figure, the repetition rate is continuously constant, and there is no fluctuation in the line. By further enhancement, this developed device has a potential to be commercial.

(a)

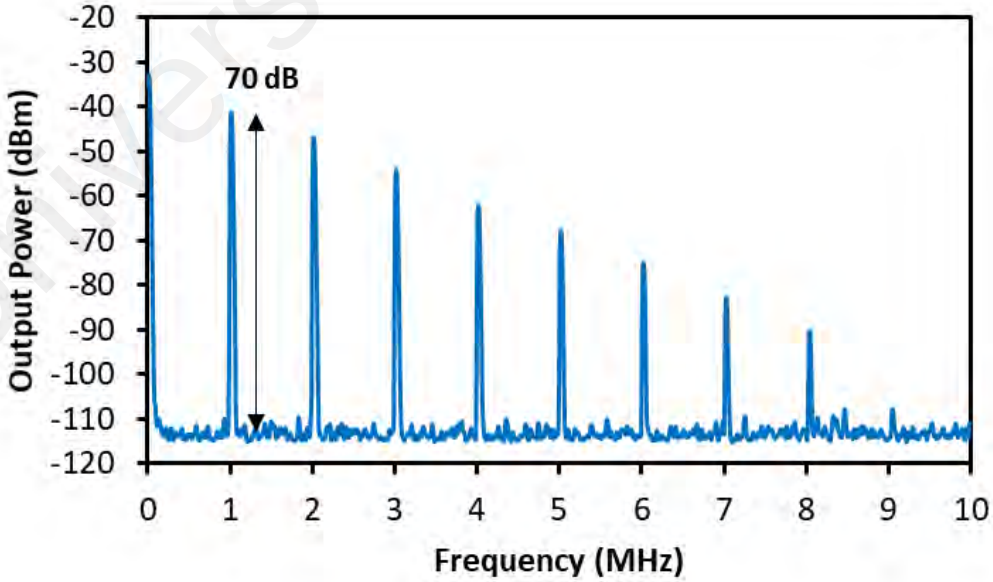

(b)

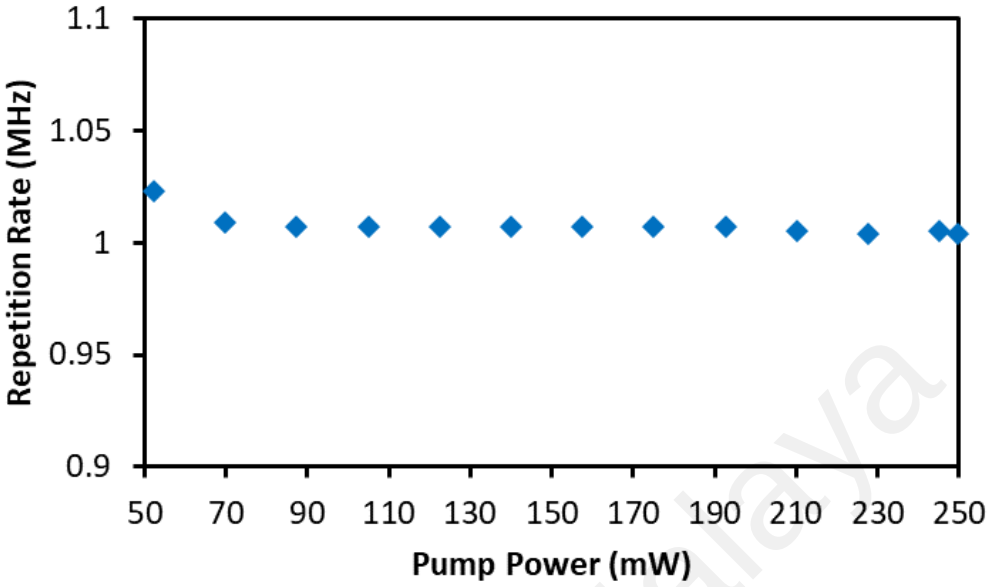

Figure 5.8: (a) RF spectrum of soliton mode-locked EDFL with 10 MHz spans. (b) Repetition rate as a function of pump power.

5.5 Mode-locked Ytterbium-doped fiber laser (YDFL) with BP SA

In this section, a fiber laser cavity was schematically designed to operate at a wavelength of 1-micron region in objective to evaluate its mode-locking ability. Figure 5.9 shows the proposed laser configuration where the obtained BP thin flakes based SA is used as the mode locker. The SA is integrated into the fiber laser cavity by sandwiching a piece of the multi-layer BP thin flakes between two FC/PC fiber ferrules via a fiber connector, adhered with index matching gel. A 10 m long double-clad YDF was used to provide amplification at 1-micron region. It has a cladding absorption coefficient of 3.95 dBm at 975 nm and the GVD of -18 ps^2/km. The fiber was pumped with a 980 nm multimode LD via an MMC. The addition of a PC enables adjustment of the polarization state within the cavity for the mode-locking action. A 10 dB fused optical fiber coupler was used to collect 10 % power from the cavity and retains 90 % of the light in the ring cavity to oscillate. Other fibers in the cavity is a standard SMF (with a GVD of 44.2

ps^2/km), which constitutes the rest of the ring. The total ring cavity length is around 14.8 m, and the net cavity dispersion is estimated in normal dispersion condition as ~ 0.39 ps^2. The laser performance was monitored and measured using similar measuring devices as in the previous chapter. The OSA is utilized for the spectral analysis of the mode-locked laser, while oscilloscope is used to analyze the output pulse train of the mode locking operation via a photodetector.

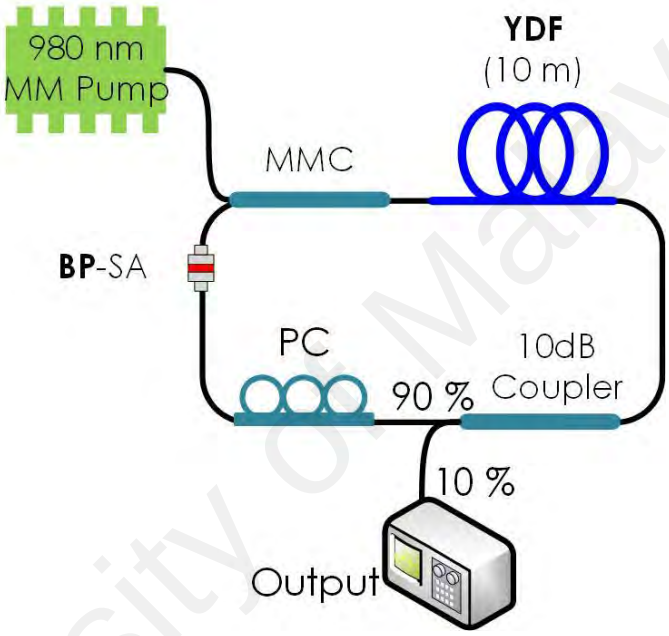

Figure 5.9: Schematic configuration of mode-locked YDFL incorporating BP-SA.

The mode-locking operation self-starts at the input multimode pump power of 816 mW provided that the intra-cavity PC is suitably adjusted. The self-starting mode-locking is maintained up to the pump power of 1322 mW and operates at the fundamental repetition frequency of the cavity of 13.5 MHz. The output spectrum of the mode-locked YDFL, which is obtained after the 10 dB coupler at the threshold pump power of 816 mW is shown in Figure 5.10. The spectrum operates at a center wavelength of 1085.5 nm with a peak power of -17.7 dBm and a 3-dB spectral bandwidth of 0.23 nm (58.52 GHz) without Kelly sideband. This confirms the mode-locked pulse operates in the normal dispersion.

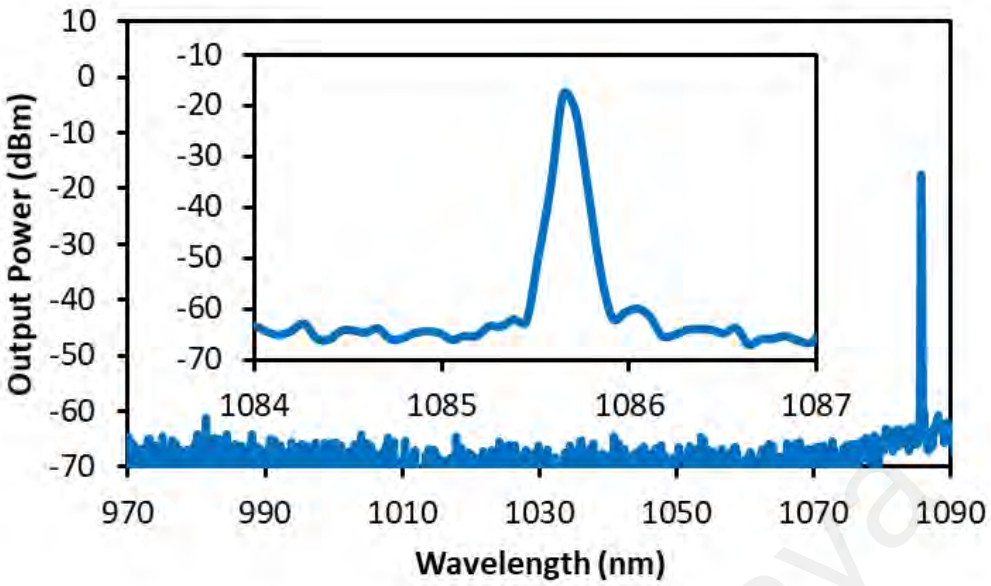

Figure 5.10: Output spectrum of mode-locked YDFL at a pump power of 816 mW.

Figure 5.11(a) shows a stable mode-locked pulse train with a peak to peak spacing of 74 ns, which matches with the cavity length of 14.8 m. The oscilloscope trace shows a pulse width of 26 ns, which is much broader than the actual pulse width. This is due to the resolution limitation of the oscilloscope. The actual pulse width can be measured using an auto-correlator or mathematically calculated based on the TBP. By assuming the TBP is 0.441 for Gaussian pulse profile, the minimum possible pulse width was estimated mathematically about 7.54 ps. The corresponding radio frequency spectrum as shown in Figure 5.11(b) indicates that our laser cavity operates at the stable regime, given that the fundamental frequency (13.5 MHz) has a high SNR (up to 45 dB). The peak of fundamental frequency decreased moderately until 7th harmonic, so this identifies the mode-locked has a narrow pulse width. At all pump power level, no presence of fundamental frequency observed when the BP thin flake is removed.

(a)

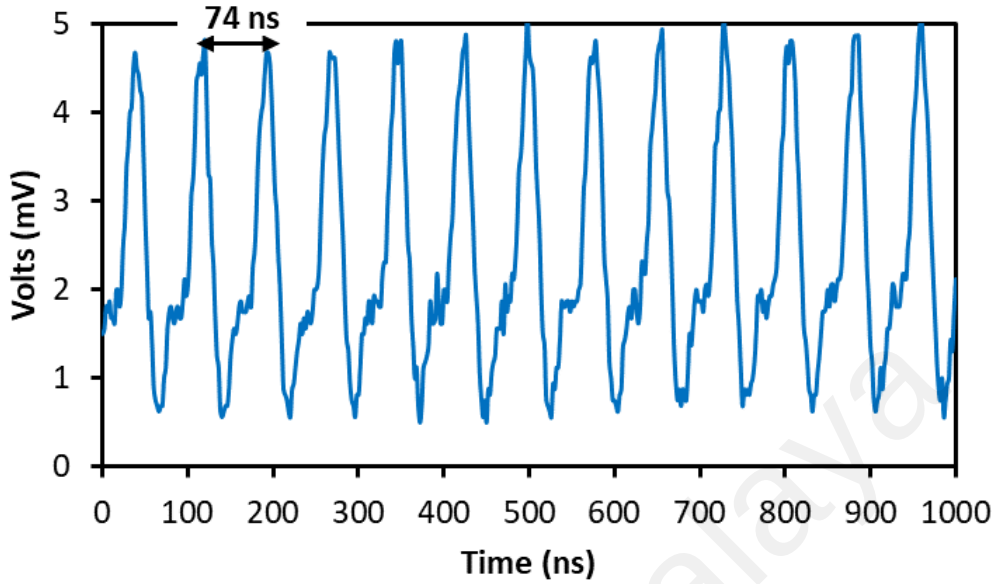

(b)

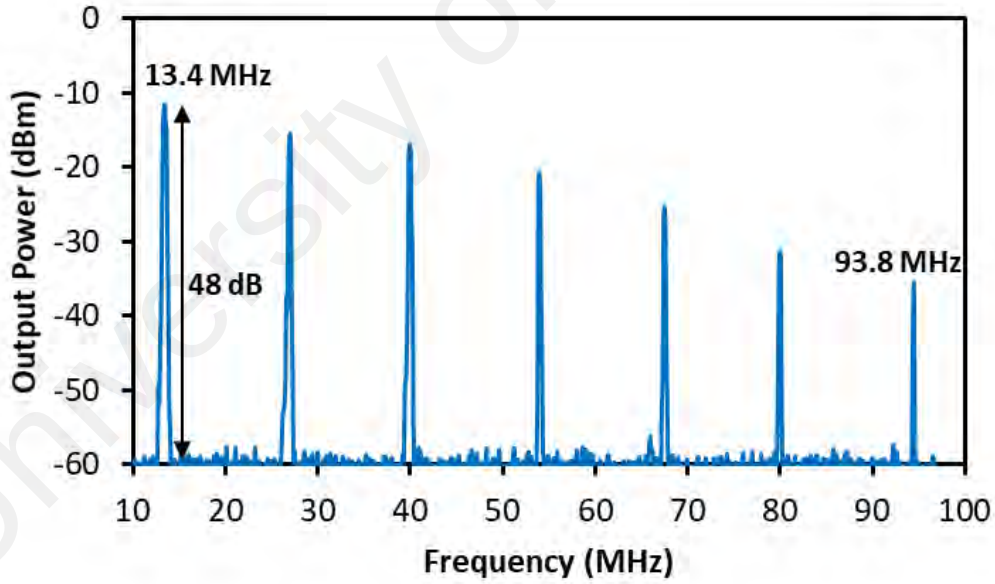

Figure 5.11: Temporal characteristics of mode-locked YDFL. (a) Pulse train. (b) RF spectrum with 100 MHz spans.

The relation between the input pump power and output power is also shown in Figure 5.12, which depicts that the output power increases from 10 mW to 80 mW with the corresponding pump power rise from 816 mW to 1322 mW. The optical-to-optical efficiency is relatively high (13.12 %) because of the low insertion loss from the SA. Figure 5.12 also presents the relation between the input signal power and the calculated pulse energy. It is observed that the pulse energy increases linearly with the pump power with the maximum pulse energy of 5.93 nJ. Due to over-saturation of the BP-SA, the mode-locked YDFL output becomes unstable and suddenly disappeared once the pump power exceeded 1322 mW. The BP-SA remain undamaged as we tuned pump power up to 1322 mW for more than a day. By keeping in an airtight container, less exposed to oxygen or water molecules helps to protect BP-SA from damage easily. The experimental results verify the mode locking ability of the newly developed few-layered BP based SA. This shows that the BP could be used to establish promising optoelectronic devices with high power tolerance, offering inroads for more practical applications, such as high energy laser mode-locking, nonlinear optical modulation and signal processing, etc.

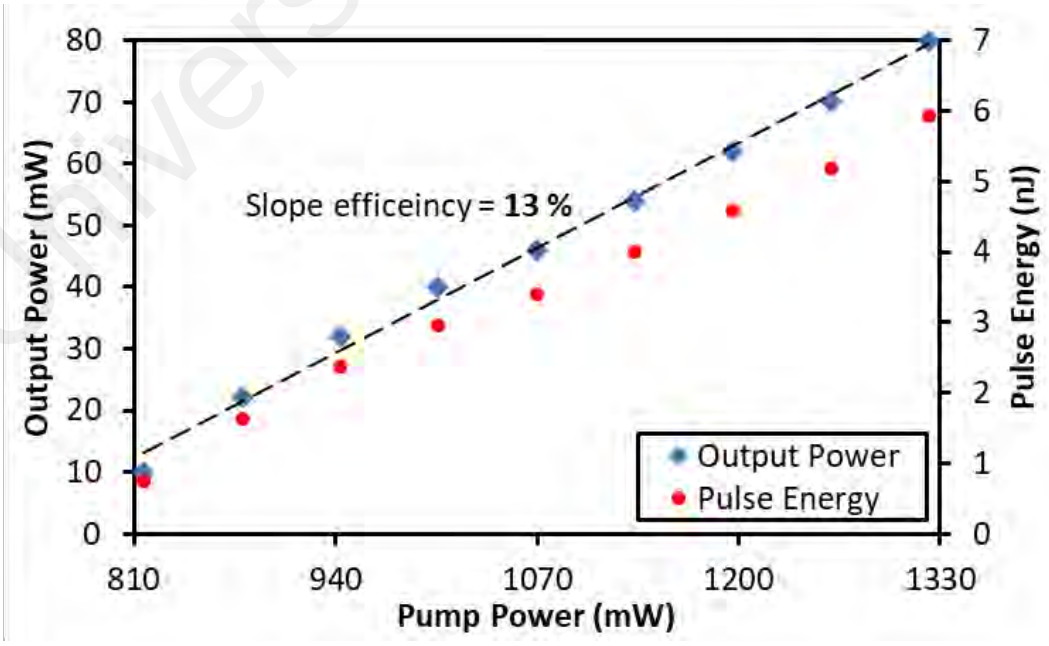

Figure 5.12: Output power and pulse energy of mode-locked YDFL.

For second observation, the mode-locked YDFL is scanned by OSA for every 20 minutes interval throughout 80 minutes. The stability of the mode-locking operation is further studied as shown in Figure 5.13. At a pump power of 816 mW, the stable operating wavelengths are maintained at 47 dB SNR with variations of peak amplitudes are within ±1 dB.

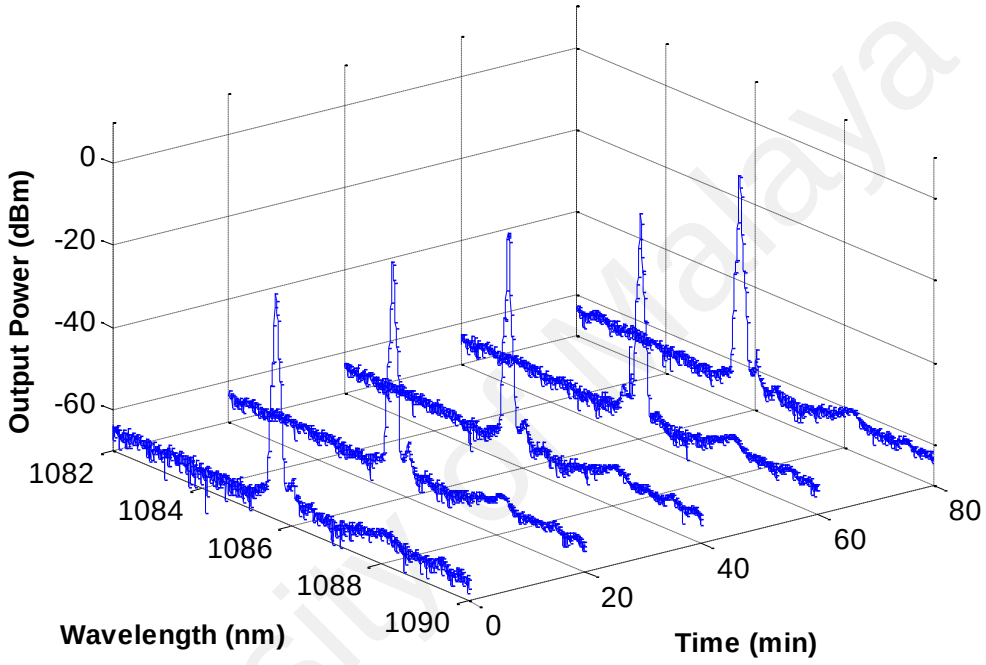

Figure 5.13: Output spectrum of mode-locked YDFL for every 20 minutes interval.

5.6 Mode-locked Thulium-doped fiber laser (TDFL) with BP SA

In this section, BP thin flake is sandwiched in the ring cavity of Thulium-doped fiber laser (TDFL) to convert continues-wave operation to mode-locking operation laser. The schematic diagram of the experimental set-up for the proposed TDFL is illustrated in Figure 5.14. The ring resonator consists of a 5 m long TDF as a gain medium. The TDF used has a numerical aperture of 0.15, core and cladding diameters of 9 and 125 μm, respectively, loss of less than 0.2 dB/km at 1900 nm, and peak core absorption at 1180

and 793 nm are 9.3 and 27 dB/m, respectively. The GVD parameter for TDF is about -84.6 ps^2/km. This fiber is pumped by a 1552 nm EYDFL via 1550/2000 nm WDM. Other fibers in the cavity is a standard SMF (-80 ps^2/km), which constituted the rest of the ring. An additional element of 15 m long ScDF is incorporated into the cavity to assist the mode-locked laser generation by providing a sufficient nonlinearity effect. The ScDF used in this work has a core diameter of 7.5 μm with background loss 50~75 dB/km at 1285 nm. The numerical aperture and GVD parameter are 0.12 and -127 ps^2/km, respectively. This cavity has a total length of 27 m and the net dispersion in the cavity is operates in anomalous dispersion condition of -2.888 ps^2. The output of the laser is collected from the cavity via a 90:10 coupler which retains 90 % of the light in the ring cavity to oscillate. The OSA is used to analyze the spectrum of the proposed TDFL whereas the oscilloscope is employed in conjunction with a photodetector to capture the output pulse train of the mode-locked emission. The rise times of the photodetector is about 50 ps.

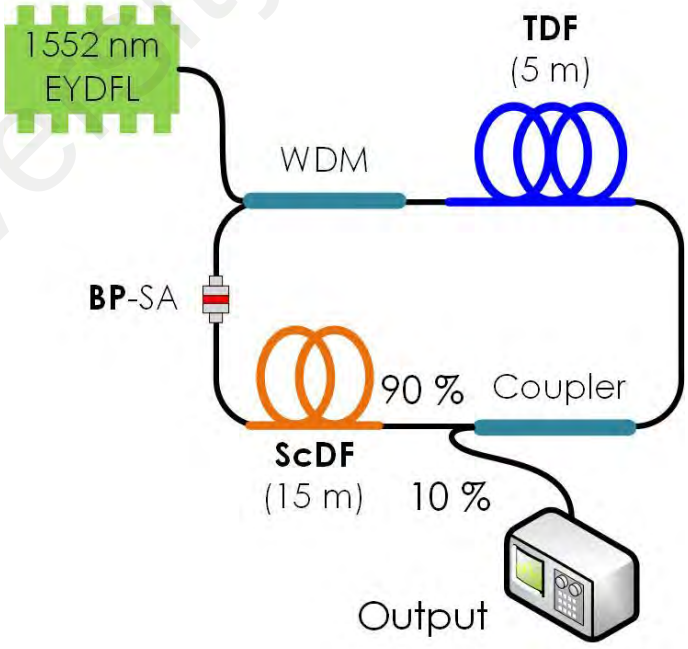

Figure 5.14: Schematic configuration of Mode-locked TDFL.

The mode-locked laser is self-started as a pump power reach 271 mW and operation maintained as a pump power increased to 363 mW. Figure 5.15(a) shows the output spectrum of mode-locked TDFL at threshold pump power. Within 1989 nm to 1998 nm wavelength, the peak lasing obtainable at 1948 nm with a peak power of -20 dBm and a 3-dB spectral bandwidth of 0.144 nm (11.38 GHz). A small ripple at a peak lasing induced due to the imperfection of surface obtained from the prepared BP thin flakes. However, this situation does not affect much on the stability of the laser temporal characteristics. Figure 5.15(b) shows the RF spectrum of fundamental repetition rate generated by mode-locked TDFL. As shown in the figure, a stable mode-locking operation is generated at 7.17 MHz with an SNR of 38 dB. The repetition rate constantly generates at 7.17 MHz within 271 mW to 363 mW as depicted in Figure 5.15(c). Under pump power level of mode-locking operation, the fundamental repetition rate will be eliminated once the BP thin flake is removed.

(a)

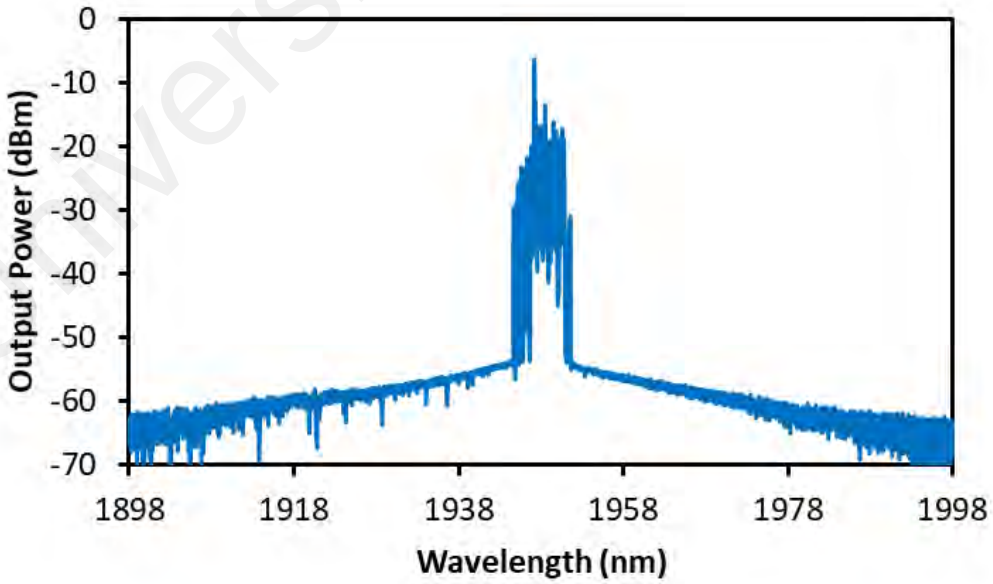

(b)

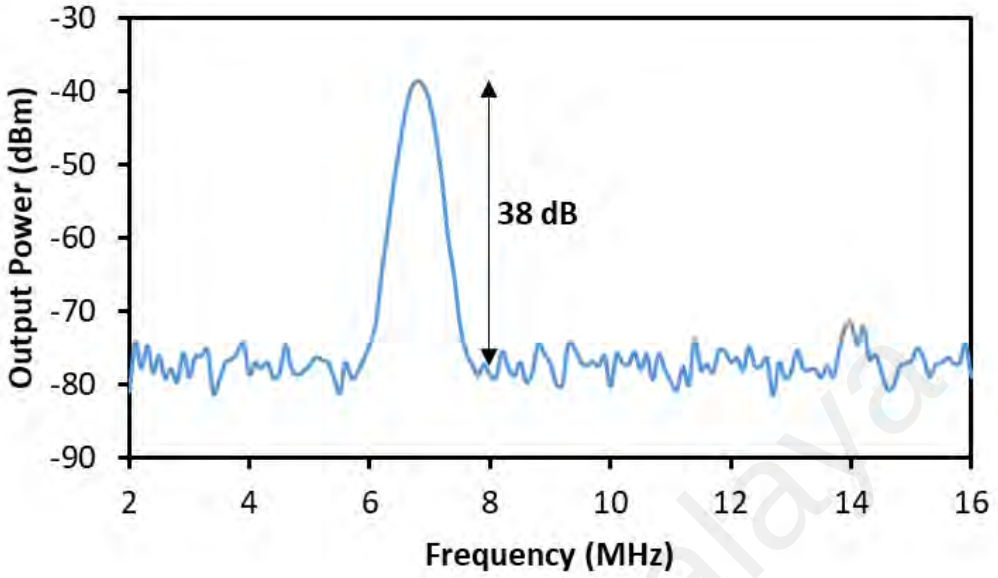

(c)

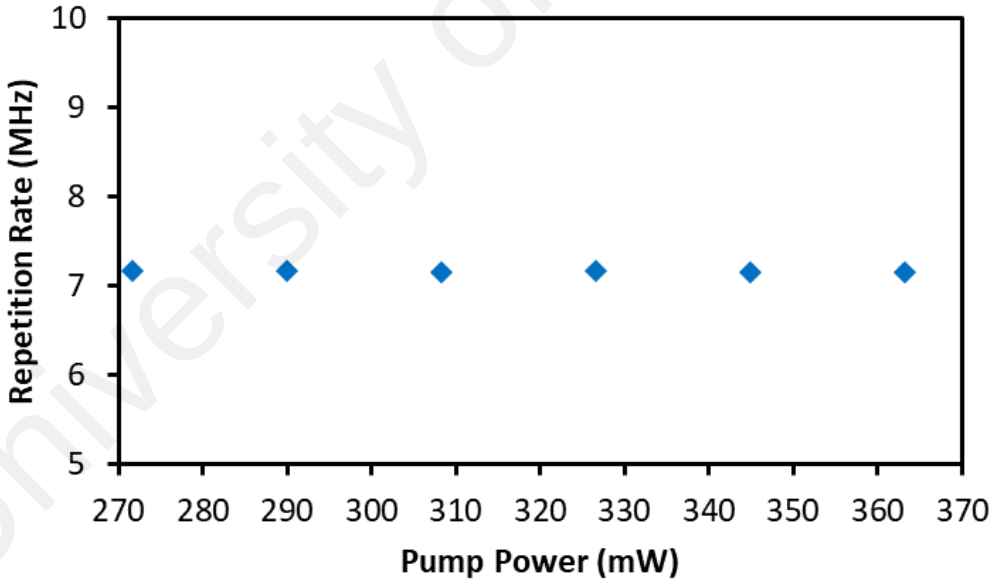

Figure 5.15: Spectral and temporal performances of mode-locked TDFL. (a) Output spectrum. (b) RF spectrum. (c) Repetition rate stability as a function of pump power.

Next observation is on pulse train profile of mode-locked TDFL. Figure 5.16 shows the output pulse train of mode-locked TDFL with an amplitude of 8.5 mV and a stable pulse period of 139.62 ns. This pulse period is corresponding to the obtained repetition rate. Direct from the oscilloscope, a single pulse envelope has a pulse width size of 67.93 ns which is much broader than the actual pulse width. The oscilloscope used in this work has a resolution limitation, then the pulse width can be numerically determined based on TBP analysis. By assuming the TBP is 0.315 for $Sech^2$ pulse fitting, the minimum possible pulse width corresponds to 3-dB spectral bandwidth is determined mathematically about 27.68 ps. This pulse size matches to existence of single harmonics generation in RF spectrum, based on Fourier transform. Moreover, it indicates only a few longitudinal modes are locked. Also, adding the ScDF has increased the cavity dispersion which leads to a pulse broadening. No pulse distortion presences. Thus, the laser is expected to have a low timing jitter and excellent mode-locking stability.

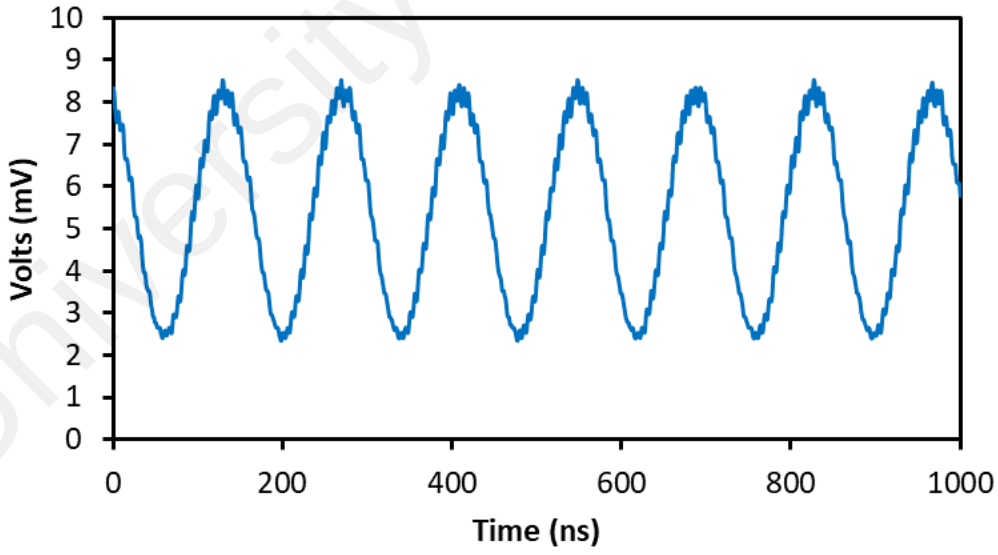

Figure 5.16: Output pulse train of mode-locked TDFL.

The relation between the pump power and output power is also shown in Figure 5.17, which depicts that the output power increases from 1.11 mW to 3.31 mW with the corresponding pump power rise from 271 mW to 363 mW. The linearity of the output power inclination determines the optical-to-optical efficiency of 2.4 %. Figure 5.17 also presents the relation between the pump power and the pulse energy. The pulse energy is obtained relatively from the division between output power and repetition rate. It is observed that the pulse energy increases linearly with the pump power with the maximum pulse energy of 0.46 nJ. Mode-locking regime becomes unstable and disappears once BP thin flakes over-saturated at above pump level of 363 mW. In next section, mode-locked Thulium Holmium co-doped fiber laser (THDFL) is demonstrated by changing the gain medium to Thulium-Holmium co-doped fiber (THDF).

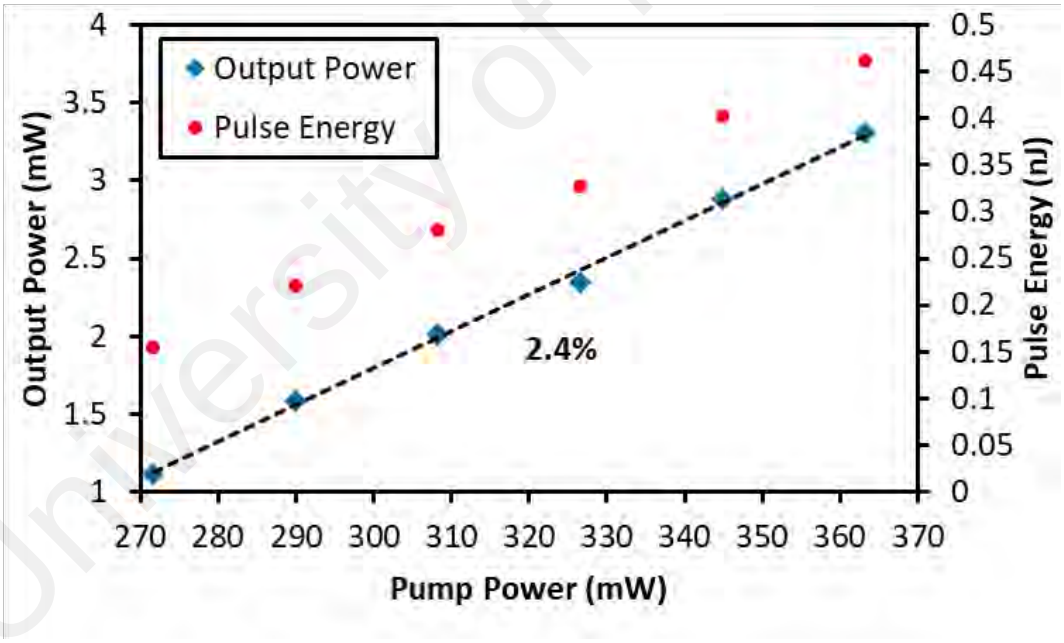

Figure 5.17: Output power and pulse energy as a function of pump power.

5.7 Mode-locked THDFL with BP SA

Mode-locking operation at 2-micron region can also be generated in THDFL configuration. Figure 5.18 illustrates the schematic diagram of ring cavity incorporating BP thin flakes as a mode-locker element with a cavity length of 22 m. The total net GDD in the cavity is operated in anomalous dispersion condition of -2.429 ps^2.This configuration consists of 1552 nm EYDFL, 1550/2000 WDM, 5 m long THDF (GVD of -72.8 ps^2/km), 90:10 coupler, and two fiber connectors with FC/PC adapter. The rest of the cavity is made of standard SMF (GVD of -80 ps^2/km) connected via fusion splicing. The EYDFL pumps a 1552 nm single wavelength to the 11.5 µm core diameter of THDF via WDM. The THDF has a numerical aperture of 0.14, thulium ion absorptions of 100 dB/m at 790 nm.

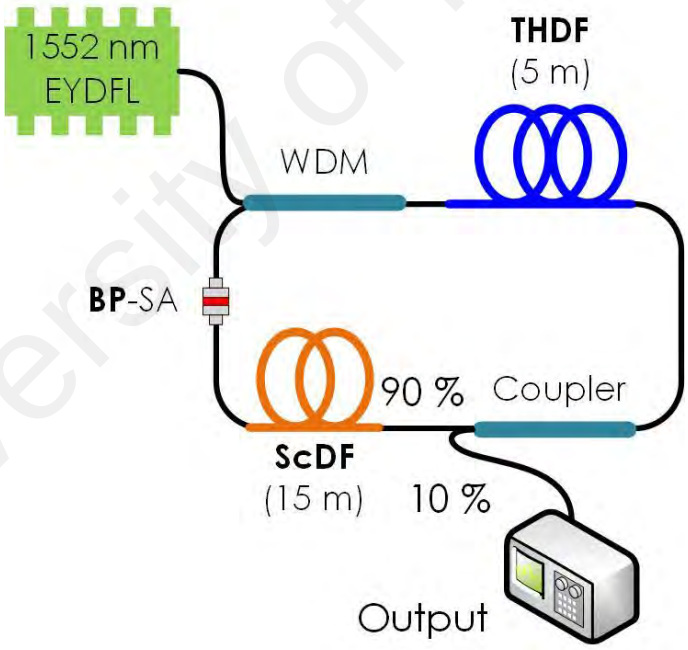

Figure 5.18: The configuration of Mode-locked THDFL ring cavity.

Towards mode-locking regime, a piece of BP thin flakes was adhered on fiber ferrule tip using index matching gel, then sandwiched between two fiber connectors. Also, similar 15 m long ScDF (GVD of -127 ps^2/km) employed in the previous section was added in the cavity to assist mode-locked laser generation. About 90 % mode-locked laser oscillates back in the cavity via a coupler. The laser performances were observed and measured from 10 % output coupler. Removing a polarization dependent isolator (PDI) and polarization controller (PC) from the cavity can avoid the mode-locking regime driven by the nonlinear polarization rotation (NPR) effects.

As the BP thin flake is integrated into the THDFL cavity, the mode-locking operation can be achieved as the pump power is varied from 949 mW to 1114 mW. Figure 5.19(a) shows the mode-locked THDFL output spectrum from 1500 nm to 2100 nm which was obtained from the output port (10%) of the coupler. As shown in the figure, the pumping wavelength drops to the peak spectrum of -55 dBm due to strong Tm ion absorption at 1.55-micron region. In addition, the gain profile up to 50 dBm is noticeable from 1900 nm to 2000 nm. A single peak lasing presence at 1969 nm with a peak spectrum of -7 dBm, where relatively 43 dB difference from peak pumping wavelength. Figure 5.19 (b) shows the enlarge peak lasing at 1969 nm within 20 nm spans. The 3-dB spectral bandwidth is 0.4 nm (30.93 GHz) with an absolute single peak lasing.

(a)

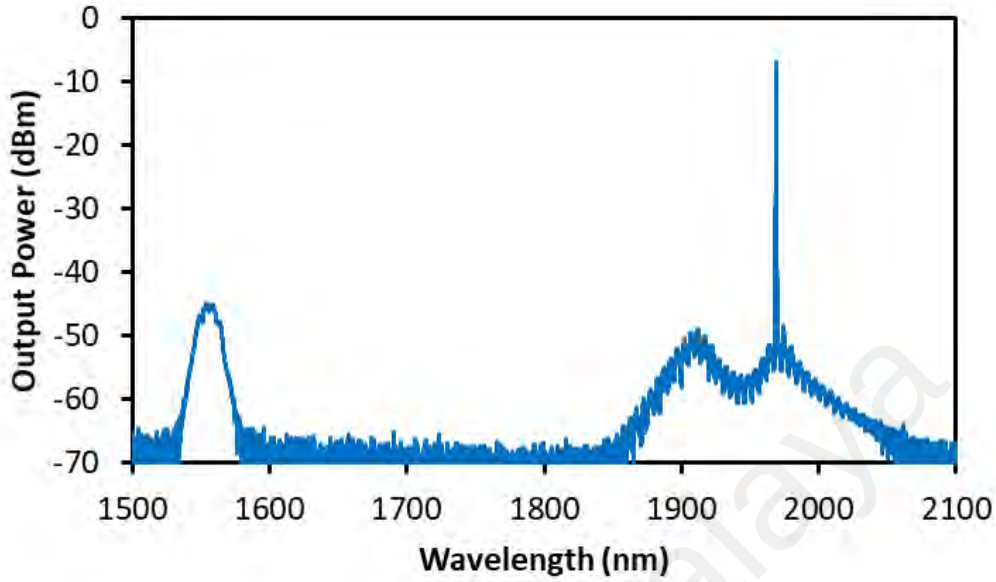

(b)

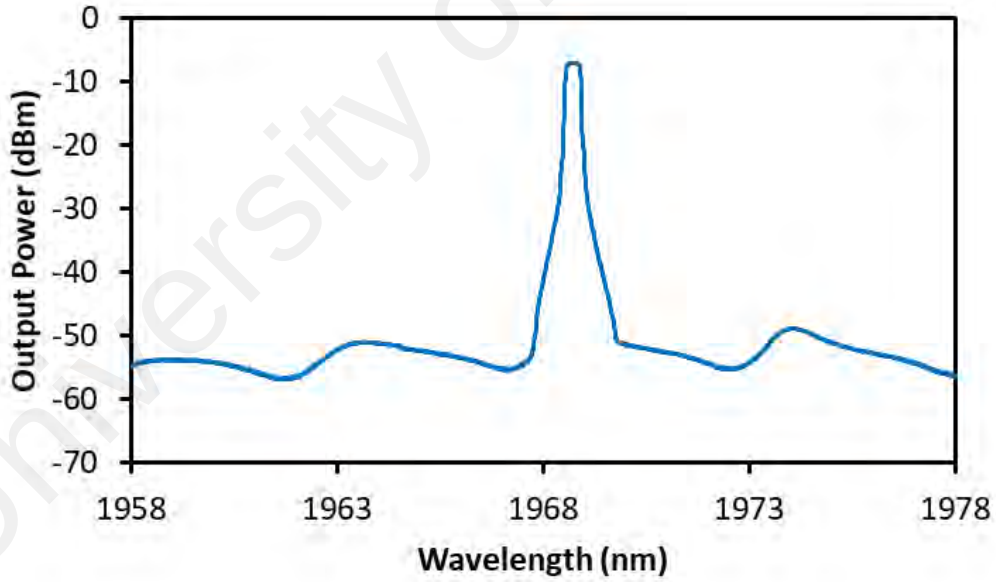

Figure 5.19: Spectral performance of mode-locked THDFL. (a) Output spectrum of 1500 nm to 2100 nm. (b) Enlarge of peak lasing at 1969 nm.

Next, observation on the temporal performances of the mode-locking regime was conducted in time- and frequency-domain. Figure 5.20(a) shows the oscilloscope train of mode-locked THDFL. The output pulse train is stable with a constant amplitude of 13.9 mV reachable along 2000 ns time spans. The 109.08 ns constantly separate two adjacent pulses as in Figure 5.20(b). This separation corresponds to the repetition rate of 9.17 MHz. Moreover, the FWHM of 53.46 ns for single pulse envelope is not an actual size of the pulse width. Through $Sech^2$ pulse profile, the TBP is 0.315 can be used to determine the minimum possible pulse width. Thus, the mode-locked THDFL has a pulse width size of 10.18 ps.

(a)

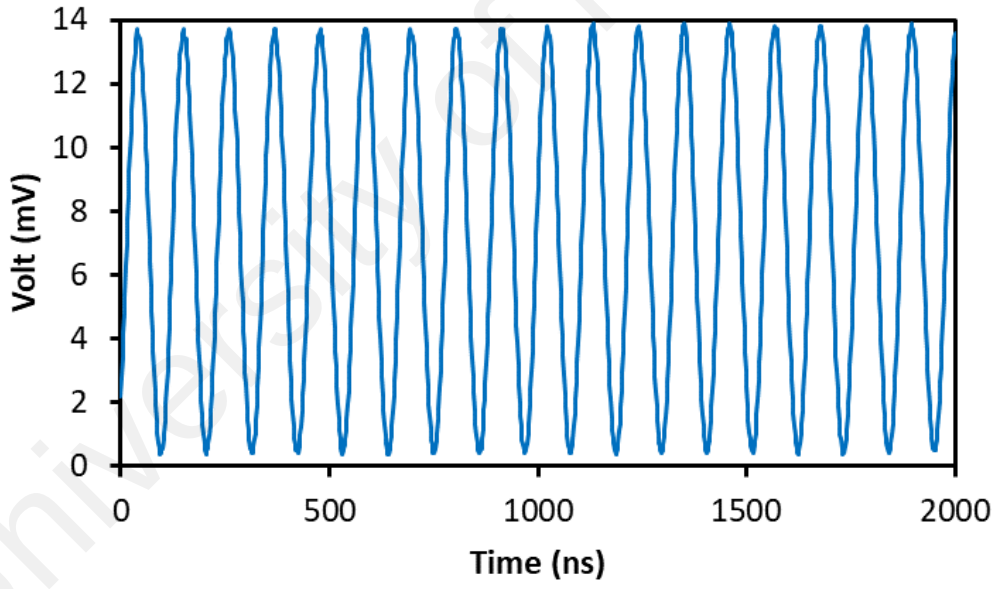

(b)

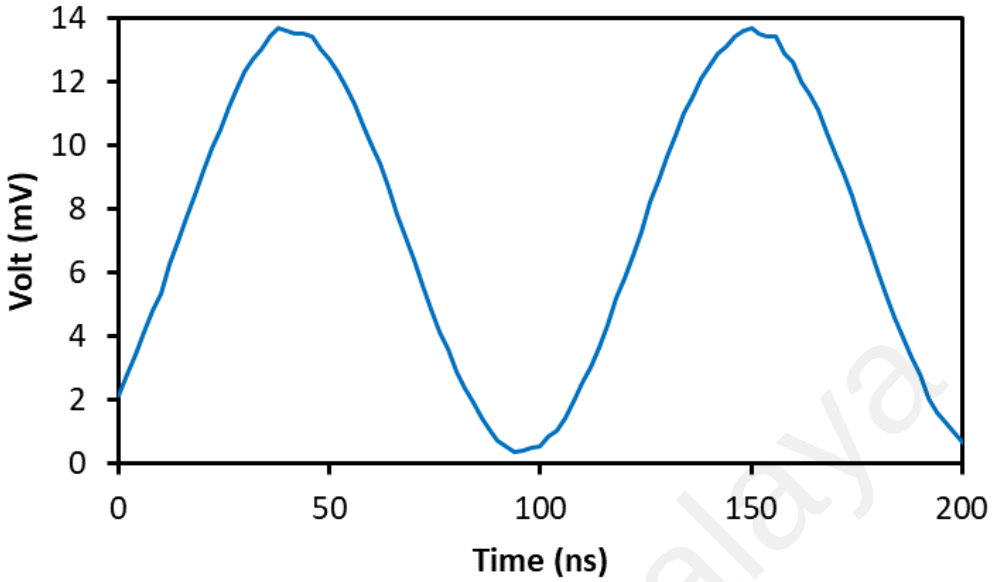

Figure 5.20: (a) Output pulse train of mode-locked THDFL. (b) Enlarge of peak envelope.

The presence of the pulse was confirmed in frequency-domain by using RF spectrum analyzer. Figure 5.21 shows the RF spectrum of mode-locked THDFL under 30 MHz spans. As shown in the figure, two main peaks visibly appear at 9.17 MHz and 18.34 MHz which represents the fundamental repetition rate and its second harmonic, respectively. The presence of harmonic indicates a few longitudinal modes has been locked together and oscillated in the laser cavity. Subsequently is related to the narrowing of the 3-dB spectral bandwidth of the output spectrum and the broadening of the pulse width. Also, a Fourier transform analysis explains a pulse width size in oscilloscope train is related to the number of harmonics with constant amplitude in RF spectrum. A stability of the mode-locking operation can be determined by measuring SNR of fundamental repetition rate from RF spectrum analyzer. The obtained pulse is stable with an SNR of 54 dB. After removing the BP thin flake from fiber ferrule with aids of alcohol swipe, no pulse train was observed in oscilloscope and RF spectrum analyzer.

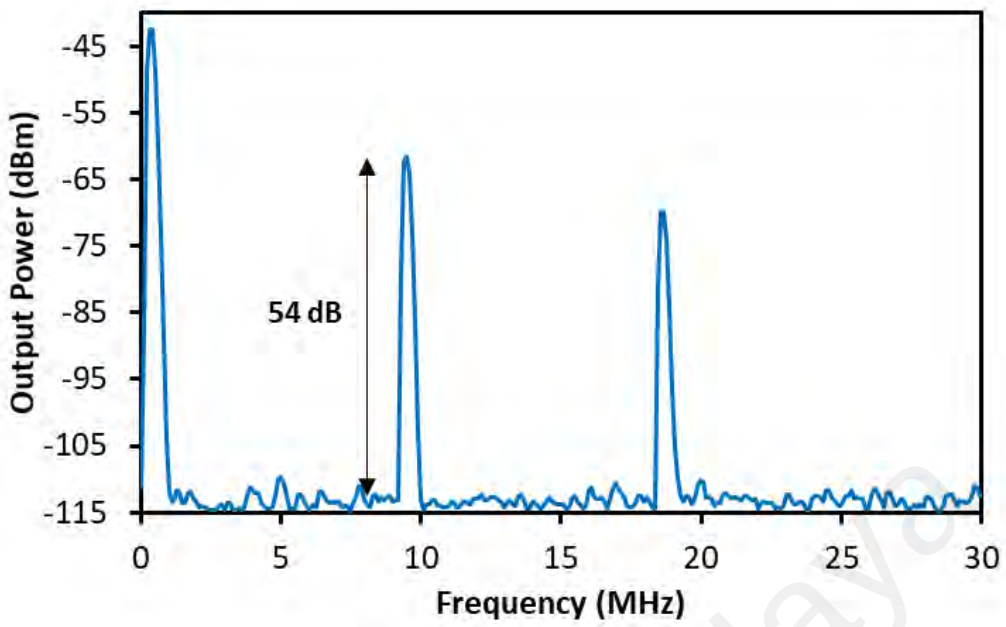

Figure 5.21: RF spectrum with 30 MHz spans.

All-related power performances of mode-locking operation are observed by using optical power meter via the thermal head detector. Figure 5.22 shows the output power as a function of pump power. The obtained output power increases linearly from 14 mW to 22 mW as a pump power rises from 949 mW to 1114 mW. The trendline of production power represents the optical-to-optical efficiency of 4.79 %. With a constant repetition rate of 9.17 MHz, a pulse energy increases from 1.56 nJ to 2.44 nJ which corresponds to the increment of output power when the pump power increases. As we launched the maximum limit pump power of 1.1 W into the laser cavity, the sandwiched BP thin flake between two fiber ferrules still generates mode-locking operation even after the pump power level is returning to 949 mW.

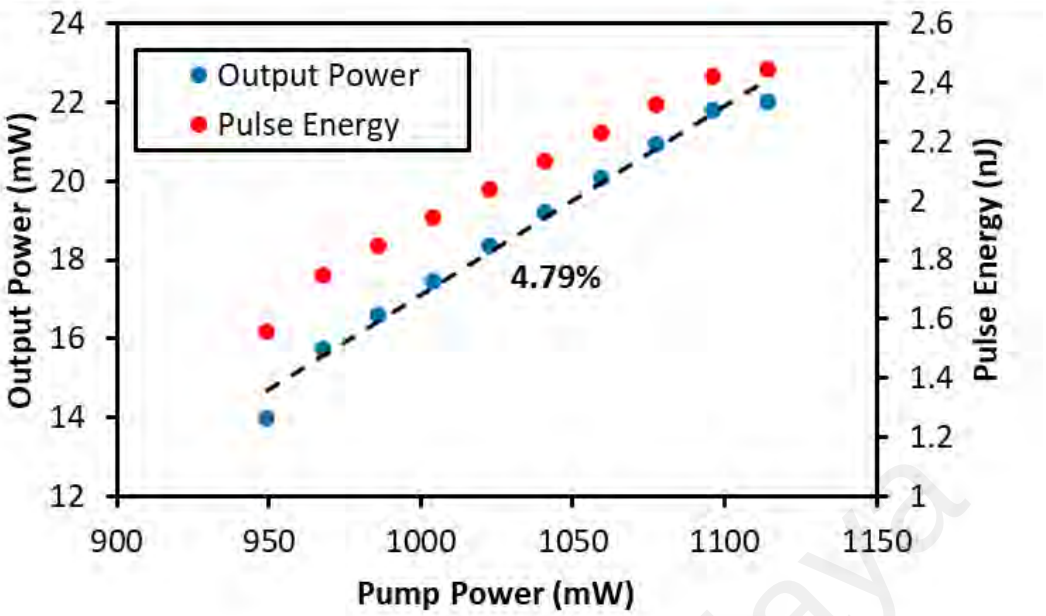

Figure 5.22: Output power and pulse energy characteristics against the pump power under the mode-locking regime.

5.8 Summary

Mode-locking operation at 1-, 1.55-, and 2-micron region have been experimentally achieved by incorporating a new BP thin flake as SA. Without comprise any chemical synthesis, the BP thin flakes were prepared by mechanically exfoliate from a commercial BP crystal using clear scotch tape. Only a piece of BP flake being peel off from the tape and then repeatedly pressing the flake on the transparent plastic surface so that the BP flake becomes thin enough to transmit light with a high efficiency. Finally, the obtained BP thin flake then being cut into a small piece and attached it onto a standard FC/PC fiber ferrule tip with aids of index matching gel. Due to hydrophilic material owned by BP, the whole preparation process was completed less than 2 minutes. The generation of the mode-locked laser was demonstrated first by using EDFL cavity. The mode-locked EDFL has a total cavity length of 204 m which enables it to operate in anomalous dispersion region of -4.44 ps^2. A stable repetition rate of the mode-locked pulse was obtained at 1 MHz with 70 dB SNR. The laser has a pulse width of 2.66 ps and TBP of 0.322. A peak

lasing of mode-locked EDFL obtainable at 1561 nm with the 3-dB spectral bandwidth of 0.985 nm (121.19 GHz) and capable of providing a pulse energy of 7.35 nJ.

The stable mode-locking operation also being demonstrated at 1085.5 nm with a 3-dB spectral bandwidth of 0.23 nm (58.52 GHz) in YDFL cavity. The cavity length is around 14.8 m with cavity dispersion is estimated in normal dispersion condition as ~ 0.39 ps^2. The maximum pulse energy of 5.93 nJ is induced under pulse width of 7.54 ps with a repetition rate of 13.5 MHz. The SNR is 45 dB.

In 2-micron mode-locked lasers, the BP thin flake was integrated into two different laser cavities; TDFL and THDFL. Stable mode-locked TDFL operated in anomalous dispersion condition of -2.888 ps^2 at a repetition rate of 7.17 MHz. The pulse width size of 27.68 ps accommodated with 0.462 nJ pulse energy presence at 1948 nm wavelength. The obtained peak lasing has a 3dB-spectral bandwidth of 0.144 nm (11.38 GHz). Overall temporal performances are stable with SNR of 38 dB. Under THDFL cavity, stable repetition obtained at 9.17 MHz with SNR of 54 dB. The mode-locked THDFL operates under anomalous dispersion condition of -2.429 ps^2 at 1969 nm with a 3-dB spectral bandwidth of 0.4 nm (30.93 GHz). Maximum output power of 22 mW is achieved with pulse energy of 2.44 nJ under pulse width size of 10.18 ps.

CHAPTER 6: CONCLUSION AND FUTURE DIRECTION

6.1 Conclusion

In this thesis, mode-locked fiber lasers that have led to short pulses with low jitter are demonstrated at 1-, 1.55-, and 2-micron regions. The successful generation of this ultrashort pulse laser is coming from passive SA devices as well as an optimized laser cavity. Through the comprehensive implementation of four work packages, the three objectives as a guideline for this research work are achieved. Each of Chapter 3, 4, and 5 answers all these objectives.

The SA used in this work was fabricated and prepared from 2D materials. Three 2D materials from three different group (TMD, TMO, BP) are utilized as a base-material for SA device. The material under TMD and TMO group are represented by MoS_2 and TiO_2, respectively. For BP, it is only one material (BP). The MoS_2 and BP SA were fabricated through a mechanical exfoliation method. Since TiO_2 SA is originally in powder form, the fabrication process involves two methods including liquid phase exfoliation and drop-casting method.

The key parameters to first indicate SA ability in the material is by observing it bandgap. The bandgap provides the absorption spectrum information of the material. So far, only graphene and bismuth have a zero energy bandgap which allows to broad spectrum absorption. Next, is investigating the relaxation time characteristic of the material. The relaxation time is related to assist a short pulse formation. The final step is to investigate the nonlinear absorption profile of the material. This profile provides the information about saturable absorption, non-saturable absorption, and saturation intensity. All parameters discussed above are summarized in Table 6.1.

Table 6.1: Summary of SA characteristics.

Material	Ideal Bandgap (eV)	Relaxation time	α_s (%)	α_{ns} (%)	I_{sat} (MW/cm^2)
MoS_2	0.86 – 1.8	2.1 ps (Wang et al., 2012)	10	12	100
TiO_2	3.2	1.5 fs (Elim et al., 2003)	34	51	195
BP	0.3	24 fs (Xiao et al., 2015)	7	58	100

Optimizing a laser cavity is also one of a key contribution to generate ultrashort pulse laser. In fiber ring laser cavity, the intra-cavity loss should be at a minimum level which important to allow enough light intensity for SA device to saturate. Also, avoid from using a polarization dependent isolator which later can induce an artificial SA under nonlinear polarization rotation (NPR) technique. Some cavity requires additional sufficient nonlinearity effects by adding additional fibers (SMF, ScDF). This effect induces more incoherent of random modes in the laser and thus becomes a key start for passive mode-locking. In fiber cavity condition of $L_{nl} > L_d$, nonlinearity dominates and causes pulse distortion. When $L_d > L_{nl}$, dispersion dominates and results in temporal broadening of the pulse. To form a fundamental soliton, L_{nl} and L_d must equal. With the MoS_2, TiO_2, and BP SA, each of the obtained ultrashort pulse lasers have generated a different laser performance at 1-, 1.55-, and 2-micron region. All findings for this work are summarized in Table 6.2. For pulsed laser parameters measurement, the most crucial part is to investigate the pulse width of single pulse envelope.

For pulse laser parameter measurements, the relationship between pulse width and 3-dB spectral bandwidth can be described through the Fourier-transform limit. By obtaining the 3-dB spectral bandwidth from the peak laser spectrum, the minimum possible pulse width can be determined by considering a pulse shape in sech^2. Twice a number of

harmonics presence in RF spectrum indicates a successful number of phase-locked of longitudinal modes in the laser cavity. So far, the lowest number phase-locked modes are two modes and consequently, broad pulse width was induced. Further increase of spectral bandwidth, the pulse width becomes shorter.

Table 6.2: Summary of ultrashort pulse fiber laser generated by 2D material SAs.

Operation state	Type of SA	Gain medium	Wavelength **(nm)**	Bandwidth (nm)	Repetition Rate	Pulse width	Pulse energy
ML[a]	**MoS_2**	**EDF**	1562	1.8	4 MHz	1.71 ps	1.66 nJ
ML		**YDF**	**1090**	**0.08**	**13.2 MHz**	**21.84 ps**	**0.74 nJ**
QS[b]		**TDF**	**1946**	**5.0**	**28.75 kHz**	**2.58 µs**	**0.66 µJ**
ML		TDF	-	-	-	-	-
ML		**THDF**	1979	2.1	9.12 MHz	1.96 ps	2.22 nJ
ML	**TiO_2**	EDF	**1559**	**0.74**	**1 MHz**	**3.52 ps**	**9.7 nJ**
QS		YDF	**1093.8**	**1.25**	**20.59 kHz**	**10.12 µs**	**0.56 nJ**
ML		YDF	-	-	-	-	-
QS		TDF	**1935**	**2.40**	**36.96 kHz**	**1.91 µs**	**0.3 µJ**
ML		TDF	-	-	-	-	-
ML		THDF	**1979**	**0.4**	**9 MHz**	**10.29 ps**	**1.66 nJ**
ML	**BP**	EDF	**1561**	**0.99**	**1 MHz**	**2.66 ps**	**7.35 nJ**
ML		YDF	1085.5	0.23	13.5 MHz	5.38 ps	2.69 nJ
ML		TDF	1948	0.14	7.17 MHz	28.48 ps	0.46 nJ
ML		THDF	**1968**	**2.0**	**9.17 MHz**	**2.03 ps**	**2.44 nJ**

[a]Mode-locking; [b]Q-switching

6.2 Future Direction

Rare-earth doped fiber recently gains attention in utilizing as SA device. So far not many work in fiber SA since the rare-earth materials used are only limits to single-mode thulium and holmium doped fiber. Relaxation time for thulium and holmium ions are in hundred microseconds and capability to produce a short pulse width is difficult (Latiff et al., 2017). In geometry perspective, fiber SA geometry has similar to standard fiber optic cable. It is easy to match to the fiber laser cavity. Less insertion loss and high threshold

damage are expected from this fiber SA. With robustness characteristics similar to standard fiber optic cable, fiber SA can be employed in the high-power laser cavity. Figure 6.1 shows overall ultrashort pulse fiber laser generation under passive technique. Fiber SA is categorized as real SA and available only to commercial rare-earth doped fiber. By doping the 2D materials into a silica glass fiber, the non-saturable absorption of MoS_2, BP, and TiO_2 are expected to minimize. Then, a laser pulse formation with high output power can be possible to achieve.

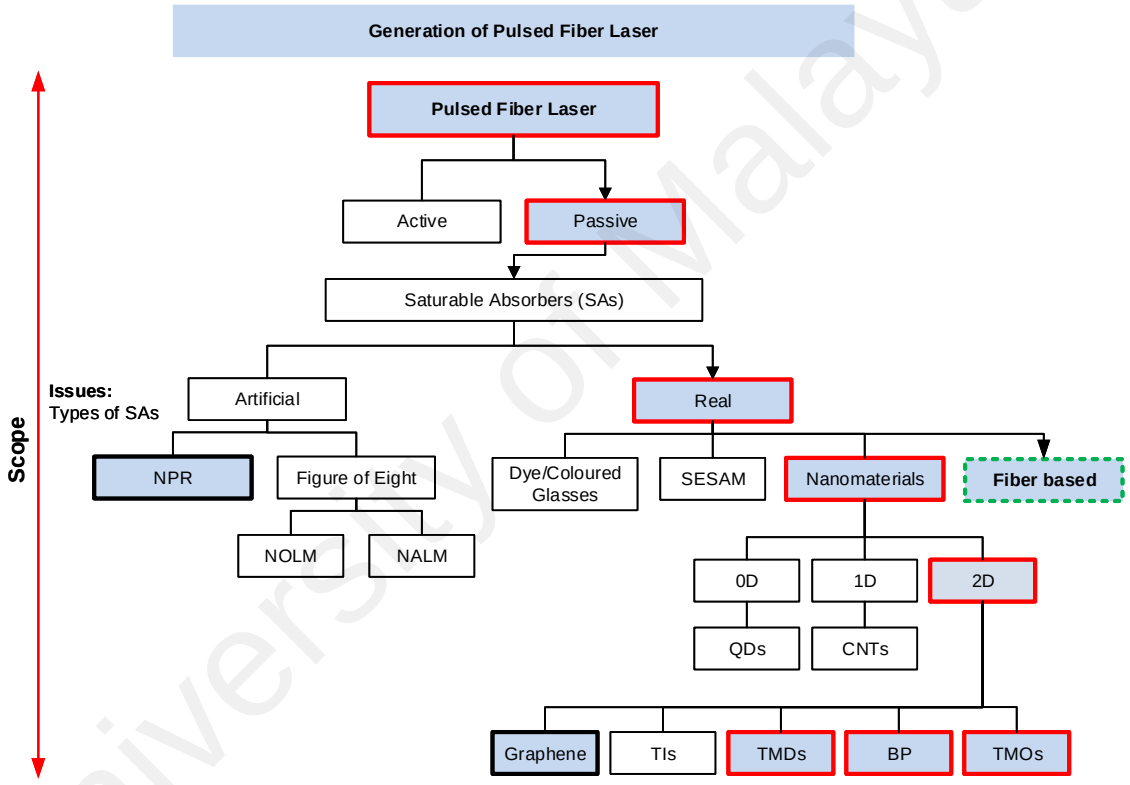

Figure 6.1: Scope of ultrashort pulse fiber laser generation.

REFERENCES

Agger, S. D., & Povlsen, J. H. (2006). Emission and absorption cross section of thulium doped silica fibers. *Optics Express, 14*(1), 50-57.

Agrawal, G. (2013). *Nonlinear Fiber Optics* (5 ed.). Great Britain: Academic Press.

Banakh, O., Schmid, P., Sanjines, R., & Levy, F. (2002). Electrical and optical properties of TiO x thin films deposited by reactive magnetron sputtering. *Surface and Coatings Technology, 151*, 272-275.

Bao, Q., Zhang, H., Wang, Y., Ni, Z., Yan, Y., Shen, Z. X., . . . Tang, D. Y. (2009). Atomic-Layer Graphene as a Saturable Absorber for Ultrafast Pulsed Lasers. *Advanced Functional Materials, 19*(19), 3077-3083. doi:10.1002/adfm.200901007

Blackmon, R. L., Hutchens, T. C., Hardy, L. A., Wilson, C. R., Irby, P. B., & Fried, N. M. (2015). Thulium fiber laser ablation of kidney stones using a 50-μm-core silica optical fiber. *Optical Engineering, 54*(1), 011004-011004.

Bonaccorso, F., Sun, Z., Hasan, T., & Ferrari, A. (2010). Graphene photonics and optoelectronics. *Nature photonics, 4*(9), 611-622.

Bradley, J. D., Evans, C. C., Choy, J. T., Reshef, O., Deotare, P. B., Parsy, F., . . . Mazur, E. (2012). Submicrometer-wide amorphous and polycrystalline anatase TiO 2 waveguides for microphotonic devices. *Optics express, 20*(21), 23821-23831.

Bret, G., & Gires, F. (1964). Giant-pulse laser and light amplifier using variable transmission coefficient glasses as light switches. *Applied Physics Letters, 4*(10), 175-176.

Butler, S. Z., Hollen, S. M., Cao, L., Cui, Y., Gupta, J. A., Gutiérrez, H. R., . . . Ismach, A. F. (2013). Progress, challenges, and opportunities in two-dimensional materials beyond graphene. *ACS nano, 7*(4), 2898-2926.

Castellanos-Gomez, A., Vicarelli, L., Prada, E., Island, J. O., Narasimha-Acharya, K., Blanter, S. I., . . . Alvarez, J. (2014). Isolation and characterization of few-layer black phosphorus. *2D Materials, 1*(2), 025001.

Chamorovskiy, A., Marakulin, A., Ranta, S., Tavast, M., Rautiainen, J., Leinonen, T., . . . Okhotnikov, O. (2012). Femtosecond mode-locked holmium fiber laser pumped by semiconductor disk laser. *Optics letters, 37*(9), 1448-1450.

Chang, Y. M., Kim, H., Lee, J. H., & Song, Y.-W. (2010). Multilayered graphene efficiently formed by mechanical exfoliation for nonlinear saturable absorbers in fiber mode-locked lasers. *Applied Physics Letters, 97*(21), 211102.

Chen, X. (2002). Preparation and property of TiO 2 nanoparticle dispersed polyvinyl alcohol composite materials. *Journal of materials science letters, 21*(21), 1637-1639.

Chen, Y., Jiang, G., Chen, S., Guo, Z., Yu, X., Zhao, C., . . . Tang, D. (2015). Mechanically exfoliated black phosphorus as a new saturable absorber for both Q-switching and Mode-locking laser operation. *Optics express, 23*(10), 12823-12833.

Choi, H. C., Jung, Y. M., & Kim, S. B. (2005). Size effects in the Raman spectra of TiO 2 nanoparticles. *Vibrational Spectroscopy, 37*(1), 33-38.

Churchill, H. O., & Jarillo-Herrero, P. (2014). Two-dimensional crystals: Phosphorus joins the family. *Nature nanotechnology, 9*(5), 330-331.

Clarkson, W., Barnes, N., Turner, P., Nilsson, J., & Hanna, D. (2002). High-power cladding-pumped Tm-doped silica fiber laser with wavelength tuning from 1860 to 2090 nm. *Optics letters, 27*(22), 1989-1991.

Daud, N. M., Saidin, M. K., Bidin, N., & Daud, Y. M. (2006). LASER BEAM MODULATION BY AN ACOUSTO OPTIC MODE LOCKER. *Jurnal Fizik UTM, 1*(2006), 16-21.

Dennis, M. L., & Duling III, I. N. (1994). Experimental study of sideband generation in femtosecond fiber lasers. *Quantum Electronics, IEEE Journal of, 30*(6), 1469-1477.

Desurvire, E., Simpson, J. R., & Becker, P. (1987). High-gain erbium-doped traveling-wave fiber amplifier. *Optics Letters, 12*(11), 888-890.

Digonnet, M. J. (2001). *Rare-earth-doped fiber lasers and amplifiers, revised and expanded*: CRC press.

Duan, N., Lin, H., Li, L., Hu, J., Bi, L., Lu, H., . . . Deng, L. (2013). ZrO 2-TiO 2 thin films: a new material system for mid-infrared integrated photonics. *Optical Materials Express, 3*(9), 1537-1545.

Dzhibladze, M. I., Esiashvili, Z., Teplitskiĭ, É. S., Isaev, S., & Sagaradze, V. (1983). Mode locking in a fiber laser. *Soviet Journal of Quantum Electronics, 13*(2), 245.

Elim, H., Jia, W., Yuwono, A., Xue, J., & Wang, J. (2003). Ultrafast optical nonlinearity in poly (methylmethacrylate)-TiO2 nanocomposites. *APPLIED PHYSICS LETTERS, 82*(16).

Etzel, H., Gandy, H., & Ginther, R. (1962). Stimulated emission of infrared radiation from ytterbium activated silicate glass. *Applied Optics, 1*(4), 534-536.

Fermann, M. (1994). Ultrashort-pulse sources based on single-mode rare-earth-doped fibers. *Applied Physics B: Lasers and Optics, 58*(3), 197-209.

Fermann, M. E., & Hartl, I. (2013). Ultrafast fibre lasers. *Nature Photon, 7*(11), 868-874. doi:10.1038/nphoton.2013.280

Franken, P. A., Hill, A. E., Peters, C. W., & Weinreich, G. (1961). Generation of Optical Harmonics. *Physical Review Letters, 7*(4), 118-119.

Fried, N. M., Lagoda, G. A., Scott, N. J., Su, L.-M., & Burnett, A. L. (2008). Noncontact stimulation of the cavernous nerves in the rat prostate using a tunable-wavelength thulium fiber laser. *Journal of Endourology, 22*(3), 409-414.

Gapontsev, V., Fomin, V., & Yusim, A. (2009). Recent progress inscaling of hih-power fiber lasers at IPG Photonics. *Technical Digest, Solid State and Diode Laser Technology Review*, 142.

Garmire, E. (2000). Resonant optical nonlinearities in semiconductors. *Selected Topics in Quantum Electronics, IEEE Journal of, 6*(6), 1094-1110.

Geim, A. K., & Grigorieva, I. V. (2013). Van der Waals heterostructures. *Nature, 499*(7459), 419-425. doi:10.1038/nature12385

Geim, A. K., & Novoselov, K. S. (2007). The rise of graphene. *Nature materials, 6*(3), 183-191.

Giles, C. R., & Desurvire, E. (1991). Modeling erbium-doped fiber amplifiers. *Journal of lightwave technology, 9*(2), 271-283.

Godard, A. (2007). Infrared (2–12 μm) solid-state laser sources: a review. *Comptes Rendus Physique, 8*(10), 1100-1128.

Gordon, J. P., Zeiger, H. J., & Townes, C. H. (1954). Molecular Microwave Oscillator and New Hyperfine Structure in the Microwave Spectrum of N H 3. *Physical Review, 95*(1), 282.

Grudinin, A. (2013). Fibre laser directions. *NATURE PHOTONICS, 7*(11), 846-847.

Guerreiro, P., Ten, S., Borrelli, N., Butty, J., Jabbour, G., & Peyghambarian, N. (1997). PbS quantum-dot doped glasses as saturable absorbers for mode locking of a Cr: forsterite laser. *Applied Physics Letters, 71*(12), 1595-1597.

Gumenyuk, R., Vartiainen, I., Tuovinen, H., & Okhotnikov, O. G. (2011). Dissipative dispersion-managed soliton 2 μm thulium/holmium fiber laser. *Optics letters, 36*(5), 609-611.

Guo, Z., Zhang, H., Lu, S., Wang, Z., Tang, S., Shao, J., . . . Yu, X. F. (2015). From black phosphorus to phosphorene: basic solvent exfoliation, evolution of Raman scattering, and applications to ultrafast photonics. *Advanced Functional Materials, 25*(45), 6996-7002.

Haris, H., Anyi, C., Ali, N., Arof, H., Ahmad, F., Nor, R., . . . Harun, S. (2014). Passively Q-switched erbium-doped fiber laser at L-band region by employing multi-walled carbon nanotubes as saturable absorber. *J. Optoelectron. Adv. Mater., 8*, 1025-1028.

Haris, H., Harun, S., Anyi, C., Muhammad, A., Ahmad, F., Tan, S., . . . Arof, H. (2015). Generation of soliton and bound soliton pulses in mode-locked erbium-doped fiber laser using graphene film as saturable absorber. *Journal of Modern Optics*, 1-6.

Harun, S., Ismail, M., Ahmad, F., Ismail, M., Nor, R., Zulkepely, N., & Ahmad, H. (2012). A Q-switched erbium-doped fiber laser with a carbon nanotube based saturable absorber. *Chinese Physics Letters, 29*(11), 114202.

Hasan, T., Sun, Z., Wang, F., Bonaccorso, F., Tan, P. H., Rozhin, A. G., & Ferrari, A. C. (2009). Nanotube-polymer composites for ultrafast photonics. *Adv. Mater, 21*(38-39), 3874-3899.

Hecht, J. (2010). Short history of laser development. *Optical Engineering, 49*(9), 091002-091002-091023.

Hecht, J. (2014). Photonic Frontiers: Fiber Lasers: Novel fiber lasers offer new capabilities. *Electronic version https://www.laserfocusworld.com/articles/print/volume-50/issue-05/features/photonics-frontiers-fiber-lasers-novel-fiber-lasers-offer-new-capabilities.html*. Retrieved from

Hong, T., Chamlagain, B., Lin, W., Chuang, H.-J., Pan, M., Zhou, Z., & Xu, Y.-Q. (2014). Polarized photocurrent response in black phosphorus field-effect transistors. *Nanoscale, 6*(15), 8978-8983.

Ippen, E., Shank, C., & Dienes, A. (1972). Passive mode locking of the cw dye laser. *Applied Physics Letters, 21*(8), 348-350.

Jackson, S. D. (2012). Towards high-power mid-infrared emission from a fibre laser. *Nature photonics, 6*(7), 423-431.

Jackson, S. D., Sabella, A., Hemming, A., Bennetts, S., & Lancaster, D. G. (2007). High-power 83 W holmium-doped silica fiber laser operating with high beam quality. *Optics letters, 32*(3), 241-243.

Javan, A., Bennett, W. R., & Herriott, D. R. (1961). Population inversion and continuous optical maser oscillation in a gas discharge containing a He-Ne mixture. *Physical Review Letters, 6*(3), 106.

Johnson, L. F., Geusic, J. E., & Uitert, L. G. V. (1965). COHERENT OSCILLATIONS FROM Tm3+, Ho3+, Yb3+ and Er3+ IONS IN YTTRIUM ALUMINUM GARNET. *Applied Physics Letters, 7*(5), 127-129. doi:10.1063/1.1754339

Kadir, N., Ismail, E., & Latiff, A. (2017). Transition Metal Dichalcogenides (WS2 and MoS2) Saturable Absorbers for Mode-Locked Erbium-Doped Fiber Lasers. *Chinese Physics Letters, 34*(01), 14202.

Keller, U. (2003). Recent developments in compact ultrafast lasers. *Nature, 424*(6950), 831-838.

Keller, U., Miller, D., Boyd, G., Chiu, T., Ferguson, J., & Asom, M. (1992). Solid-state low-loss intracavity saturable absorber for Nd: YLF lasers: an antiresonant semiconductor Fabry–Perot saturable absorber. *Optics letters, 17*(7), 505-507.

Keller, U., Weingarten, K. J., Kärtner, F. X., Kopf, D., Braun, B., Jung, I. D., . . . Au, J. A. d. (1996). Semiconductor saturable absorber mirrors (SESAM's) for

femtosecond to nanosecond pulse generation in solid-state lasers. *Selected Topics in Quantum Electronics, IEEE Journal of, 2*(3), 435-453.

Kim, J., Koo, J., & Lee, J. H. (2017). All-fiber acousto-optic modulator based on a cladding-etched optical fiber for active mode-locking. *Photonics Research, 5*(5), 391-395. doi:10.1364/PRJ.5.000391

Kitamura, R., Pilon, L., & Jonasz, M. (2007). Optical constants of silica glass from extreme ultraviolet to far infrared at near room temperature. *Applied optics, 46*(33), 8118-8133.

Kobtsev, S., Kukarin, S., & Fedotov, Y. (2011). Mode-locked Yb-fiber laser with saturable absorber based on carbon nanotubes. *Laser Physics, 21*(2), 283-286.

Koenig, S. P., Doganov, R. A., Schmidt, H., Neto, A. C., & Oezyilmaz, B. (2014). Electric field effect in ultrathin black phosphorus. *Applied Physics Letters, 104*(10), 103106.

Koester, C. J., & Snitzer, E. (1964). Amplification in a fiber laser. *Applied optics, 3*(10), 1182-1186.

Lamb Jr, W. E. (1964). Theory of an optical maser. *Physical Review, 134*(6A), A1429.

Latiff, A., Kadir, N., Ismail, E., Shamsuddin, H., Ahmad, H., & Harun, S. (2017). All-fiber dual-wavelength Q-switched and mode-locked EDFL by SMF-THDF-SMF structure as a saturable absorber. *Optics Communications, 389*, 29-34.

Latiff, A., Rusdi, M., Hisyam, M., Ahmad, H., & Harun, S. (2016). A generation of 2 μm Q-switched thulium-doped fibre laser based on anatase titanium (IV) oxide film saturable absorber. *Journal of Modern Optics*, 1-4.

Latiff, A., Rusdi, M., Hisyam, M., Ahmad, H., & Harun, S. (2017). A generation of 2 μm Q-switched thulium-doped fibre laser based on anatase titanium (IV) oxide film saturable absorber. *Journal of Modern Optics, 64*(2), 187-190.

Latiff, A., Shamsudin, H., Ahmad, H., & Harun, S. (2015). Q-switched thulium-doped fiber laser operating at 1940 nm region using a pencil-core as saturable absorber. *Journal of Modern Optics*, 1-5.

Lee, C., Yan, H., Brus, L. E., Heinz, T. F., Hone, J., & Ryu, S. (2010). Anomalous Lattice Vibrations of Single- and Few-Layer MoS2. *ACS Nano, 4*(5), 2695-2700. doi:10.1021/nn1003937

Lee, E. J., Choi, S. Y., Jeong, H., Park, N. H., Yim, W., Kim, M. H., . . . Kim, S. J. (2015). Active control of all-fibre graphene devices with electrical gating. *Nature communications, 6*.

Li, D., Jussila, H., Karvonen, L., Ye, G., Lipsanen, H., Chen, X., & Sun, Z. (2015). Polarization and Thickness Dependent Absorption Properties of Black Phosphorus: New Saturable Absorber for Ultrafast Pulse Generation. *Scientific Reports, 5*, 15899. doi:10.1038/srep15899

Li, H., Zhang, Q., Yap, C. C. R., Tay, B. K., Edwin, T. H. T., Olivier, A., & Baillargeat, D. (2012). From bulk to monolayer MoS2: evolution of Raman scattering. *Advanced Functional Materials, 22*(7), 1385-1390.

Li, L., Yu, Y., Ye, G. J., Ge, Q., Ou, X., Wu, H., . . . Zhang, Y. (2014). Black phosphorus field-effect transistors. *Nature nanotechnology, 9*(5), 372-377.

Li, X., Tao, L., Chen, Z., Fang, H., Li, X., Wang, X., . . . Zhu, H. (2017). Graphene and related two-dimensional materials: Structure-property relationships for electronics and optoelectronics. *Applied Physics Reviews, 4*(2), 021306.

Lin, Y.-H., Lin, S.-F., Chi, Y.-C., Wu, C.-L., Cheng, C.-H., Tseng, W.-H., . . . Lin, G.-R. (2015). Using n-and p-type Bi2Te3 topological insulator nanoparticles to enable controlled femtosecond mode-locking of fiber lasers. *ACS Photonics, 2*(4), 481-490.

Lin, Y.-H., Yang, C.-Y., Lin, S.-F., Tseng, W.-H., Bao, Q., Wu, C.-I., & Lin, G.-R. (2014). Soliton compression of the erbium-doped fiber laser weakly started mode-locking by nanoscale p-type Bi2Te3 topological insulator particles. *Laser Physics Letters, 11*(5), 055107.

Lin, Y. H., & Lin, G. R. (2013). Kelly sideband variation and self four-wave-mixing in femtosecond fiber soliton laser mode-locked by multiple exfoliated graphite nano-particles. *Laser Physics Letters, 10*(4), 045109.

Liu, H., Luo, A.-P., Wang, F.-Z., Tang, R., Liu, M., Luo, Z.-C., . . . Zhang, H. (2014). Femtosecond pulse erbium-doped fiber laser by a few-layer MoS 2 saturable absorber. *Optics letters, 39*(15), 4591-4594.

Liu, X., Du, D., & Mourou, G. (1997). Laser ablation and micromachining with ultrashort laser pulses. *EEE Journal of Quantum Electronics, 33*(10), 1706-1716.

Lu, S., Miao, L., Guo, Z., Qi, X., Zhao, C., Zhang, H., . . . Fan, D. (2015). Broadband nonlinear optical response in multi-layer black phosphorus: an emerging infrared and mid-infrared optical material. *Optics express, 23*(9), 11183-11194.

Lu, S., Zhao, C., Zou, Y., Chen, S., Chen, Y., Li, Y., . . . Tang, D. (2013). Third order nonlinear optical property of Bi 2 Se 3. *Optics express, 21*(2), 2072-2082.

Luo, Z.-C., Liu, M., Guo, Z.-N., Jiang, X.-F., Luo, A.-P., Zhao, C.-J., . . . Zhang, H. (2015). Microfiber-based few-layer black phosphorus saturable absorber for ultra-fast fiber laser. *arXiv preprint arXiv:1505.03035*.

Luo, Z., Li, Y., Zhong, M., Huang, Y., Wan, X., Peng, J., & Weng, J. (2015). Nonlinear optical absorption of few-layer molybdenum diselenide (MoSe 2) for passively mode-locked soliton fiber laser [Invited]. *Photonics Research, 3*(3), A79-A86.

Maiman, T. H. (1960a). Optical and microwave-optical experiments in ruby. *Physical review letters, 4*(11), 564.

Maiman, T. H. (1960b). Stimulated optical radiation in ruby. *nature, 187*(4736), 493-494.

Mao, D., Liu, X., Sun, Z., Lu, H., Han, D., Wang, G., & Wang, F. (2013). Flexible high-repetition-rate ultrafast fiber laser. *Scientific reports, 3*, 3223.

Martev, I. (2000). Oxygen-ion-assisted deposition of TiO films. *Vacuum, 58*(2), 327-334.

Martín-Palma, R. J., Martínez-Duart, J., & Agulló-Rueda, F. (2006). *Nanotechnology for microelectronics and optoelectronics*: Elsevier.

Martinez, A., Fuse, K., & Yamashita, S. (2011). Mechanical exfoliation of graphene for the passive mode-locking of fiber lasers. *Applied Physics Letters, 99*(12), 121107.

Martinez, A., & Sun, Z. (2013). Nanotube and graphene saturable absorbers for fibre lasers. *Nat Photon, 7*(11), 842-845. doi:10.1038/nphoton.2013.304

Mas-Balleste, R., Gomez-Navarro, C., Gomez-Herrero, J., & Zamora, F. (2011). 2D materials: to graphene and beyond. *Nanoscale, 3*(1), 20-30.

Mears, R., Reekie, L., Jauncey, I., & PAYNE, D. N. (1987). *High-gain rare-earth-doped fiber amplifier at 1.54 μm.* Paper presented at the Optical Fiber Communication Conference.

Mears, R., Reekie, L., Poole, S., & Payne, D. (1985). Neodymium-doped silica single-mode fibre lasers. *Electronics Letters, 21*(17), 738-740.

Méndez, A., & Morse, T. F. (2011). *Specialty optical fibers handbook*: Academic Press.

Moulton, P. F., Rines, G., Slobodtchikov, E. V., Wall, K. F., Frith, G., Samson, B., & Carter, A. L. (2009). Tm-doped fiber lasers: fundamentals and power scaling. *Selected Topics in Quantum Electronics, IEEE Journal of, 15*(1), 85-92.

Nelson, L., Jones, D., Tamura, K., Haus, H., & Ippen, E. (1997). Ultrashort-pulse fiber ring lasers. *Applied Physics B: Lasers and Optics, 65*(2), 277-294.

Nishizawa, N. (2014). Ultrashort pulse fiber lasers and their applications. *Japanese Journal of Applied Physics, 53*(9), 090101.

Novoselov, K. (2011). Nobel lecture: Graphene: Materials in the flatland. *Reviews of Modern Physics, 83*(3), 837.

Novoselov, K., Jiang, D., Schedin, F., Booth, T., Khotkevich, V., Morozov, S., & Geim, A. (2005). Two-dimensional atomic crystals. *Proceedings of the National Academy of Sciences of the United States of America, 102*(30), 10451-10453.

Novoselov, K. S., Fal, V., Colombo, L., Gellert, P., Schwab, M., & Kim, K. (2012). A roadmap for graphene. *Nature, 490*(7419), 192-200.

Oh, K., Morse, T., Weber, P., Kilian, A., & Reinhart, L. (1994). Continuous-wave oscillation of thulium-sensitized holmium-doped silica fiber laser. *Optics letters, 19*(4), 278-280.

Ohsaka, T., Izumi, F., & Fujiki, Y. (1978). Raman spectrum of anatase, TiO2. *Journal of Raman Spectroscopy, 7*(6), 321-324.

Okamoto, K. (2010). *Fundamentals of optical waveguides*: Academic press.

Onae, A., Okumura, K., Yoda, J., Nakagawa, K., & Kourogi, M. (2000, 14-19 May 2000). *A frequency measurement system for an optical frequency standard at 1.5 /spl mu/m.* Paper presented at the Conference on Precision Electromagnetic Measurements. Conference Digest. CPEM 2000 (Cat. No.00CH37031).

Pask, H., Carman, R. J., Hanna, D. C., Tropper, A. C., Mackechnie, C. J., Barber, P. R., & Dawes, J. M. (1995). Ytterbium-doped silica fiber lasers: versatile sources for the 1-1.2/spl mu/m region. *IEEE Journal of Selected Topics in Quantum Electronics, 1*(1), 2-13.

Reekie, L., Mears, R. J., Poole, S. B., & Payne, D. N. (1986). Tunable single-mode fiber lasers. *Lightwave Technology, Journal of, 4*(7), 956-960.

Rustad, G., & Stenersen, K. (1996). Modeling of laser-pumped Tm and Ho lasers accounting for upconversion and ground-state depletion. *Quantum Electronics, IEEE Journal of, 32*(9), 1645-1656.

Saraceno, C. J., Schriber, C., Mangold, M., Hoffmann, M., Heckl, O. H., Baer, C. R., . . . Keller, U. (2012). SESAMs for high-power oscillators: design guidelines and damage thresholds. *Selected Topics in Quantum Electronics, IEEE Journal of, 18*(1), 29-41.

Satoh, N., Nakashima, T., Kamikura, K., & Yamamoto, K. (2008). Quantum size effect in TiO2 nanoparticles prepared by finely controlled metal assembly on dendrimer templates. *Nature nanotechnology, 3*(2), 106-111.

Schawlow, A. L., & Townes, C. H. (1958). Infrared and optical masers. *Physical Review, 112*(6), 1940.

Scholle, K., Lamrini, S., Koopmann, P., & Fuhrberg, P. (2010). 2 μm Laser Sources and Their

Possible Applications. In B. Pal (Ed.), *Frontiers in Guided Wave Optics and Optoelectronics*. Croatia: InTech.

Set, S. Y., Yaguchi, H., Tanaka, Y., & Jablonski, M. (2004a). Laser mode locking using a saturable absorber incorporating carbon nanotubes. *Lightwave Technology, Journal of, 22*(1), 51-56.

Set, S. Y., Yaguchi, H., Tanaka, Y., & Jablonski, M. (2004b). Ultrafast fiber pulsed lasers incorporating carbon nanotubes. *IEEE Journal of Selected Topics in Quantum Electronics, 10*(1), 137-146.

Shcherbakov, E., Fomin, V., Abramov, A., Ferin, A., Mochalov, D., & Gapontsev, V. P. (2013). *Industrial grade 100 kW power CW fiber laser.* Paper presented at the Advanced Solid State Lasers.

Shi, H., Yan, R., Bertolazzi, S., Brivio, J., Gao, B., Kis, A., . . . Huang, L. (2013). Exciton dynamics in suspended monolayer and few-layer MoS2 2D crystals. *ACS nano, 7*(2), 1072-1080.

Singh, S. P., & Singh, N. (2007). Nonlinear effects in optical fibers: Origin, management and applications. *Progress In Electromagnetics Research, 73*, 249-275.

Smith, N. J., Blow, K., & Andonovic, I. (1992). Sideband generation through perturbations to the average soliton model. *Lightwave Technology, Journal of, 10*(10), 1329-1333.

Snitzer, E. (1961). Optical maser action of Nd+ 3 in a barium crown glass. *Physical Review Letters, 7*(12), 444.

Sobon, G. (2015). Mode-locking of fiber lasers using novel two-dimensional nanomaterials: graphene and topological insulators [Invited]. *Photonics Research, 3*(2), A56-A63. doi:10.1364/PRJ.3.000A56

Soffer, B. (1964). Giant pulse laser operation by a passive, reversibly bleachable absorber. *Journal of applied physics, 35*(8), 2551-2551.

Solodyankin, M. A., Obraztsova, E. D., Lobach, A. S., Chernov, A. I., Tausenev, A. V., Konov, V. I., & Dianov, E. M. (2008). Mode-locked 1.93 μm thulium fiber laser with a carbon nanotube absorber. *Optics letters, 33*(12), 1336-1338.

Sotor, J., Sobon, G., Kowalczyk, M., Macherzynski, W., Paletko, P., & Abramski, K. M. (2015). Ultrafast thulium-doped fiber laser mode locked with black phosphorus. *Optics letters, 40*(16), 3885-3888.

Standardization, I. O. f. (2006). Optics and photonics: Lasers and laser-related equipment: Test methods for laser beam power, energy and temporal characteristics Switzerland: ISO.

Straumann, N., & Zürich, U. (2017). History of Physics (17). *COMMUNICATIONS DE LA SSP*, 26.

Sun, Z., Hasan, T., Torrisi, F., Popa, D., Privitera, G., Wang, F., . . . Ferrari, A. C. (2010). Graphene mode-locked ultrafast laser. *ACS nano, 4*(2), 803-810.

Sun, Z., Rozhin, A., Wang, F., Hasan, T., Popa, D., O'neill, W., & Ferrari, A. (2009). A compact, high power, ultrafast laser mode-locked by carbon nanotubes. *Applied Physics Letters, 95*(25), 253102.

Svelto, O., & Hanna, D. (1998). Principles of lasers, 4-th ed: Springer.

Svelto, O., & Hanna, D. C. (1976). *Principles of lasers*: Springer.

Tamura, K., Jacobson, J., Ippen, E., Haus, H., & Fujimoto, J. (1993). Unidirectional ring resonators for self-starting passively mode-locked lasers. *Optics letters, 18*(3), 220-222.

Tanabe, S. (2002). Rare-earth-doped glasses for fiber amplifiers in broadband telecommunication. *Comptes Rendus Chimie, 5*(12), 815-824.

Tang, H., Prasad, K., Sanjines, R., Schmid, P., & Levy, F. (1994). Electrical and optical properties of TiO2 anatase thin films. *Journal of applied physics, 75*(4), 2042-2047.

Tian, Z., Wu, K., Kong, L., Yang, N., Wang, Y., Chen, R., . . . Tang, Y. (2015). Mode-locked thulium fiber laser with MoS2. *Laser Physics Letters, 12*(6), 065104.

Tropper, A. C., Smart, R. G., Perry, I. R., Hanna, D. C., Lincoln, J. R., & Brocklesby, W. S. (1991). *Thulium-doped silica fiber lasers.* Paper presented at the San Jose-DL tentative.

Tünnermann, A., Schreiber, T., & Limpert, J. (2010). Fiber lasers and amplifiers: an ultrafast performance evolution. *Applied optics, 49*(25), F71-F78.

Wallace, J. (2015). Ultrafast scientific lasers expand on their legacy: PENNWELL PUBL CO 98 SPIT BROOK RD, NASHUA, NH 03062-2801 USA.

Wang, Q., Ge, S., Li, X., Qiu, J., Ji, Y., Feng, J., & Sun, D. (2013). Valley carrier dynamics in monolayer molybdenum disulfide from helicity-resolved ultrafast pump–probe spectroscopy. *ACS nano, 7*(12), 11087-11093.

Wang, Q. H., Kalantar-Zadeh, K., Kis, A., Coleman, J. N., & Strano, M. S. (2012). Electronics and optoelectronics of two-dimensional transition metal dichalcogenides. *Nature nanotechnology, 7*(11), 699-712.

Wang, R., Chien, H.-C., Kumar, J., Kumar, N., Chiu, H.-Y., & Zhao, H. (2013). Third-harmonic generation in ultrathin films of MoS2. *ACS applied materials & interfaces, 6*(1), 314-318.

Wang, S., Yu, H., Zhang, H., Wang, A., Zhao, M., Chen, Y., . . . Wang, J. (2014). Broadband few-layer MoS2 saturable absorbers. *Advanced materials, 26*(21), 3538-3544.

Wang, Y., Huang, G., Mu, H., Lin, S., Chen, J., Xiao, S., . . . He, J. (2015). Ultrafast recovery time and broadband saturable absorption properties of black phosphorus suspension. *Applied Physics Letters, 107*(9), 091905.

Wang, Y., Qin, Y., Li, G., Cui, Z., & Zhang, Z. (2005). One-step synthesis and optical properties of blue titanium suboxide nanoparticles. *Journal of crystal growth, 282*(3), 402-406.

Woodward, R., Howe, R., Hu, G., Torrisi, F., Zhang, M., Hasan, T., & Kelleher, E. (2015). Few-layer MoS 2 saturable absorbers for short-pulse laser technology: current status and future perspectives [Invited]. *Photonics Research, 3*(2), A30-A42.

Woodward, R., Kelleher, E., Howe, R., Hu, G., Torrisi, F., Hasan, T., . . . Taylor, J. (2014). Tunable Q-switched fiber laser based on saturable edge-state absorption in few-layer molybdenum disulfide (MoS 2). *Optics express, 22*(25), 31113-31122.

Woodward, R. I., & Kelleher, E. J. (2015). 2D Saturable Absorbers for Fibre Lasers. *Applied Sciences, 5*(4), 1440-1456.

Wu, K., Zhang, X., Wang, J., & Chen, J. (2015). 463-MHz fundamental mode-locked fiber laser based on few-layer MoS 2 saturable absorber. *Optics letters, 40*(7), 1374-1377.

Xia, F., Wang, H., & Jia, Y. (2014). Rediscovering black phosphorus as an anisotropic layered material for optoelectronics and electronics. *Nat Commun, 5*. doi:10.1038/ncomms5458

Xia, F., Wang, H., Xiao, D., Dubey, M., & Ramasubramaniam, A. (2014). Two-dimensional material nanophotonics. *Nature Photonics, 8*(12), 899-907.

Xia, H., Li, H., Lan, C., Li, C., Zhang, X., Zhang, S., & Liu, Y. (2014). Ultrafast erbium-doped fiber laser mode-locked by a CVD-grown molybdenum disulfide (MoS 2) saturable absorber. *Optics express, 22*(14), 17341-17348.

Xiao, J., Long, M., Zhang, X., Zhang, D., Xu, H., & Chan, K. S. (2015). First-principles prediction of the charge mobility in black phosphorus semiconductor nanoribbons. *The journal of physical chemistry letters, 6*(20), 4141-4147.

Yan, P., Liu, A., Chen, Y., Wang, J., Ruan, S., Chen, H., & Ding, J. (2015). Passively mode-locked fiber laser by a cell-type WS2 nanosheets saturable absorber. *Scientific reports, 5*.

Yang, C. Y., Lin, Y. H., Chi, Y. C., Wu, C. L., Lo, J. Y., & Lin, G. R. (2015). Pulse-width saturation and Kelly-sideband shift in a graphene-nanosheet mode-locked fiber laser with weak negative dispersion. *Physical Review Applied, 3*(4), 044016.

Yang, S., Huang, N., Jin, Y. M., Zhang, H. Q., Su, Y. H., & Yang, H. G. (2015). Crystal shape engineering of anatase TiO 2 and its biomedical applications. *CrystEngComm, 17*(35), 6617-6631.

Zhang, H., Bao, Q., Tang, D., Zhao, L., & Loh, K. (2009). Large energy soliton erbium-doped fiber laser with a graphene-polymer composite mode locker. *Applied Physics Letters, 95*(14), 141103.

Zhang, H., Lu, S., Zheng, J., Du, J., Wen, S., Tang, D., & Loh, K. (2014). Molybdenum disulfide (MoS 2) as a broadband saturable absorber for ultra-fast photonics. *Optics express, 22*(6), 7249-7260.

Zhang, L., Zhou, J., Wang, Z., Gu, X., & Feng, Y. (2014). SESAM mode-locked, environmentally stable, and compact dissipative soliton fiber laser. *Photonics Technology Letters, IEEE, 26*(13), 1314-1316.

Zhang, Z., & Wu, H. (2014). Multiple band light trapping in ultraviolet, visible and near infrared regions with TiO2 based photonic materials. *Chem. Commun., 50*(91), 14179-14182.

Zheng, Z., Zhao, C., Lu, S., Chen, Y., Li, Y., Zhang, H., & Wen, S. (2012). Microwave and optical saturable absorption in graphene. *Optics express, 20*(21), 23201-23214.

Zirngibl, M., Stulz, L., Stone, J., Hugi, J., DiGiovanni, D., & Hansen, P. (1991). 1.2 ps pulses from passively mode-locked laser diode pumped Er-doped fibre ring laser. *Electronics Letters, 27*(19), 1734-1735.

Zitter, R. N. (1969). Saturated optical absorption through band filling in semiconductors. *Applied Physics Letters, 14*(2), 73-74.

LIST OF PUBLICATIONS AND PAPERS PRESENTED

SCIENTIFIC PUBLICATION

1. K. Tey, M. Rahman, A. Rosol, M. Rusdi, M. Mahyuddin, S. Harun, et al., "Q-switched double-clad Ytterbium-doped fiber laser using MoS2 flakes saturable absorber," in Materials Science and Engineering Conference Series, 2017, p. 012054.
2. A. A. L. Sulaiman Wadi Harun, Ezzatul Irradah Ismail, Hamzah Arof, Mohamad Badrol Hisyam Mahyuddin, "New 2D-Material Saturable Absorber for Ultrashort-Pulsed Fiber Laser Generation," in Fiber Lasers: Advances in Research and Applications, ed: Nova science publishers, 2017.
3. M. F. M. Rusdi, A. A. Latiff, M. C. Paul, S. Das, A. Dhar, H. Ahmad, et al., "Titanium Dioxide (TiO 2) film as a new saturable absorber for generating mode-locked Thulium-Holmium doped all-fiber laser," Optics & Laser Technology, vol. 89, pp. 16-20, 2017.
4. A. Rosol, H. Rahman, E. Ismail, Z. Jusoh, A. Latiff, and S. Harun, "Mode-locked fiber laser with a manganese-doped cadmium selenide saturable absorber," Chinese Optics Letters, vol. 15, p. 071405, 2017.
5. A. Rosol, Z. Jusoh, H. Rahman, M. Rusdi, S. Harun, and A. Latiff, "Graphene Oxide saturable absorber for generating eye-safe Q-switched fiber laser," in Materials Science and Engineering Conference Series, 2017, p. 012042.
6. Z. Rizman, U. Zakaria, A. Latiff, S. Harun, and Z. Jusoh, "Continues-wave Brillouin-Raman fiber ring laser using 7.7 km long dispersion compensating fiber at 1563 nm wavelength," in Materials Science and Engineering Conference Series, 2017, p. 012047.

7. Z. Rizman, U. Zakaria, Z. Jusoh, A. Latiff, and S. Harun, "Investigation of Brillouin Raman fiber laser operating at 1558 nm using THDF saturable absorber," in Materials Science and Engineering Conference Series, 2017, p. 012048.
8. N. N. Razak, A. A. Latiff, Z. Zakaria, and S. W. Harun, "Q-switched Erbium-doped Fiber Laser with a Black Phosphorus Saturable Absorber," Photonics Letters of Poland, vol. 9, pp. 72-74, 2017.
9. M. Rahman, M. Rusdi, M. Lokman, M. Mahyuddin, A. Latiff, A. Rosol, et al., "Holmium Oxide Film as a Saturable Absorber for 2 μm Q-Switched Fiber Laser," Chinese Physics Letters, vol. 34, p. 054201, 2017.
10. A. Nady, M. Ahmed, A. Numan, S. Ramesh, A. Latiff, C. Ooi, et al., "Passively Q-switched erbium-doped fibre laser using cobalt oxide nanocubes as a saturable absorber," Journal of Modern Optics, pp. 1-6, 2017.
11. A. Nady, M. Ahmed, A. Latiff, C. R. Ooi, and S. Harun, "Femtoseconds soliton mode-locked erbium-doped fiber laser based on nickel oxide nanoparticle saturable absorber," Chinese Optics Letters, vol. 15, p. 100602, 2017.
12. A. Nady, M. Ahmed, A. Latiff, A. Numan, C. R. Ooi, and S. Harun, "Nickel oxide nanoparticles as a saturable absorber for an all-fiber passively Q-switched erbium-doped fiber laser," Laser Physics, vol. 27, p. 065105, 2017.
13. M. Mahyuddin, A. Latiff, M. Rusdi, N. Irawati, and S. Harun, "Quantum dot cadmium selenide as a saturable absorber for Q-switched and mode-locked double-clad ytterbium-doped fiber lasers," Optics Communications, vol. 397, pp. 147-152, 2017.
14. A. Latiff, M. Rusdi, M. Hisyam, H. Ahmad, and S. Harun, "A generation of 2 μm Q-switched thulium-doped fibre laser based on anatase titanium (IV) oxide film saturable absorber," Journal of Modern Optics, vol. 64, pp. 187-190, 2017.

15. A. Latiff, N. Kadir, E. Ismail, H. Shamsuddin, H. Ahmad, and S. Harun, "All-fiber dual-wavelength Q-switched and mode-locked EDFL by SMF-THDF-SMF structure as a saturable absorber," Optics Communications, vol. 389, pp. 29-34, 2017.
16. N. Kadir, E. Ismail, A. Latiff, H. Ahmad, H. Arof, and S. Harun, "Transition Metal Dichalcogenides (WS2 and MoS2) Saturable Absorbers for Mode-Locked Erbium-Doped Fiber Lasers," Chinese Physics Letters, vol. 34, p. 014202, 2017.
17. N. Hisamuddin, Z. Jusoh, U. Zakaria, M. Zulkifli, A. Latiff, M. Yasin, et al., "Q-switched Raman fiber laser with titanium dioxide based saturable absorber," Optoelectronics and Advanced Materials-Rapid Communications, vol. 11, pp. 127-130, 2017.
18. N. Aziz, A. Latiff, M. Lokman, E. Hanafi, and S. Harun, "Zinc Oxide-Based Q-Switched Erbium-Doped Fiber Laser," Chinese Physics Letters, vol. 34, p. 044202, 2017.
19. S. W. H. Anas Abdul Latiff, Harith Ahmad, Mukul Chandra Paul, Shyamal Das, Anirba, Mohamad Farid Mohd Rusdi, "Q-Switched Fiber Lasers at the 2-Micron Region," in Fiber Lasers: Advances in Research and Applications, ed: Nova Science Publsihers, 2017.
20. A. Al-Masoodi, M. Ahmed, A. Latiff, H. Arof, and S. Harun, "Passively Q-switched Ytterbium doped fiber laser with mechanically exfoliated MoS2 saturable absorber," Indian Journal of Physics, vol. 91, pp. 575-580, 2017.
21. M. Ahmed, A. Al-Masoodi, A. Latiff, H. Arof, and S. Harun, "Mechanically exfoliated 2D nanomaterials as saturable absorber for Q-switched erbium doped fiber laser," Indian Journal of Physics, pp. 1-6, 2017.
22. A. Zulkifli, A. Latiff, M. C. Paul, M. Yasin, H. Ahmad, and S. Harun, "Dual-wavelength nano-engineered Thulium-doped fiber laser via bending of singlemode-

multimode-singlemode fiber structure," Optical Fiber Technology, vol. 32, pp. 96-101, 2016.

23. S. N. F. Zuikafly, F. Ahmad, M. H. Ibrahim, A. A. Latiff, and S. W. Harun, "Dual-wavelength passively Q-switched Erbium-doped fiber laser with MWCNTs slurry as saturable absorber," Photonics Letters of Poland, vol. 8, pp. 98-100, 2016.
24. H. Shamsudin, A. Latiff, N. Razak, Z. Jusoh, H. Ahmad, and S. Harun, "Performance comparison of single-mode single-cladding thulium doped and thulium/holmium co-doped fiber lasers in ring cavity," Journal of Optoelectronics and Advanced Materials, vol. 18, pp. 757-762, 2016.
25. H. Shamsudin, A. Latiff, N. Razak, H. Ahmad, and S. Harun, "Multi-wavelength thulium-doped fiber laser operating at slope efficiency of 16.57% in linear cavity configuration," Optoelectronics and Advanced Materials-Rapid Communications, vol. 10, pp. 129-132, 2016.
26. Z. Salleh, E. Ismail, N. Kadir, A. Latiff, M. Yasin, Z. Jusoh, et al., "Mode-Locked Erbium-Doped Fiber Laser with Titanium Dioxide Saturable Absorber," Digest Journal of Nanomaterials and Biostructures, vol. 11, pp. 1173-1178, 2016.
27. M. Rusdi, A. Latiff, E. Hanafi, M. Mahyuddin, H. Shamsudin, K. Dimyati, et al., "Molybdenum Disulphide Tape Saturable Absorber for Mode-Locked Double-Clad Ytterbium-Doped All-Fiber Laser Generation," Chinese Physics Letters, vol. 33, p. 114201, 2016.
28. M. C. Paul, A. Latiff, M. Hisyam, M. Rusdi, and S. Harun, "Generating 2 micron continuous-wave ytterbium-doped fiber laser-based optical parametric effect," Laser Physics Letters, vol. 13, p. 105109, 2016.
29. A. A. Latiff, M. B. Hisyam, M. F. M. Rusdi, Z. Jusoh, M. Yasin, S. W. Harun, "Dual-Wavelength Q-Switched Fiber Laser Using Mechanically Exfoliated Black

Phosphorus as a Saturable Absorber," Journal of Optoelectronics and Biomedical Materials, vol. 8, pp. 89-95, 2016.

30. A. Latiff, H. Shamsudin, Z. Tiu, H. Ahmad, and S. Harun, "Switchable soliton mode-locked and multi-wavelength operation in thulium-doped all-fiber ring laser," Journal of Nonlinear Optical Physics & Materials, vol. 25, p. 1650034, 2016.
31. A. Latiff, H. Shamsudin, N. Aziz, A. Hashim, N. Irawati, H. Ahmad, et al., "Mode-locked generation in thulium-doped fiber linear cavity laser," Optik-International Journal for Light and Electron Optics, vol. 127, pp. 11119-11123, 2016.
32. A. Latiff, H. Shamsudin, H. Ahmad, and S. Harun, "Q-switched thulium-doped fiber laser operating at 1940 nm region using a pencil-core as saturable absorber," Journal of Modern Optics, vol. 63, pp. 783-787, 2016.
33. A. Latiff, M. Rusdi, Z. Jusoh, M. Yasin, H. Ahmad, and S. Harun, "1941 nm Q-switched thulium-doped fiber laser with a multi-layer black phosphorus saturable absorber," Optoelectronics and Advanced Materials-Rapid Communications, vol. 10, pp. 801-806, 2016.
34. A. Latiff, M. Rusdi, M. Hisyam, H. Ahmad, and S. Harun, "Black phosphorus as a saturable absorber for generating mode-locked fiber laser in normal dispersion regime," in Second International Seminar on Photonics, Optics, and Its Applications (ISPhOA 2016), 2016, pp. 101500U-101500U-6.
35. A. Latiff, A. Dhar, S. Harun, I. Babar, S. Das, M. C. Paul, et al., "Dual-Wavelength Holmium-Doped Fiber Laser Pumped by Thulium–Ytterbium Co-Doped Fiber Laser," Chinese Physics Letters, vol. 33, p. 054202, 2016.
36. E. Ismail, N. Kadir, A. Latiff, H. Ahmad, and S. Harun, "Black phosphorus crystal as a saturable absorber for both a Q-switched and mode-locked erbium-doped fiber laser," RSC Advances, vol. 6, pp. 72692-72697, 2016.

37. E. Ismail, A. Kadir, A. Latiff, H. Ahmad, and S. Harun, "Q-switched erbium-doped fiber laser operating at 1502 nm with molybdenum disulfide saturable absorber," Journal of Nonlinear Optical Physics & Materials, vol. 25, p. 1650025, 2016.

38. M. Hisyam, M. Rusdi, A. Latiff, and S. Harun, "PMMA-doped CdSe quantum dots as saturable absorber in a Q-switched all-fiber laser," Chinese Optics Letters, vol. 14, p. 081404, 2016.

39. M. Hisyam, M. Rusdi, A. Latiff, and S. Harun, "Generation of Mode-locked Ytterbium doped fiber ring laser using few-layer black phosphorus as a saturable absorber," 2016.

40. N. Hisamuddin, U. Zakaria, M. Zulkifli, A. Latiff, H. Ahmad, and S. Harun, "Q-Switched Raman Fiber Laser with Molybdenum Disulfide-Based Passive Saturable Absorber," Chinese Physics Letters, vol. 33, p. 074208, 2016.

41. A. Al-Masoodi, M. Ahmed, A. Latiff, H. Arof, and S. Harun, "Q-switched ytterbium-doped fiber laser using black phosphorus as saturable absorber," Chinese Physics Letters, vol. 33, p. 054206, 2016.

42. M. H. M. Ahmed, A. A. Latiff, H. Arof, H. Ahmad, and S. W. Harun, "Soliton mode-locked erbium-doped fibre laser with mechanically exfoliated molybdenum disulphide saturable absorber," IET Optoelectronics, vol. 10, pp. 169-173, 2016.

43. M. Ahmed, A. Latiff, H. Arof, and S. Harun, "Ultrafast erbium-doped fiber laser mode-locked with a black phosphorus saturable absorber," Laser Physics Letters, vol. 13, p. 095104, 2016.

44. M. Ahmed, A. Latiff, H. Arof, and S. Harun, "Mode-locking pulse generation with MoS 2–PVA saturable absorber in both anomalous and ultra-long normal dispersion regimes," Applied optics, vol. 55, pp. 4247-4252, 2016.

45. M. Ahmed, A. Latiff, H. Arof, H. Ahmad, and S. Harun, "Femtosecond mode-locked erbium-doped fiber laser based on MoS 2–PVA saturable absorber," Optics & Laser Technology, vol. 82, pp. 145-149, 2016.

46. M. Ahmed, A. Banabila, A. Latiff, N. Irawati, N. Ali, S. Harun, et al., "Tunable Q-switched erbium doped fiber laser with graphene oxide paper based saturable absorber," Optoelectronics and Advanced Materials-Rapid Communications, vol. 10, pp. 791-796, 2016.

47. I. M. Babar, A.A. Latiff, H. Shamsudin, M.C. Paul, A. Hal-der, S. Das, S.K. Bhadra, H. Ahmad, S.W. Harun, "Highly Efficient Cladding Pumped Dual-Wavelength Thulium Ytterbium Co-Doped Fiber Laser," Acta Physica Polonica A, vol. 130, p. 1332, 2016.

48. M. Paul, A. Dhar, S. Das, A. Latiff, M. Ahmad, and S. Harun, "Development of Nano-engineered Thulium-doped Fiber Laser With Low Threshold Pump Power and Tunable Operating Wavelength," IEEE Photonics Journal, 2015.

49. A. A. Latiff, M. T. Ahmad, Z. Zakaria, H. Ahmad, and S. W. Harun, "Q-Switched Thulium-Doped Fiber Laser at 2 Micron Region by 802 nm Pumping," Jurnal Teknologi, vol. 74, pp. 81-84, 2015.

50. M. T. Ahmad, A. A. Latiff, Z. Zakaria, Z. Jusoh, H. Ahmad, and S. W. Harun, "AMPLIFICATION AND LASING CHARACTERISTICS OF THULIUM YTTERBIUM CO-DOPED FIBER," Jurnal Teknologi, vol. 74, pp. 63-67, 2015.

51. M. Ahmad, A. Latiff, H. Shamsudin, Z. Zakaria, H. Ahmad, and S. Harun, "Wavelength-tuneable thulium-doped fiber laser based on fiber Bragg grating stretching," Optoelectronics and Advanced Materials-Rapid Communications, vol. 9, pp. 623-625, 2015.

52. C. Fauziah, A. Rosol, A. Latiff, and S. Harun, "The generation of Q-switched erbium-doped fiber laser using black phosphorus saturable absorber with 8% modulation depth."

PATENT

1. S. W. Harun, A. A. Latiff, and H. Ahmad, "A Method of Producing Q-switched Thulium Doped Fibre Lasers," Application No. PI2015700623 (MyIPO Patents, 27th February 2015).
2. S. W. Harun, A. A. Latiff, and H. Ahmad, " Titanium Oxide Film as A Passive Saturable Absorber for Eye-Safe Pulsed Fiber Laser Generation," Ref. No. 603/1217 (UMCIC Level, 31st July 2017).

EXHIBITION

1. S. W. Harun, A. A. Latiff, H. Shamsudin, and H. Ahmad, “Two Micron Q-switched Fibre Laser”, PECIPTA 2015 - Bronze Medal
2. S. W. Harun, A. A. Latiff, H. Shamsudin, and H. Ahmad, “CAHAYA: 2 Micron Q-switched Fiber Laser”, MTE 2016 – Silver Medal
3. S. W. Harun, A. A. Latiff, H. Shamsudin, and Z. Jusoh, “High Power Compact Pulsed Laser”, IIDEX 2016 – Gold Medal
4. S. W. Harun, A. A. Latiff, H. Shamsudin, and Z. Jusoh, “Eye-Safe Laser Module” Q-switched Fiber Laser”, MPI’16 – Gold Medal
5. S. W. Harun, A. A. Latiff, M. B. Hisham, and Z. Jusoh, “Holmium Pulsed Laser Converter”, Si2te 2017 – Gold Medal
6. S. W. Harun, A. A. Latiff, M. F. A. Rahman, A. H. A. Rosol, M. F. M. Rusdi, M. B. Hisham, and H. Ahmad, “Holmium Pulsed Laser Converter”, PECIPTA 2017 – Gold Medal